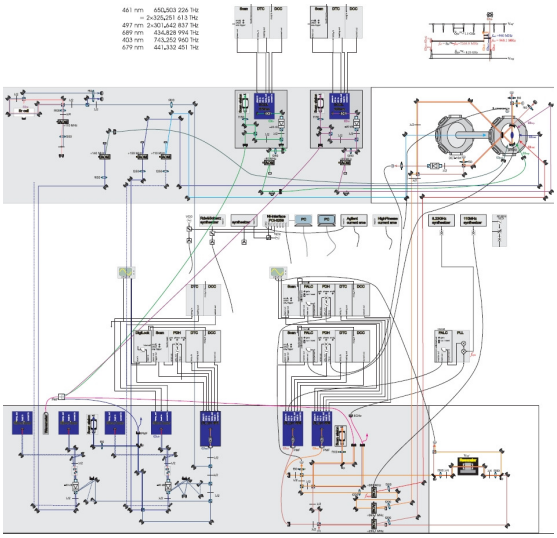

A practical course in

Optical Spectroscopy

Ph.W. Courteille
Universidade de São Paulo
Instituto de Física de São Carlos
01/05/2024

2

.

.

Preface

This script was developed for the course *Optical Spectroscopy* (7600048) offered by the São Carlos Institute of Physics (IFSC) of the University of São Paulo (USP). The script is a preliminary version being continuously subject to correction and modification. Error notifications and suggestions for improvement are always welcome. The script incorporates exercises the solutions of which can be obtained from the author.

Information and announcements regarding the course will be posted on the web page: http://www.ifsc.usp.br/ strontium/ − > Teaching

Information and announcements regarding the course will be published on the website:
http://www.ifsc.usp.br/ strontium/ − > Teaching − > Semester

The student's assessment will be based on written tests and a seminar on a special topic chosen by the student. In the seminar the student will present the chosen topic in 15 minutes. He will also deliver a 4-page scientific paper in digital form. Possible topics are:
- The Jaynes-Cummings model and the quantization of the electro-magnetic field,
- The method of quantum Monte-Carlo wavefunction simulation,
- Elitzur and Vaidman bomb testing problem,
- Saturation spectroscopy,
- Short pulses and time-resolved spectroscopy,
- Principle of the lock-in amplifier,
- Intensity stabilization techniques,
- Pound-Drever-Hall stabilization,
- Magneto-optical trap,
- The frequency comb.

The following literature is recommended for preparation and further reading:

Ph.W. Courteille, script on *Optical spectroscopy: A practical course* (2020)

Ph.W. Courteille, script on *Electrodynamics: Electricity, magnetism, and radiation* (2020)

Ph.W. Courteille, script on *Quantum mechanics applied to atomic and molecular physics* (2020)

H. Kogelnik and X.Y. Li, Appl. Opt. **5**, 155 (1966) *Laser beams and resonators*

W. Demtröder, *Laser spectroscopy: basic concepts and instrumentation*, 2. ed., Berlin, Springer Verlag (1996)

G.R. Fowles, *Introduction to Modern Optics*, New York, Holt, Rinehart and Winston (1968)

S.C. Zilio, *Óptica Moderna*, IFSC-USP (2009)

M. Born, *Principles of Optics*, 6.ed. Pergamon Press New York (1980)

P. Horowitz and W. Hill, *The Art of Electronics*, Cambridge University Press (2001)

A. Yariv, *Quantum Electronics*, John Wiley & Sons (1989)

A. Yariv and P. Yeh, *Optical waves in crystals*, Wiley (2002)

U. Tietze & Ch. Schenk, *Halbleiterschaltungstechnik*, Springer-Verlag (1978)

O. Föllinger, Hüthig-Verlag, *Regelungstechnik*, Heidelberg (1985)

H.J. Metcalf, P. van der Straten, *Laser Cooling and Trapping*, (Graduate Texts in Contemporary Physics, Springer, 1999)

J. Weiner and P-T. Ho, *Light-Matter Interaction: Fundamentals and Applications* (Springer-Verlag, Berlin, 2003)

R. Loudon, *The quantum theory of light*, Oxford Science Publications, Oxford (1973)

Content

Part I

Theoretical Foundations

Chapter 1

Atoms and photons

Our perception of the macroscopic world is dominated by light and matter. Since ancient Greek philosophy our conceptions of light and matter follow a capricious evolution, culminating with the discovery of the atom and the formulation of the theories of *electrodynamics and quantum mechanics*. Combining those two theories and accepting that both, light and matter exhibit particle-like and wave-like features, we believe to have nowadays at hand a reasonably sound picture. This confidence is alimented by the predictive power of modern physics. Nevertheless, there remain many open questions, in particular, when it comes to cooperative effects in light scattering from ensembles of atoms: On one hand, Maxwell's equations tell us how light interacts with macroscopic bodies via reflection, refraction, emission of radiation, and even exerting radiative forces. On the other hand, atomic physics tells us to break down matter into indivisible atoms, with Niels Bohr teaching us, how light interacts with those atoms. Now, the transition from the microscopic quantum world to the classical macroscopic world is particularly tricky, and much can be learned extending the quantum concepts to collective effects gradually increasing the number of atoms and their density. Some of this will be done during this school. In this series of lectures, we will mostly concentrate on the interaction of light with individual atoms and only in the last lecture discuss an example of a collective effect in a dilute gas.

We start the lecture with a brief historical survey and a definition of the area of research in physics covered by this lecture, which is the *interaction of light with cold atoms*. As already mentioned the correct framework of this area is provided by the theories of *electrodynamics and quantum mechanics*. We will review quantum mechanical time-dependent perturbation theory, which we apply to the Rabi problem of two levels interacting with a coherent radiation field. We will briefly introduce the notions of the dressed states and of quantum jumps.

1.1 Introduction

1.1.1 The discovery of the atom

The fundamental idea of quantum mechanics is the assumption of the existence of entities that can not be subdivided beyond a certain limit. Examples are the mass of a body, the speed of an electron orbiting an atom, or the intensity of a beam of light. This idea was first uttered by *Leucippus* 500 years a.c. and his student *Democritus*, who imagined matter being made of smallest particles which they called *atoms*. These

atoms move freely, collide, combine, and separate: 'There is nothing else than atoms and free space.' The microscopic atoms would have the same characteristics as the macroscopic objects they form when they combine, for example, color and shape. The idea of the atom resurfaced and was refined in the course of the 18^{th} century (see Tab. 1.1 below). Today, we know that the basic idea was good, but reality is a little more complicated.

Table 1.1: *Historical time line of the quantization of matter*

500 a.c.	Democritus	invention of the atom
1800	Avogadro, Dalton	reinvention of the atom
1897	Thomson	charge transport, raisin-in-a-cake model
1909	Rutherford, Geiger, Marsden	α-scattering, charge localized in nuclei
1911	Rutherford	planetary model
1900	Bohr	quantized orbitals
1923	de Broglie	matter has characteristics of waves
1927	Davisson, Germer, Stern	electron and atoms diffraction

Still, at the end of the 19^{th} century, the physical world seemed rather simple: matter and light was all that existed. Matter was made up of atoms and light was a wave. Therefore, to describe a real system, it was enough to calculate the trajectories of its elementary particles, the propagation of light, and the way they interact.

However, new experimental observations, such as the ultraviolet divergence of black-body radiation, that appeared in the late 19^{th} century, were incompatible with these traditional concepts. New ideas were pioneered by *Max Planck* who, in 1905, with a little help from Einstein quantized the electromagnetic field, and therefore the light, into small harmonic oscillators. This was the starting point for the development of a new theory called quantum mechanics. Soon, this theory was applied to explain the photoelectric effect. The second important step was initialized by *Niels Bohr*, who quantized the hydrogen atom in 1913 into discrete excitation levels.

Table 1.2: *Historical time line of the quantization of light*

1801	Young	light is diffracted like a wave
1860	Maxwell	unified theory of electrodynamics including light
1888	Hertz	detection of radio waves
$\sim$ 1890		accurate measurements of the black-body radiation spectrum
1900	Planck	quantum hypothesis: $E = h\nu$
1905	Einstein	photoelectric effect, light behaves like a particle

Nowadays we know that our universe is not as simple as classical mechanics suggested, and that atoms are also waves and light also behaves like particles. This *duality principle* is one of the fundamental ideas of quantum mechanics. The appearance of an object as a wave or as a particle depends on the situation in which it is observed. While the wave nature of light was well established in classical physics since

a long time, Louis de Broglie was the first in 1924 to apply the duality principle also to massive particles and to predict that particles, under certain conditions, behave like waves the wavelengths of which increase as their velocity decreases. Each particle (or body) is delocalized along a distance corresponding to this 'de Broglie wavelength'. This feature of matter was soon discovered experimentally in electron beams and is still used today in commercial devices, for example in electron microscopes.

1.1.2 Definition of the research area

Having decomposed our world into its elementary components, light and atoms, we may now recompose it by identifying the relevant degrees of freedom and gradually increasing the complexity of the system we want to study. In quantum mechanics we associate an energy to every degree of freedom and to its interaction with other degrees of freedom.

Looking for example at a *single atom*: it has a mass and therefore mechanical degrees of freedom which may carry kinetic and potential energy,

$$\hat{H}_{cm} = \frac{\mathbf{P}^2}{2M} + V(\mathbf{R}) \ . \tag{1.1}$$

On the other hand, we learn in atomic physics, that atoms also have an internal structure, which is due to the motion of negatively charged electrons orbiting around a positively charged nucleus. The details of the internal structure, which is organized into discrete energy levels, are very complicated, and its derivation will not be the topic of this course. Instead we assume the structure of energy levels $\hbar\omega_i$ as given, we write it down as,

$$\hat{H}_{ele} = \sum_i \hbar\omega_i |i\rangle\langle i| \ , \tag{1.2}$$

and illustrate it in so-called Grotrian diagrams, which exhibit the orbital quantum numbers in a compact way. An example is shown in Fig. 1.1. Note that not only the *energy* of an orbital is important, but also its *configuration*, because this determines the transition probability between different orbitals via selection rules.

Since Planck's treatment of blackbody radiation, we know that any radiation field is composed of quanta called *photons*. Since, in a radiation mode (denoted by its wavevector $\mathbf{k}$) all photons have equal energy $\hbar\omega_{\mathbf{k}}$, we may treat it like a harmonic oscillator and write the Hamiltonian of a radiation field in terms of photon creation and annihilation operators,

$$\hat{H}_{rad} = \sum_{\mathbf{k}} \hbar\omega_{\mathbf{k}} \left(\hat{a}^\dagger_{\mathbf{k}} \hat{a}_{\mathbf{k}} + \tfrac{1}{2} \right) \ . \tag{1.3}$$

It is important to be aware that radiation fields do not only carry energy (via their intensity), but they also carry momentum (via their Poynting vector).

Obviously, the energy associated with every degree of freedom (atomic or radiative) is *conserved*, and this also holds for linear and angular momentum. Degrees of freedom may interact, where we understand any interaction in terms of collisions which must conserve energy, momentum, and angular momentum, as well. In quantum mechanics we describe a collision by a concatenation of creation, annihilation or

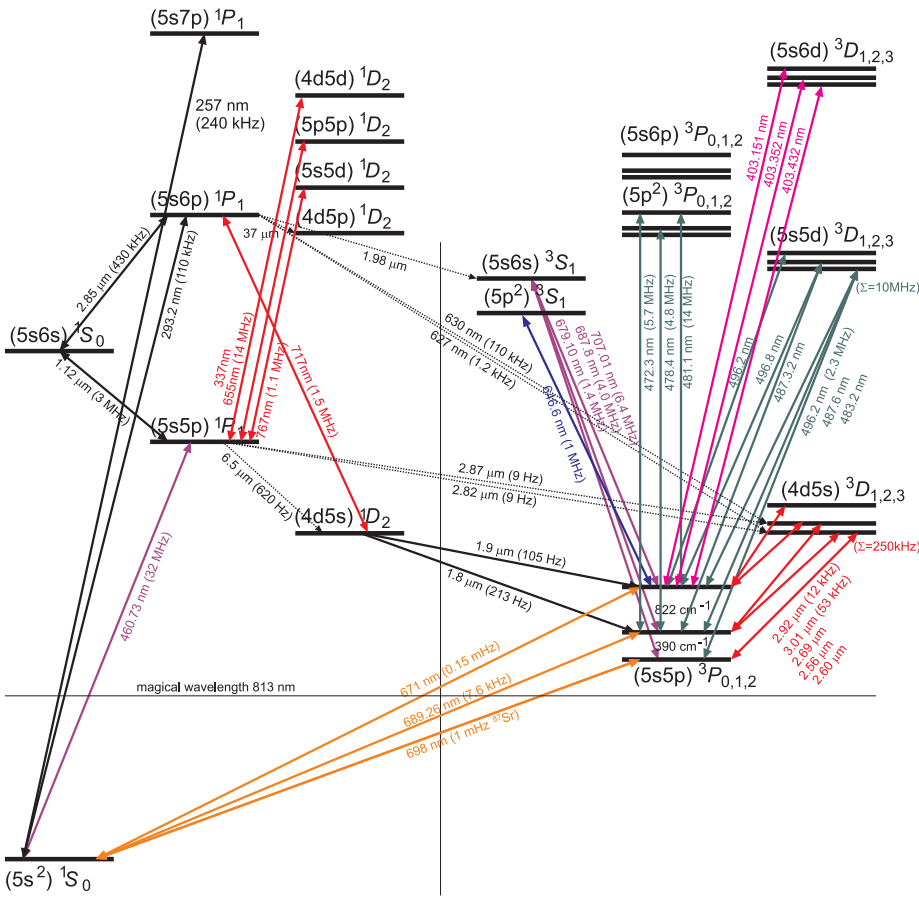

Figure 1.1: Grotrian diagram of strontium.

transition operators acting on different degrees of freedom. For example, if $\hat{a}^\dagger_{\mathbf{k}}$ means the creation of a photon in mode $\mathbf{k}$ and $\hat{\sigma}^- \equiv |1\rangle\langle 2|$ the transition of an atom from an excited state $|2\rangle$ to a ground state $|1\rangle$, then the operator,

$$\hat{H}_{int} \propto \hat{a}^\dagger_{\mathbf{k}} \hat{\sigma}^- e^{\imath \mathbf{k}\cdot\hat{\mathbf{R}}} \tag{1.4}$$

describes the process of a photon emission in compliance with Bohr's model. Here, the term $e^{\imath \mathbf{k}\cdot\hat{\mathbf{R}}} = |\mathbf{P} + \hbar\mathbf{k}\rangle\langle\mathbf{P}|$ describes the transition of the motional state of the atomic center-of-mass to a momentum state accelerated by the photonic recoil $\hbar\mathbf{k}$.

The operator (1.4) represents the most fundamental process in light-matter interaction, which involves three degrees of freedom: the atomic center-of-mass motion, a photon, and the internal atomic excitation. Not all three degrees of freedom are always relevant for the understanding of a phenomenon, as we will study in many examples. On the other hand, there are other possible degrees of freedom, which may couple. In this lecture we will mostly disregard interaction with other atoms (van der Waals, collisions) and quantum statistics. Furthermore, we will mostly treat light

as a classical field, which is justified whenever the light modes are macroscopically populated.

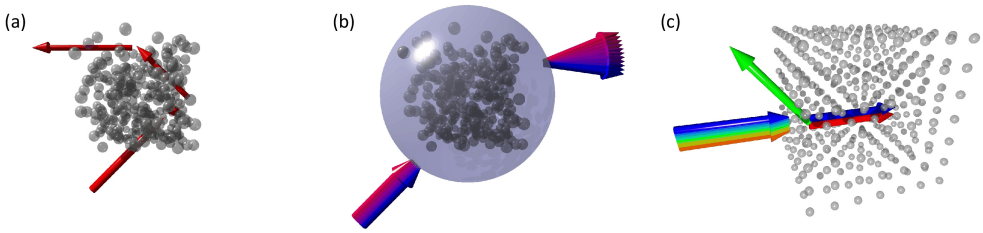

Figure 1.2: (a) Artist's view of multiple scattering of a photon through a dilute cloud. (b) Atomic cloud as a bulk object characterized by a refraction index $n(\mathbf{r})$. (c) Illustration of a photonic band in an optical lattice.

1.1.2.1 Why studying ultracold atomic gases?

Cold atoms have a lot of advantages (and no major inconvenience). Cold atomic clouds are in the same time macro- and microscopic: On one hand, a cloud of one billion atoms represents a macroscopic object so large, that it can be characterized by a refraction index and its fluorescence can be seen by eye. On the other hand, with a typical density 10 orders of magnitude lower than the air we breathe, it is so dilute that the distance between atoms is much larger than a wavelength of visible light. We can thus picture the propagation of light inside a cloud as photons bouncing off individual atoms by microscopic scattering, as illustrated in Fig. 1.2. Hence, atomic clouds allow us to study macro- and microscopic aspects of scattering in the same time.

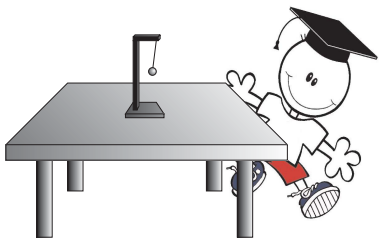

Figure 1.3: Most quantum optics experiments are table top experiment.

Second, we dispose today of incredibly powerful techniques for controlling and measuring atoms. Clouds can be isolated from all kinds of noise sources. We control energy and particle exchange with the environment over the time scale of experiments. We can manipulate all essential control parameters, such as size, temperature, and even the interatomic interaction strength. We can measure thermodynamic quantities such as the internal energy, chemical potential or heat capacity. All relevant degrees of freedom can be controlled up to a level, where the *quantum nature of the degrees of freedom dominates the dynamics*, for example in cavity QED experiments of single atoms trapped by single photons. Moreover, we can today simulate other fields of physics, such solid state physics, with atoms trapped and periodically ordered in optical lattices and detect effects that had been predicted but never observed in solids. An interesting particularity is that all experiments are performed on trapped, i.e. inhomogeneous samples.

An important practical advantage is the fact, that atom optical experiments are table top experiments. Even though the creation of a cold atomic cloud or Bose-Einstein condensate is still difficult, it can, in principle, be done by a single medium-sized PhD student.

The general importance of the field of atom optics has been acknowledged with 20 Nobel prices in the last 25 years awarded to Dehmelt, Paul, Ramsey, Cohen-Tannoudji, Chu, Phillips, Cornell, Wieman, Ketterle, Hänsch, Glauber, Hall, Wineland, Haroche, Ahskin, plus several Nobel prices granted to closely related areas of physics (De Gennes, Leggett, Thouless, Haldane, Kosterlitz).

1.1.2.2 The atom optical toolbox

Let us now give a brief overview on the atom optical toolbox: Typically, we work with between 1 and 10^{10} atoms (or sometimes ions).

External trapping potentials compress the clouds to low or high densities of $n = 10^9 ... 10^{14}\,\mathrm{cm}^{-3}$, which however are still ten orders of magnitude below atmospheric pressure. This means that all experiments must be conducted in extreme ultrahigh vacuum (XUHV) chambers. The greatest breakthrough in atomic optics, in the eighties and nineties, was the invention of optical cooling techniques, which could bring atomic clouds to 1 μK cold and even picoKelvin ultracold temperatures.

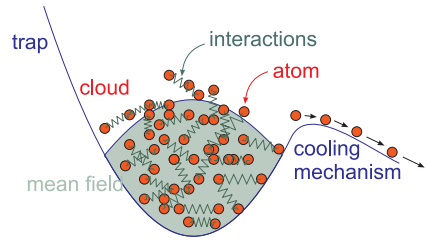

Figure 1.4: Cold trapped atoms.

Another important breakthrough was the observation of so-called Feshbach resonances, which allow to vary the self-interaction of the gases over extremely wide ranges, with collision cross sections ranging from 0 to at least $\sigma_{collision} \simeq 10^{-9}\,\mathrm{cm}^2$, and even in real-time. Consequently, we have separate influence over all contributions to the total energy: over the potential energy by compressing, deforming or shaking the trap, over the kinetic energy by cooling or exciting collective vibrations, and finally over the self-energy via the Feshbach resonances [22, 44],

$$\begin{array}{lccc} & \text{trapping} & \text{cooling} & \text{Feshbach resonances} \\ & \downarrow & \downarrow & \downarrow \\ E & = E_{pot} & + E_{kin} & + E_{self} \end{array} \tag{1.5}$$

1.1.3 Exercises

1.1.3.1 Ex: Radiation of an oscillating dipole

Calculate the angular distribution of the power radiated by an oscillating electric or magnetic dipole from expressions for the emitted electric and magnetic fields found in literature.

1.1.3.2 Ex: Bohr's atom

In 1913, Niels Bohr presented his atomic model adapting Rutherford's model to the quantization ideas proposed by Max Planck.
a. Impose the quantization rule for the angular momentum ($L = n\hbar$) of an electron orbiting an atom of atomic number Z to find an expression for the radii of the allowed orbits.
b. According to Bohr's model, the transition between different orbits is accompanied by the emission (or absorption) of a photon. Determine the energy of a photon emitted during a transition between the first excited state and the ground state of a hydrogen atom.
c. Consider an electron trapped in an infinite one-dimensional box potential of width a. Determine an expression for the electronic energy levels.
d. What should be the width a of this potential, in terms of the Bohr radius, so ensure that a photon emitted during a transition between the first excited state and the ground state equals that obtained in item (b)?

1.1.3.3 Ex: The hydrogen atom

The hydrogen atom can be seen as a point-like proton and an electron distributed over space with charge density $\rho = Ae^{-2r/a_B}$ around the proton that is in the center. Here, A is a constant and r is the distance from the center.
a. Calculate A considering the fact that the atom is electrically neutral.
b. Calculate the amplitude of the electric field at a radius $r = a_B$.

1.2 The discovery of the photon

The concept of the nature of light has a variable history. Newton proposed around ~ 1650 a corpuscular model to explain Snellius' law on the refraction of a light beam penetrating a crystal. Around the same time Huygens found a wave-based interpretation. The two models predicted different speeds of light within the dense medium. Newton found, that the speed of light is greater in the medium than outside, while Huygens found the opposite [1]. In the late 1800's the wave nature of light was established through observations of interference effects confirming Huygens' hypothesis. At that time, the world appeared to be simple: Light was a wave and matter was composed of particles. However, some observations made were incompatible with this simplistic ideas, for example, the spectrum of blackbody radiation, the Compton effect, the specific heat of the solid, the radiation pressure, and the photoelectric effect. All these observations are readily understood by assuming a corpuscular nature of the light [2].

Nowadays, knowing the theory of quantum mechanics, we know that both ideas have their range of validity and that the electromagnetic radiation is dual: In general, propagation and interference effects are best described by waves. However, when interacting with matter, light tends to localize into small particles called photons.

[1] Note, until today there remain doubts about the correct value of the momentum of light in dielectric media [60].

[2] The corpuscular hypothesis is now called the second quantization of quantum theory or quantization of the electromagnetic field.

1.2.1 Radiation in a conductive cavity

In the age of lasers a classical treatment of the emission and absorption of light may seem an atavism. However, even with coherent and monochromatic radiation sources, the most commonly used physical picture is that of a classical optical field interacting with an atom or a molecule whose energetic structure is treated quantum mechanically. And even the atomic or molecular dipole is often treated like a classical oscillator. The exposition of such a dipole to simple boundary conditions prepares the analogous development of a quantum oscillator and provides a direct path to quantization of the radiation field.

Even if we rarely do experiments by throwing light into a small hole in a metallic box, the electromagnetic fields obtained by solving Maxwell's equation are particularly simple for boundary conditions, where the fields disappear on the inner surfaces of the box. Before discussing the physics of radiation in a perfectly conducting cavity, we have to introduce some basic relations between electromagnetic amplitudes, stored energy, and intensity.

The electric field of a plane wave oscillating with frequency ω and propagating through vacuum in the direction of propagation defined by the *wave vector*,

$$\mathbf{k} = \frac{2\pi}{\lambda}\hat{\mathbf{k}} \,, \tag{1.6}$$

can be written,

$$\vec{\mathcal{E}} = \vec{\mathcal{E}}_0 e^{\imath(\mathbf{k}\cdot\mathbf{r}-\omega t)} \,, \tag{1.7}$$

where $\vec{\mathcal{E}}_0 = \mathcal{E}_0\hat{\mathbf{e}}$ consists of an amplitude $\mathcal{E}_0$ and a polarization $\hat{\mathbf{e}}_1$. Since the field $\vec{\mathcal{E}}_0$ is transverse to the direction of propagation, the polarization has two components perpendicular to $\mathbf{k}$. The magnetic induction field associated with the wave is,

$$\mathcal{B}_0 = \tfrac{1}{c}\mathcal{E}_0 \,. \tag{1.8}$$

For a propagating wave $\vec{\mathcal{E}}$ and $\vec{\mathcal{B}}$ are in phase, while for a standing wave they are out of phase.

For a given cavity mode we can express the standing wave in this mode as,

$$\vec{\mathcal{E}} = \vec{\mathcal{E}}_0(\mathbf{r})e^{-\imath\omega t} \,. \tag{1.9}$$

The energy of the electromagnetic field of a standing wave, averaged over one oscillation of the frequency ω is,

$$\bar{U} = \frac{1}{2}\int\left(\frac{\varepsilon_0}{2}|\vec{\mathcal{E}}|^2 + \frac{1}{2\mu_0}|\vec{\mathcal{B}}|^2\right)dV \,. \tag{1.10}$$

Now, the *energy density* of the oscillating electromagnetic field is given by,

$$\boxed{\bar{u} = \frac{d\bar{U}}{dV} = \frac{1}{4}\left(\varepsilon_0|\vec{\mathcal{E}}|^2 + \frac{1}{\mu_0}|\vec{\mathcal{B}}|^2\right)} \,. \tag{1.11}$$

From the equation (1.8) we can see that the contributions of the electric and magnetic fields are equal. Therefore,

$$\bar{U} = \tfrac{1}{2}\int\varepsilon_0|\vec{\mathcal{E}}|^2 dV \qquad \text{and} \qquad \bar{u} = \tfrac{1}{2}\varepsilon_0|\vec{\mathcal{E}}|^2 \,. \tag{1.12}$$

Another important quantity is the *flux of electromagnetic energy* through a surface. The *Poynting vector* describing this flux is defined by,

$$\mathbf{I} = \tfrac{1}{\mu_0}\vec{\mathcal{E}} \times \vec{\mathcal{B}} \; . \tag{1.13}$$

Again using the equation (1.8), we find the value averaged over a time period,

$$\boxed{\bar{I} = \tfrac{1}{2}\varepsilon_0 c|\vec{\mathcal{E}}|^2} \; . \tag{1.14}$$

This quantity, called *intensity*, describes the fact that the flux is a density of energy multiplied with the velocity of propagation in vacuum,

$$\bar{u}c = \tfrac{1}{2}\varepsilon_0 c|\vec{\mathcal{E}}|^2 = \bar{I} \; . \tag{1.15}$$

The intensity can also be written,

$$\bar{I} = \frac{1}{2}\sqrt{\frac{\varepsilon_0}{\mu_0}}|\vec{\mathcal{E}}|^2 \; . \tag{1.16}$$

where the factor $\sqrt{\mu_0/\varepsilon_0}$ is called *impedance of free space*, because it has the unit of a resistance and the last equation has the same form as the power dissipated in a resistor,

$$W = \frac{1}{2}\frac{V^2}{R} \; . \tag{1.17}$$

1.2.2 Black body radiation

We now want to calculate the energy density inside the cavity before using the result to describe the interaction between light and a sample of two-level atoms located inside the cavity. The basic idea is to say that the electrons inside the conducting surface of the cavity oscillate because of thermal motion. The oscillation generates a dipolar radiation leading to stationary waves developing within the cavity. As the walls of the cavity are conducting, the electric field $\vec{\mathcal{E}}$ must disappear inside the wall and on its surfaces. The task is now twofold: first count the number of possible standing waves, which satisfy the boundary conditions as a function of frequency; second, determine the energy for each wave and then calculate the spectral distribution of the energy within the cavity.

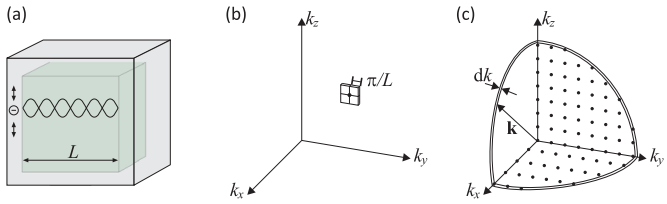

Figure 1.5: (a) Cavity in position space showing the thermal motion of the electrons inside the walls. (b and c) Density-of-states in a cavity in momentum space.

The equations describing the radiated energy in free space are,

$$\nabla^2\vec{\mathcal{E}} = \frac{1}{c^2}\frac{\partial^2\vec{\mathcal{E}}}{\partial t^2} \qquad \text{and} \qquad \nabla\cdot\vec{\mathcal{E}} = 0\ . \tag{1.18}$$

The stationary waves solutions separate into terms oscillating in time and in space. Now, respecting the boundary conditions for a three-dimensional box of length L, we have for the components of $\vec{\mathcal{E}}$ [3],

$$\begin{aligned}\vec{\mathcal{E}}(\mathbf{r},t) = e^{-\imath\omega t}[&\hat{\mathbf{e}}_x\cos(k_x x)\sin(k_y y)\sin(k_z z)\\ &+\hat{\mathbf{e}}_y\sin(k_x x)\cos(k_y y)\sin(k_z z)\\ &+\hat{\mathbf{e}}_z\sin(k_x x)\sin(k_y y)\cos(k_z z)]\ ,\end{aligned} \tag{1.19}$$

with the components,

$$k_x = \frac{\pi n_x}{L} \qquad \text{for} \qquad n_x = 0,1,2,... \tag{1.20}$$

and similar for k_y and k_z. Note, that for each component $E_{x,y,z}$ the transverse amplitudes disappear in 0 and L. By inserting this solution into Helmholtz's equation (1.18), we obtain,

$$k_x^2 + k_y^2 + k_z^2 = \frac{\omega^2}{c^2}\ . \tag{1.21}$$

The states $k_{x,y,z}$ (enumerated by $n_{x,y,z}$) form a three-dimensional orthogonal lattice of points in space $\mathbf{k}$ separated by a distance along the axes k_x, k_y, k_z of $\frac{\pi}{L}$, as shown in Fig. 1.5. In principle, the number of states that can be placed within a sphere of radius k in the momentum space is,

$$N = \int_{\text{sphere}} dn_x dn_y dn_z\ . \tag{1.22}$$

However, the periodic boundary conditions for $|\mathbf{k}|$ limit the components k_x, k_y, k_z to positive values ($n \geq 0$), that is, the volume under consideration is limited to an octant. On the other hand, we must multiply the number of states by two because of the degeneracy of polarizations,

$$4N = \int_0^n 4\pi n^2 dn = \left(\frac{L}{\pi}\right)^3 \int_0^k 4\pi k^2 dk = \frac{4L^3}{\pi^2}\frac{k^3}{3} = \frac{4L^3\omega^3}{3\pi^2 c^3}\ . \tag{1.23}$$

With this, we obtain the *mode density*,

$$\frac{N}{L^3} = \frac{\omega^3}{3\pi^2 c^3}\ . \tag{1.24}$$

The *spectral density of modes* ϱ can be given in several units,

$$\int \varrho(n)dn = \int \varrho(k)dk = \int \varrho(\omega)d\omega = \frac{N}{L^3}\ , \tag{1.25}$$

[3] See script on *Electrodynamics* (2023).

such that,

$$\boxed{\varrho(n) = \frac{\pi n^2}{L^3} \quad \text{or} \quad \varrho(k) = \frac{k^2}{\pi^2} \quad \text{or} \quad \varrho(\omega) = \frac{\omega^2}{\pi^2 c^3}} \ . \tag{1.26}$$

The density of oscillating modes within the cavity grows like the square of the frequency. Now, the mean energy per mode in a sample of oscillators in thermal equilibrium is, following the equipartition law, equal to,

$$\bar{E} = k_B T \ , \tag{1.27}$$

where k_B is the Boltzmann constant. We conclude that the *spectral energy density* $u_{RJ}(\omega)$ in the cavity is,

$$\boxed{u_{RJ}(\omega)d\omega = k_B T \varrho(\omega)d\omega = k_B T \frac{\omega^2}{\pi^2 c^3} d\omega} \ . \tag{1.28}$$

This law is known as the *Rayleigh-Jeans law* of *black-body radiation*. As seen in Fig. 1.6, this law suggests the physically impossible fact, called *ultraviolet catastrophe*, that the energy storage in the cavity grows without limits like the square of frequency.

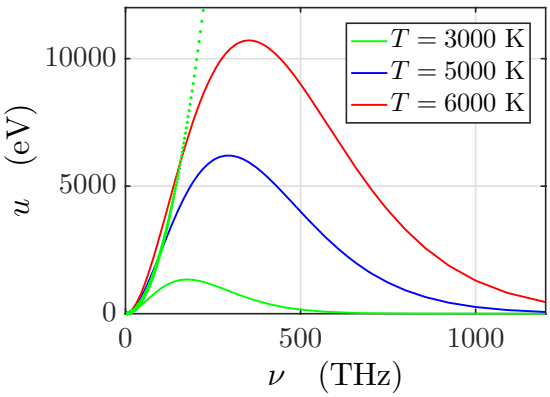

Figure 1.6: Spectral energy density following Rayleigh-Jeans' and Planck's laws.

1.2.3 Planck's distribution of modes

We obtained the result (1.27) by multiplying the number of modes with the mean energy per mode. As there is no doubt about our method of counting the modes, the problem with the ultraviolet catastrophe can only root in the use of the equipartition principle for assigning energy to the oscillators.

Planck's idea to solve this problem was to first consider the probability distribution for exciting the modes (thermal states) for a sample of oscillators in thermal equilibrium at temperature T. This probability distribution p comes from mechanical

statistics and can be written in terms of the *Boltzmann factor*, e^{-E_n/k_BT}, and the partition function $q = \sum_{n=0}^{\infty} e^{-E_n/k_BT}$ as,

$$p_n = \frac{e^{-E_n/k_BT}}{q} \ . \tag{1.29}$$

Now Planck hypothesized that the energy be quantized, that is, it must be assigned in discrete portions, proportional to the frequency, such that,

$$\boxed{E_n = n\hbar\omega} \ , \tag{1.30}$$

where $n = 0, 1, 2, ..$ and the proportionality constant $\hbar$ is called *Planck's constant*. With the abbreviation $Z \equiv e^{-\hbar\omega/k_BT}$ and using the rule $\sum_{n=0}^{\infty} Z^n = (1-Z)^{-1}$, we find the average number,

$$\bar{n} = \sum_n n p_n = (1-Z)\sum_n n Z^n = (1-Z)Z\frac{\partial}{\partial Z}\sum_n Z^n = \frac{Z}{1-Z} = \frac{1}{e^{\hbar\omega/k_BT}-1} \ . \tag{1.31}$$

The probability of occupancy of state n is,

$$p_n = (1-Z)Z^n = \frac{\bar{n}^n}{(1+\bar{n})^{1+n}} \ , \tag{1.32}$$

and the average energy is,

$$\bar{E} = \sum_n E_n p_n = \sum_n n\hbar\omega e^{-n\hbar\omega/k_BT} = \frac{\hbar\omega}{e^{\hbar\omega/k_BT}-1} \ , \tag{1.33}$$

in contrast to the initial assumption (1.28).

Finally, we obtain Planck's expression for the energy density inside the cavity by substituting $\bar{\epsilon}$ for the factor k_BT in Rayleigh-Jeans' law (1.27),

$$\boxed{u(\omega)d\omega = \bar{E}\varrho(\omega)d\omega = \frac{\omega^2}{\pi^2c^3}\frac{\hbar\omega}{e^{\hbar\omega/k_BT}-1}d\omega} \ . \tag{1.34}$$

This result, drawn in Fig. 1.6, is much more satisfactory, because now the energy density has an upper bound, and coincides with the results of experiments. Note, that for high temperatures or low excitation energies, $\hbar\omega \ll k_BT$, Planck's distribution converges to that of Rayleigh-Jeans', $u(\omega) \to u_{RJ}(\omega)$.

Note that the form of the expression for the energy depends on the parametrization and must be derived respecting $u(\omega)d\omega = u(\lambda)d\lambda$, etc.. Often the blackbody radiation is expressed in terms of the *spectral radiance*,

$$L(\omega) \equiv \frac{c}{4\pi}u(\omega) \ , \tag{1.35}$$

which can be understood as the (isotropic) energy flux into all directions of space.

Solve the Excs. 1.2.8.1 to 1.2.8.7.

1.2.4 The corpuscular nature of the photon

1.2.4.1 The photoelectric effect

Light incident on a metallic surface can expel electrons. For this to occur, the light must have a *minimum frequency*. If the frequency is below this value, there is no point in increasing the light intensity: the electrons won't be expelled. The main experimental observations are: 1. Electrons are ejected without apparent delay, i.e. it is not necessary (and it doesn't help) to accumulate a certain amount of energy. 2. Higher light intensities increase the number of electrons, but not their kinetic energy after expulsion. 3. Red light does not eject electrons, even at high intensities. 4. Weak ultraviolet light only ejects few electrons, but with high kinetic energy.

These observations challenge the classical electromagnetic model according to which the Lorentz acceleration of the electrons should be proportional to the field *amplitude*. The observations were explained by Einstein's theory of the *photoelectric effect*, which assumes the light to be quantized (unlike Planck, who preferred to quantize the process of light absorption),

$$E = h\nu \ . \tag{1.36}$$

Assuming a fixed exit work A for the extraction of an electron, we can measure the constant $\hbar$:

$$h\nu = A + \tfrac{mv^2}{2} = A + eV \qquad \rightarrow \qquad h = \frac{eV}{\nu - \nu_g} \ . \tag{1.37}$$

The energy of the fastest electrons is measured through the decelerating voltage by varying ν and I.

1.2.5 Einstein's transitions rates

Bohr's atom model explained for the first, time how light interacts with matter: Atoms have discrete excitation levels. They absorb and emit energy packets $\hbar\omega$. Unfortunately, Bohr's model can not predict transition rates. Here, Einstein helped out by developing a useful theory (see Fig. 1.7).

Figure 1.7: Bohr model and Einstein rate diagram.

We consider a two-level atom or a sample of atoms within a conducting cavity. We have N_1 atoms in the lower energy state E_1 and N_2 in the upper state E_2. Light interacts with these atoms through stimulated resonant absorption and emission. The rates, $B_{12}u(\omega)$ and $B_{21}u(\omega)$ are proportional to the energy spectral density $u(\omega)$ of the cavity modes. The central idea of Einstein is to postulate that atoms in the higher state can emit light spontaneously at a rate A_{21}, which depends only on the density

of modes of the cavity, i.e. the volume of the cavity, but not the energy of the field of radiation. With the Einstein coefficients we can formulate valid rate equations in situations, where the spectral distribution of the radiation is wider than the spectral width of the atomic transition and where the spectral distribution of the light flux from the source, $\bar{I}(\omega)$, is weak compared to the saturation intensity of the atomic transition. Even if modern light sources generally have very narrow and intense spectral emission bands, Einstein's coefficients are often used in the spectroscopic literature to characterize the light-matter interaction with atoms and molecules.

The Einstein rate equations describe the energy flux between atoms and the optical modes of the cavity,

$$\begin{aligned} \frac{dN_1}{dt} = -\frac{dN_2}{dt} &= -R_{1\to 2} + R_{2\to 1} + \mathcal{S}_{2\to 1} \\ &= -N_1 B_{12} u(\omega) + N_2 B_{21} u(\omega) + N_2 A_{21} \ . \end{aligned} \tag{1.38}$$

$R_{1\to 2}$ is the *absorption rate*, $R_{2\to 1}$ the *stimulated emission rate* and $\mathcal{S}_{2\to 1}$ the *spontaneous emission rate*. The assumption of a third type of transition, called spontaneous emission, is necessary, if $B_{12} = B_{21}$ but $N_1 > N_2$ in thermal equilibrium. In thermal equilibrium we have the condition of stationarity, $\frac{dN_1}{dt} = -\frac{dN_2}{dt} = 0$ for a given energy density value $u(\omega) = u_{th}(\omega)$, such that,

$$u_{th}(\omega) = \frac{A_{21}}{\left(\frac{N_1}{N_2}\right) B_{12} - B_{21}} \ . \tag{1.39}$$

The *Boltzmann distribution law* controlling the distribution of the number of atoms in the lower and upper states is given by,

$$\frac{N_1}{N_2} = \frac{g_1}{g_2} e^{-(E_1 - E_2)/k_B T} \ , \tag{1.40}$$

where $g_{1,2}$ are the degeneracies of the lower and upper states and $E_2 - E_1 = \hbar\omega_0$. We find,

$$u_{th}(\omega) = \frac{A_{21}}{\frac{g_1}{g_2} e^{\hbar\omega_0/k_B T} B_{12} - B_{21}} \ . \tag{1.41}$$

But this result must be consistent with the Planck's distribution (1.34). Therefore, by comparing this equation with the equation (1.41), it must be,

$$\frac{g_1}{g_2}\frac{B_{12}}{B_{21}} = 1 \ . \tag{1.42}$$

and also,

$$\frac{A_{21}}{B_{21}} = \frac{\hbar\omega_0^3}{\pi^2 c^3} \ . \tag{1.43}$$

This equation shows that, once we know one of the three transition rates, we can always calculate the others.

It is useful to compare the rate A_{21} with B_{21} from the equation (1.41) inserting the equation (1.42),

$$\frac{A_{21}}{B_{21} u_{th}(\omega)} = e^{\hbar\omega_0/k_B T} - 1 \ . \tag{1.44}$$

This expression shows that, when $\hbar(\omega_2 - \omega_1) \gg k_B T$, that is, for optical, UV, or X-ray frequencies, spontaneous emission dominates. But in low-frequency regimes, that is, IR, microwave, or radio waves, stimulated emission is more important. Note that even when stimulated emission dominates, spontaneous emission is always present and plays an important role, for example, in processes ultimately limiting the emission bandwidth of lasers.

1.2.6 Absorption spectrum for a single molecule

Every light source has a certain spectral width. Conventional light sources, such as incandescent bulbs or plasmas have relatively broad emission bands compared to atomic or molecular absorbers, at least when the latter ones are studied in dilute gases. Even when we use pure spectral sources, such as a laser tuned to the peak of a resonance, the transition line always exhibits an intrinsic width associated with the interruption of the phase evolution of the excited state. Phase interruptions such as spontaneous or stimulated emission and collisions are common examples of line broadening mechanisms. The emission or absorption of radiation occurs within a frequency distribution centered about $\omega_0 \equiv \omega_2 - \omega_1$, and we must account for this spectral distribution in our calculation of the energy transfer.

The total power P absorbed by a two-level atom with resonance frequency ω_0 from a radiation field with the spectral intensity distribution $I(\omega)$ with the total intensity of the laser beam $\bar{I} = \int I(\omega) d\omega$ can be expressed as the integral,

$$\boxed{P = \int \sigma(\omega) I(\omega) d\omega} \,, \tag{1.45}$$

with the *frequency-dependent optical cross section* [4],

$$\boxed{\sigma(\omega) = \frac{g_2}{g_1}\lambda^2 \frac{\Gamma}{2\pi} \frac{\frac{1}{4}\Gamma}{(\omega - \omega_0)^2 + \frac{1}{4}\Gamma^2} = \frac{g_2}{g_1}\lambda^2 \frac{\Gamma}{4} \mathcal{L}_\Gamma(\omega - \omega_0)} \,. \tag{1.46}$$

where we defined the Lorentzian profile as,

$$\mathcal{L}_\beta(\Delta) \equiv \frac{\beta}{2\pi} \frac{1}{\Delta^2 + (\beta/2)^2} \qquad \text{with} \qquad \int_{-\infty}^{\infty} \mathcal{L}_\beta(\Delta) d\Delta = 1 \,. \tag{1.47}$$

The quantity, $\sigma(\omega_0) = \frac{g_2}{g_1}\frac{\lambda^2}{2\pi}$ is called the *resonant optical cross section*.

> **Example 1 (*Limiting cases*):** Let us analyze the two limiting cases when either one of the spectral distributions $I(\omega)$ or $\sigma(\omega)$ is much narrower than the other.
> For a *narrow laser*, we may assume a δ-peaked spectral intensity distribution,
>
> $$I(\omega) = \bar{I}\delta(\omega - \omega_L) \,. \tag{1.48}$$
>
> When it drives a *broad transition* described by an optical cross section given by (1.46), the scattered power is,
>
> $$P = \bar{I}\sigma(\omega_L) \,. \tag{1.49}$$

[4] At low saturation.

For a *narrow transition*, we may substitute the Lorentzian in (1.46) by a Dirac δ-function,

$$\sigma(\omega) \xrightarrow{\Gamma\to 0} \frac{g_2}{g_1}\lambda^2\frac{\Gamma}{4}\delta(\Delta)\ . \tag{1.50}$$

When it is driven by a *broad laser*, for which we assume a spectral intensity distribution,

$$I(\omega) = \bar{I}\mathcal{L}_\beta(\omega-\omega_L) \qquad \text{with} \qquad \bar{I} = \int I(\omega)d\omega = \frac{I(\omega_L)}{\mathcal{L}_\beta(0)} = \frac{\pi\beta}{2}I(\omega_L) \tag{1.51}$$

we obtain for the scattered power,

$$P = \int \frac{g_2}{g_1}\lambda^2\frac{\Gamma}{4}\delta(\omega-\omega_0)\bar{I}\mathcal{L}_\beta(\omega-\omega_L)d\omega = \frac{g_2}{g_1}\lambda^2\frac{\Gamma}{4}\bar{I}\mathcal{L}_\beta(\omega_0-\omega_L)\ . \tag{1.52}$$

1.2.6.1 Broad laser driving a broad transition

Until now we assumed a fixed laser frequency ω_L (with finite emission bandwidth) driving a fixed resonance frequency ω_0. What we call *absorption spectrum* is what we obtain when we tune either the laser frequency or when we (somehow) vary the resonance frequency, such that $\Delta \equiv \omega_L - \omega_0$ is ramped. Assuming Lorentzian profiles with finite linewidths for both, $\bar{I}$ and σ, we get,

$$\begin{aligned} P(\Delta) = P(\omega_L-\omega_0) &= \int \sigma(\omega)I(\omega)d\omega = \int \frac{g_2}{g_1}\frac{\lambda^2\Gamma}{4}\mathcal{L}_\Gamma(\omega-\omega_L)\bar{I}\mathcal{L}_\beta(\omega-\omega_0)d\omega \\ &= \frac{g_2}{g_1}\frac{\lambda^2\Gamma}{4}\bar{I}\int \mathcal{L}_\Gamma(\omega'+\omega_0-\omega_L)\mathcal{L}_\beta(\omega')d\omega'\ . \end{aligned} \tag{1.53}$$

That is, the absorption spectrum is obtained as a convolution of both profiles,

$$\boxed{P(\Delta) = \frac{g_2}{g_1}\frac{\lambda^2\Gamma\bar{I}}{4}(\mathcal{L}_\Gamma \star \mathcal{L}_\beta)(\Delta)}\ . \tag{1.54}$$

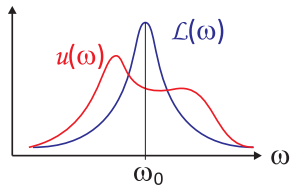

Figure 1.8: Absorption spectrum (blue) and spectral energy distribution of the source (red).

This result reproduces the two limiting cases discussed in the above example, since for narrow transitions, $\Gamma \to 0$, that is $\mathcal{L}_\Gamma \to \delta$, we recover the results (1.52), and for narrow lasers, $\beta \to 0$, that is, $\mathcal{L}_\beta \to \delta$, we recover (1.49). Obviously, this formula holds for other line profiles e.g. when the resonance is broadened by some perturbations [5].

[5] Let us here remind the following identities holding for Lorentzian and Gaussian line profiles:

$$(\mathcal{L}_\gamma \star \mathcal{L}_\beta)(\Delta) = \mathcal{L}_{\gamma+\beta}(\Delta) \qquad \text{and} \qquad (\mathcal{G}_\Gamma \star \mathcal{G}_\beta)(\Delta) = \mathcal{G}_{\sqrt{\gamma^2+\beta^2}}(\Delta)\ .$$

1.2.6.2 Two-level atom in a blackbody radiation field

When considering a two-level atom interacting with a blackbody a radiation field, we describe the spectral intensity distribution by (1.34),

$$I(\omega) = \frac{\omega^2}{\pi^2 c^2} \frac{\hbar\omega}{e^{\hbar\omega/k_B T} - 1} \tag{1.55}$$

$$\text{with} \qquad \bar{I} = \int I(\omega) d\omega = \frac{\hbar}{\pi^2 c^2} \left(\frac{k_B T}{\hbar}\right)^4 \int_0^\infty \frac{x^3 dx}{e^x - 1} = \frac{\pi^2}{15 c^2 \hbar^3} (k_B T)^4 \ .$$

Since the width of the transition is negligibly small in comparison with the blackbody spectrum, $\Gamma \to 0$, we may evaluate the scattered power as,

$$P = \int \frac{g_2}{g_1} \frac{\lambda^2 \Gamma}{4} \mathcal{L}_\Gamma(\omega - \omega_0) \frac{\omega^2}{\pi^2 c^2} \frac{\hbar\omega}{e^{\hbar\omega/k_B T} - 1} d\omega \tag{1.56}$$

$$\xrightarrow{\Gamma \to 0} \frac{g_2}{g_1} \frac{\lambda^2 \Gamma}{4} \frac{\omega_0^2}{\pi^2 c^2} \frac{\hbar\omega_0}{e^{\hbar\omega_0/k_B T} - 1} \ .$$

1.2.7 Absorption in a gas

Let us now generalize the results to a gas of two-level atoms. As long as the transition linewidth is narrow [case (1.50)], the power is removed from the system only by spontaneous emission; absorption only converts radiation into atomic excitation which, subsequently, can be returned to the radiation field by stimulated emission. At steady-state the Einstein rate equation (1.38) reads,

$$0 = -N_1 B_{12} u(\omega_0) + N_2 B_{21} u(\omega_0) + N_2 A_{21} \ . \tag{1.57}$$

Using the result (1.42), we can write the amount of power removed from the system by spontaneous emission as,

$$P = N_2 A_{21} \hbar\omega_0 = u(\omega_0) B_{12} (N_1 - \tfrac{g_1}{g_2} N_2) \hbar\omega_0 \ . \tag{1.58}$$

On the other hand, the power absorbed from the radiation field $u(\omega_0)$, by atoms whose transition is described by the cross section (1.46), is given by,

$$P = \int (N_1 - \tfrac{g_1}{g_2} N_2) \sigma(\omega) I(\omega) d\omega \ . \tag{1.59}$$

Remembering $I(\omega) = c u(\omega)$ and assuming a large radiation spectrum, $I(\omega) \simeq I(\omega_0)$, a comparison of equations (1.58) and (1.59) yields,

$$\boxed{B_{12} = \frac{c}{\hbar\omega_0} \int \sigma(\omega) d\omega} \ . \tag{1.60}$$

1.2.7.1 Lambert-Beer law

The absorption probability distribution is convoluted with the spectral energy distribution of the light source, $u(\omega) = d\bar{u}/d\omega$, which in turn is related to the energy *density* via, $\bar{U} = V\bar{u}$, where V is the mode volume of the light field. Assuming that light

propagates toward z and converting the time dependence into a spatial dependence, we have on one hand,

$$P = -\frac{dU}{dt} = -\frac{d\bar{u}}{dt}\Delta V = -c\frac{d\bar{u}}{dz}\Delta V = -\frac{d\bar{I}}{dz}\Delta V \ . \tag{1.61}$$

On the other hand, assuming a narrow laser, $I(\omega) = \bar{I}\delta(\omega - \omega_L)$, we get,

$$P = \int (N_1 - \tfrac{g_1}{g_2}N_2)\sigma(\omega)I(\omega)d\omega = \bar{I}(N_1 - \tfrac{g_1}{g_2}N_2)\sigma(\omega_L) \ , \tag{1.62}$$

Now comparing both results,

$$\frac{d\bar{I}}{\bar{I}} = -\frac{N_1 - \frac{g_1}{g_2}N_2}{\Delta V}\sigma(\omega_L)dz \simeq -n\sigma(\omega_L)dz \ , \tag{1.63}$$

The solution of this differential equation is,

$$\boxed{\bar{I} = \bar{I}_0 e^{-\sigma(\omega_L)nz}} \ . \tag{1.64}$$

Here, z is the total distance, over which absorption takes place. The last equation is the *Lambert-Beer law* for light absorption. It is very useful for measuring atomic densities in gas cells or of atomic beams. Solve the Excs. 1.2.8.8 to 1.2.8.10 [53, 57, 80].

1.2.8 Exercises

1.2.8.1 Ex: Resistance of vacuum

Show that $\sqrt{\mu_0/\varepsilon_0}$ has the dimension of a resistance and the value of $376.7\,\Omega$.

1.2.8.2 Ex: The laws of Planck and Rayleigh-Jeans

Show that Planck's law reproduces the Rayleigh-Jeans law in the low-frequency limit.

1.2.8.3 Ex: The laws of Wien and Stefan-Boltzmann

a. Derive the parametrization of Planck's law in terms of frequency ν and wavelength λ.
b. Derive the law of *Stefan-Boltzmann* according to which the total power radiated per unit surface area of a black body across all wavelengths (also known as the black-body radiant emittance) is given by σT^4, where $\sigma \equiv \pi^2 k_B^4/60c^2\hbar^3$ is called the Stefan-Boltzmann constant.
c. Derive *Wien's displacement law* according to which the maximum emission of a blackbody spectrum occurs at $\lambda_{\max}T = 2.898\times10^{-3}\,\mathrm{Km}$ in the wavelength parametrization and $\nu_{\max}/T = 0.0588\,\mathrm{THz/K}$ in the frequency parametrization. Determine the frequency of the maximum emission for the $2.7\,\mathrm{K}$ background radiation of the universe.

1.2.8.4 Ex: Photons in a resonator

a. The light power emitted by a laser ($\lambda = 633\,\text{nm}$) be $P = 1\,\text{nW}$. How many photons does the laser emit per second? How many laser photons are in a mode volume of $L = 10\,\text{cm}$ length?
b. How many photons on average are inside an optical cavity having the same mode volume at ambient temperature, when there is no incident light?

1.2.8.5 Ex: Number of modes in a cavity

a. How many modes do fit into a cubical box of 10 cm size for a frequency interval of 1000 Hz centered at a wavelength of 500 nm?
b. How many photons are in the box supposing it has a temperature of $T = 300\,\text{K}$, respectively, $T = 6000\,\text{K}$?

1.2.8.6 Ex: Number of photons emitted from lasers and blackbodies

a. Calculate the total number of photons per area per unit time emitted by a blackbody at temperature T.
b. The linewidth of a helium-neon laser is $\Delta\nu = 1000\,\text{Hz}$. The operating wavelength is $\lambda = 632.8\,\text{nm}$, the power is $P = 1\,\text{mW}$, and the beam size $w_0 = 1\,\text{mm}$. How many photons are emitted per second?
c. What would be the temperature of a blackbody radiator emitting the same number of photons from an equal area and over the same frequency interval as the laser?

1.2.8.7 Ex: Number of photons per radiation mode

Assume the isotropic emission of a pulsed flashlamp with spectral bandwidth $\Delta\lambda = 100\,\text{nm}$ around $\lambda = 400\,\text{nm}$ amounts to $P_0 = 100\,\text{W}$ peak power out of a volume of $1\,\text{cm}^3$. Calculate the spectral power density $u(\nu)$ and the spectral intensity $I(\nu)$ through a spherical surface $r = 2\,\text{cm}$ away from the center of the emitting sphere. How many photons per mode are contained in the radiation field?

1.2.8.8 Ex: Atoms in an optical cavity

a. Consider a closed optical cavity at $T = 600°\,\text{C}$. The cavity has the shape of a $L = 1\,\text{m}$-long and $d = 3\,\text{cm}$-diameter tube. Calculate the total energy of the blackbody radiation inside the cavity.
b. Inside the cavity there is a gas with strontium atoms (1 fundamental level and 3 degenerate excited levels, $\lambda = 461\,\text{nm}$). Using the expression (1.34), assuming thermal equilibrium, calculate the number of excited atoms for a partial pressure of the strontium gas of $10^{-3}\,\text{mbar}$.
c. Calculate the optical density for a laser in resonance with the transition traversing the cavity along the symmetry axis.

1.2.8.9 Ex: Sodium atoms in an optical cavity

A sodium atom is placed in a cavity of volume $V = 1\,\text{cm}^3$ with walls at the temperature T, producing a thermal radiation field with spectral energy density $\bar{u}(\nu)$. At

what temperature T are the spontaneous and induced transition probabilities equal
a. for the transition $3P \to 3S$ with the transition wavelength $\lambda = 589\,\text{nm}$ and the excited state lifetime $\tau_{3P} = 16$ ns;
b. for the hyperfine transition $3S$ $(F = 3 \to F = 2)$ with the transition frequency $\nu = 1772\,\text{MHz}$ and the excited state lifetime $\tau_{3F} \simeq 1\,\text{s}$?

1.2.8.10 Ex: Applying the Lambert-Beer law

The beam of a monochromatic laser passes through an absorbing atomic vapor with path length $L = 5\,\text{cm}$. If the laser frequency is tuned to the center of an absorbing transition $|i\rangle \to |k\rangle$ with absorption cross section $\sigma_0 = 10^{-14}\,\text{cm}^2$, the attenuation of the transmitted intensity is 10%. Calculate the atomic density n_i in the absorbing level $|i\rangle$.

1.3 Two-level systems in quantum mechanics

In this section we will start to develop the quantum mechanical framework for treating the interaction of a single atomic two-level system with an oscillatory perturbation coupling the two levels. Such temporal perturbations typically occur when we suddenly switch on an external field that influences the motion or spin of the particles, or when the field varies over time, for example, an electromagnetic field.

1.3.1 Time-dependent perturbations

The time-dependent Schrödinger equation is,

$$\hat{H}\psi(\mathbf{r},t) = \imath\hbar\frac{\partial\psi(\mathbf{r},t)}{\partial t} \ , \tag{1.65}$$

with $\psi(\mathbf{r},t) = \langle\mathbf{r}|\psi(t)\rangle$. We write the perturbation as [6],

$$\hat{H} = \hat{H}^{(0)} + \hat{H}^{(1)}(t) \ . \tag{1.66}$$

and the eigenenergies and -functions of the unperturbed system as,

$$\hat{H}^{(0)}|n\rangle = E_n|n\rangle \ , \tag{1.67}$$

where $|n\rangle$ are the possible states (energy levels) in which the system can be. Recalling that this stationary Schrödinger equation was obtained from the time-dependent Schrödinger equation via a separation ansatz, the temporal evolution of these eigenfunctions is given by,

$$|\psi_n^{(0)}(t)\rangle = |n\rangle e^{-\imath E_n t/\hbar} \ . \tag{1.68}$$

Since the eigenfunctions form a complete set, we may expand any solution of the Schrödinger equation as,

$$|\psi^{(1)}(t)\rangle = \sum_n a_n(t)|\psi_n^{(0)}(t)\rangle = \sum_n a_n(t)|n\rangle e^{-\imath E_n t/\hbar} \ . \tag{1.69}$$

[6] See script on *Quantum mechanics* (2023), Sec. 5.4.1.

Insertion into the Schrödinger equation and multiplying from the right with $\langle j|$, we get in first order,

$$\imath\hbar\frac{da_j(t)}{dt} = \sum_n a_k(t)\langle j|\hat{H}^{(1)}|n\rangle e^{\imath\omega_{jn}t} \ , \tag{1.70}$$

where $\hbar\omega_{jn} \equiv E_j - E_n$. Equation (1.70) is exactly equivalent to the Schrödinger equation (1.65): no approximations have been made. However, for the case of an atom in a radiation field it is unsolvable, and so approximations are required. In perturbation theory one considers the atom to be initially in its ground state $|1\rangle$, that is, $a_n(0) = \delta_{n1}$. The approximation now consists in assuming

$$a_n(t) \ll 1 \tag{1.71}$$

for all $n \neq 1$ and doing a formal time integration of Eq. (1.70) to calculate these $a_n(t)$ values. The small components $a_n(t)$ of the excited states $|\psi_n^{(0)}\rangle$ for $n \neq 1$ that are mixed into $|\psi^{(1)}(t)\rangle$ become the transition amplitudes and their squares are the transition rates. For transitions to the continuum, such as photoionization, averaging over the density of final states results in the familiar *Fermi's golden rule* of quantum mechanics. For transitions between discrete states driven by radiation whose spectral width is larger than the natural width of the transition, averaging over the spectral density gives the same golden rule.

This approach is not suitable for narrow-band laser excitation of atoms, however, because large excited-state populations are possible, thereby violating Eq. (1.71). Instead, a different approximation is made, which consists in truncating the summation of the exact Eq. (1.70) to just two terms, a ground and an excited state connected by the laser frequency, and solving the resulting coupled differential equations directly. Such a calculation for a two-level system was first studied by Rabi [65] in connection with magnetic resonance, and is described in many textbooks [21, 66].

The expansion now reads,

$$|\psi^{(1)}(t)\rangle = a_1(t)|\psi_1^{(0)}(t)\rangle + a_2(t)|\psi_2^{(0)}(t)\rangle \ . \tag{1.72}$$

Note that not only do eigenfunctions oscillate, but the coefficients also depend on time, because the composition of the states can change. The instantaneous probability of finding the system in state $|n\rangle$ is $|a_n(t)|^2$. Importing the above linear combination into the Schrödinger equation,

$$[\hat{H}^{(0)} + \hat{H}^{(1)}(t)]|\psi^{(1)}(t)\rangle = \imath\hbar\frac{\partial}{\partial t}|\psi^{(1)}(t)\rangle \ , \tag{1.73}$$

we find,

$$\begin{aligned} &a_1\hat{H}^{(0)}|\psi_1^{(0)}\rangle + a_2\hat{H}^{(0)}|\psi_2^{(0)}\rangle + a_1\hat{H}^{(1)}|\psi_1^{(0)}\rangle + a_2\hat{H}^{(1)}|\psi_2^{(0)}\rangle \\ &\qquad = \imath\hbar\left[\frac{\partial a_1}{\partial t}|\psi_1^{(0)}\rangle + \frac{\partial a_2}{\partial t}|\psi_2^{(0)}\rangle + a_1\frac{\partial|\psi_1^{(0)}\rangle}{\partial t} + a_2\frac{\partial|\psi_2^{(0)}\rangle}{\partial t}\right] \\ \implies &a_1\hat{H}^{(1)}|\psi_1^{(0)}\rangle + a_2\hat{H}^{(1)}|\psi_2^{(0)}\rangle = \imath\hbar\dot{a}_1|\psi_1^{(0)}\rangle + \imath\hbar\dot{a}_2|\psi_2^{(0)}\rangle \ , \end{aligned} \tag{1.74}$$

because the other terms satisfy the Schrödinger equation of zero order. Replacing the stationary eigenfunctions,

$$a_1 e^{-\imath E_1 t/\hbar}\hat{H}^{(1)}|1\rangle + a_2 e^{-\imath E_2 t/\hbar}\hat{H}^{(1)}|2\rangle = i\hbar\dot{a}_1 e^{-\imath E_1 t/\hbar}|1\rangle + i\hbar\dot{a}_2 e^{-\imath E_2 t/\hbar}|2\rangle \ , \tag{1.75}$$

and multiplying this equation with $\langle 1|\times$ and $\langle 2|\times$, we find with the abbreviation $\hbar\omega_0 \equiv E_2 - E_1$,

$$\begin{aligned} \imath\hbar\dot{a}_1 &= a_1\langle 1|\hat{H}^{(1)}|1\rangle + a_2 e^{-\imath\omega_0 t}\langle 1|\hat{H}^{(1)}|2\rangle \ , \\ \imath\hbar\dot{a}_2 &= a_1 e^{\imath\omega_0 t}\langle 2|\hat{H}^{(1)}|1\rangle + a_2\langle 2|\hat{H}^{(1)}|2\rangle \ . \end{aligned} \tag{1.76}$$

Frequently, the perturbation induces only a coupling, but does not directly influence the energies, $\langle n|\hat{H}^{(1)}|n\rangle = 0$,

$$\boxed{\dot{a}_1 = a_2\frac{e^{-\imath\omega_0 t}}{\imath\hbar}\langle 1|\hat{H}^{(1)}|2\rangle \quad \text{and} \quad \dot{a}_2 = a_1\frac{e^{\imath\omega_0 t}}{\imath\hbar}\langle 2|\hat{H}^{(1)}|1\rangle} \ . \tag{1.77}$$

Without perturbation, $\langle m|\hat{H}^{(1)}|n\rangle = 0$, no dynamics develops; the eigenfunctions evolve independently.

Let us now consider a periodic perturbation oscillating at frequency $\omega = \omega_0 + \Delta$, where Δ is called the *detuning* from the resonance ω_0,

$$H^{(1)} = -e\vec{\mathcal{E}}(\mathbf{r},t)\cdot\mathbf{r} = -e\mathcal{E}_0\hat{\varepsilon}\cos(kz-\omega t)\cdot\mathbf{r} \ . \tag{1.78}$$

Then,

$$\langle 2|H^{(1)}|1\rangle = -e\mathcal{E}_0\cos(kz-\omega t)\langle 2|r|1\rangle = \hbar\Omega\cos(kz-\omega t) \ , \tag{1.79}$$

where we call

$$\Omega \equiv \frac{-e\mathcal{E}_0\langle 2|r|1\rangle}{\hbar} \tag{1.80}$$

the *Rabi frequency*. This yields,

$$\dot{a}_1 = -\imath\Omega a_2 e^{-\imath\omega_0 t}\cos(kz-\omega t) \quad \text{and} \quad \dot{a}_2 = -\imath\Omega^* a_1 e^{\imath\omega_0 t}\cos(kz-\omega t) \ . \tag{1.81}$$

Neglecting fast-rotating terms doing the so-called *rotating wave approximation* (RWA) and choosing the position of the atom to be $z = 0$,

$$\dot{a}_1 \simeq -\frac{\imath\Omega}{2}a_2 e^{\imath\Delta t} \quad \text{and} \quad \dot{a}_2 \simeq -\frac{\imath\Omega^*}{2}a_1 e^{-\imath\Delta t} \ . \tag{1.82}$$

With the equations of motion we can, starting from initial values for $a_1(0)$ and $a_2(0)$, calculate the temporal evolution.

We solve this system of differential equations by differentiating one and substituting the other,

$$\ddot{a}_2 = -\imath\dot{a}_1\frac{\Omega^*}{2}e^{-\imath\Delta t} - a_1\Delta\frac{\Omega^*}{2}e^{-\imath\Delta t} = -\frac{|\Omega|^2}{4}a_2 - \imath\Delta\dot{a}_2 \ . \tag{1.83}$$

We find solutions via the ansatz $a_2 = e^{-\imath\Delta t/2}(Ae^{\imath Gt/2} + Be^{-\imath Gt/2})$. The equation for a_2 yields,

$$\begin{aligned} &(\tfrac{\imath}{2}G - \tfrac{\imath}{2}\Delta)^2 Ae^{\imath(G-\Delta)t/2} + (-\tfrac{\imath}{2}G - \tfrac{\imath}{2}\Delta)^2 Be^{\imath(-G-\Delta)t/2} \\ &= -\tfrac{|\Omega|^2}{4}(Ae^{\imath(G-\Delta)t/2} + Be^{\imath(-G-\Delta)t/2} \\ &- \imath\Delta\left[(\tfrac{\imath}{2}G - \tfrac{\imath}{2}\Delta)Ae^{\imath(G-\Delta)t/2} + (-\tfrac{\imath}{2}G - \tfrac{\imath}{2}\Delta)Be^{\imath(-G-\Delta)t/2}\right] \ . \end{aligned} \tag{1.84}$$

Separating the parts in A and in B we obtain two equations with the same result,

$$G^2 = |\Omega|^2 + \Delta^2 \ . \tag{1.85}$$

G is called the *generalized Rabi frequency*. Using the initial conditions, $a_1(0) = 1$ and $a_2(0) = 0$, we can fix one of the coefficients A and B, since $a_2(0) = A + B = 0$,

$$a_2 = 2\imath A e^{-\imath\Delta t/2} \sin \tfrac{G}{2} t \ . \tag{1.86}$$

We now import this solution into the differential equation for a_1,

$$\dot{a}_1 = -\imath \frac{\Omega}{2} a_2 e^{\imath\Delta t} = \Omega A e^{\imath\Delta t/2} \sin \tfrac{G}{2} t \ . \tag{1.87}$$

The integral is,

$$a_1(t) = \int_0^t \Omega A e^{\imath\Delta t'/2} \sin \tfrac{G}{2} t' dt' = -\frac{2A}{\Omega^*} e^{\imath\Delta t/2} \left(G \cos \tfrac{G}{2} t - \imath\Delta \sin \tfrac{G}{2} t \right) \ . \tag{1.88}$$

Using the normalization condition,

$$\begin{aligned} 1 = |a_1|^2 + |a_2|^2 &= \left| -\frac{2A}{\Omega^*} e^{\imath\Delta t/2} \left(G \cos Gt - \imath\Delta \sin \tfrac{G}{2} t \right) \right|^2 + \left| 2\imath A e^{-\imath\Delta t/2} \sin Gt \right|^2 \\ &= \frac{4A^2}{|\Omega|^2} \left(G^2 \cos^2 \tfrac{G}{2} t + \Delta^2 \sin^2 \tfrac{G}{2} t \right) + 4A^2 \sin^2 \tfrac{G}{2} t = 4A^2 \frac{G^2}{|\Omega|^2} \ . \end{aligned} \tag{1.89}$$

Hence, $A = |\Omega|/2G$, or $2AG/\Omega^* = \sqrt{\Omega/\Omega^*}$. In general, we can choose Ω real, and the final solution is,

$$\boxed{a_1(t) = -e^{\imath\Delta t/2} \left(\cos \tfrac{G}{2} t + \tfrac{-\imath\Delta}{G} \sin \tfrac{G}{2} t \right) \qquad \text{and} \qquad a_2(t) = \tfrac{\imath\Omega}{G} e^{-\imath\Delta t/2} \sin \tfrac{G}{2} t} \ . \tag{1.90}$$

When the detuning Δ is zero, under the influence of the perturbation, the populations of the system oscillate with the Rabi frequency Ω. When the light frequency is detuned from resonance, however, the oscillation frequency G is higher, but the amplitude decreases as well. The initially empty state never reaches unitary population. In Exc. 1.3.5.1 we calculate the time required to allow the perturbation to invert the population of a two-level system, in Exc. 1.3.5.2 we study the maximum achievable inversion as a function of detuning, and in Exc. 1.3.5.3 we analyze the dynamics of a system subject to sequences of pulses.

1.3.2 Light-shift and dressed states

From Eqs. (1.82) written in matrix form as,

$$\begin{pmatrix} \imath\dot{a}_1 \\ \imath\dot{a}_2 \end{pmatrix} = \begin{pmatrix} 0 & \frac{1}{2}\Omega e^{\imath\Delta t} \\ \frac{1}{2}\Omega^* e^{-\imath\Delta t} & 0 \end{pmatrix} \begin{pmatrix} a_1 \\ a_2 \end{pmatrix} = \tfrac{1}{\hbar}\hat{H} \begin{pmatrix} a_1 \\ \tilde{a}_2 \end{pmatrix} \ , \tag{1.91}$$

via a simple transformation $\tilde{a}_2 \equiv e^{\imath\Delta t} a_2$, we arrive at an equivalent system of equations,

$$\begin{pmatrix} \imath\dot{a}_1 \\ \imath\dot{\tilde{a}}_2 \end{pmatrix} = \begin{pmatrix} 0 & \frac{1}{2}\Omega \\ \frac{1}{2}\Omega^* & -\Delta \end{pmatrix} \begin{pmatrix} a_1 \\ \tilde{a}_2 \end{pmatrix} = \tfrac{1}{\hbar}\hat{H}' \begin{pmatrix} a_1 \\ \tilde{a}_2 \end{pmatrix} \ , \tag{1.92}$$

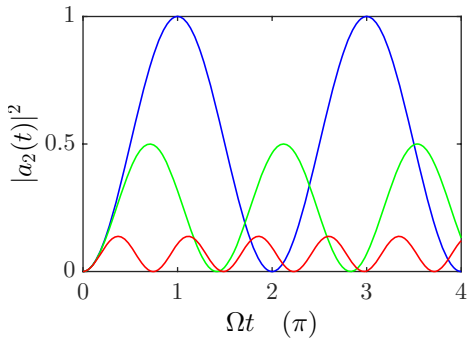

Figure 1.9: (code for download) Probability $|a_2(t)|^2$ for the atom to be in the excited state for $\Omega = \Gamma$ and $\Delta = 0$ (blue), $\Delta = \Gamma$ (green), and $\Delta = 2.5\Gamma$ (red). Time is in units of $1/\Gamma$.

which has the advantage of a time-independent Hamiltonian, the time dependence having been transformed into the wavefunctions [7]. From the total Hamiltonian in Eq. (1.92), we find for the eigen-energies,

$$E_{1,2} = \tfrac{\hbar}{2}\Delta \pm \tfrac{\hbar}{2}G \ . \tag{1.93}$$

Because the light intensity is proportional to Ω^2, the energy correction $\Delta E_{1,2} \equiv E_{1,2} - \frac{\hbar\Delta}{2}$ is appropriately called the *light shift*. In the limit of large detunings, $\Omega \ll |\Delta|$ we may expand,

$$E_{1,2} \simeq \pm\frac{\hbar\Omega^2}{4\Delta} \ . \tag{1.94}$$

The eigenstates corresponding to $\Delta E_{1,2}$ are called the *dressed state*s of the atom and are calculated in the next section. Very often the light field is not homogeneous (e.g., in a standing light wave) producing a spatially dependent light shift $\Delta E_{1,2}(\mathbf{r})$. The force that results from this gradient of energy is called the dipole force. In Exc. 1.3.5.4 we generalize the calculation of the light-shift to the presence of spontaneous decay.

1.3.2.1 Dressed states

The eigenfunctions of the Schrödinger equation for a two-level atom in a monochromatic field are best described in terms of the 'dressed states' of the atom [21] [8]. It begins with the total Hamiltonian,

$$\hat{H} = \hat{H}_{rad} + \hat{H}_{at} + \hat{H}_{int} \ , \tag{1.95}$$

where $\hat{H}_{at}$ is the usual atomic part that gives the atomic energy levels, $\hat{H}_{rad} = \hbar\omega(\hat{a}^\dagger\hat{a} + \frac{1}{2})$ is the radiation part whose eigenvalues are $E_n = (n + \frac{1}{2})\hbar\omega$, and $\hat{H}_{int}$ is the atom-field interaction that causes transitions as well as light shifts.

[7] The general transformation rule for time-dependent Hamiltonians is $\hat{H}' = U^\dagger\hat{H}U + \imath\hbar\dot{U}^\dagger U$ [see *Quantum mechanics* (2019), Sec. 14.1.2]. In the present case the Hamiltonians follow from each other with $U = \begin{pmatrix} 1 & 0 \\ 0 & e^{\imath\Delta t} \end{pmatrix}$.

[8] See script on *Quantum mechanics* (2023), Sec. 14.1.2.

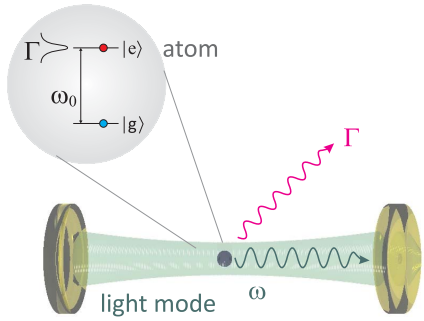

Figure 1.10: (code for download) Two-level atom interacting with a cavity mode.

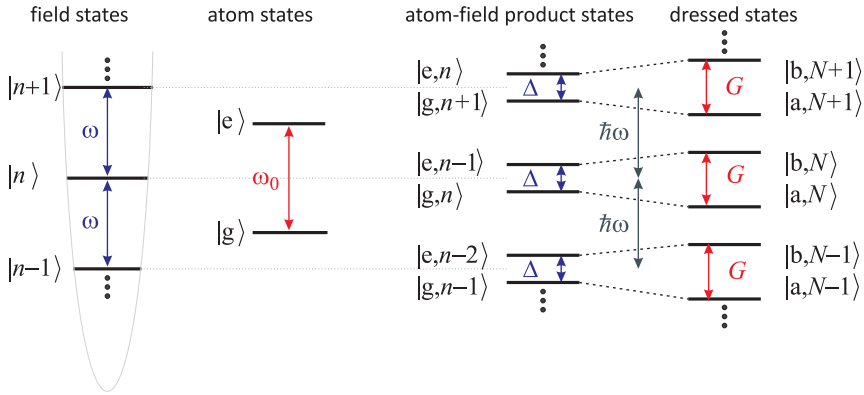

Figure 1.11: From left to right: Photon number states (eigenstates of $\hat{H}_{rad}$), the two stationary eigenstates of the two-level atom $\hat{H}_{at}$, double ladder showing the basis of product states of photon number and atomic states (eigenstates of $\hat{H}_{rad} + \hat{H}_{at}$), and dressed states constructed by diagonalization of the full Hamiltonian $\hat{H}$ in the basis of the product states.

The energy level diagram of the first two terms in Eq. (1.95) consists of a ladder of photon number states $|n\rangle$ separated by $\hbar\omega$ and the ordinary atomic energies, as shown schematically in Fig. 1.11. Coupled by the laser light the two atomic states form closely spaced pairs of one excited state $|e, n\rangle$ and one ground state $|g, n + 1\rangle$ separated by $\hbar\Delta$. They are each mixtures of ground and excited states, found by as the eigenvalues of $\hat{H}_{rad} + \hat{H}_{at}$.

The third term in the Hamiltonian, the interaction $\hat{H}_{int}$ between the atom and the field couples the ground and excited states through the off-diagonal matrix elements $\hat{H}^{(1)}(t)$. This splits the energy levels farther apart to $\hbar G = E_1 - E_2$, as given in Eq. (1.93). G is independent of the sign of Δ, and the shift $\hbar(G - |\Delta|)/2$ is the light shift of each dressed state [see Eq. (1.93)].

The light also mixes the states by an amount expressed in terms of a mixing angle θ given by $\cos(2\theta) \equiv -\Delta/G$, so that each ground state is mixed with a component of excited state and vice versa. These eigenstates of the Hamiltonian including this interaction are called the 'dressed states' of the atom in the field [21]. The eigenfunctions

are given by,

$$|a,N\rangle = \cos\theta|g,n\rangle - \sin\theta|e-1,n\rangle \ , \qquad (1.96)$$
$$|b,N\rangle = \sin\theta|g,n\rangle + \cos\theta|e-1,n\rangle \ .$$

While n denotes the number of photons in the system, N means the number of excitations, which can be free photons or the photon that has been absorbed by the atom. The interaction of a single two-level atom with a single field mode, as illustrated in Fig. 1.10 is studied in the paradigmatic *Jaynes-Cummings model* [9].

1.3.3 Numerical simulations and quantum jumps

The softwares 'Maple', 'Scientific Workplace, or 'Mathematics' are useful for analytical calculations, that is, multiplying matrices or determining eigenvalues. For numerical calculations the softwares 'Matlab' or 'Python' are more adapted. For example, the time evolution of a Schrödinger equation,

$$|\psi(t)\rangle = e^{-\imath\hat{H}t/\hbar}|\psi(0)\rangle \ , \qquad (1.97)$$

can be simulated in a single command line using the Matlab 'expm' function.

When the system varies in time, $\hat{H}(t)$, we may divide time into small units dt and propagate the wavefunction as,

$$|\psi(t+dt)\rangle = e^{-\imath\hat{H}(t)dt/\hbar}|\psi(t)\rangle \simeq \left(1-\imath\frac{\hat{H}}{\hbar}dt\right)|\psi(t)\rangle \ , \qquad (1.98)$$

continuously reinserting the solution into the equation. This *Newton method* does not converge quickly (dt should be chosen small enough when $\hat{H}(t)$ varies rapidly), but there are other more sophisticated procedures like the *Runge-Kutta method*.

A variation of this method is called *steepest descent method*. This method is similar to the Newton mewthod (1.98), but replaces the time dt with an imaginary time. Thus, the coherent temporal evolution of the Schrödinger equation is replaced by a dissipative evolution. The loss of energy automatically takes the system to the ground state. The method also applies to more complicated equations than the Schrödinger equation, for example, the *Gross-Pitaevskii equation*.

Another numerical method often used in quantum mechanics is called quantum *Monte Carlo simulation* of the wavefunction [61]. This method simulates trajectories of quantum systems treating intrinsic quantum noise as random processes disrupting the uniformity of the trajectory. The advantage of this method is that it also applies to dissipative systems. We will introduce this method in the next section.

1.3.3.1 Quantum jumps

The preceding discussions ignored the existence of spontaneous decay of the excited states resulting from their interaction with the zero-point energy of the electromagnetic field. Spontaneous emission has played an important role in atomic physics since the conception of discrete atomic states by Bohr in 1913.

[9] See script on *Quantum mechanics* (2023), Sec. 14.2.

The problem of radiative transitions between discrete states in atoms was discussed by Einstein in 1917 [31], where he considered three radiative processes. In the first process, an amount of optical energy $\hbar\omega$ (a 'photon') is absorbed from an applied radiation field of angular frequency ω, and atoms make transitions from the ground to the excited state. The newly introduced second process is stimulated emission, where a photon is emitted into the applied radiation field and the atoms make a transition from the excited to the ground state. Note that in both of these processes the total energy of the system consisting of the applied radiation field and the atoms is conserved. The third process is spontaneous emission, where a photon is also emitted and the atoms also make transitions from the excited to the ground state. However, unlike stimulated emission, the photon is not emitted in the mode of the radiation field, but has a random direction or polarization (see Fig. 1.10). Since the photon is emitted into the vacuum field, there is no longer conservation of energy for the system of radiation field plus atoms, since the vacuum field is outside the system. Finally, from the distribution of black-body radiation, Einstein deduced that the fourth process, spontaneous absorption, is not possible (or at least very unlikely).

The discussion in this chapter so far has properly accounted for the two stimulated processes discussed above [see Eqs. (1.90)]. The combined action of these two processes causes the oscillation in both the excited and ground state probabilities (see Fig. 1.9). For atoms initially in the ground state, the probability for absorption is large and the probability for them to go into the excited state increases. Once the atoms have a large probability to be in the excited state, however, the probability for absorption decreases and the probability for stimulated emission increases. This leads to the Rabi oscillations exhibited in Fig.1.9.

To include spontaneous emission, one way could be to include the vacuum field in the description of the system, which would then be closed as before. However, the task of doing so is formidable because both the spontaneous emission direction and the polarization direction are random. Thus it would be necessary to include the entire continuum of these parameters in the system, which is beyond the scope of this book. Furthermore, in most cases the properties of the emitted photon are not of interest, and information on the atom and the applied radiation field suffices.

The usual way to treat this problem in quantum mechanics is to introduce the density matrix $\hat{\rho}$ and to discuss the excitation of the atoms in terms of populations and coherences instead of amplitudes. This is beyond the topic of this course in the next chapter. Here, an alternative view of this problem is presented.

This view is called the Monte Carlo wavefunction method and was recently described anew [61]. It is a numerical simulation that treats the evolution of the system with the same coupled equations (1.77). However, at each instant there is some probability that an atom will undergo spontaneous emission within a certain, small time interval. This probability is proportional to the probability $|a_2|^2$ for the atom of being in the excited state. In this 'Gedankenexperiment' the state of the system is observed by detecting the emitted photons with a photon counter. At each instant, the output of a random number generator is compared with the probability for a spontaneous emission, and if the random number is smaller, it is assumed that spontaneous emission has occurred (this is why this method is named after a city most famous for gambling). At that instant the evolution starts again from the values $a_1 = 1$ and $a_2 = 0$. Since there is no interest in the emitted photon, it is disregarded.

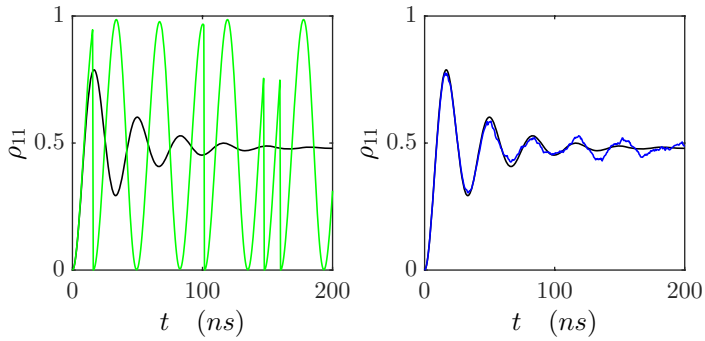

Figure 1.12: (code for download) (a) Quantum Monte Carlo wavefunction simulation. It is important to be aware, that a trajectory generated by a MCWF simulation only represents *one* of many possible trajectories of the system. (b) The evolution of the density matrix $\rho(t) = |\psi(t)\rangle\langle\psi(t)|$ (blue curve) is nothing else than the average (black curve) over all possible MCWF trajectories for the system.

Numerical results from this method, obtained in Exc. 1.3.5.5, are shown in Fig. 1.12. Note that the time when a spontaneous emission occurs is intrinsically unpredictable (otherwise the emission wouldn't be spontaneous). This randomness translates in trajectories of the wavefunction which, when we repeat the simulation procedure many times with the same starting condition, are all different. That is, a particular simulation results in a particular trajectory for a certain atom, but infinitely many different trajectories are possible. The green line in Fig. 1.12(a) shows one possible trajectory for one atom. The oscillatory behavior is evident, as suggested in Fig. 1.9; however, the oscillations are interrupted by spontaneous emission events projecting the atom into its ground state. Repeating the procedure with $N = 100$ atoms [see Fig. 1.12(b)] still results in oscillatory behavior for small time periods; however, these oscillations damp out for longer times. Also the discrete jumps, clearly visible for $N = 1$, can are longer discernible. This results from the averaging process, since the emission times are random and thus different for different atoms. This causes the oscillations to be damped and the excitation probability reaches its steady-state value. In Exc. 1.3.5.6 we present an analytical calculation of the time evolution of a resonantly driven two-level system subject to spontaneous decay.

One common misconception that may arise from Fig. 1.12 is that the atoms eventually cease oscillating between the ground and excited states. In most experiments, measurement are made on a large number of atoms and indeed the oscillations are damped. However, Fig. 1.12(a) clearly shows that each individual atom still oscillates, but that these oscillations are damped out by the averaging process. This topic will reappear in the density matrix approach that describes the evolution of an ensemble of atoms [10]. Let us finally note that quantum jumps, whose existence have been the subject of longstanding controversies [71], have been observed experimentally in three-level systems (see Fig. 1.13) [63, 68, 69, 11, 53].

[10] See script on *Quantum mechanics* (2023), Sec. 16.1.2.

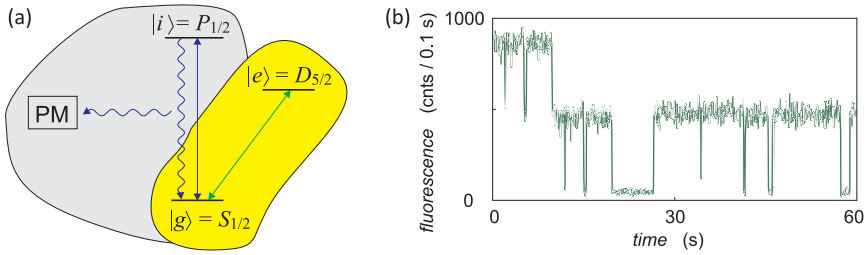

Figure 1.13: (a) Quantum measurement at the example of a three-level atom incorporating a weak (sample) transition and a strong (meter) transition. (b) Random Telegraph signal in the resonance fluorescence due to quantum jumps.

1.3.4 Phenomenological inclusion of spontaneous emission

Spontaneous emission can be phenomenologically introduced by assuming that any excited state decays with a probability that only depends on the instantaneous population and a decay constant $\Gamma = 1/\tau$, where τ is the lifetime of the state,

$$\dot{N}_2(t) = -\Gamma N_2(t) \ . \tag{1.99}$$

Remembering $N_2 = |a_2|^2$, we are led to complement the differential equations governing the two-level dynamics (1.82),

$$\boxed{\dot{a}_1 \simeq -\frac{\imath\Omega}{2} a_2 e^{\imath\Delta t} \quad \text{and} \quad \dot{a}_2 \simeq -\frac{\imath\Omega^*}{2} a_1 e^{-\imath\Delta t} - \frac{\Gamma}{2} a_2} \ . \tag{1.100}$$

In the absence of a driving field, $\Omega = 0$, we recover the expression (1.99), but the general solution now more complicated [11].

1.3.5 Exercises

1.3.5.1 Ex: Rabi oscillation

The population of a two-level system be initially in state $|1\rangle$. What should be the duration of a perturbation to transfer the population to state $|2\rangle$?

1.3.5.2 Ex: Rabi method

Free atoms be illuminated by light pulses characterized by the Rabi frequency Ω, whose pulse area is (i) $\int_0^t \Omega \ dt = \pi$ and (ii) $= 2\pi$. For which frequency tuning $\Delta = \omega - \omega_0$ the excited state population is maximum? Draw the spectral profile of the population in the range $-5 < \Delta/\Omega < 5$.

1.3.5.3 Ex: Ramsey fringes

a. Consider a two-level atom illuminated by a $\frac{\pi}{2}$-pulse of nearly resonant light, $G \simeq \Omega$, and calculate the ground and excited state amplitudes.

[11] A more thorough derivation is shown in [58] or in the script *Atom-Light Interaction*, Sec. 2.1.2, or in the script *Quantum mechanics*, Sec. 14.3.

b. How do the amplitudes evolve after the pulse if the detuning Δ is small but non-zero?
c. Derive the solution for $|a_2(t)|^2$ of the equations (1.82) for the resonant case ($\Delta = 0$) assuming the following initial conditions, $a_1(0) = -\frac{e^{\imath\phi/2}}{\sqrt{2}}$ and $a_2(0) = \imath\frac{e^{-\imath\phi/2}}{\sqrt{2}}$.
d. Discuss the case of two consecutive $\frac{\pi}{2}$-pulses separated by a time interval T.

1.3.5.4 Ex: Light-shift

Radiative coupling of levels leads to a shift of their energies called *light shift*. Calculate the light shift in a driven two-level system from the *effective Hamiltonian*,

$$\hat{H}_{eff} = \begin{pmatrix} 0 & \frac{1}{2}\Omega \\ \frac{1}{2}\Omega & \Delta - \frac{\imath}{2}\Gamma \end{pmatrix} . \tag{1.101}$$

Prepare spectra of the eigenvalues for $\Gamma/\Omega = 0$, 0.5, and 2.

1.3.5.5 Ex: Monte Carlo wavefunction simulation of quantum jumps

The possible occurrence of spontaneous emission produces a dynamics called *quantum trajectory*, which can be described by a non-hermitian *effective Hamiltonian*,

$$\hat{H}_{eff} = \hbar\Delta\sigma_z + \hbar\Omega\sigma^+ + c.c. - \tfrac{\imath}{2}\Gamma\sigma_z = \begin{pmatrix} 0 & \Omega \\ \Omega & \Delta - \frac{\imath}{2}\Gamma \end{pmatrix} ,$$

aiming at including energy dissipation processes.
a. Assuming $\Delta = 0 = \Omega$ verify that Γ is indeed the decay rate of the excited state.
b. How does the norm of an arbitrary state $|\psi(t)\rangle$ evolve in time?
c. Verify that the time evolution $|\psi'(t+dt)\rangle = e^{-\imath\hat{H}_{eff}dt}|\psi(t)\rangle$ followed by a renormalization $|\psi'(t+dt)\rangle \longrightarrow \frac{|\psi'(t+dt)\rangle}{\sqrt{\langle\psi'(t+dt)|\psi'(t+dt)\rangle}}$ conserves the norm of the wavefunction.
d. What is the probability for a spontaneous decay to occur within a time interval $[0, t]$?
e. Now, dissipative processes can be simulated by playing dices with random numbers ζ. We divide time into small intervals dt and propagate the wavefunction from $\psi(t)$ to $\psi(t+dt)$. Next, we generate a random number ζ, uniformly distributed between 0 and 1, which we compare to probability the probability p. In case, $\zeta > 1 - \langle\psi(t)|\psi(t)\rangle$, we conclude that there was no dissipative process, and we let the system proceed in peace, only renormalizing the wavefunction to compensate for the losses [59, **?**]. Otherwise, if $\zeta < 1 - \langle\psi(t)|\psi(t)\rangle$, we conclude that there was a dissipative process, and the system is projected into the eigenstate ψ_0. This projection is abrupt and called *quantum jump*. Now, the evolution restarts from zero, ruled by the effective Hamiltonian. Implement a numerical simulation via,

$$|\psi(t)\rangle \curvearrowright |\psi(t+dt)\rangle \equiv \begin{pmatrix} \frac{(1-\imath\hat{H}dt)|\psi(t+dt)\rangle}{\sqrt{\langle\psi(t)|\psi(t)\rangle}} & \text{if} \quad \zeta > 1 - \langle\psi(t)|\psi(t)\rangle \\ |\psi_0\rangle \quad \text{if} \quad \zeta < 1 - \langle\psi(t)|\psi(t)\rangle \end{pmatrix} .$$

This is the method called *quantum Monte Carlo wavefunction simulation*.

1.3.5.6 Ex: Non-hermitian time evolution

We study the time evolution $|\psi(t)\rangle = e^{-\imath \hat{H}_{eff} t}|\psi(0)\rangle$ with the effective Hamiltonian (we set $\hbar = 1$),

$$\hat{H}_{eff} = \begin{pmatrix} 0 & \frac{1}{2}\Omega \\ \frac{1}{2}\Omega & -\frac{\imath}{2}\Gamma \end{pmatrix}$$

starting from the initial condition $\langle 2|\psi(0)\rangle = 1$.
a. Calculate the eigenvalues $E_\pm$ and the unitary transformation matrix U, where $U\hat{H}_{eff}U^{-1} = \hat{E}$ and

$$\hat{E} \equiv \begin{pmatrix} E_+ & 0 \\ 0 & E_- \end{pmatrix} .$$

b. Now calculate the evolution of $|\psi(t)\rangle$ and the norm $\langle\psi(t)|\psi(t)\rangle$.

1.4 Width of spectral lines and broadening mechanisms

1.4.1 Discrete and continuous spectra

Radiators may emit light in a *continuous spectrum*, as in the case of a blackbody, or in a *discrete spectrum*. For example the light emitted by a gas of excited hydrogen atoms undergoing transitions to lower excitation states is composed of characteristic frequencies. In the former case, the spectral energy density $u(\omega)$ is continuous over wide frequency ranges, in the latter it exhibits sharp peaks at the frequency components. Spectra are discrete when the radiation involves discrete energy levels, as in the case of electronic orbits of atoms or vibrational states of molecules. They are continuous when at large energy bands are involved, as in the case of ionizing transitions or transitions between semiconductor bandgaps.

A satisfactory theory of line broadening mechanisms necessitates the introduction of the notion of the density matrix, whose evolution is governed by master equations. This however is beyond the scope of this script, and we will restrict in the following to some qualitative or even hand-waving arguments [53, 58, 79].

1.4.2 Natural linewidth of a transition

Be Γ the spontaneous decay rate of a state $|2\rangle$. This means that its population is decreasing,

$$\dot{N}_2 = -\Gamma N_2 \ . \tag{1.102}$$

Since $N_2 = \langle\psi_2|\psi_2\rangle$, we have $|\psi_2(t)\rangle = |\psi_2(0)\rangle e^{\imath\omega_0 t - \Gamma t/2}$. The Fourier transform is,

$$\begin{aligned} |\xi(\omega)\rangle &= \frac{1}{\sqrt{2\pi}}\int_0^\infty |\psi_2(t)\rangle e^{-\imath\omega t}dt = \frac{1}{\sqrt{2\pi}}\int_0^\infty e^{\imath\omega_0 t - \imath\omega t - \Gamma t/2}dt|\psi_i(0)\rangle \\ &= \frac{1}{\sqrt{2\pi}}\lim_{t\to\infty}\frac{e^{\imath(\omega_0-\omega)t-\Gamma t/2}-1}{\imath(\omega_0-\omega)-\Gamma/2}|\psi_2(0)\rangle = \frac{1}{\sqrt{2\pi}}\frac{1}{\imath(\omega-\omega_0)+\Gamma/2}|\psi_2(0)\rangle \ . \end{aligned} \tag{1.103}$$

The spectrum,

$$\boxed{|\xi(\omega)|^2 = \frac{1}{2\pi}\frac{1}{(\omega-\omega_0)^2-\Gamma^2/4}}\,, \tag{1.104}$$

is a *Lorentz distribution* whose width is the so-called *natural linewidth*.

Excited states can sometimes decay into various states of lower energy. In this case the linewidth is simply given by the sum of the partial decay rates, since the convolution of Lorentz distributions $\mathcal{L}_{\Gamma_k}$ with widths Γ_k is again a Lorentzian with the total width $\Gamma = \sum_k \Gamma_k$.

In many circumstances, the natural line profile is broadened by external influences. Power broadening (also called saturation broadening) [12], collision broadening, as well as transit time broadening are homogenous and lead to a broader Lorentz profiles. Thermal motion leads to inhomogeneous broadening characterized by Gaussian lineshapes.

1.4.3 Saturation broadening

Strong driving of a transition leads to its saturation and causes line broadening. To see this we go back to Einstein's rate equations in steady-state (1.38) additionally simplifying by assuming $g_1 = 1 = g_2$, such that $B_{12} = B_{21}$. Resolving these equations by N_1 and N_2 and using $N_1 + N_2 = N$ and $N_1 - N_2 \equiv \Delta N$, we get,

$$N_1 = N\frac{B_{21}u(\omega)+A_{21}}{2B_{21}u(\omega)+A_{21}} \qquad \text{and} \qquad N_2 = N\frac{B_{12}u(\omega)}{2B_{21}u(\omega)+A_{21}}\,. \tag{1.105}$$

For vanishing pump rate we expect, $N_1 \overset{u\to 0}{\longrightarrow} N$ and $N_2 \overset{u\to 0}{\longrightarrow} 0$. In contrast, when the pump rate becomes much larger than the relaxation rates, $N_1, N_2 \overset{u\to\infty}{\longrightarrow} \frac{1}{2}$. This means that the absorption coefficient $\alpha = \sigma(N_1 - N_2)$ goes to zero, and the medium becomes completely transparent,

$$\Delta N = N\frac{A_{21}}{2B_{21}u(\omega)+A_{21}} = \frac{N}{1+s(\omega)}\,. \tag{1.106}$$

The *saturation parameter*

$$s(\omega) \equiv \frac{2B_{12}u(\omega)}{A_{21}} \tag{1.107}$$

represents the ratio of pumping rate to the relaxation rate. The pump rate due to a monochromatic wave with intensity $\bar{I}$ is obtained by comparing (1.58) with (1.62),

$$B_{12}u(\omega) = \frac{\sigma(\omega)\bar{I}}{\hbar\omega}\,. \tag{1.108}$$

We obtain for the saturation parameter,

$$s(\omega) = \frac{2\sigma(\omega)\bar{I}}{\hbar\omega A_{21}}\,. \tag{1.109}$$

[12] See script on *Quantum mechanics* (2023), Sec. 34.3.1 and Sec. 35.4.

According to (1.58) and (1.106) the power absorbed per unit volume on the transition by atoms with the populations $N_{1,2}$ in a radiation field with a broad spectral profile and spectral energy density $u(\omega)$ is,

$$P = \hbar\omega B_{12} u(\omega) \Delta N = \hbar\omega B_{12} u(\omega) \frac{N}{1 + s(\omega)} \ . \tag{1.110}$$

With (1.107) this can be written as,

$$P = \hbar\omega \frac{A_{21}}{2} \frac{N}{1 + s(\omega)^{-1}} \ . \tag{1.111}$$

Let us now remember that the absorption cross section (1.46) of a homogeneously broadened line is Lorentzian. This means that the saturation parameter itself becomes Lorentzian. We can assume that the relaxation rate A_{21} is independent of ω within the frequency range of the line profile,

$$\boxed{s(\omega) = s(\omega_0) \frac{(\Gamma/2)^2}{\Delta^2 + (\Gamma/2)^2}} \ . \tag{1.112}$$

Substituting this into (1.111) yields the frequency dependence of the absorbed radiation power per unit frequency interval $d\omega$,

$$P = \hbar\omega \frac{A_{21} N}{2} \frac{s(\omega_0)(\Gamma/2)^2}{(\omega - \omega_0)^2 + (\Gamma/2)^2 [1 + s(\omega_0)]} = N \bar{I} \sigma(\omega_0) \frac{(\Gamma/2)^2}{\Delta^2 + (\gamma_s/2)^2} \ , \tag{1.113}$$

where we introduced the increased halfwidth of the Lorentzian profile,

$$\boxed{\gamma_s \equiv \Gamma \sqrt{1 + s(\omega_0)}} \ . \tag{1.114}$$

Apparently, the halfwidth of the saturation-broadened line increases with the resonant saturation parameter $s(\omega_0)$. If according to (1.107) the induced transition rate at resonance equals the total relaxation rate $A_{21}/2$, the resonant saturation parameter becomes $s(\omega_0) = 1$, which increases the linewidth by a factor $\sqrt{2}$, compared to the unsaturated linewidth Γ for weak radiation fields. Starting from (1.113) we can define a *saturated* absorption cross section,

$$\boxed{\sigma_s(\omega) = \sigma_s(\omega_0) \frac{(\gamma_s/2)^2}{\Delta^2 + (\gamma_s/2)^2} = \sigma(\omega_0) \frac{(\Gamma/2)^2}{\Delta^2 + (\gamma_s/2)^2} = \sigma(\omega) \frac{1}{1 + s(\omega)}} \ , \tag{1.115}$$

where the unsaturated absorption profile is,

$$\sigma(\omega) = \sigma(\omega_0) \frac{(\gamma/2)^2}{\Delta^2 + (\gamma/2)^2} \ . \tag{1.116}$$

This shows that the saturation decreases the absorption coefficient by the factor $1 + s(\omega)$. At the line center, this factor has its maximum value $1 + s(\omega_0)$, while it decreases to 1 for increasing $|\Delta|$, see (1.114), see Fig. 1.14. This is the reason why the line broadens.

From (1.109) we see, that unity saturation, $s(\omega_0) = 1$, corresponds to a light intensity of,

$$\bar{I}_{sat} \equiv \frac{\hbar\omega}{2\sigma(\omega_0)}\Gamma = \frac{2\pi^2 c\hbar}{3\lambda^2}\Gamma \ . \tag{1.117}$$

This intensity is called *saturation intensity*. Taking account of the degeneracies g_j of the levels the saturation intensity becomes [13],

$$\boxed{I_{sat} = \frac{g_1}{g_2}\frac{2\pi^2 c\hbar}{3\lambda_0^3}\Gamma} \ . \tag{1.118}$$

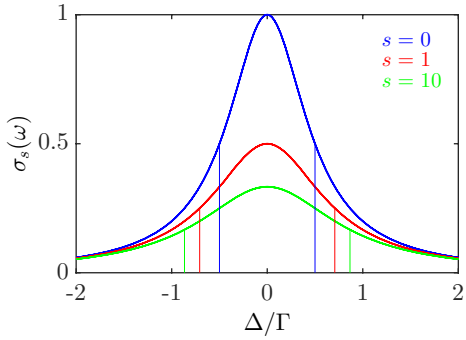

Figure 1.14: (code for download) Optical cross section at various saturation parameters.

Finally, we note that the resonant saturation parameter is basically a measure for the ratio between the stimulated population transfer rate, given by the the Rabi frequency Ω and the spontaneous decay rate Γ,

$$s(\omega_0) = \frac{2\Omega^2}{\Gamma^2} \ . \tag{1.119}$$

We thus obtain the important relationship between laser intensity and Rabi frequency,

$$\boxed{\Omega^2 = \sigma(\omega_0)\frac{\bar{I}}{\hbar\omega_0}\Gamma} \ . \tag{1.120}$$

1.4.4 Collision broadening

We have seen in Sec. 1.3.3 that spontaneous emission leads to random interruptions of the coherent evolution of the atomic dipole moment driven by an external radiation field, which results in a homogeneous line broadening characterized by a Lorentzian profile. Elastic interatomic collisions have a very similar impact on an atomic resonance as spontaneous emission, because they also induce unpredictable interruptions of the coherent evolution, although they generally do not deexcite the atoms. Consequently, *collision broadening* simply leads to a larger Lorentzian linewidth,

$$\boxed{\gamma' = \Gamma + \gamma_{col}} \ , \tag{1.121}$$

[13] Some authors define the saturation for $s = 2$, as happens when $\Omega = \Gamma$.

which, however, is not associated to a faster decay time. The decay time is still given by the inverse of Γ.

The theory of atomic collisions covers a large area of research, including elastic and inelastic, reactive and ionizing processes. In low-pressure gases at room temperature or hotter we need only consider the simpler processes: long-range van der Waals interactions that result in *elastic collisions*. The 'low pressure' criterion requires that the average free path between collisions be greater than any linear dimension of the gas volume. Under these conditions, collisions can be modeled with straight trajectories, along which the interaction time is short and the time between collisions is long in comparison with the radiative lifetime of the excited atomic state. Then, the impact of a collision on the emission of a radiating atom causes a loss of coherence due to a phase interruption of the excited state atomic wavefunction. The term 'elastic' means that the collision does not disturb the populations of the internal states. The inverse of the collision rate is simply the time between phase interruptions or the time between collisions. Now, for collisions between hard cores of atoms of mass m (with reduced mass $m_{red} = m/2$) and with radius ρ in a gas with density n consisting of a single species, a standard analysis based on the kinetic theory of dilute gases shows that the time between collisions is given by the *collision rate*,

$$\gamma_{col} = \tau_{col}^{-1} = \sigma_{col} n \bar{v} \ , \tag{1.122}$$

where $\bar{v} = \sqrt{\frac{8k_BT}{\pi m_{red}}}$ is the average collision velocity in a homogeneous gas at the temperature T and $\sigma_{col} = \sqrt{8}\pi\rho^2$ the collision cross section. Thereby,

$$\boxed{\gamma_{col} = \frac{8\rho^2 n}{\sqrt{m_{red}/\pi k_B T}}} \ . \tag{1.123}$$

1.4.4.1 Doppler broadening

Doppler broadening is simply the apparent frequency distribution of a sample of radiating atoms at temperature T. The contribution of each atom to the radiation appears detuned by the *Doppler shift* because of its velocity. The frequency shift for a non-relativistically moving particle is $\omega = \omega_0/(1 - \frac{v}{c})$, such that,

$$\Delta \equiv \omega - \omega_0 \simeq \omega_0 \frac{v}{c} = \mathbf{k} \cdot \mathbf{v} = k v_z \ , \tag{1.124}$$

where $\mathbf{k}$ is the wavevector of the light and $\mathbf{v}$ is the velocity of the atom. This distribution of Doppler shifts of a gaseous sample in thermal equilibrium follows the probability distribution of velocities,

$$\begin{aligned} P(v_z)dv_z &= N\sqrt{\frac{2m}{\pi k_B T}} e^{-mv_z^2/2k_BT} dv_z \\ &= P(\omega)d\omega = \sqrt{\frac{2}{\pi}} \frac{N}{\sigma} e^{-\Delta^2/2\sigma^2} d\omega = 2N\mathcal{G}_\sigma(\omega - \omega_0)d\omega \end{aligned} \tag{1.125}$$

which is normalized to $N = \int_0^\infty P(v_z)dv_z = \int_0^\infty P(\omega)d\omega$. Obviously, the line profile is a Gaussian function,

$$\mathcal{G}_\delta(\Delta) = (2\pi\delta^2)^{-1/2} e^{-\Delta^2/2\delta^2} \qquad \text{with} \qquad \int_{-\infty}^{\infty} \mathcal{G}_\delta(\Delta)d\Delta = 1 \ , \tag{1.126}$$

centered at $\omega = \omega_0$ and with the width,

$$\text{FWHM} = 2\omega_0 \left(\frac{2k_B T \ln 2}{mc^2} \right)^2 . \tag{1.127}$$

A measure of the width is also the *standard deviation*,

$$2\sigma = \frac{2\omega_0}{c} \sqrt{\frac{k_B T}{m}} = \frac{\text{FWHM}}{1.177} . \tag{1.128}$$

Doppler broadening is a property of the atomic ensemble, each atom suffering a unique but different displacement than the other atoms. Hence, it is called *inhomogeneous broadening*.

1.4.4.2 Voigt profile

It is clear that in many practical circumstances homogeneous and inhomogeneous processes simultaneously contribute to the broadening of lines. In these cases, we can consider that the radiation of each atom, homogeneously broadened by phase-interruption processes (such as spontaneous emission or collisions), is displaced by the Doppler effect within the Maxwell-Boltzmann distribution corresponding to the temperature T. The profile of the gaseous sample, therefore, is a convolution of homogeneous and inhomogeneous profiles. The resulting profile is called *Voigt profile*:

$$\begin{aligned} \mathcal{V}(\omega - \omega_0) &= \int_{-\infty}^{\infty} \mathcal{L}(\omega - \omega_0 - \omega') \mathcal{D}(\omega - \omega_0) d\omega' \\ &= \frac{\gamma}{2\sigma\sqrt{2\pi}} \int_{-\infty}^{\infty} \frac{e^{-(\omega-\omega_0)^2/2\sigma^2}}{(\omega - \omega_0 - \omega')^2 + (\gamma/2)^2} d\omega' . \end{aligned} \tag{1.129}$$

This integral has no analytical solution, but it is easy to solve numerically. Resolve Excs. 1.4.5.1 to 1.4.5.9.

1.4.5 Exercises

1.4.5.1 Ex: Optical pumping

An excited molecular level $|E_i\rangle$ is connected with three lower levels $|n\rangle$ and the ground state $|0\rangle$ by radiative transitions with spontaneous probabilities $A_{i0} = 4 \cdot 10^7\,\text{s}^{-1}$, $A_{i1} = 3 \cdot 10^7\,\text{s}^{-1}$, $A_{i2} = 1 \cdot 10^7\,\text{s}^{-1}$, $A_{i3} = 5 \cdot 10^7\,\text{s}^{-1}$.
a. Calculate the spontaneous lifetime τ_i and the relative population densities N_n/N_i under cw excitation of $|i\rangle$ when $\tau_1 = 500\,\text{ns}$, $\tau_2 = 6\,\text{ns}$, and $\tau_3 = 10\,\text{ns}$.
b. Determine the Einstein coefficient B_{0i} for the excitation of $|i\rangle$ from the ground state with $\tau_0 = \infty$ and with the statistical weights $g_0 = 1$ and $g_1 = 3$. At which spectral energy density ρ_ν is the induced absorption rate equal to the spontaneous decay rate of level $|i\rangle$? What is the intensity of a laser with a bandwidth of 10 MHz at this radiation density?
c. How large is the absorption cross-section σ_{0i} if the absorption linewidth is solely determined by the lifetime of the upper level?

1.4.5.2 Ex: Rabi oscillations

Under the conditions of Exc. 1.4.5.1 there is an inversion between levels $|i\rangle$ and $|2\rangle$ which allows laser action on this transition. What is the minimum field amplitude E_0 and energy density ρ of this transition that cause a Rabi oscillation between levels $|2\rangle$ and $|i\rangle$ with a period $T = 1/\Omega$ which is shorter than the lifetime of $|2\rangle$?

1.4.5.3 Ex: Young's interference fringes

Calculate the maximum slit separation in Young's interference experiments that still gives distinct interference fringes, if the two slits are illuminated a. by incoherent light of $\lambda = 500\,\text{nm}$ from a hole with 1 mm diameter, 1 m away from the slits;
b. by a star with 10^6 km diameter, at a distance of 4 light-years;
c. by two partial beams of a He-Ne laser with a spectral width of 1 MHz (Fig. 2.36).

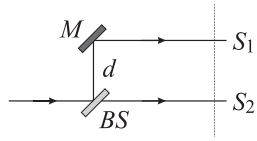

Figure 1.15: Schematic diagram of Michelson's star interferometer.

1.4.5.4 Ex: Quenching collisions

An optically excited sodium atom Na($3P$) with a spontaneous lifetime $\tau(3P) = 16\,\text{ns}$ is placed in a cell filled with 10 mbar nitrogen gas at a temperature of $T = 400\,\text{K}$. Calculate the effective lifetime $\tau_{eff}(3P)$ if the quenching cross section for Na($3P$)-N_2 collisions is $\sigma_q = 4 \cdot 10^{-15}\,\text{cm}^2$.

1.4.5.5 Ex: Line broadening mechanisms

Determine the natural linewidth, the Doppler width, pressure broadening and shifts for the neon transition $3s_2 \rightarrow 2p_4$ at $\lambda = 632.8\,\text{nm}$ in a HeNe discharge at $p_{\text{He}} = 2\,\text{mbar}$, $p_{\text{Ne}} = 0.2\,\text{mbar}$ at a gas temperature of 400 K. The relevant data are: $\tau(3s_2) = 58\,\text{ns}$, $\tau(2p_4) = 18\,\text{ns}$, $\sigma_B(\text{Ne-He}) \approx 6 \cdot 10^{-14}\,\text{cm}^2$, $\sigma_S(\text{Ne-He}) \approx 1 \cdot 10^{-14}\,\text{cm}^2$, $\sigma_B(\text{Ne-Ne}) = 1 \cdot 10^{-13}\,\text{cm}^2$, $\sigma_S(\text{Ne-Ne}) = 1 \cdot 10^{-14}\,\text{cm}^2$.

1.4.5.6 Ex: Dominant broadening mechanisms

What is the dominant broadening mechanism for absorption lines in the following examples:
a. The output from a CO_2 laser with 50 W at $\lambda = 10\,\mu\text{m}$ is focused into a sample of SF_6 molecules at the pressure p. The laser beam waist w in the focal plane is 0.25 mm. Use the numerical parameters $T = 300\,\text{K}$, $p = 1\,\text{mbar}$, the broadening cross section $\sigma_b = 5 \cdot 10^{-14}\,\text{cm}^2$ and the absorption cross section $\sigma_a = 10^{-14}\,\text{cm}^2$.
b. Radiation from a star passes through an absorbing interstellar cloud of H-atoms, which absorb on the hfs-transition at $\lambda = 21\,\text{cm}$ and on the Lyman-α transition

$1S \rightarrow 2P$ at $\lambda = 121.6\,\text{nm}$. The Einstein coefficient for the $\lambda = 21\,\text{cm}$ line is $A_{ik} = 4 \cdot 10^{-15}\,\text{s}^{-1}$, that for the Lyman-$\alpha$ transition is $A_{ik} = 1 \cdot 10^{9}\,\text{s}^{-1}$. The atomic density of H atoms is $n = 10\,\text{cm}^{-3}$ and the temperature $T = 10\,\text{K}$. At which path lengths has the radiation decreased to 10% of I_0 for the two transitions?
c. The expanded beam from a HeNe laser at $\lambda = 3.39\,\mu\text{m}$ with 10 mW power is sent through a methane cell ($T = 300\,\text{K}$, $p = 0.1\,\text{mbar}$, beam diameter: 1 cm). The absorbing CH_4 transition is from the vibrational ground state ($\tau \approx \infty$) to an excited vibrational level with $\tau \approx 20\,\mu\text{s}$. Give the ratios of Doppler width to transit-time width to natural width to pressure-broadened linewidth for a collision cross section $\sigma_b = 10^{-16}\,\text{cm}^2$.
d. Calculate the minimum beam diameter that is necessary to bring about the transit-time broadening in Exercise 3.2c below the natural linewidth. Is saturation broadening important, if the absorption cross section is $\sigma = 10^{-10}\,\text{cm}^2$?

1.4.5.7 Ex: Lorentzian and Gaussian line profiles

The sodium D-line at $\lambda = 589\,\text{nm}$ has a natural linewidth of $\gamma/(2\pi) = 10\,\text{MHz}$.
a. How far away from the line center do the wings of the Lorentzian line profile exceed the Doppler profile at $T = 500\,\text{K}$ if both profiles are normalized to $I(\omega_0) = I_0$?
b. Calculate the intensity $I(\omega - \omega_0)$ of the Lorentzian which equals that of the Gaussian profile at this frequency ω_c relative to the line center ω_0.
c. Compare the intensities of both profiles normalized to 1 at $\omega = \omega_0$ at a distance $0.1(\omega_0 - \omega_c)$ from the line center.
d. At what laser intensity is the power broadening equal to half of the Doppler width at $T = 500\,\text{K}$, when the laser frequency is tuned to the line center ω_0 and pressure broadening can be neglected?

1.4.5.8 Ex: Quenching collisions

An excited atom with spontaneous lifetime τ suffers quenching collisions. Show that the line profile stays Lorentzian and doubles its linewidth if the mean time between two collisions is $\bar{t}_c = \tau$. Calculate the pressure of N_2 molecules at $T = 400\,\text{K}$ for which $\bar{t}_c = \tau$ for collisions Na^*+N_2 with the quenching cross section $\sigma_a = 4 \cdot 10^{-15}\,\text{cm}^2$.

1.4.5.9 Ex: Evaluation of broadening mechanism

A cw laser with 100 MHz output power excites K atoms at low potassium pressures in a cell with 10 mbar neon as a buffer gas at a temperature $T = 350\,\text{K}$. Estimate the different contributions to the total linewidth. At which laser intensities does the power broadening at low pressures exceeds the pressure broadening at 10 mbar (the lifetime of the upper level is $\tau_{sp} = 25\,\text{ns}$) and how strong has the laser beam to be focused that power broadening at 10 mbar exceeds the Doppler width?

1.5 Atomic level structure

Up to here we have focused on the two-level atom problem where the light field couples a single ground and excited state. In practice atoms have many levels, and in general the light field couples more than two levels at the same time. Particularly in laser

cooling one must deal with the coupling of large numbers of states by light. This section discusses the nature of these states and shows their origin for specific atoms confusing on alkali-metals. The discussion is generally restricted to the ground and first excited states, since these are the only ones that play a significant role in laser cooling.

1.5.1 Level structure of alkali-metal atoms

Alkali-metal atoms were the first ones to be cooled and trapped. Their popularity stems has several reasons. Most important is that the excitation frequency from the lowest to the first excited state is in the visible region, which makes it relatively simple to generate light for the optical transitions. Another reason is that it is easy to generate an atomic beam for the alkalis, which have a large vapor pressure at a modest temperature of only a few hundred degrees Celsius. Heating alkali-metals in an oven with a small opening produces an effusive beam of atoms that can be readily manipulated by laser light.

The ground states of all the alkali-metal atoms have a closed shell with one valence electron. For example for sodium (Na) the electron configuration is given by ^{23}Na $(1s)^2(2s)^2(2p)^6(3s)$ = [Ne] $(3s)$. Since the core is a closed shell, it does not contribute to the orbital angular momentum of the atom, and there remains only the outer, valence electron. The state of this electron is completely determined by its orbital angular momentum ℓ and spin angular momentum s. These two momenta couple in the usual way to form the total angular momentum j of the electron:

$$|\ell - s| \leq j \leq \ell + s \ . \tag{1.130}$$

Since the only contribution to the total angular momentum of the atom comes from the valence electron, the total orbital angular momentum is $\mathbf{L} = \vec{\ell}$, spin angular momentum $\mathbf{S} = \mathbf{s}$, and total angular momentum $\mathbf{J} = \mathbf{j}$ for all electrons. Different values of $\mathbf{J}$ lead to different energies of the states, since the spin-orbit interaction $V_{so} = A\mathbf{L}\cdot\mathbf{S}$ depends on the orientation of $\mathbf{S}$ with respect to $\mathbf{L}$. This splitting of the states by the spin-orbit interaction is called the fine structure of the atom. The LS-coupling discussed above is therefore only valid if this spin-orbit interaction is small compared to the level separation of the states.

For the alkali-metal atoms the electronic states are fully specified in the Russell-Saunders notation as $n^{(2S+I)}L_J$, where n is the principal quantum number of the valence electron. The lowest state of Na is the $3^2S_{1/2}$ state, whereas the first excited states are the $3^2P_{1/2,3/2}$ states, where the valence electron is excited to the $(3p)$-state. In this case the angular momentum $L = 1$ can couple with the total spin $S = \frac{1}{2}$ to form either $J_e = \frac{1}{2}$ or $J_e = \frac{3}{2}$. The fine structure splitting between these two states is $\approx 515\,\mathrm{GHz}$ in Na.

The structure of the alkali-metal atoms becomes somewhat more complicated when the interaction of the nuclear spin $\mathbf{I}$ with the total angular momentum of the electron $\mathbf{J}$ is included. These angular momenta couple in the usual way to form the total angular momentum as $\mathbf{F} = \mathbf{I} + \mathbf{J}$. Different values of $\mathbf{F}$ for the same values of both $\mathbf{I}$ and $\mathbf{J}$ are split by the $A\mathbf{I}\cdot\mathbf{J}$ interaction between the nuclear spin and the electronic angular momentum. The resulting energy structure is called the hyperfine structure (hfs). This hfs is generally much smaller than the fine structure because of the much

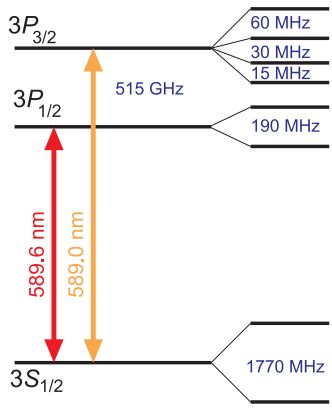

Figure 1.16: The ground S state and lowest lying P states of atomic Na, showing the hyperfine structure schematically.

smaller size of the nuclear magnetic moment. For Na, with a nuclear spin of $I = \frac{3}{2}$, the ground state has $F_g = 1$ and 2, and the hfs is $\approx 1.77\,\text{GHz}$. The excited state has $F_e = 0, 1, 2, 3$, and the resulting hfs is only on the order of 100 MHz. In general, the shift of the energy levels because of the hyperfine interaction can be written as [14] [66, 5],

$$\Delta E_{hfs} = \tfrac{1}{2}hAK + hB\frac{\frac{3}{2}K(K+1) - 2I(I+1)J(J+1)}{2I(2I-1)2J(2J-1)}\,, \tag{1.131}$$

where $K = F(F+1) - I(I+1) - J(J+1)$ and A and B are two parameters, that are adjusted using experimental data [5]. The splitting between adjacent levels becomes,

$$\Delta E_{hfs}(F) - \Delta E_{hfs}(F-1) = hAF + 3hBF\frac{F^2 - I(I+1) - J(J+1) + \frac{1}{2}}{2I(2I-1)J(2J-1)}\,, \tag{1.132}$$

where F denotes the highest value of the total angular momentum of the two adjacent levels. A schematic diagram for the fine and hyperfine structure of Na, or other alkalis with $I = 3/2$, is given in Fig. 1.16 [15].

Each of these states of alkali-metal atoms is further split into $(2I+1)(2J+1)$ Zeeman sublevels. In the case of Na with $I = \frac{3}{2}$, this leads to 8 Zeeman sublevels in the ground state ($J_g = \frac{1}{2}$), 8 sublevels in the first excited state ($J_e = \frac{1}{2}$), and 16 sublevels in the next excited state ($J_e = \frac{3}{2}$). In principle, the light can drive all transitions between ground and excited sublevels. However, certain selection rules have to be obeyed, and these limit the number of transitions considerably. These selection rules are discussed in more detail in Sec. 1.5.2.

In the absence of any perturbations, many of these Zeeman sublevels are degenerate, but application of an external field lifts the degeneracy. It has already been shown in Sec. 1.3.2 that the presence of a light field not only induces transitions, but also shifts the energy levels. Later in this chapter it is shown that the transition strengths vary among the Zeeman sublevels, and thus a laser field can lift the degeneracy through the different light shifts.

[14] See script on *Quantum mechanics* (2023), Sec. 8.2.4.
[15] See script on *Quantum mechanics* (2023), Sec. 7.3.2.

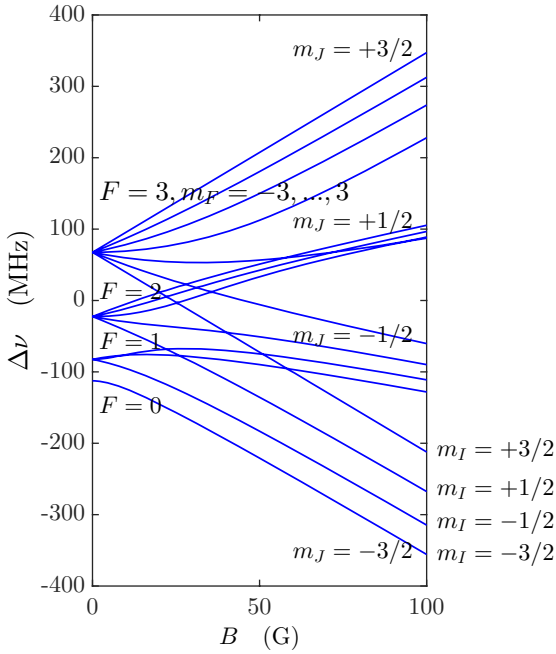

Figure 1.17: (code for download) Hyperfine splitting of the $3P_{3/2}$ state of Na (see Fig. 1.16). m_F is the projection of the total angular momentum of the atom on the magnetic field axis.

An applied magnetic field B can also lift these degeneracies, producing the well-known Zeeman effect, as shown in Fig. 1.17. At low fields the energy level shifts ΔE are proportional to the field strengths according to,

$$\Delta E_{zeem} = g\mu_B m B \ , \tag{1.133}$$

where $\mu_B \equiv e\hbar/2m_e c$ is the Bohr magneton, m is the projection of the angular momentum along B, and g is the Lande g-factor (here m_e is the electron mass). The presence of the nuclear spin changes the g-factor from its usual g_J value given by

$$g_J = 1 + \frac{J(J+1) + S(S+1) - L(L+1)}{2J(J+l)} \tag{1.134}$$

to

$$g_F = g_J \frac{F(F+1) + J(J+1) - I(I+1)}{2F(F+1)} \ . \tag{1.135}$$

Here L, S, and J refer to the electron's angular momenta, I is the nuclear spin, and F is the total atomic angular momentum that ranges from $F = |J - I|$ to $F = J + I$ in integer steps. Thus the different manifolds of Fig. 1.17 have different slopes at small field values. In Exc. 1.5.6.1 we verify that the Zeeman shift depends only on the absolute value of the magnetic field.

1.5.2 Angular momentum and selection rules

For optical transitions the coupling between the atomic states is given by the dipole moment, and selection rules exist for such transitions. Selection rules can be inferred from the equations derived in the next section, but they can also be quite simply calculated from the commutation relations [37]. For the z-component of the orbital angular momentum $\hat{L}_z$ of the atom, the following commutation rules apply:

$$[\hat{L}_z, \hat{x}] = \imath\hbar\hat{y} \ , \qquad [\hat{L}_z, \hat{y}] = -\imath\hbar\hat{x} \ , \qquad [\hat{L}_z, \hat{z}] = 0 \tag{1.136}$$

The eigenfunctions of the atoms are denoted by $|\alpha LM\rangle$, where α represents all the other properties of the state besides its orbital angular momentum. The third relation of Eqs. (1.136) leads to,

$$(m' - m)\langle\alpha' L' m'|\hat{z}|\alpha L m\rangle = \langle\alpha' L' m'|[\hat{L}_z, \hat{z}]|\alpha L m\rangle = 0 \ , \tag{1.137}$$

where the last equality holds because the last commutator in Eq. (1.136) is 0. As the next section shows, the coupling between two states by linearly polarized light is proportional to the matrix element for $\hat{z}$, so linearly polarized light can couple two states only if $\Delta m = 0$. Using the same procedure for $\hat{x}$ and $\hat{y}$ leads to,

$$\begin{aligned} \hbar(m' - m)\langle\alpha' L' m'|\hat{x}|\alpha L m\rangle &= \langle\alpha' L' m'|[\hat{L}_z, \hat{x}]|\alpha L m\rangle = \imath\hbar\langle\alpha' L' m'|\hat{y}|\alpha L m\rangle \\ \hbar(m' - m)\langle\alpha' L' m'|\hat{y}|\alpha L m\rangle &= \langle\alpha' L' m'|[\hat{L}_z, \hat{y}]|\alpha L m\rangle = -\imath\hbar\langle\alpha' L' m'|\hat{x}|\alpha L m\rangle \ . \end{aligned} \tag{1.138}$$

The combination of these two relations requires that either $\Delta m = \pm 1$ or that the matrix element for $\hat{x}$ or for $\hat{y}$ must vanish. Again, the next section shows that for circularly polarized light the appropriate matrix element is a combination of $\hat{x}$ and $\hat{y}$. The selection rules for circularly polarized light are thus $\Delta m = \pm 1$, where the $(+)$-sign is for right-handed and the $(-)$-sign for left-handed circular polarization.

Note that these selection rules reflect the conservation of angular momentum. Since each photon carries an angular momentum 1, the projection of this angular momentum on the z-axis can be $0, \pm 1$. Conservation of angular momentum requires that absorption of a photon be accompanied by a corresponding change of the projection of the angular momentum of an atom. In the case of fine or hyperfine interaction, the orbital angular momentum L can be replaced by the total angular momentum J of the electron or F of the atom, respectively. The same selection rules thus apply for m_J and m_F.

For the selection rules for $\hat{\mathbf{L}}^2$, we consider the commutation relation,

$$\left[\hat{L}^2, [\hat{L}^2, \hat{\mathbf{r}}]\right] = 2\hbar^2(\hat{\mathbf{r}}\hat{L}^2 + \hat{L}^2\hat{\mathbf{r}}) \ , \tag{1.139}$$

which can be obtained from the usual algebra for commutators [37]. Eq. (1.139) explicitly depends on the fact that $\mathbf{L} = \mathbf{r} \times \mathbf{p}$ is the orbital angular momentum of the atom, and this relation *cannot be generalized* for either $\mathbf{J}$ or $\mathbf{F}$. Calculating the matrix element for both sides of Eq. (1.139) results in

$$\begin{aligned} \langle\alpha' L' m'|\left[\hat{L}^2, [\hat{L}^2, \hat{\mathbf{r}}]\right]|\alpha L m\rangle &= 2\hbar^4[L(L+1) + L'(L'+1)]\langle\alpha' L' m'|\hat{\mathbf{r}}|\alpha L m\rangle \\ &= \hbar^4[L(L+1) - L'(L'+1)]^2\langle\alpha' L' m'|\hat{\mathbf{r}}|\alpha L m\rangle \ . \end{aligned} \tag{1.140}$$

Thus the coupling between two states is zero for any polarization, unless the two factors in front of the matrix elements in Eq. (1.140) are equal. Rearrangement of this requirement leads to [37],

$$[(L' + L + 1)^2 - 1][(L' - L)^2 - 1] = 0 \; . \tag{1.141}$$

The first term can only be zero if $L = L' = 0$, but this is prohibited since L' is the vector sum of L and $\kappa = 1$ for the photon, and thus cannot be zero. The second term is zero only if $\Delta L = \pm 1$, so this is the selection rule for $\hat{\mathbf{L}}^2$. Again, this selection rule reflects the conservation of angular momentum for absorption of one photon.

Also for $\Delta L = 0$ the final state angular momentum L' can be the vector sum of L and κ. But the parity of the state for a one-electron system is given by $(-1)^L$ and $\mathbf{r}$ is antisymmetric, so symmetry demands that the matrix element be zero between states where L and L' are both either odd or even. The selection rules for J and F are $\Delta J = 0, \pm 1$ and $\Delta F = 0, \pm 1$. In contrast with the case for $\Delta L, \Delta J = 0$ is allowed, since L and S couple to J, so $\Delta J = 0$ does not imply $\Delta L = 0$. Only for $J = J' = 0$ is $\Delta L = 0$ a necessary consequence, and therefore transitions with $J = 0 \; \rightarrow \; J' = 0$ are forbidden. The same rule applies to F, namely, $F = 0 \; \rightarrow \; F' = 0$ is also forbidden.

In laser cooling, selection rules play a very important role. In order to slow atoms from their thermal velocity down to zero velocity, a large number of photons have to be scattered. Therefore, the coupling strength between the two levels involved in the laser cooling has to be sufficiently high. Furthermore, since the atoms have to undergo a very large number of cycles, the decay from the excited to the ground state must be to only the sublevel coupled by the light. This restricts the number of possible cooling transitions. The selection rules can be used to determine whether two states are coupled by the laser light without extensive calculations.

For the alkali-metal atoms, the hfs complicates the level structure and most of the optically accessible transitions do not meet these criteria. Since the same selection rules for excitation are valid for spontaneous emission, the $\Delta F = 0, \pm 1$ selection rule allows the decay of one excited state to many ground states, and some of these may not be coupled by the laser to an excited state. This is because the laser's spectral width is generally much smaller than the ground-state hfs-splitting. However, for the states with $J = L + \frac{1}{2}$, the decay from the highest F_e-state can only occur to the highest F_g-state, since the other ground state has $F_g = F_e - 2$ (see Fig. 1.16). Therefore these two states form a closed two-level system. A similar system exists between the lowest F_e and F_g states. However, since the hfs splitting between the two lowest excited states is usually very small, exciting the lowest F_e-state can often also partially excite the next F_e state, which can then decay to the other hyperfine ground-state sublevels. Laser cooling in the alkalis is therefore usually carried out on the highest F_g and F_e states.

These complications do not appear in the metastable noble gas atoms, where the splitting between the states is caused by the spin-orbit interaction instead of the hyperfine interaction. For Ne* only the $^3P_{0,2}$ states are truly metastable. The only closed system can be formed by the $^3P_2 \; \rightarrow \; ^3D_3$ transition, which is the one most often used for laser cooling. Similar transitions exist for the other metastable noble gases and for the earth-alkali metals.

1.5.3 Optical transitions in multilevel atoms

The optical transitions considered in so far were restricted to the particularly simple case of a two-level atom, and these transitions can be described by a single Rabi frequency. Real atoms have more than two levels that can be coupled by the optical field, and furthermore, the relative strengths of their multiple transitions depend on the orientation of the atomic dipole moment with respect to the polarization of the light. The single Rabi frequency that describes the coupling is given by $\hbar\Omega = -d_{eg}\mathcal{E}_0$ [see Eq. (1.81)], where,

$$d_{eg} = e\langle e|\hat{\epsilon}\cdot\hat{\mathbf{r}}|g\rangle \ . \tag{1.142}$$

The value of the dipole moment of Eq. (1.142) depends on the wavefunctions of the ground and excited states, and is generally complicated to calculate. It is often convenient to introduce the spherical unit vectors given by [16],

$$\hat{\mathbf{e}}_{-1} \equiv \tfrac{1}{\sqrt{2}}(\hat{\mathbf{e}}_x - \imath\hat{\mathbf{e}}_y) \quad , \quad \hat{\mathbf{e}}_{+1} \equiv -\tfrac{1}{\sqrt{2}}(\hat{\mathbf{e}}_x + \imath\hat{\mathbf{e}}_y) \quad , \quad \hat{\mathbf{e}}_0 \equiv \hat{\mathbf{e}}_z \tag{1.143}$$

and to expand the polarization vector $\hat{\epsilon}$ in terms of these vectors. Note that $\hat{\mathbf{e}}_\pm$ corresponds to circularly polarized light, whereas $\hat{\mathbf{e}}_z$ corresponds to linearly polarized light. For simplicity, only cases where the polarization of the light field is given by just one of these vectors will be considered, and this will be indicated by the symbol q ($q = 0, \pm'$ is the subscript of $\hat{\mathbf{e}}_q$). In this notation the components of the dipole moment can be written as,

$$\hat{\epsilon}\cdot\hat{\mathbf{r}} = \hat{\mathbf{e}}_q\cdot\hat{\mathbf{r}} = \sqrt{\tfrac{4\pi}{3}}\hat{r}Y_{1q}(\theta,\phi) \ , \tag{1.144}$$

where the Y_{1q}'s represent the simplest of the spherical harmonic functions.

The matrix element of Eq. (1.142) can be broken up into two parts, one depending on all the various quantum numbers of the coupled states and the other completely independent of m, the projection of $\mathbf{L}$ on the quantization axis z. This separation is embodied in the well-known Wigner-Eckart theorem discussed in many quantum mechanics texts [12]. Here, the treatment will be somewhat different, since this section treats the simplest case, namely, that fine and hyperfine structure are absent. The more general case will be treated in Sec. 1.5.4. Thus the hydrogenic wavefunctions for the ground and excited state can be used,

$$|g\rangle = |n\ell m\rangle = R_{n\ell}Y_{\ell m}(\theta,\phi) \qquad \text{and} \qquad |e\rangle = |n'\ell'm'\rangle = R_{n'\ell'}Y_{\ell'm'}(\theta,\phi) \ , \tag{1.145}$$

Substitution of Eqs. (1.144) and (1.145) into Eq. (1.142) leads to,

$$= e\langle n'\ell'm'|\hat{\epsilon}\cdot\hat{\mathbf{r}}|n\ell m\rangle = e\langle n'\ell'||r||n\ell\rangle\langle\ell'm'|\sqrt{\tfrac{4\pi}{3}}\hat{r}Y_{1q}|\ell m\rangle \equiv eR_{n'\ell',n\ell}A_{\ell'm',\ell m} \ . \tag{1.146}$$

The following sections first treat the radial or physical part $R_{n'\ell',n\ell}$, also known as the reduced or double-bar matrix element, and then the angular or geometric part $A_{\ell'm',\ell m}$.

[16] See script on *Quantum mechanics* (2023), Sec. 12.2.2.

1.5.3.1 Radial part of the dipole matrix element

The radial part of the matrix element is generally less important in laser cooling because experiments typically use an optical transition joining a set of states that all share the same ground- and excited-state radial wavefunctions. Therefore it becomes an overall multiplicative factor that determines only the magnitude of the coupling (e.g., the overall Rabi frequency). It is given by,

$$R_{n'\ell',n\ell} = \langle R_{n'\ell'}(r)|\hat{r}|R_{n\ell}(r)\rangle = \int_0^\infty r^2 dr\ R_{n'\ell'}(r) r R_{n\ell}(r)\ , \tag{1.147}$$

with $R_{n\ell}$ the radial wavefunction of the state. Here the r^2dr term in the integral originates from the radial part of d^3r. The radial part can be evaluated if the eigenfunctions are known. For all atoms except hydrogen, the eigenfunctions can only be calculated approximately and therefore only approximate values for the radial part can be found. However, for the hydrogen atom the eigenfunctions of the bound states are known and the radial matrix elements can be calculated exactly [12]. For instance, for the first optical allowed transition in hydrogen, the $1s \rightarrow -2p$ transition, the radial wavefunctions involved are $R_{1s}(r) = 2e^{-r/a_B}/a_B^{3/2}$ and $R_{2p}(r) = (r/a_B)e^{-r/2a_B}/\sqrt{3}(2a_B)^{3/2}$. Thus the integral becomes,

$$R_{2p,1s} = \int_0^\infty R_{2p}(r) r R_{1s}(r) r^2 dr = 2^7\sqrt{6}a_B/3^5 \approx 1.290 a_B\ . \tag{1.148}$$

For other transitions in hydrogen similar integrals can be evaluated. The hydrogenic wavefunctions are given by [12],

$$R_{n'\ell',n\ell} = N_{n\ell}\rho^\ell e^{-\rho/2} L_{n-\ell-1}^{2\ell+1}(\rho)\ , \tag{1.149}$$

where $\rho \equiv 2r/na_B$ and $L_n^m(r)$ are the Laguerre polynomials, and $N_{n\ell}$ is a normalization constant.

Substitution of Eq. (1.149) into Eq. (1.147) and integrating over r with the help of standard integrals, the matrix element for any transition can be found. Note that the radial matrix elements increase with increasing n, since the radius of the electron orbit increases with n.

For all other atoms, the situation is more complicated. In the case of alkali-metal atoms with only one active electron, the matrix elements can be quite accurately expressed in terms of the effective principal quantum number $n_\ell^* = n - \delta_\ell$ of the valence electron, where δ_ℓ is called the quantum defect and depends on the orbital quantum number ℓ [15]. The same analysis as in the hydrogen case can be applied for the alkali-metal atoms; however, in the summation n is now replaced by n^* [9].

1.5.3.2 Angular part of the dipole matrix element

The angular part $A_{\ell' m\,\ell m}$ of the dipole moment for atoms with $S = 0 = I$ is defined by Eq. (1.146):

$$A_{\ell' m\,\ell m} = \sqrt{\frac{4\pi}{3}}\langle Y_{\ell' m'}|Y_{1q}|Y_{\ell m}\rangle\ , \tag{1.150}$$

where the integration limits are over 4π. The integral can be expressed in terms of the $\{3j\}$-symbols as,

$$A_{\ell' m\, \ell m} = (1)^{\ell'-m'} \sqrt{\max(\ell, \ell')} \begin{pmatrix} \ell' & 1 & \ell \\ -m' & q & m \end{pmatrix} . \tag{1.151}$$

The $\{3j\}$-symbols are related to the Clebsch-Gordan coefficients and are tabulated in [67] [see Eq. (1.154)]. The symmetry of the $\{3j\}$-symbols dictates that they are only nonzero when the sum of the entries in the bottom row is zero, which means $m + q = m'$. Thus circularly polarized light only couples states that differ in m by ± 1, whereas linearly polarized light only couples states that have equal m's. This result is thus identical to the result obtained in Sec. 1.5.2.

1.5.4 Fine and hyperfine interactions

In case of fine and hyperfine interaction the situation changes considerably. For the fine structure, the energy levels are split by the spin-orbit interaction and $\mathbf{L}$ is no longer a good quantum number. Here ℓ is replaced with $\mathbf{L}$ to be more general. The states are now specified by $\mathbf{J}$, the vector sum of $\mathbf{L}$ and $\mathbf{S}$. However, the optical electric field still couples only to the orbital angular momentum $\mathbf{L} = \mathbf{r} \times \mathbf{p}$ of the states. In this situation the Wigner-Eckart theorem could also be applied to calculate the transition strength [30], but again this section will follow a different route that provides more insight in the problem. Although the formulas below may appear rather complicated, the principle is simple.

The atomic eigenstates are denoted by $|\alpha J m_J\rangle$ in the J-basis, and m_J explicitly indicates for which angular momentum the magnetic quantum number M is the projection. In most cases, this is obvious from the notation, but in this section it is not. The dipole transition matrix element is therefore given by,

$$d_{eg} = e\langle \alpha' J' m' | \hat{\epsilon} \cdot \hat{\mathbf{r}} | \alpha J m_J \rangle . \tag{1.152}$$

Since the optical electric field only couples the $\mathbf{L}$ component of these $\mathbf{J}$ states, these eigenfunctions must be first expanded in terms of the L and S wavefunctions:

$$|\alpha J m_J\rangle = \sum_i C_i |\alpha L m_L\rangle |S m_S\rangle , \tag{1.153}$$

where i represents an appropriate set of angular momentum quantum numbers. The C_i's are Clebsch-Gordan coefficients that can also be expressed in terms of the more symmetrical $\{3j\}$-symbols as,

$$C_i = \langle L m_L, S M_S | J m_J \rangle = (-1)^{-L+S-m_J} \sqrt{2J+1} \begin{pmatrix} L & S & J \\ m_L & m_S & -m_J \end{pmatrix} . \tag{1.154}$$

The fact that Eq. (1.151) for the integral of the product of three spherical harmonics and Eq. (1.154) both contain the $\{3j\}$-symbols is a result of the important connection between the $Y_{\ell m}$'s and atomic angular momenta.

Substitution of Eq. (1.153) in Eq. (1.152) twice leads to a double summation, which contains matrix elements in the (L, S) basis of the form,

$$\langle \alpha' L' m'_L | \langle S' m'_S | \hat{r} | \alpha L M_L \rangle | S m_S \rangle = \langle \alpha' L' m'_L | \hat{r} | \alpha L m_L \rangle \delta_{SS'} \delta_{m_S m'_S} . \tag{1.155}$$

The first term on the right-hand side is the matrix element that has been evaluated before (see Eq. (1.146)). The δ-functions reflect the notion that the light couples the orbital angular momenta of the states, and not the spin. The spin and its projection are not changed by the transition. Substitution of Eq. (1.155) into Eq. (1.152), expansion of the matrix elements in the L-basis, and recoupling of all the Clebsch-Gordan coefficients leads to,

$$d_{eg} = e(-1)^{L'-m'_J}\sqrt{(2J+1)(2J'+1)}\,\langle\alpha' L'||\hat{r}||\alpha L\rangle \begin{Bmatrix} L' & J' & S \\ J & L & 1 \end{Bmatrix} \begin{pmatrix} J & 1 & J' \\ m_J & q & -m'_J \end{pmatrix}. \tag{1.156}$$

The array of quantum numbers in the curly braces is not a $\{3j\}$-symbol, but is called a $\{6j\}$-symbol. It summarizes the recoupling of six angular momenta. Values for the $\{6j\}$-symbols are also tabulated in Ref. [67]. Note that the radial part of the dipole moment has remained unchanged, and so the results of the previous section can still be used.

In case of hyperfine interactions the situation becomes even more complicated. However, the procedure is the same. First the eigenfunctions in the F-basis are expanded in the (J, I)-basis, where I is the nuclear spin, and a $\{6j\}$-symbol involving I, J, and F appears. Then the eigenfunctions of the J-basis are further reduced into the (L, S)-basis. Since the procedure is similar to the procedure for the fine structure interaction, only the result is shown:

$$d_{eg} = e(-1)^{1+L'+S+J+J'+I-M'_F}\,\langle\alpha' L'||\hat{r}||\alpha L\rangle\sqrt{(2J+1)(2J'+1)(2F+1)(2F'+1)} \begin{Bmatrix} L' & J' & S \\ J & L & 1 \end{Bmatrix} \begin{Bmatrix} J' & F' & I \\ F & J & 1 \end{Bmatrix} \begin{pmatrix} F & 1 & F' \\ m_F & q & -m'_F \end{pmatrix}. \tag{1.157}$$

Since S can be parallel or anti-parallel to $L, J' = 1/2, 3/2$ and the fine-structure interaction is usually large compared to the hyperfine interaction.

1.5.5 Selection rules for emission in certain directions

As seen by Eq. (1.152), the excitation rate induced by a light field depends on the relative orientation of the laser polarization $\hat{\epsilon}$ and the magnetic field $\mathbf{B}$. To take this dependence into account, we decompose the polarization vector (which can be linear or elliptical) on a coordinate basis, as shown in Eq. (1.143). Thus, the relative amplitude of the transitions $\Delta m_J = 0$ is proportional to the projection of the polarization vector onto the magnetic field axis, $\epsilon_0 \equiv \hat{\epsilon}\cdot\hat{\mathbf{e}}_0$. To estimate the amplitude of the transitions $\Delta m_J = \pm 1$, we must project onto the coordinates $\epsilon_{\pm 1} \equiv \hat{\epsilon}\cdot\hat{\mathbf{e}}_\pm$. Note that the direction of incidence of the beam, given by the wavevector $\mathbf{k}$, does not influence the transition probability directly (after all, the spatial dependence $e^{i\mathbf{k}\cdot\mathbf{r}}$ was removed by the dipolar approximation; only through the fact, that the polarization is perpendicular to the propagation vector, $\hat{\epsilon} \perp \mathbf{k}$ [57, 58].

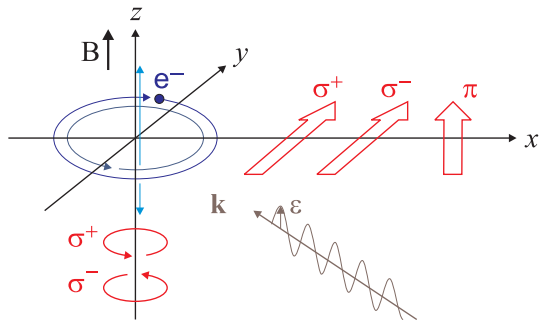

Figure 1.18: Selection rules due to polarization $\hat{\epsilon}$ of the incident light. The projection of this vector onto the axes $\pi = \hat{\epsilon} \cdot \hat{\mathbf{e}}_0$ and $\sigma_\pm = \hat{\epsilon} \cdot \hat{\mathbf{e}}_\pm$ is proportional to the excitation probability (and, obviously, also to the emission probability).

1.5.6 Exercises

1.5.6.1 Ex: Zeeman shift and quantization axes

Choosing the fixed quantization axis $\hat{\mathbf{e}}_z$ and a magnetic field $\vec{\mathcal{B}}$ in an arbitrary direction, calculate the Hamiltonian of the Zeeman interaction with an angular momentum $J = 1$ and show that the energy shift depends only on the absolute value $|\vec{\mathcal{B}}|$.

1.5.6.2 Ex: The Stern-Gerlach effect

Consider initially motionless ^{87}Rb atoms in their electronic ground state $^2S_{1/2}$ trapped in a superposition of two the trappable Zeeman states $|F, m_F\rangle = |2, +2\rangle$ and $|1, -1\rangle$. Suddenly a magnetic gradient of $\partial_z \mathcal{B} = 100\,\mathrm{G/cm}$ is applied for 2 ms. Calculate the spatial separation of the atoms being in either one of the two states after 10 ms of ballistic expansion.

1.6 Further reading

W. Demtröder, *Atoms, Molecules and Photons: An Introduction to Atomic- Molecular- and Quantum Physics* [DOI]

H. Kogelnik et al., *Laser Beams and Resonators* [DOI]

L. Allen et al., *Orbital Angular Momentum of Light and the Transformation of Laguerre-Gaussian Laser Modes* [DOI]

J. Weiner et al., *Light-matter interaction, Fundamentals and applications* [DOI]

T. Mayer-Kuckuk, *Atomphysik* [DOI]

H. J. Metcalf et al., [DOI]

J. Weiner et al., *Experiments and Theory in Cold and Ultracold Collisions* [DOI]

W. Nagourney et al., *Shelved Optical Electron Amplifier: Observation of Quantum Jumps* [DOI]

Th. Sauter et al., *Observation of Quantum Jumps* [DOI]

Th. Sauter et al., *Quantum jumps observed in the fluorescence of a single ion* [DOI]

J.C. Bergquist et al., *Observation of Quantum Jumps in a Single Atom* [DOI]

R. Loudon et al., *The Quantum Theory of Light* [DOI]

Part II

Instrumentation of a Quantum Optics Lab

Chapter 2

Gaussian optics and the polarization of light

The objective of this part of the course is to introduce the student into the basics of *Gaussian optics* and *polarizations optics*. The student will learn how to transform the diameter and the divergence of a Gaussian beam using lenses and telescopes and to analyze and manipulate the polarization of a laser beam.

2.1 Some more basic notions

2.1.1 Definition of photometric quantities

The *radiant energy* W is the total energy emitted from a source. The *radiant power* P (or radiant flux) is the total energy emitted per second. The *radiance* $L(\Omega)$ is defined as the power radiated (emitted, reflected, transmitted or received) under an angle θ through a surface element $d\mathbf{A}$ into a solid angle element $d\Omega = \sin\theta d\theta d\phi$. It is a directional quantity indicating how much of the power will be received by an optical system looking at that surface from a specified angle of view,

$$\boxed{P = \int L(\Omega) dA_n d\Omega} \,. \tag{2.1}$$

Spectral densities are denoted by an index ν, e.g. $P = \int P_\nu(\nu) d\nu$. In (2.1), $dA_n \equiv \hat{\mathbf{n}} \cdot d\mathbf{A} = dA \cos\theta$ is the projection of the surface element onto the surface normal. The quantity,

$$I^* = \int L(\Omega) d\Omega \tag{2.2}$$

is called *radiant intensity*.

> **Example 2 (*Angular distribution of thermal radiation*):** In a blackbody in thermal equilibrium with its surroundings (e.g the walls of a cavity) the radiation is isotropic with a spectral energy distribution given by Planck's law. This means that at any point of the volume of the blackbody radiator an imaginary volume element radiates energy in all directions of space, such that the radiance into a specific solid angle element is,
>
> $$L(\Omega) = \bar{u} \frac{c}{4\pi} \,. \tag{2.3}$$

Radiation passing under an angle θ through a hole of size $dA = dA_n/\cos\theta$ into a specific solid angle element $d\Omega$ generates the radiance,

$$\frac{\partial^2 P}{\partial\Omega\partial A} = L(\Omega)\cos\theta \ . \tag{2.4}$$

In *any* direction we get,

$$\frac{\partial P_\nu}{\partial A} = \int_{\text{half sphere}} L_\nu(\Omega)\cos\theta d\Omega = \bar{u}\frac{c}{4\pi}\int_0^{2\pi} d\phi \int_0^{\pi/2} \cos\theta\sin\theta d\theta = \frac{c\bar{u}}{4} \ . \tag{2.5}$$

Summing up over all surface elements of a sphere of radius R,

$$P = \int \frac{\partial P}{\partial A} dA = \frac{c\bar{u}}{4} R^2 \int_0^{2\pi} d\phi \int_0^{\pi} \sin\theta d\theta = \pi R^2 c\bar{u} \ . \tag{2.6}$$

Accordingly, the spectral distribution is, using Planck's law,

$$P_\nu = P\frac{8\pi h\nu^3}{c^3}\frac{1}{e^{\beta\hbar\omega}-1} = \frac{8\pi^2 R^2 h\nu^3}{c^2}\frac{1}{e^{\beta\hbar\omega}-1} \ . \tag{2.7}$$

A detector covers itself a finite solid angle $d\Omega = \frac{dA'\cos\theta'}{r^2}$. The radiant flux for $r^2 \gg dA, dA'$ can then be expressed as,

$$d\Phi = L(\Omega)dA\cos\theta d\Omega = L(\Omega)dA\cos\theta\frac{dA'\cos\theta'}{r^2} \tag{2.8}$$

$$\text{that is} \qquad \Phi = \int_A\int_{A'} \frac{L(\Omega)}{r^2}\cos\theta\cos\theta' dA dA' \ .$$

Note that for isotropic sources (2.8) is symmetric upon interchanging emitter and detector with regard to θ and θ' or dA and dA'. Furthermore, the formula demonstrates that the radiant flux emitted into the unit solid angle is proportional to $\cos\theta$ (Lambert's law). An example for such a source is a hole with the area dA in a blackbody radiation cavity (see Fig. 2.1). Solve Excs. 2.1.2.1 and 2.1.2.2.

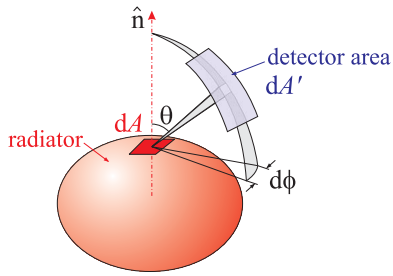

Figure 2.1: Illustration of the radiance.

Note that it is impossible to increase the radiance of a source by any sophisticated imaging optics [26]. This means that the image dA^* of a radiation source dA never has a larger radiance than the source itself. It is true that the flux density can be increased by focussing the radiation. The solid angle, however, into which radiation

from the image dA^* is emitted is also increased by the same factor. Therefore, the radiance does not increase. In fact, because of inevitable reflection, scattering, and absorption losses of the imaging optics, the radiance of the image dA^* is, in practice, always less than that of the source. A strictly parallel light beam would be emitted into the solid angle $d\Omega = 0$. With a finite radiant power this would imply an infinite radiance L, which is impossible. This illustrates that such a light beam cannot be realized. The radiation source for a strictly parallel beam anyway has to be a point source in the focal plane of a lens. Such a point source with zero surface cannot emit any power.

Example 3 (*Radiance of the sun*): An area $A = 1\,\mathrm{m}^2$ of the Earth's surface receives at normal incidence from the sun about $P/A = 1.35\,\mathrm{kW/m}^2$ of intensity. Since the sun covers an angle of $\theta = 0.53^\circ$ seen from the Earth, we can estimate the sun's radiance as,

$$L = \frac{P}{A\Omega} = \frac{P}{A\int_0^{2\pi}\int_0^{\theta}\sin\theta d\theta d\phi} \simeq \frac{P}{A\pi\theta^2} \approx 2\cdot 10^4\,\mathrm{kW\ m^{-2}\ ster^{-1}}\ .$$

The total power received by the Earth is $\frac{P}{A}\pi R_{Earth}^2$. The total power emitted by the sun is $\frac{P}{A}4\pi d_{sun-Earth}^2$.

Example 4 (*Radiance of a HeNe laser*): We consider a HeNe laser emitting $P = 1\,\mathrm{mW}$ of power from a $w_0 = 1\,\mathrm{mm}$ beam waist into an angle of $2\theta = 0.067^\circ$. With a typical emission bandwidth of $\Delta\nu = 1\,\mathrm{MHz}$ the spectral radiance is,

$$L_\nu = \frac{P_\nu}{A\Omega} \simeq \frac{P}{\pi w_0^2\ \pi\theta^2\ \Delta\nu} \approx 1\,\mathrm{kWsm^{-2}\ ster^{-1}}\ .$$

For comparison, the sun's radiance at it's surface ($T = 6000\,\mathrm{K}$) at the same wavelength as the HeNe laser is,

$$L_\nu = \frac{Lu_\nu}{\bar{u}} \approx 5\,\mathrm{nWsm^{-2}\ ster^{-1}}\ .$$

2.1.2 Exercises

2.1.2.1 Ex: Emission of an argon laser

The angular divergence of the output from a $P = 1\,\mathrm{W}$ argon laser is assumed to be $\alpha = 4\cdot 10^{-3}\,\mathrm{rad}$.
a. Calculate the radiance L and the radiant intensity I_1 of the laser beam and the irradiance I (intensity) at a surface 1 m away from the output mirror, when the laser beam diameter at the mirror is $2w_s = 2\,\mathrm{mm}$.
b. What is the spectral power density $u(\nu)$ if the laser bandwidth is 1 MHz?

2.1.2.2 Ex: Photosynthetically active radiation

The photon flux density and the photosynthetically active radiation (PAR) are defined as,

$$\eta_{photon} \equiv \frac{\int_{\lambda_1}^{\lambda_2} u(\lambda,T)\frac{\lambda}{hcN_A}d\lambda}{\int_{\lambda_1}^{\lambda_2} u_{Pl}(\lambda,T)d\lambda} \qquad \text{and} \qquad \eta_{PAR} = \frac{\int_{\lambda_1}^{\lambda_2} u(\lambda,T)d\lambda}{\int_0^{\infty} u(\lambda,T)d\lambda}\ ,$$

where $\lambda_1 = 400\,\mathrm{nm}$ and $\lambda_2 = 700\,\mathrm{nm}$ delimit the range, where photosynthesis takes place. Calculate both quantities for a blackbody at $T = 5800\,\mathrm{K}$ temperature. Plot them as a function of temperature in the range $T = 300..6000\,\mathrm{K}$.

2.2 Introduction to Gaussian optics

2.2.1 Wave equation and beam parameters

At first sight, one might think that the propagation of laser light is well described by the laws of geometrical optics. On closer inspection it turns out, however, that laser beams behave in many respects more like plane waves with their energy is concentrated near an optical axis. The electro-magnetic fields satisfy the *wave equation*,

$$k^2 u + \nabla^2 u = 0 \ . \tag{2.9}$$

For waves propagating in z direction, $u = \psi(x, y, z)e^{-\imath kz}$, one obtains a Schrödinger-like equation [47],

$$2\imath k\frac{\partial \psi}{\partial z} - \frac{\partial^2 \psi}{\partial x^2} - \frac{\partial^2 \psi}{\partial y^2} = 0 \ , \tag{2.10}$$

where $\partial^2\psi/\partial z^2$ has been neglected.

To describe a *Gaussian beam*, we choose an exponential ansatz and introduce two parameters, which can vary along the propagation axis z: $P(z)$ is a complex phase shift and $q(z)$ a complex parameter, whose imaginary part describes the diameter of the beam. The ansatz,

$$\psi = e^{-\imath\left[P(z)+k(x^2+y^2)/2q(z)\right]} \tag{2.11}$$

leads to [1],

$$0 = (q' - 1)\frac{\imath k(x^2 + y^2)}{q^2} - 2\imath P' + \frac{2}{q} \ . \tag{2.12}$$

In order for Eq. (2.12) to hold for all x and y, we need $q' = 1$ and $P' = \frac{-\imath}{q}$. Integrating q', we find

$$q = q_0 + z \ . \tag{2.13}$$

It is useful to introduce real beam parameters,

$$\frac{1}{q} \equiv \frac{1}{R} - \imath\frac{\lambda}{\pi w^2} \ . \tag{2.14}$$

Inserting these into Eq. (2.10),

$$\psi = e^{-\imath P - \imath\frac{k(x^2+y^2)}{2R} - \frac{(x^2+y^2)}{w^2}} \ , \tag{2.15}$$

it becomes clear that $R(z)$ is the radius of curvature and $w(z)$ the beam diameter. Evaluating q_0 at the position of the focus (waist of the beam), where $R = \infty$, we obtain from (2.13) and (2.14)

$$w^2(z) = w_0^2\left[1 + \left(\frac{\lambda z}{\pi w_0^2}\right)^2\right] \quad \text{and} \quad R(z) = z\left[1 + \left(\frac{\pi w_0^2}{\lambda z}\right)^2\right] \ . \tag{2.16}$$

[1] See script on *Electrodynamics* (2023), Sec. 7.4.2..

Normalizing the intensity to the total power, we may write the radial intensity distributions as,

$$I_z(x,y) = \frac{2P}{\pi w(z)^2} e^{-2(x^2+y^2)/w(z)^2} \ . \tag{2.17}$$

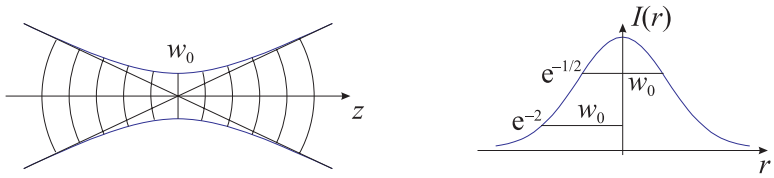

Figure 2.2: (Left) Propagation of the beam along the optical axis. (Right) Cross section of a Gaussian laser beam.

2.2.2 Transfer matrices

For the practical work with Gauss beams it is helpful to introduce transfer matrices, which describe the transformation of a Gauss beam through optical components along the optical axis. The matrix

$$\mathbf{M} = \begin{pmatrix} a & b \\ c & d \end{pmatrix} \tag{2.18}$$

transforms the beam parameter q in the following way:

$$q(z) = \frac{aq(0)+b}{cq(0)+d} \ . \tag{2.19}$$

Transfer matrices allow to calculate, how the parameters R and w transform along the optical axis across the optical elements or in free space. The most common optical elements are lenses, crystals, prisms, mirrors and cavities. For example, the matrix for propagation in free space of a beam over a distance d is,

$$\mathbf{M} = \begin{pmatrix} 1 & d \\ 0 & 1 \end{pmatrix} \tag{2.20}$$

and the matrix for transformation through a thin lens with focal distance f,

$$\mathbf{M} = \begin{pmatrix} 1 & 0 \\ -1/f & 1 \end{pmatrix} \ . \tag{2.21}$$

It is interesting to note that the transfer matrices are the same as those, which in classical beam optics transform the vector, whose components are the distance of the beam from the optical axis y and its divergence $y'(z)$:

$$\begin{pmatrix} y(z) \\ y'(z) \end{pmatrix} = \mathbf{M} \begin{pmatrix} y(0) \\ y'(0) \end{pmatrix} \ . \tag{2.22}$$

Fig. 2.3 shows that coupling a Gaussian beam of light into a cavity requires matching of the phase fronts. Solve the Excs. 2.2.3.1 to 2.2.3.16 [26, 47, 80].

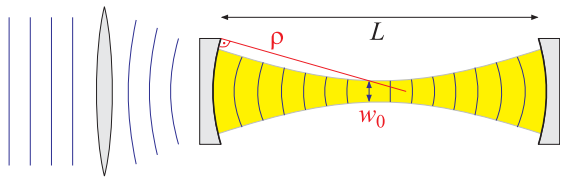

Figure 2.3: Coupling a Gaussian beam of light into cavity requires matching of the phase fronts.

2.2.3 Exercises

2.2.3.1 Ex: Imaging through a thin lens

In classical ray optics the equations describing the focusing of a thin lens are given by,

$$\frac{1}{f} = \frac{1}{g} + \frac{1}{b} \qquad \text{and} \qquad \frac{b}{g} = \frac{B}{G} \ ,$$

where f is the focal distance of the lens, g the distance between the object and the lens, b the distance between the image and the lens, G the size of the object, and B the size of the image.
At what distance from an object of size $G = 1$ mm do you have to place a thin lens with focal distance $f = 100$ mm in order to obtain a ten times larger image? Test your result in practice.

2.2.3.2 Ex: Image of a convex lens

Show that with a convex lens of focal distance f the smallest distance between object and image should be $s = 4f$.

2.2.3.3 Ex: Telescope with ray optics

In classical optics the transfer matrix for the propagation of a beam through free space and through a thin lens are given, respectively, by

$$M_{free} = \begin{pmatrix} 1 & d \\ 0 & 1 \end{pmatrix} \qquad \text{and} \qquad M_{lens} = \begin{pmatrix} 1 & 0 \\ -1/f & 1 \end{pmatrix} \ .$$

The transfer between a point z_0 of the optical axis and a point z_1 is described by

$$\begin{pmatrix} y(z_1) \\ y'(z_1) \end{pmatrix} = M_{free} \begin{pmatrix} y(z_0) \\ y'(z_0) \end{pmatrix} \ .$$

Here, y is the distance of a beam ray from the optical axis and $y' = \frac{dy}{dx}$ its divergence. Use this formalism to design a 3 times magnifying telescope with two lenses have, respectively, the focal lengths $f_1 = 100\,\text{mm}$ and $f_2 = 300\,\text{mm}$.

2.2.3.4 Ex: Ray tracing

Simulate the trajectory of a ray of light traversing under an angle a layer of a material with a refraction index characterized by a Gaussian profile.

2.2.3.5 Ex: The eye

The effective distance between the cornea and the lens of the eye is 2.5 cm, and the lens is in contact with the eye. To resolve two very close points, their images on the retina must be on two non-adjacent cone cells (i.e. there must be at least one non-activated cone cell between the images). The cone cells are about 1 µm apart.
a. What is the smallest angle ϵ under which two points are still separately perceptible? Assume that the direct beams P, P' are not refracted.
b. How close can the two points P_1 and P_2 be, at a distance of 20 m from the eye, so that they are still separately perceptible?

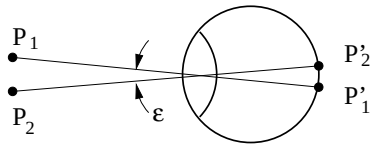

Figure 2.4: The eye.

2.2.3.6 Ex: Microscope

A simple homemade microscope consists of two convex lenses, each one with a diffractive power of 20 dpt, fixed at the extremities of a 30 cm long tube.
a. Wie groß ist die Tubuslänge dieses Mikroskops?
b. Wie groß ist der Abbildungsmaßstab des Mikroskops?
c. Welche Vergrößerung erreicht das Mikroskop? Gehen Sie davon aus, dass die deutliche Sehweite 25 cm beträgt.
d. Wie weit muss sich der Gegenstand vor dem Objektiv befinden, damit er im Auge des Betrachters scharf abgebildet wird?

2.2.3.7 Ex: Classical cloaking with four lenses

Can you design a system of four lenses (focal distances f_1, f_2, $f_3 = f_2$, and $f_4 = f_1$) separated by three distances $t_1 = f_1 + f_2$, t_2, and $t_3 = t_1$, such that the system appears to be invisible for an observer looking through the lenses [19]?

2.2.3.8 Ex: Diameter of a Gaussian beam

You are blocking part of a laser beam with a razor blade mounted on a translation stage allowing you to vary the horizontal position. At the same time, you observe the transmitted power P. You observe that, for varying the power between 16% and 84%, you need to vary the translation by 140 µm. What is the diameter of the Gaussian beam?

2.2.3.9 Ex: Diffraction of a Gaussian beam at a slit

a. Determine the power loss suffered by a Gaussian beam passing through a one-dimensional slit, assuming that the beam hits the slit in its center.

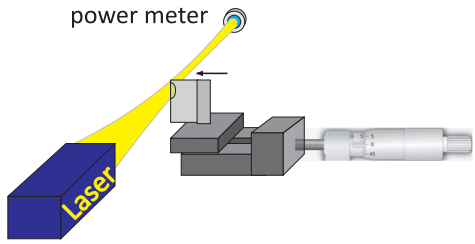

Figure 2.5: Diameter of a Gaussian beam.

b. Calculate the diffraction pattern produced by the slit.
c. A laser beam ($\lambda = 633\,\text{nm}$) looses 50% of its power after being passed through a slit. At a distance of $L = 1\,\text{m}$ behind the slit appear diffraction patterns exhibiting first minima at $\Delta x = 1\,\text{mm}$ to both sides of the central peak. Determine the diameter of the Gaussian beam.

2.2.3.10 Ex: Diffraction of a Gaussian beam at a pinhole

a. Determine the power loss suffered by a Gaussian beam passing through the center of a a pinhole of radius R.
b. A laser beam ($\lambda = 633\,\text{nm}$) looses 50% of its power after being passed through a slit. At a distance of $L = 1\,\text{m}$ behind the slit appear diffraction patterns exhibiting a first minimum at a distance $\Delta b = 1\,\text{mm}$ from the optical axis. Determine the diameter of the Gaussian beam. Help: The first ring of destructive interference occurs under an angle of $\sin\theta = 1.22\frac{\lambda}{2R}$.

2.2.3.11 Ex: Focusing a HeNe laser

The output beam from an HeNe laser with a confocal resonator ($\rho = L = 30\,\text{cm}$) is focused by a lens of $f = 30\,\text{cm}$, 50 cm away from the output mirror. Calculate the location of the focus, the Rayleigh length, and the beam waist in the focal plane.

2.2.3.12 Ex: Spatial filtering

A nearly parallel Gaussian beam with $\lambda = 500\,\text{nm}$ is expanded by a telescope with two lenses of focal lengths $f_1 = 1\,\text{cm}$ and $f_2 = 10\,\text{cm}$, illustrated in the figure. The spot size at the entrance lens is $w = 1\,\text{mm}$.
a. Why does an aperture in the focal plane improve the quality of the wave fronts in the expanded beam by eliminating perturbations due to diffraction effects by dust and other imperfections on the lens surfaces?
b. What is the diameter of this aperture, if 95% of the intensity is transmitted?

2.2.3.13 Ex: Transverse mode selection in an Ar laser

An argon laser oscillating at $\lambda = 488\,\text{nm}$ with resonator length $d = 100\,\text{cm}$ and two mirrors with radius $R_1 = \infty$ and $R_2 = 400\,\text{cm}$ has an intracavity circular aperture close to the spherical mirror to prevent oscillation on transversal modes. Estimate the maximum diameter of the aperture that introduces losses $\gamma_{diffr} < 1\%$ for the

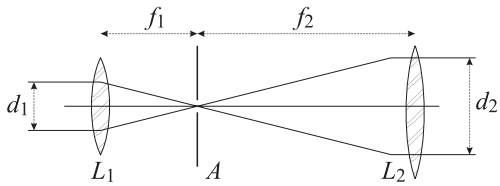

Figure 2.6: Beam-expanding telescope with an aperture in the focal plane.

TEM_{00} mode, but prevents oscillation of higher transverse modes, which without the aperture have a net gain of 10%.

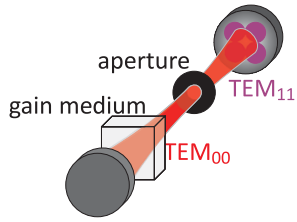

Figure 2.7: Transverse mode selection in an Ar laser.

2.2.3.14 Ex: Anamorphic prism

A prism can be used for expansion of a laser beam if the incident beam is nearly parallel to the prism surface. Calculate the angle of incidence α for which a laser beam transmitted through a rectangular glass prism with an $\varepsilon = 45°$ base angle is expanded tenfold.

2.2.3.15 Ex: Anamorphic prism pair

An *anamorphic prism* pair is a setup consisting of two prisms through which a laser beam is passed under specific angles. The angles can be chosen such as to change the beam diameter only in the p-plane.
a. Calculate, for a single prism with refractive index $n = 1.5$, the beam expansion for an incidence angle of $\theta_1 = 57°$ and an exit angle of 0°. How large must the base angle β of the prism be for this to be possible?
b. How must the second prism be aligned in order for the beam transmitted to this second prism to remain parallel to the incident beam? Note, that an anamorphic prism pair does not allow to correct for astigmatism. This requires cylindrical lenses.

2.2.3.16 Ex: Beam steering with two wedged substrates

The wavevector of a laser beam is generally aligned with one or more adjustable reflective mirrors. Alternatively, one may use a pair of rotatable transmissive wedged substrates. Calculate the wave vector of a laser beam after its transmission through

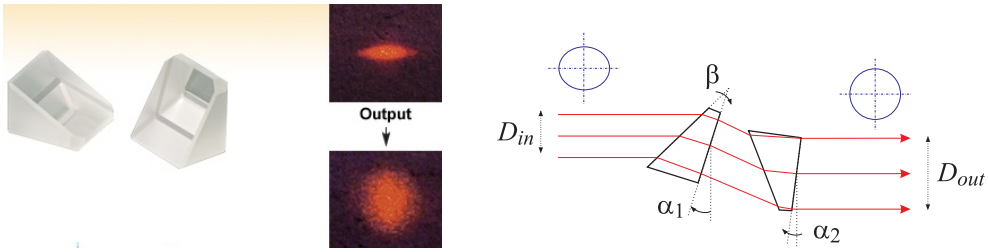

Figure 2.8: (Left) Anamorphic prisms (Thorlabs, PS870). (Right) Geometry of the beam transformation. The entrance side of a prism is often chosen close to the Brewster angle, while the exit side treated carries an anti-reflexion coating.

two $\epsilon = 3°$ wedged, 2 mm thick, AR-coated substrates with the refraction index $n_{rfr} = 1.5134$ at 689 nm, each one rotated by $\theta_{1,2}$ from some normal position.

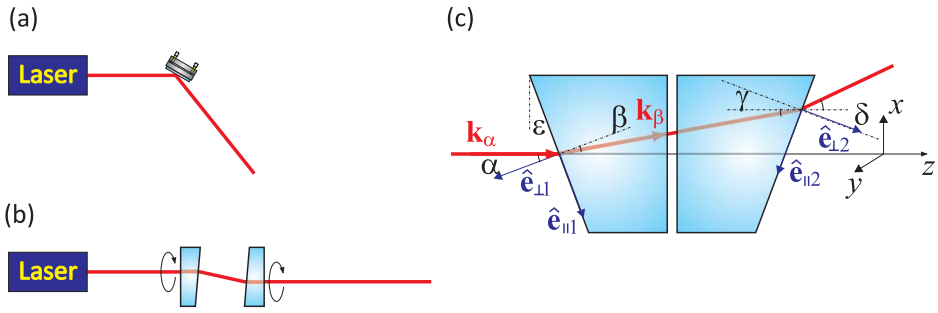

Figure 2.9: Beam steering with two rotatable wedged substrates (see Thorlabs, PS810).

2.2.4 *Experiment: Measuring the diameter of a Gaussian laser beam*

Most laser beams exhibit a Gaussian shape transverse intensity distribution, as we will study in this experiment.

1. Measure the phase profile of a helium-neon laser. To this end fix a razor blade on a translation stage and move it sideways into the beam. From the power of the partially blocked beam $\int_F I(x,y)dxdy$, where F is the cross section of the unblocked part of the beam, $w(z)$ can be determined (see Excs. 2.2.3.8 to 2.2.3.10).

2.2.5 *Experiment: Measuring the parameters of a Gaussian laser beam*

Once a Gaussian beam has been characterized at a given position z, the transfer matrix formalism allows us to calculate its shape at any position along the optical axis. In this experiment, we will study the propagation of a Gaussian beam through

free space [see Eqs. (2.16)] and its transformation through a thin lens with focal distance f. For the latter one, we obtain directly after the lens,

$$\frac{1}{R(z \searrow 0)} = \frac{1}{R(z \nearrow 0)} - \frac{1}{f} \,. \tag{2.23}$$

1. Focus the beam with a lens. Measure the beam diameter at 3 different locations. Compare with the prediction of Gaussian optics.

2. Set up a 1:3 telescope and verify that the outgoing beam is collimated.

2.2.6 *Experiment: Spatial filtering with a pinhole*

Laser light emitted from diode lasers is often astigmatic and has an irregular beam profile. The beam profile can be purified by passing it through an optical fiber or a pinhole, however, at the price of losing power.

1. Focus the beam of a HeNe laser with a lens of $f = 100\,\text{mm}$ focal distance onto a pinhole. Observe the interference fringes and, from their distance from the optical axis, infer the diameter of the pinhole.

2. Remove the higher-order diffraction rings with an iris and compare the beam profile with that of a Gaussian beam. What are the divergence and the waist of the spatially filtered beam (see Exc. 2.2.3.10)?

2.3 Introduction to polarization optics

A laser usually has a well-defined polarization, e.g. , linear or circular. The polarizations can be transformed into one another through a *quarter waveplate* ($\lambda/4$) or a *half waveplate* ($\lambda/2$) by a Fresnel rhomb or other birefringent elements. Superpositions of polarizations can be separated by a *polarizing beam splitter*.

Waveplates consist of thin sheets of *birefringents crystal*s, which are transparent material characterized by anisotropic refraction indices. Cut in a particular way, a birefringent crystal can exhibit a polarization-dependent refraction index, allowing to control the retardation of a light beam as a function of its polarization. The thickness of a waveplate determines the retardation of one polarization axis with respect to the other.

In practice, the degree of freedom of polarization is often used for separating counterpropagating light fields, e.g. in ring lasers, by means of elements called *optical diode* or *optical isolator*, which consist of a Faraday rotator and $\lambda/2$ waveplate. Another practical example is the use of $\lambda/4$ in double passage. An incoming beam can be separated from a returning beam by using a $\lambda/4$ waveplate and a polarizing beam splitter.

2.3.1 Jones matrices

The term *polarization* is defined in relation to a fixed coordinate system, while the term *helicity* denotes the direction of rotation of the polarization vector with respect to

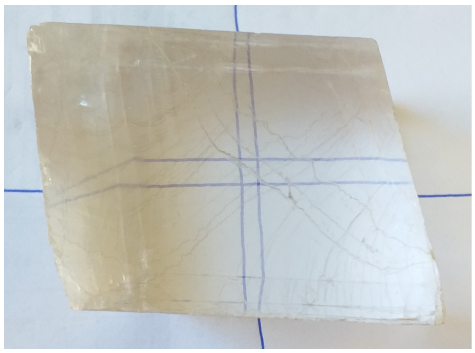

Figure 2.10: (Left) Transmission through a birefringent crystal. (Right) $\lambda/2$-waveplate mounted in a rotation stage.

the direction of propagation of the light beam. The polarization of a beam propagating in z-direction can easily be expressed by a vector of complex amplitude,

$$\vec{\mathcal{E}}(\mathbf{r},t) = \begin{pmatrix} a \\ b \\ 0 \end{pmatrix} e^{\imath kz - \imath\omega t} = \begin{pmatrix} 1 \\ e^{-\imath\phi}|b|/|a| \\ 0 \end{pmatrix} |a| e^{\imath kz - \imath\omega t} \ . \tag{2.24}$$

The angle $\phi = \arctan \frac{\Im\mathfrak{m}\ ab^*}{\Re\mathfrak{e}\ ab^*}$ determines the polarization of the light beam. A polarization is linear when $\phi = 0$ and circular when $\phi = \pi/2$. $|b|/|a|$ is, hence, the degree of ellipticity. A polarization rotator for linearly polarized light (e.g., a sugar solution) is described by the following *Jones matrix* (we will restrict to the x-y-plane)

$$M_{rotator}(\phi) = \begin{pmatrix} \cos\phi & \sin\phi \\ -\sin\phi & \cos\phi \end{pmatrix} \ , \tag{2.25}$$

where ϕ is the rotation angle. For the Faraday rotator the sign of the rotation angle depends on the propagation direction of the laser beam. A *polarizer* projects the polarization onto a specific axis. In the case of the x-axis Jones matrix is,

$$M_{polarizer} = \begin{pmatrix} 1 & 0 \\ 0 & 0 \end{pmatrix} \ . \tag{2.26}$$

If the rotation angle is ϕ,

$$M_{polarizer}(\phi) = \begin{pmatrix} \cos\phi & \sin\phi \\ -\sin\phi & \cos\phi \end{pmatrix} \begin{pmatrix} 1 & 0 \\ 0 & 0 \end{pmatrix} \begin{pmatrix} \cos\phi & \sin\phi \\ -\sin\phi & \cos\phi \end{pmatrix}^{-1} \ . \tag{2.27}$$

Other components, such as electro-optical modulators or phase plates are birefringent crystals, which act only on one of the two optical axes. If only the y axis is optically active, the Jones' matrix is,

$$M_{\theta\text{-waveplate}} = \begin{pmatrix} 1 & 0 \\ 0 & e^{\imath\theta} \end{pmatrix} \ . \tag{2.28}$$

For $\theta = 2\pi/n$ we obtain a λ/n-waveplate. When we rotate the waveplate and therefore the optically inactive axis to an angle ϕ, the Jones matrices are,

$$M_{\theta\text{-waveplate}}(\phi) = \begin{pmatrix} \cos\phi & \sin\phi \\ -\sin\phi & \cos\phi \end{pmatrix} \begin{pmatrix} 1 & 0 \\ 0 & e^{\imath\theta} \end{pmatrix} \begin{pmatrix} \cos\phi & \sin\phi \\ -\sin\phi & \cos\phi \end{pmatrix}^{-1} \tag{2.29}$$
$$= \begin{pmatrix} \cos^2\phi + e^{\imath\theta}\sin^2\phi & -\sin\phi\cos\phi + e^{\imath\theta}\sin\phi\cos\phi \\ -\sin\phi\cos\phi + e^{\imath\theta}\sin\phi\cos\phi & \sin^2\phi + e^{\imath\theta}\cos^2\phi \end{pmatrix} .$$

In most cases, we use quarter waveplates $\lambda/4$,

$$M_{\lambda/4}(\phi) = \begin{pmatrix} \cos^2\phi + \imath\sin^2\phi & (-1+\imath)\sin\phi\cos\phi \\ (-1+\imath)\sin\phi\cos\phi & \sin^2\phi + \imath\cos^2\phi \end{pmatrix} \tag{2.30}$$

and half waveplates $\lambda/2$,

$$M_{\lambda/2}(\phi) = \begin{pmatrix} \cos 2\phi & -\sin 2\phi \\ -\sin 2\phi & -\cos 2\phi \end{pmatrix} . \tag{2.31}$$

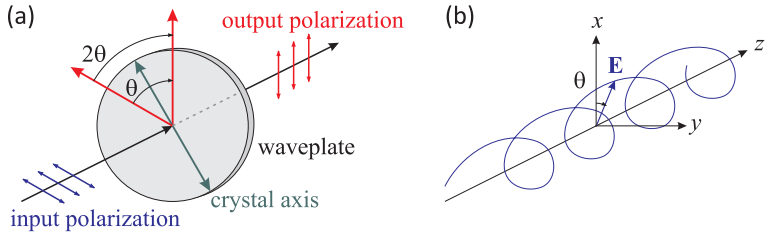

Figure 2.11: (a) Rotation of the polarization by a birefringent waveplate. (b) Illustration of a circularly polarized light wave.

Combinations of $\lambda/2$ waveplates and *Faraday rotator*s are used as *optical isolator*, also called *optical diode*.

2.3.2 Fresnel formulae

Reflection and transmission of a beam of light at a surface depend on the polarization of the light and the angle of incidence. They are described by the *Fresnel formula*:

$$\left(\frac{I_{0t}}{I_{0i}}\right)_s = T_s = \left(\frac{2\sin\theta_t\cos\theta_i}{\sin(\theta_i+\theta_t)}\right)^2 \tag{2.32}$$
$$\left(\frac{I_{0r}}{I_{0i}}\right)_s = R_s = \left(-\frac{\sin(\theta_i-\theta_t)}{\sin(\theta_i+\theta_t)}\right)^2$$
$$\left(\frac{I_{0t}}{I_{0i}}\right)_p = T_p = \left(\frac{2\sin\theta_t\cos\theta_i}{\sin(\theta_i+\theta_t)\cos(\theta_i-\theta_t)}\right)^2$$
$$\left(\frac{I_{0r}}{I_{0i}}\right)_p = R_p = \left(\frac{\tan(\theta_i-\theta_t)}{\tan(\theta_i+\theta_t)}\right)^2 .$$

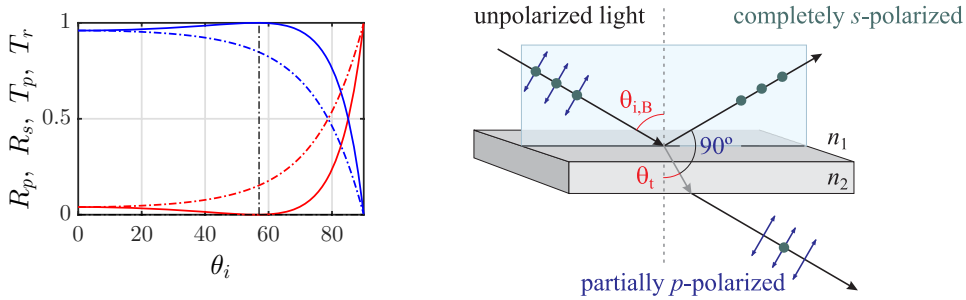

Figure 2.12: (code) (Left) Fresnel formulae showing the angular dependence of t_s (red solid), r_s (green dash-dotted), t_p (blue dashed), and r_p (cyan dotted) for reflection from and transmission through a piece of glass-air interface. (Right) Interfaces between optical media with different reflection indices can act like polarizers: Light reflected from a glas surface under the Brewster angle is completely s-polarized, while the transmitted light is partially p-polarized. The notation s comes from *senkrecht*, i.e. perpendicular to the plane spanned by the incident and reflected light beams, while p means *parallel* to this plane.

The angles of incidence and transmission are related by Snell's law: $n_1 \sin\theta_i = n_2 \sin\theta_t$.

The *Brewster angle* $\theta_{i,B}$ is reached, when $\theta_{i,B} + \theta_t = 90°$, i.e., when following Snell's law,

$$n_1 \sin\theta_{i,B} = n_2 \sin(90° - \theta_{i,B}) = n_2 \cos\theta_{i,B} \ . \tag{2.33}$$

Hence, the Brewster angle is given by,

$$\tan\theta_{i,B} = \frac{n_2}{n_1} \ . \tag{2.34}$$

Resolve the exercises 2.3.4.1 to 2.3.4.5.

2.3.3 Stokes parameters

In quantum mechanics the *Stokes parameters* of a light beam with horizontal and vertical polarizations, $\hat{a}_h$ and $\hat{a}_v$, satisfying,

$$[\hat{a}_k, \hat{a}_m^\dagger] = \delta_{km} \ , \tag{2.35}$$

with $k, m = h, v$ are defined by,

$$\boxed{\begin{aligned} \hat{S}_0 &\equiv \hat{a}_h^\dagger \hat{a}_h + \hat{a}_v^\dagger \hat{a}_v \\ \hat{S}_1 &\equiv \hat{a}_h^\dagger \hat{a}_h - \hat{a}_v^\dagger \hat{a}_v \\ \hat{S}_2 &\equiv \hat{a}_h^\dagger \hat{a}_v e^{\imath\theta} + \hat{a}_v^\dagger \hat{a}_h e^{-\imath\theta} \\ \hat{S}_3 &\equiv -\imath(\hat{a}_h^\dagger \hat{a}_v e^{\imath\theta} - \hat{a}_v^\dagger \hat{a}_h e^{-\imath\theta}) \end{aligned}} \ . \tag{2.36}$$

The Stokes parameters exhaustively describe the polarization state of a light beam. It is interesting, that the vector $\hat{\mathbf{S}}$ with components S_j with $j = 1, 2, 3$ satisfies the SU(2) spin algebra,

$$[\hat{S}_k, \hat{S}_m] = 2\imath\epsilon_{kmn}\hat{S}_n \qquad \text{and} \qquad \hat{\mathbf{S}}^2 = \hat{S}_0^2 + 2\hat{S}_0 \ , \tag{2.37}$$

as will be shown in Exc. 2.3.4.6. It is conveniently pictured on a Poincaré sphere or as a polarization ellipse. In the classical limit we get,

$$\begin{aligned} \hat{S}_0 &= I \\ \hat{S}_1 &= Ip\cos 2\psi \cos 2\chi \\ \hat{S}_2 &= Ip\sin 2\psi \cos 2\chi \\ \hat{S}_3 &= Ip\sin 2\chi \ , \end{aligned} \tag{2.38}$$

with I the light intensity (eventually normalized to the single-photon light intensity), the degree of polarization p. Obviously,

$$\hat{S}_1^2 + \hat{S}_2^2 + \hat{S}_3^2 = p^2\hat{S}_0^2 \ . \tag{2.39}$$

2.3.4 Exercises

2.3.4.1 Ex: Light power control using polarization optics

The power of a laser beam can be regulated by a combination of a half-wave plate and a polarizing beam splitter. By how many degrees do you have to rotate the waveplate in order to reduce the light power by a factor of 2? Use the Jones matrices to justify your response. **Advice:** Look up the Jones matrices (2.31) and (2.26). Test your result in practice.

2.3.4.2 Ex: Jones matrices

Consider a linearly polarized laser beam passing twice through a $\lambda/4$, first in direction of the optical axis, the second time in opposite direction. Calculate the final polarization.

2.3.4.3 Ex: Intensity transmitted through a polarizer

Unpolarized light of intensity I_0 is transmitted through a polarizer with thickness $d = 1\,\text{mm}$. Calculate the transmitted intensity when the absorption coefficients for the two polarizations are $\alpha_\parallel = 100\,\text{cm}^{-1}$ and $\alpha_\perp = 5\,\text{cm}^{-1}$.

2.3.4.4 Ex: Thickness of a half-waveplate

A birefringent quartz crystal is characterized by different refraction indices of the ordinary beam $n_o = 1.544$ and the extraordinary beam $n_e = 1.553$. Calculate the necessary thickness of a quartz waveplate to be used as a $\lambda/2$ retarder at 633 nm. Choose an appropriate waveplate from the Thorlabs catalogue. How thick would a calcite waveplate ($n_o = 1.658$, $n_e = 1.486$)?

2.3.4.5 Ex: Faraday isolator

A Faraday rotator is a device exploiting the Faraday effect to rotate the polarization of a light beam according to the Jones matrix,

$$M_{Faraday}(\phi) = \begin{pmatrix} \cos\phi & -\mathbf{k}\cdot\hat{\mathbf{e}}_z \sin\phi \\ \mathbf{k}\cdot\hat{\mathbf{e}}_z \sin\phi & \cos\phi \end{pmatrix} , \tag{2.40}$$

where $\mathbf{k}$ is the wavevector of the light beam. An optical diode is composed by a $\phi = 45°$ Faraday rotor sandwiched between two polarizers rotated by $\phi = 45°$ with respect to each other.
a. How is the polarization of a light beam changed after a double passage (back and forth) through a Faraday rotator?
b. Calculate what happens to a light beam upon a single passage through a Faraday rotator in either direction $\mathbf{k}$ and $-\mathbf{k}$?

2.3.4.6 Ex: Stokes parameters

For the Stokes parameters defined in (2.42) prove the following relationships,

$$[\hat{S}_k, \hat{S}_m] = 2\imath\epsilon_{kmn}\hat{S}_n \qquad \text{and} \qquad \hat{\mathbf{S}}^2 = \hat{S}_0^2 \ .$$

2.3.5 *Experiment: Polarization of a helium-neon laser*

We will now analyze and manipulate the polarization of a laser beam in practice.

1. Pass the beam of a helium-neon laser through a polarizer and a quarter- resp. half-waveplate. Analyze the polarization using a rotatable second polarizer for various rotation angles of the waveplate. Sketch the transmitted intensity as a function of the rotation angle of the beamsplitter in a polar diagram. How good can you achieve linear and circular polarization?

2. Characterize the polarization of a helium-neon laser by sketching the transmitted intensity through a polarizing beamsplitter as a function of the rotation angle of the beamsplitter in a polar diagram. Now couple the laser beam to a Fabry-Pérot interferometer. What do you observe? Place a quarter-waveplate at the output of the helium-neon laser and characterize again the polarization. What do you observe at the Fabry-Pérot interferometer?

3. Use a quarter-waveplate to separate a beam of light from a counterpropagating beam according to Fig. 2.13.

4. Characterize an optical insulator. Optimize its extinction.

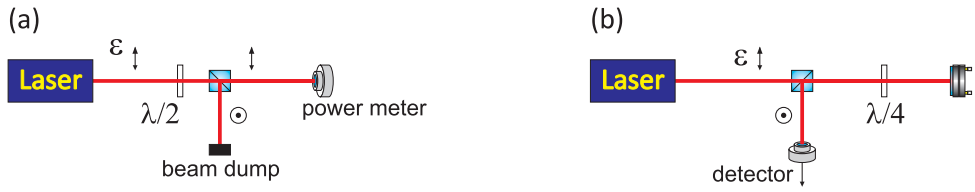

Figure 2.13: (a) Power control of a light beam and (b) separation of counterpropagating beams through polarization optics.

2.3.6 *Experiment: Measuring the Brewster angle*

Any interface between two transparent materials with different refraction indices reflects a part of incident light depending on the polarization and the angle of incidence, as predicted by Fresnels formulae (2.32).

1. Measure the transmission by a glass plate as a function of the angle of incidence for two orthogonal polarizations and determine the Brewster angle.

2. Mirrors can change the polarization of a light beam and, for example, transform a linear polarization into elliptical. Determine the degree of ellipticity for a given mirror.

3. How does a mirror transform the polarization and the helicity of a reflected laser beam?

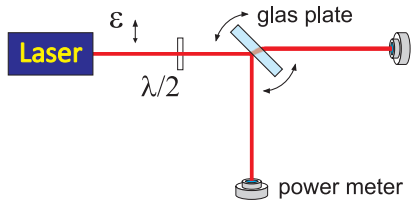

Figure 2.14: Measuring the Brewster angle by varying the tilt of a glas plate.

2.3.7 *Experiment: Pockels cell*

Pockels cells are birefringent crystals allowing to manipulate the polarization of a laser beam by application of a voltage.

1. Prepare a laser beam by passing it through a polarizer followed by a half-waveplate and a second polarizer. Observe the intensity transmitted and reflected through the last polarizer as a function of the rotation angle of the half-waveplate.

2. Use the EOM as a Pockels cell by placing it between the half-waveplate and the second polarizer. Supply a voltage between 0 V and 350 V to the EOM. Measures the intensity of reflected and transmitted light as a function of the

supplied voltage and prepare a diagram. What do you observe when you rotate either the half-waveplate or the EOM?

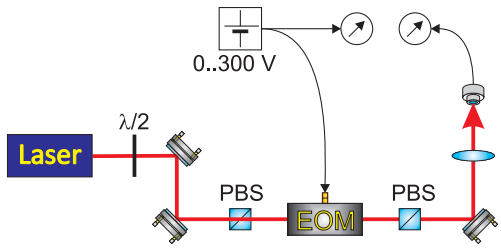

Figure 2.15: Scheme for using an EOM as a Pockels cell.

2.4 Laguerre-Gaussian light modes

Light beams not only possess polarization, but can also have orbital angular momentum. This property of light can impressively demonstrated at the so-called *Laguerre-Gaussian mode*s.

These modes can be produced by means of masks resembling *Fresnel zone plate*. Fresnel zone plates are masks consisting of concentric sequences of bright (transmitting) and dark (absorbing) rings. The diameters of the rings are selected in such a way that the diameters of the rings defined by the bright rings interfere constructively at a certain distance f_1 on the optical axis and form a 'focus' there. For this purpose, the distance d_n of the n^{th} ring must satisfy the condition,

$$d_n = \sqrt{(f_1 + n\lambda)^2 - f_1^2} \simeq \sqrt{2f_1 n\lambda}\ . \tag{2.41}$$

For a given zone plate there are other focuses at smaller distances,

$$f_k = \frac{d_n^2 - k^2 n^2 \lambda^2}{2kn\lambda} \simeq \frac{d_n^2}{2kn\lambda} = \frac{f_1}{k}\ . \tag{2.42}$$

In order to separate the beams diffracted by the zone plate into a given focus from those diffracted into other focuses or not being diffracted at all, we pass the beam through an iris diaphragm localized at the desired focus and recollimate the beam by means of a lens, as shown in Fig. 2.16.

The phase profile of the beam can be viewed interferometrically (see Fig. 2.16) by overlapping a plane wave laser beam. With a *neutral density filter* the intensities of the overlapping beams can be adjusted to maximize the contrast.

Now, for realizing Laguerre-Gaussian light modes, we use Fresnel zone plates with spiral patterns, instead of concentric rings. In contrast to the Gaussian mode, the Laguerre-Gauß modes exhibit an intensity minimum on the optical axis (doonat mode). Their phase profiles can be viewed by interferometry [4].

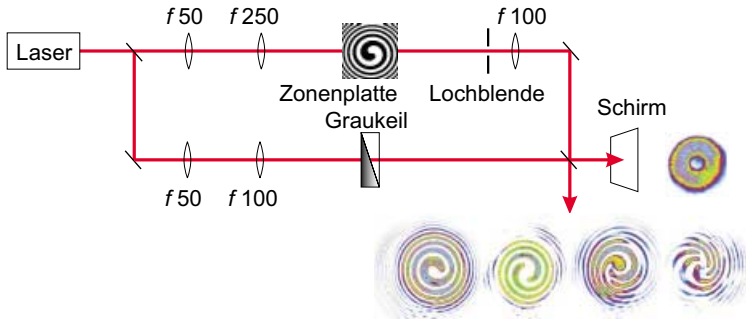

Figure 2.16: Creation of Laguerre-Gaussian modes.

2.4.1 *Experiment: Generating a Laguerre-Gaussian mode*

In this experiment, we will...

1. Construct the interferometer sketched in Fig. 2.16 using adequate Fresnel zone plates. What do you observe in the diffracted beam and in the interferogram, when instead of filtering the principal focus f_1 you filter a higher order focus?

2. Pass a Laguerre-Gauß laser beam through a $\lambda/2$ waveplate. How does the angular orbital momentum change when you change the rotation? What happens upon reflection from a mirror?

3. Slightly misalign the mode-matching between the Laguerre-Gauß beam and the Gaussian reference beam until you observe multiple fringes. What do you observe?

2.5 Further reading

M. Born, *Principles of Optics* [ISBN]

H. Kogelnik et al., *Laser Beams and Resonators* [DOI]

W. Demtröder, *Atoms, Molecules and Photons: An Introduction to Atomic, Molecular, and Quantum Physics* [ISBN]

J. Weiner et al., *Light-matter interaction, Fundamentals and applications* [DOI]

G.A. Fowles, *Introduction to Modern Optics* [ISBN]

J.S. Choi et al., *Paraxial ray optics cloaking* [DOI]

2.5.1 on Stokes parameters

W.P. Bowen et al., *Polarization Squeezing of Continuous Variable Stokes Parameters* [DOI]

2.5.2 on Laguerre-Gauss modes

L. Allen et al., *Orbital Angular Momentum of Light and the Transformation of Laguerre-Gaussian Laser Modes* [DOI]

Chapter 3

Electronics and radiofrequency

For the control and regulation of important quantum optical devices, such as EOMs, AOMs, laser diodes, photodiodes, piezos etc., *electronic circuit*s are necessary. The aim of this chapter is to provide practical know-how in the basics of electronics.

3.1 Introduction to electronic circuits

3.1.1 Passive electronic components

Electronic components which are characterized by a fixed impedance are called *passive*. The most common devices are resistors, capacitors, and inductances. For their handling, it is useful to be able to identify their impedance from their labeling.

The values of the resistances of resistors are generally codified by colored rings. The first ring to be considered is the one closest to a terminal. In case of 4 rings, the first two rings are to be considered as digits, the third ring gives the exponent 10. With five rings, the first three are digits and the forth gives the exponent of 10. The last ring, in both cases specifies the tolerance of the value of the resistance.

There are various types of capacitors depending on the employed materials for the dielectric medium (paper, ceramics, polyester, electrolyte made of aluminum and electrolyte made of tantalum). Electrolyte capacitors have a defined polarity, and an reversion of their voltage supply can result in their explosion. The value of the capacitance is generally written on their body, as well as their maximum allowed operating voltage. Also the polarity of electrolyte capacitors is always indicated (although there can be some confusion with regard to the physical and technical direction of the current flow). Ceramic and polyester capacitors can have their values either written in letters or color coded. The color code sequence is similar to that of resistors, with the first two digits devoted to the digits, the third to the multiplier exponent, the forth to the tolerance, and the fifth for the maximum voltage. In case of printed numbers, the first two numbers represent the first two digits, and the third one represents the numbers of 0 before the decimal point. In all cases (colors or digits), the value is given in picoFarads. With more modern serigraphic techniques, some capacitors have their values printed directly in Farads (micro, nano and pico). In these cases, the letter denoting the unit also serves to mark the decimal point. For example, 2n2 means 2.2 nF.

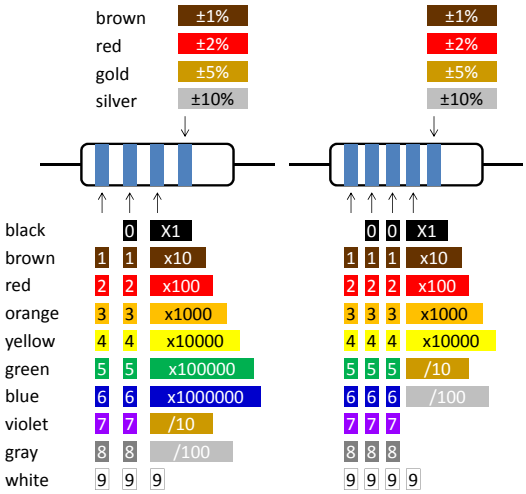

Figure 3.1: Color code for resistors with 4 and 5 rings.

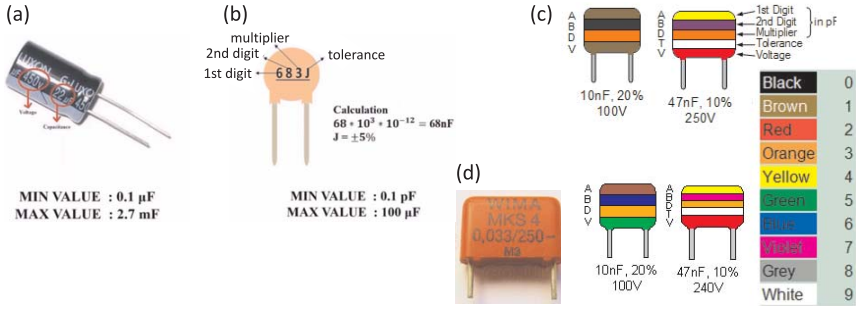

Figure 3.2: (Left) Electrolyte aluminum capacitors. (Center) Polyester capacitor and color code. (Right) Ceramic capacitor.

3.1.2 Active electronic components and the *pn*-junction

Diodes, transistors, photodiodes, operational amplifiers are called *active components*, because their current-to-voltage curve is non-linear, their response $I = I(U)$ cannot be described by a single constant value, but depends on the applied voltage.

During this course we will work a lot with *operational amplifiers* (OpAmp), which are integrated circuits designed to amplify input signals with characteristics that are entirely determined by external components. This feature makes them easy to use and extremely versatile.

OpAmps are generally found encapsulated in DIL type housings (dual in line), which means that they have two lines of 4 pins. The sequence of pins is numerated in counter-clockwise orientation, and they have a mark on the side of pin 1. It is always recommend to obtain the datasheet of the OpAmp since, despite a usual pin compatibility ensured by the various OpAmp manufacturers, deviations are frequent.

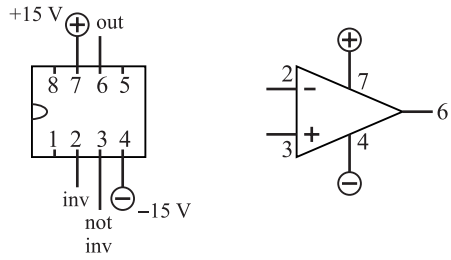

Figure 3.3: (Left) Schematic symbol of an OpAmp; (Right) Pin layout of a standard OpAmp.

3.1.3 Electronic circuits

Amplification or control circuits are nowadays mostly realized with *operational amplifiers* (*OpAmp*). The advantage of an OpAmp compared to circuits based on transistors is, that their properties are almost independent of their internal structure. Hence, their properties can be personalized via an external feedback realized with external components. The input of an OpAmp does not require current. OpAmps amplify the voltage difference between the non-inverting input (+) and the inverting (-). For most practical matters we can assume, that the OpAmp has infinite amplification and negligible input impedance.

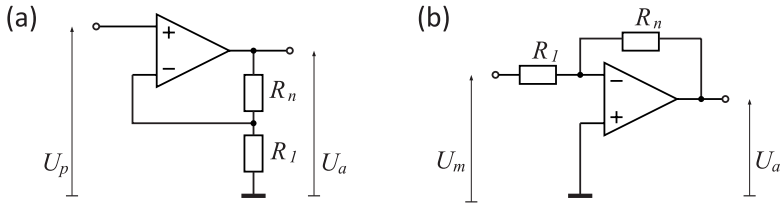

Figure 3.4: (Left) Principle scheme of a standard OpAmp. (Center) Non-inverting amplifier. (Right) Inverting amplifier.

OpAmps can be used as *inverting amplifiers* or *non-inverting amplifiers*. Using *Kirchhoff's rules* for the *loops* and *nodes* of the circuit, we find for a non-inverting amplifier,

$$\frac{U_e}{R_1} = -\frac{U_a}{R_1 + R_n} \quad , \quad G = 1 + \frac{R_n}{R_1} \; . \tag{3.1}$$

This becomes clear noting that, since no voltage is dropped between the inputs (+) and (-), the input voltage must be equal to the voltage drop at R_1. And since the non-inverting input does not deliver current, the currents traversing the resistances R_n and R_1 must be equal. For the inverting amplifier, we find,

$$\frac{U_a}{R_n} = -\frac{U_e}{R_1} \quad , \quad G = -\frac{R_n}{R_1} \; . \tag{3.2}$$

This becomes clear noting that, since the input (-) does not drag current, the currents traversing the resistances R_n and R_1 must cancel each other.

Changing the resistances R to inductances L or capacitances C, it becomes possible to influence the frequency response of the amplifying circuit. The impedance are,

$$Z_L = \imath L\omega \quad , \quad Z_C = \frac{1}{\imath C\omega} \ . \tag{3.3}$$

For the calculation of the amplification wit complex impedances, we just take the absolute value of the gain G.

3.1.4 The thermoelectric effect

3.1.4.1 Seebeck effect

The Seebeck effect is a classic example of an electromotive force (EMF) and leads to measurable currents or voltages in the same way as any other EMF. The local current density is given by,

$$\mathbf{J} = \sigma(-\nabla V + \mathbf{E}_{emf}) \ , \tag{3.4}$$

where V is the local voltage, and σ is the local conductivity. In general, the Seebeck effect is described locally by the creation of an electromotive field,

$$\mathbf{E}_{emf} = -S\nabla T \ , \tag{3.5}$$

where S is the Seebeck coefficient (also known as thermopower), a property of the local material, and ∇T is the temperature gradient.

The Seebeck coefficients generally vary as function of temperature and depend strongly on the composition of the conductor. For ordinary materials at room temperature, the Seebeck coefficient may range in value from $-100\,\mu\text{V/K}$ to $+1000\,\mu\text{V/K}$.

If the system reaches a steady state, where $\mathbf{J} = 0$, then the voltage gradient is given simply by the emf:

$$-V = S\Delta T \ . \tag{3.6}$$

This simple relationship, which does not depend on conductivity, is used in the thermocouple to measure a temperature difference; an absolute temperature may be found by performing the voltage measurement at a known reference temperature. A metal of unknown composition can be classified by its thermoelectric effect if a metallic probe of known composition is kept at a constant temperature and held in contact with the unknown sample that is locally heated to the probe temperature. It is used commercially to identify metal alloys. Thermocouples in series form a *thermopile*. Thermoelectric generators are used for creating power from heat differentials.

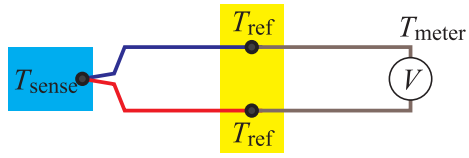

Figure 3.5:

3.1.4.2 Peltier effect

When an electric current is passed through a circuit of a thermocouple, heat is evolved at one junction and absorbed at the other junction. This is known as Peltier Effect and is named after a physicist. The Peltier effect is the presence of heating or cooling at an electrified junction of two different conductors. When a current is made to flow through a junction between two conductors, A and B, heat may be generated or removed at the junction. The Peltier heat generated at the junction per unit time is,

$$\dot{Q} = (\Pi_A - \Pi_B)I \ , \tag{3.7}$$

where Π_A and Π_B are the Peltier coefficients of conductors A and B, and I is the electric current (from A to B). The total heat generated is not determined by the Peltier effect alone, as it may also be influenced by Joule heating and thermal-gradient effects (see below).

The Peltier coefficients represent how much heat is carried per unit charge. Since charge current must be continuous across a junction, the associated heat flow will develop a discontinuity if Π_A and Π_B are different. The Peltier effect can be considered as the back-action counterpart to the Seebeck effect (analogous to the back-EMF in magnetic induction): if a simple thermoelectric circuit is closed, then the Seebeck effect will drive a current, which in turn (by the Peltier effect) will always transfer heat from the hot to the cold junction. The close relationship between Peltier and Seebeck effects can be seen in the direct connection between their coefficients [43, 77]:

$$\Pi = TS \ . \tag{3.8}$$

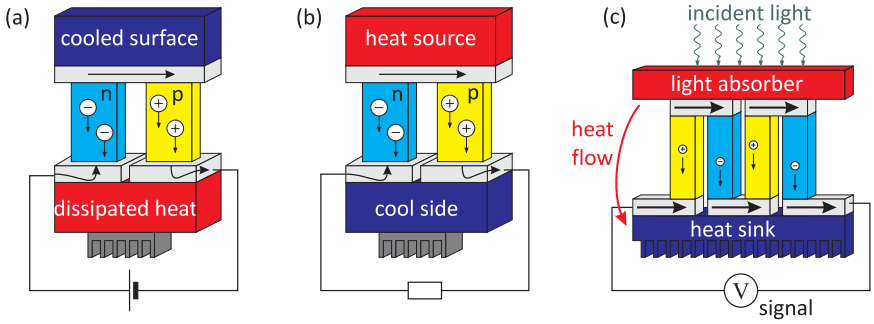

Figure 3.6: (a) Peltier cooler, (b) voltage generator or heat sensor, and (c) heat or radiation sensor with thermocouples connected in parallel.

3.1.5 Exercises

3.1.5.1 Ex: Integrator with operational amplifier

Based on the two golden rules for operational amplifiers, (1) $I_+ = I_- = 0$ A and (2) $U_+ = U_-$, show that the output voltage U_a at the integrated circuit shown in the figure is: $U_a = \frac{1}{RC} \int U_e dt$.

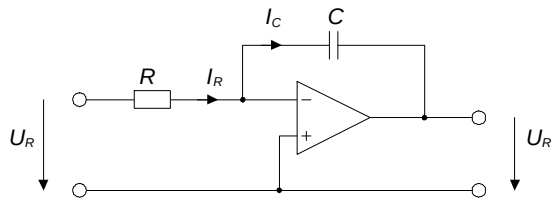

Figure 3.7: Integrator with operational amplifier.

3.1.5.2 Ex: Low-pass filter using an OpAmp

Using an inverting operational amplifier design a simple low-pass filter with a constant amplification of 10 at low frequencies and diminishing gain above 10 kHz. Calculate the Bode diagram (i.e. the frequency-dependent gain and phase-shift of your circuit. What is the gain reduction per octave?

3.1.6 *Experiment: Amplifiers and active filters*

Here, we will learn how to use OpAmps: We will start mounting a 10-fold inverting amplifier on a breadboard and then modify the external passive components, such as to build a low-pass filter.

1. Assemble on a breadboard a simple inverting amplifier using an OpAmp. Use 10 kΩ resistors at the input aim for an amplification factor of 10.

2. Test the circuit with a frequency generator and an oscilloscope.

3. Modify the circuit such as to obtain a low-pass filter with $f_g = 50$ kHz bandwidth and test the circuit again.

3.1.7 *Experiment: Peltier element and thermistor*

Here, we will learn how to use a Peltier element and a thermistor. A *thermistor* is nothing else than a well-calibrated resistor with temperature-dependent resistance (see Fig. 3.9).

1. Connect a Peltier element to a 1 A current source and bring one of the two surfaces of the Peltier element into thermal contact with a heat sink. What do you observe?

2. Bring a 10 kΩ thermistor in thermal contact with either of the two surfaces of the Peltier element and measure its resistance. What do you observe?

3. Can you imagine a feedback logic evaluating the measured resistance in order to control the current applied to the Peltier element such as to maintain constant the temperature of the surface not connected to the heat sink.

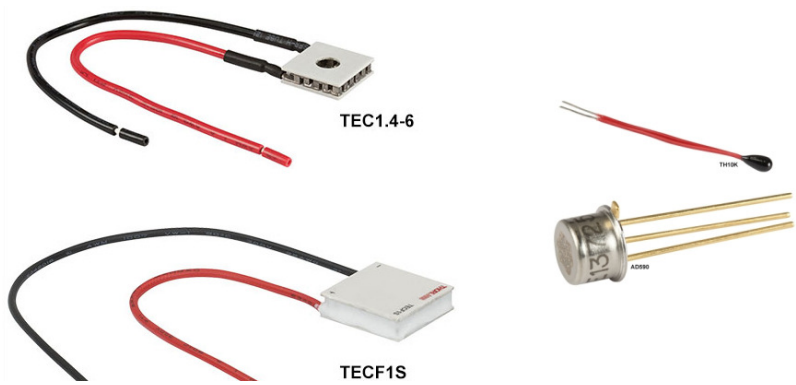

Figure 3.8: Pictures of Peltier elements, a thermistor, and an AD590 temperature transducer.

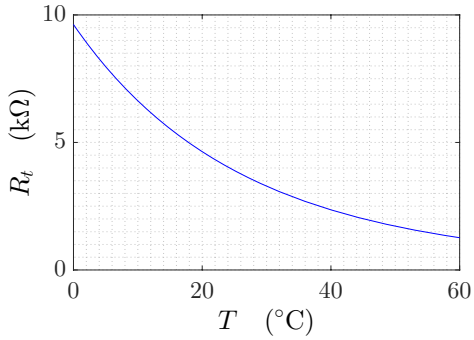

Figure 3.9: Calibration curve for a 10 kΩ thermistor from Thorlabs.

3.2 Detectors

3.2.1 Photodiodes

Most active components are many of *semiconductor* characterized by a relatively large band gap between the valence band and the conduction band. By appropriate doping of the material with donors (p-type) or acceptors (n-type) a semiconductor can be made conductive. The most basic semiconductor element, which is the *diode* consists of a junction of two types of semiconductors, as shown in Fig. 3.10.

Our first task will be to construct a *photo detector*. The central part of a photodetector is the photodiode. We have at our disposal silicium *pin*-photodiodes of the type C30822E of the company Perkin Elmer and of the type FFD100.

Photodiodes exploit an intrinsic photoeffect of semiconductor pn-junctions. In the transition region, free electrons of the n-type semiconductor and excess holes of the p-type semiconductor are drifting into the respective opposite semiconductor, where they recombine. The consequence is a transition zone with a charge carrier depletion, which acts as a barrier and has an intrinsic capacitance. The charge carrier imbalance gives rise to an electric field across the junction. The energy liberated during the

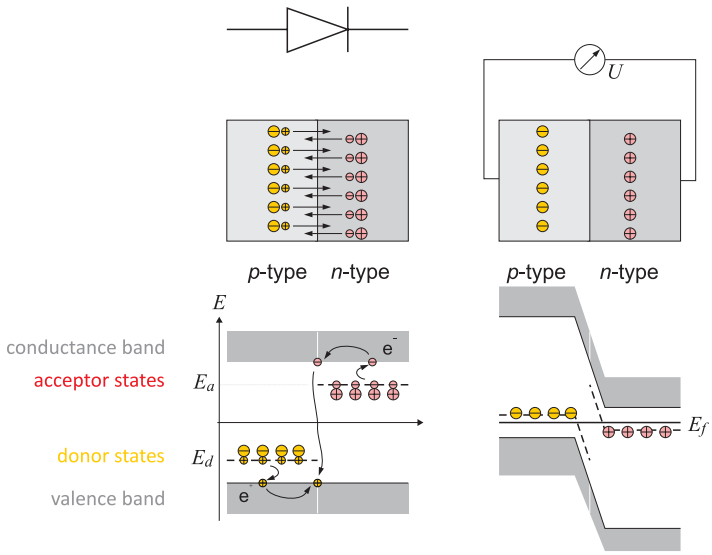

Figure 3.10: Joining a p-type and a n-type doped semiconductor (left) one observes a charge carrier redistribution across the pn transition (right).

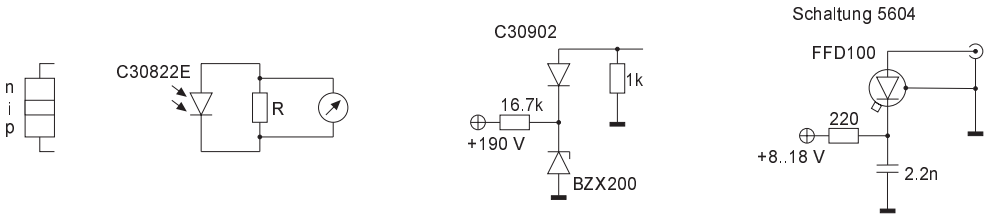

Figure 3.11: Circuit with photodiode.

recombination process can be dissipated via emission of light.

The reverse process is also possible: Via the intrinsic photoeffect, light irradiated into the pn-junction can lift electrons from the valence into the conduction band, thus generating pairs of charge carriers. Under the influence of the electric field across the junction, the holes flow to the edge of the p domain and the electrons flow to the n domain. This part of the current is called *drift current*. A smaller part, called the *diffusion current*, has its origin in the diffusion of the electron-hole pairs formed in the edge regions. Since these minority charge carriers have only a limited lifetime before they recombine, only the part of the current generated within a few units of the diffusion lengths near the charge carrier zone contributes. This results in an external photovoltaic voltage at the electrodes of the photodiode. If the photodiode is connected to a load, a photocurrent will flow, which is composed, as mentioned above, by the drift current of the charge carrier zone and the diffusion current from its edges.

The principal scheme of a pin diode is illustrated in Fig. 3.12(left): A weakly doped intrinsic layer separates the p and the n conductor. This reduces the capacity of the

barrier. The current at short circuit is proportional to the light power. A photodiode is always operated in blocking direction. A negative offset voltage reduces the capacity of the *pn*-junction.

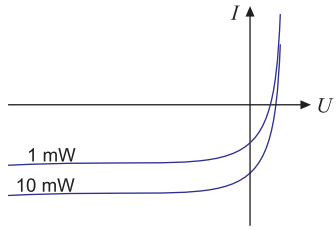

Figure 3.12: (code) U-I dependence of a photodiode.

Despite all measures the *pn*-junction capacity remains finite. One can model the impact of the *pn*-junction capacity via a replacement diagram. The voltage drop is

$$\frac{U(\omega)}{U_0} = \frac{R_L||\frac{1}{\imath\omega C}}{R_i + \left(R_L||\frac{1}{\imath\omega C}\right)} = \frac{\frac{R_i||R_L}{R_i}}{1+\imath\omega C(R_i||R_L)} \,. \tag{3.9}$$

For high load resistances the frequency response obviously becomes load-independent. For small loads, $R_L < R_i$, the band width of the photodiode is dramatically increased to $\omega_g = 1/R_L C$. In the same time, however, the amplification drops to $V = R_L/R_i$.

3.2.2 Exercises

3.2.2.1 Ex: Photomultiplier

The anode of a photomultiplier tube is connected by a resistor of $R = 1\,\mathrm{k\Omega}$ to ground. The stray capacitance is 10 pF, the current amplification 10^6, and the anode rise time 1.5 ns. What is the peak amplitude and the halfwidth of the anode output pulse produced by a single photoelectron? What is the dc output current produced by 10^{-12} W cw radiation at $\lambda = 500\,\mathrm{nm}$, if the quantum efficiency of the cathode is $\eta = 0.2$ and the anode resistor $R = 10^6\,\Omega$? Estimate the necessary voltage amplification of a preamplifier (a) to produce 1 V pulses for single-photon counting; and (b) to read 1 V on a dc meter of the cw radiation?

3.2.2.2 Ex: Optical image intensifier

A manufacturer of a two-stage optical image intensifier states that incident intensities of 10^{-17} W at $\lambda = 500\,\mathrm{nm}$ can still be 'seen' on the phosphor screen of the output state. Estimate the minimum intensity amplification, if the quantum efficiency of the cathodes and the conversion efficiency of the phosphor screens are both 0.2 and the collection efficiency of light emitted by the phosphor screens is 0.1. The human eye needs at least 20 photons/s to observe a signal.

3.2.2.3 Ex: Photovoltaic detector

Estimate the maximum output voltage of an open photovoltaic detector at room temperature under 10 µW irradiation when the photocurrent of the shortened output is 50 µA and the dark current is 50 nA.

3.2.3 *Experiment: Taking the response function of a photodiode*

In this part of the lab course, we will learn to solder and set up simple electronic circuits. We will also learn how to identify the connections of a photodiode and mount into a case with BNC connectors. Finally, we will characterize the photodiode for use in future applications. Initially, we will work without offset voltage, later we will apply a voltage and identify its impact [1].

1. Connect an LED to a function generator and make it blink at low frequencies adjusting the offset and the amplitude of the output voltage. Shine the light onto your photodiode and monitor the signal on an oscilloscope. Explain your observations.

2. Reduce the amplitude and adjust the offset until you observe a sinusoidal signal. Increase the frequency and explain your observations. (Note that the response of LEDs is extremely fast (MHz).) Determine the bandwidth of your detector.

3. Measure the current at short circuit. Connect a $R = 10\,\mathrm{k\Omega}$ resistive load in parallel to the photodiode output and measure the voltage drop into this load.

4. Characterize the photodetector with respect to its sensitivity (in A/W) by varying the load.

5. How is the frequency response of the photodiode modified by the load? Measure bandwidth as a function of the load. Adjust the load until the detector (circuit including photodiode and resistor) has a bandwidth of 10 kHz (which is sufficient for many applications).

6. Apply a 10 V voltage in reverse direction and analyze again the sensitivity and the bandwidth of your photodetector. Note that the blinking LED can be replaced by a rotating chopper wheel.

Example of a measured characterization of a photodiode.

3.3 Introduction to radiofrequency components

3.3.1 VCOs and the generation of rf-sidebands

Voltage-controlled oscillators (*VCO*) serve to generate variable radiofrequencies. They are the basis for most function generators. A useful particularity of VCOs is the

[1] Datasheet for the Photodiode FFD100 see appendix Fig. 7.21,
data sheet for the Photodiode C30822E see appendix Fig. 7.22.

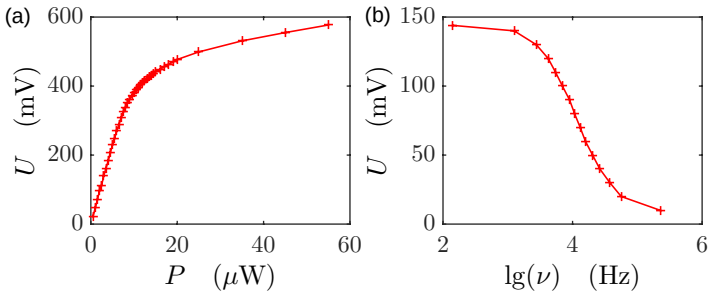

Figure 3.13: (a) Calibration of a photodiode, measured voltage as a function of the incident light power. (b) Low-pass behavior of a resistive charge of 90 kΩ.

possibility modulate the frequency and phase of an optical carrier wave by modulating the control voltage of a VCO at low frequency.

The modulation of the carrier wave generates sidebands. This can be seen by expanding the signal which carries the phase modulation into a Fourier series,

$$Ae^{\imath\omega t+\imath\beta\sin\Omega t} = Ae^{\imath\omega t}\sum_{k=-\infty}^{\infty} J_k(\beta)e^{\imath k\Omega t} \simeq Ae^{\imath\omega t} + J_1(\beta)Ae^{\imath\omega t+\imath\Omega t} + J_{-1}(\beta)Ae^{\imath\omega t-\imath\Omega t} \tag{3.10}$$

when the *modulation index* β is small. Here, $J_{-k}(\beta) = (-1)^k J_k(\beta)$ are the Bessel functions. This is in contrast to amplitude modulation, which is described by only two symmetric sidebands,

$$A(1+\beta\sin\Omega t)e^{\imath\omega t} = Ae^{\imath\omega t}\left(1+\frac{\beta}{2\imath}(e^{\imath\Omega t}-e^{-\imath\Omega t})\right) . \tag{3.11}$$

For *amplitude modulation* (*AM*) the beat signals between the carrier frequency and the two sidebands are in phase, i.e.,

$$\left|e^{\imath\omega t}+e^{\imath(\omega\pm\Omega)t}\right|^2 = 2+e^{\imath\Omega t}+e^{-\imath\Omega t} . \tag{3.12}$$

For *phase modulation* (*PM*) the beat signal are in counter-phase, i.e.,

$$\left|e^{\imath\omega t}+e^{\imath(\omega\pm\Omega)t+\imath\pi/2}\right|^2 = 2+\imath e^{\pm\imath\Omega t}-\imath e^{\mp\imath\Omega t} . \tag{3.13}$$

In the case of AM, the amplitude is blurred, but the phase at zero-crossing is well defined. In the case of PM, the amplitude in the antinode is sharp, but the phase of the zero-crossing is blurred.

It is not easy to transform AM into PM, and vice versa. In fact, the phase between carrier and sidebands can be varied, for example by adding an AC voltage, $\sqrt{2}e^{\imath\omega t+3\imath\pi/4}$ to the signal; however, it is not easy to transform synchronized phases into opposite phases.

As shown in Eq. (3.10), the spectrum of a signal with phase modulation (PM) consists of discrete lines, called sidebands, whose amplitudes are given by Bessel

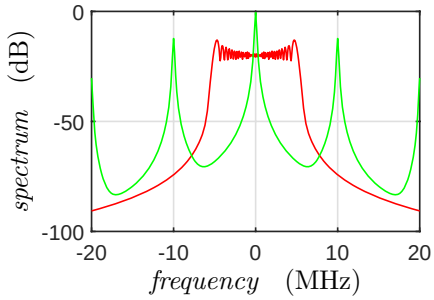

Figure 3.14: (code) Frequency spectra of a phase-modulated carrier frequency for $\Delta\omega = 5\,\mathrm{MHz}$ modulation excursion and (red) $\omega = 100$ kHz modulation frequency ($\beta = \frac{\Delta\omega}{\Omega} = 50$) and (green) $\omega = 10\,\mathrm{MHz}$ modulation frequency ($\beta = 0.5$). Furthermore, a $\gamma = 100\,\mathrm{kHz}$ resolution linewidth is assumed.

functions,

$$S(\omega) = \sum_{k=-\infty}^{\infty} |A\mathcal{J}_k(\beta)|^2 \delta(\omega + k\Omega) \ . \tag{3.14}$$

In real systems, the sidebands have finite widths γ due to frequency noise or the finite resolution of the detectors. In the case of Lorentzian line profiles, we have,

$$S(\omega) = \sum_{k=-\infty}^{\infty} |A\mathcal{J}_k(\beta)|^2 \frac{\beta^2}{(\omega - k\Omega)^2 + \beta^2} \ . \tag{3.15}$$

3.3.2 Mixers

A *frequency mixer* is a nonlinear electrical circuit that creates new frequencies from two input signals, e.g. the sum and difference of the input frequencies. A device that has a non-linear (e.g. exponential) characteristic can act as a mixer. Passive mixers use one or more diodes and rely on their non-linear relation between voltage and current. Active mixers use an amplifying device (such as a transistor) to increase the strength of the product signal.

Mixers may be classified by their topology: An unbalanced mixer, in addition to producing a product signal, allows both input signals to pass through and appear as components in the output. A single-balanced mixer is arranged with one of its inputs applied to a balanced (differential) circuit so that either the local oscillator (LO) or signal input (RF) is suppressed at the output, but not both. A double-balanced mixer has both its inputs applied to differential circuits, so that neither of the input signals and only the product signal appears at the output. Double balanced mixers are more complex and require higher drive levels than unbalanced and single-balanced designs.

In practice, mixers are widely used to shift signals from one frequency range to another, a process known as *heterodyning*, in order to facilitate signal transmission or further signal processing. Frequency mixers are also used to modulate a carrier signal in radio transmitters, as product detectors, phase detectors, or frequency multipliers.

3.3.2.1 Diode

The non-linearity (or non-Ohmic behavior) of a diode can be used to create a simple unbalanced mixer producing the original frequencies as well as their sum and their difference. The current I through an ideal diode as a function of the voltage U across it is given by an exponential function,

$$I = I_0(e^{qU/k_BT} - 1) \ . \tag{3.16}$$

The exponential can be expanded as $e^x - 1 \simeq x + \frac{x^2}{2}$. Suppose that the sum of the two input signals $U_1 + U_2$ is applied to a diode, and that an output voltage is generated that is proportional to the current through the diode [e.g. by providing the voltage that is present across a resistor in series with the diode, as shown in Fig. 3.15(a)]. Then, disregarding the constants in the diode equation, the output voltage will have the form,

$$\begin{aligned} U_0 &= (U_1 + U_2) + \tfrac{1}{2}(U_1 + U_2)^2 + ... \\ &= (U_1 + U_2) + \tfrac{1}{2}(U_1^2 + 2U_1U_2 + U_2^2) + ... \ . \end{aligned} \tag{3.17}$$

The ellipsis represents all the higher powers of the sum which we assume to be negligible for small signals.

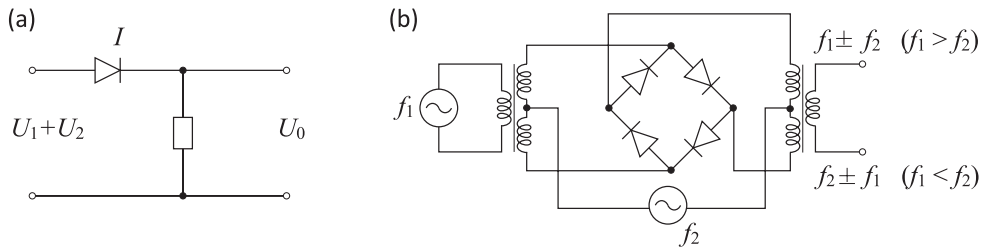

Figure 3.15: (a) Mixing two signal at a diode. (b) Schematic diagram of a double-balanced passive diode mixer (also known as a ring modulator). There is no output unless both f_1 and f_2 inputs are present, though f_2 (but not f_1) can be DC.

Suppose that two input sinusoids of different frequencies, $U_1 = \sin\omega_1 t$ and $U_2 = \sin\omega_2 t$ are fed into the diode. The signal U_0 becomes:

$$U_0 = (\sin\omega_1 t + \sin\omega_2 t) + \tfrac{1}{2}(\sin^2\omega_1 t + 2\sin\omega_1 t \sin\omega_2 t + \sin^2\omega_2 t) + ... \ . \tag{3.18}$$

Ignoring all terms except for the $\sin\omega_1 t \sin\omega_2 t$ term we get,

$$U_0 = 2\sin\omega_1 t \sin\omega_2 t + ... = \cos(\omega_1 t - \omega_2 t) - \cos(\omega_1 t + \omega_2 t) + ... \ , \tag{3.19}$$

demonstrating how new frequencies are created from the mixer.

3.3.2.2 Switching

Another form of mixer operates by switching, with the smaller input signal being passed inverted or non-inverted according to the phase of the local oscillator (LO).

This would be typical of the normal operating mode of a packaged double balanced mixer, with the local oscillator drive considerably higher than the signal amplitude.

The aim of a switching mixer is to achieve linear operation over the signal level by means of hard switching, driven by the local oscillator. Mathematically, the switching mixer is not much different from a multiplying mixer. Instead of the LO sine wave term, we would use the signum function. In the frequency domain, the switching mixer operation leads to the usual sum and difference frequencies, but also to further terms, e.g. $\pm 3f_{LO}$, $\pm 5f_{LO}$, etc.. The advantage of a switching mixer is that it can achieve (with the same effort) a lower noise figure and larger conversion gain. This is because the switching diodes or transistors act either like a small resistor (switch closed) or large resistor (switch open), and in both cases only a minimal noise is added. From the circuit perspective, many multiplying mixers can be used as switching mixers, just by increasing the LO amplitude.

3.3.2.3 Modulation and demodulation

Mixers are often used for modulation or demodulation purposes. Suppose we have on one hand a *carrier* signal, $U_{carrier} = \cos \omega t$, also called *local oscillator*. This may be a constant radiofrequency emitted by an antenna or a microwave. On the other hand, we have a reference signal which we want to transport somewhere else, $U_{ref} = \cos \Omega t$. Used as a modulator the mixer will simple multiply,

$$U_{mod} = U_{carrier} U_{ref} = \cos \omega t \cos \Omega t = \tfrac{1}{2} \cos[(\omega - \Omega)t] + \tfrac{1}{2} \cos[\omega + \Omega)t] \ . \qquad (3.20)$$

Thus the mixer output contains two frequencies, the sum and the difference. Supposing that ω is a frequency in a range that can be radiated by antenna and Ω an acoustic frequency, both frequency components $\omega \pm \Omega \simeq \omega$ will be radiated.

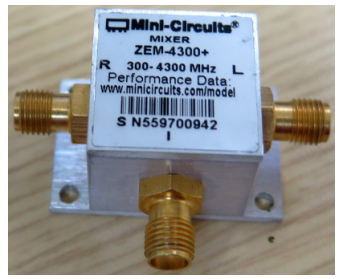

Figure 3.16: Picture of a radiofrequency mixer.

On the side of the receiver, who also has access to a synthesizer generating a signal $U_{carrier} = \cos \omega t$, we will use the mixer as a demodulator,

$$U_{demod} = U_{carrier} U_{mod} = \cos^2 \omega t \cos \Omega t = \tfrac{1}{2}(\cos 2\omega t + 1) \cos \Omega t \ . \qquad (3.21)$$

If $\omega \gg \Omega$, the carrier oscillation can easily be removed by a low-pass filter,

$$U_{filtered} = \tfrac{1}{2} \cos \Omega t \propto U_{ref} \ . \qquad (3.22)$$

That is, we recover the original information. And this holds even when the reference signal is (slowly) varying in amplitude or frequency, such as in the case of an acoustic signal [2]. Resolve Exc. 3.3.3.1.

3.3.2.4 Filtering with a mixer

Suppose we have a signal containing many frequency components (which may vary slowly in time), $U_{noisy}(t) = \sum_n A(\omega_n)e^{\imath\omega_n t}$ in complex notation, and that the signal we are interested in is an amplitude at a known particular frequency ω_0. By demodulating,

$$U_{sig}(t) = U_{noisy}(t)e^{-\imath\omega_0 t} = \sum_n A(\omega_n)e^{\imath\omega_n t}e^{-\imath\omega_0 t} = \sum_n A(\omega_n)e^{\imath(\omega_n-\omega_0)t} \ , \quad (3.23)$$

and low-pass filtering the lowest frequency component, i.e. $\omega_n - \omega_0 \simeq 0$,

$$U_{filtered} = A(\omega_0) \ . \quad (3.24)$$

This even holds for continuous noise spectra, $U_{noisy}(t) = \int A(\omega)e^{\imath\omega t}d\omega$, since,

$$U_{sig}(t) = U_{noisy}(t)e^{-\imath\omega_0 t} = \int_{-\infty}^{\infty} A(\omega)e^{\imath\omega t}e^{-\imath\omega_0 t}d\omega = \int_{-\infty}^{\infty} A(\omega+\omega_0)e^{\imath\omega t}d\omega \ , \quad (3.25)$$

and low-pass filtering with a filter bandwidth $\Delta\omega$,

$$U_{filtered} = \int_{-\Delta\omega}^{\Delta\omega} A(\omega+\omega_0)e^{\imath\omega t}d\omega \simeq A(\omega_0)2\Delta\omega \ . \quad (3.26)$$

Such techniques are widely used in lock-in amplifiers (see Sec. 3.4.3).

3.3.3 Exercises

3.3.3.1 Ex: Phase modulation

a. Show that it is not possible to construct a periodic phase modulation function such that the signal has only two sidebands.
b. Compare the spectra $\sum_{k=-\infty}^{\infty} J_k(M)e^{\imath k\Omega t} = e^{\imath M\sin\Omega t}$ and $\sum_{k=-\infty}^{\infty} |J_k(M)|e^{\imath k\Omega t}$. Can you detect phase modulation of a photodetector signal on a spectrum analyzer? How about amplitude modulation?

3.3.4 *Experiment: Creating sidebands on a radiofrequency*

In this exercise, we will understand the origin of sidebands as we'll see them emerge from a modulation spectrum when we gradually increase the modulation index [3].

1. Take a VCO, for example, ZOS-100+ from MiniCircuits. Study the datasheet and drive the VCO with an AC voltage. Vary the amplitude and the frequency of the voltage and observe the output signal of the VCO on a spectrum analyzer.

[2] In complex notation, $U_{in} = e^{\imath\omega t}$, $U_{mod} = U_{in}e^{\imath\Omega t} = e^{\imath(\omega+\Omega)t}$, $U_{demod} = U_{mod}e^{-\imath\omega t} = e^{\imath\Omega t}$.
[3] Datasheet for the VCO see appendix Fig. 7.16,
data sheet for the variable attenuator see appendix Fig. 7.17,
data sheet for the mixer see appendix data sheet Fig. 7.19.

2. Try to understand the spectrum observing the limiting cases $\Omega \gg \Delta\omega$ and $\Omega \ll \Delta\omega$. How can you read Ω and Δf from the spectra in both cases?

3. Write a MATLAB program to simulate the spectrum.

3.4 Measurement instrumentation

3.4.1 Sample-and-hold circuit

sample-and-hold circuit Solder on euroboard

3.4.2 Box-car integrator

box-car integrator Solder on euroboard

3.4.3 Lock-in amplifier

An *lock-in amplifier* (also called a phase-sensitive rectifier or *mixer*) is an amplifier that can measure a weak electrical signal by modulating the signal by a reference signal with a known frequency and phase. The device represents a bandpass filter with an extremely narrow bandwidth and, therefore, improves the signal-to-noise ratio (SNR). DC or AC noise components are efficiently filtered.

Download an illustration of the working principle of a *lock-in amplifier* here.

3.4.4 *Experiment: Building a lock-in amplifier*

Let's now build a lock-in amplifier. The principle is illustrated in Fig. 3.17(a). The sinusoidal signal discriminated at a non-linear line is switched on and off in the lock-in by a switch. At the same time, the inverted signal (i.e., phase shifted by 180°) is turned off and on. Both signals are combined and low-pass filtered. As Fig. 3.17(b) shows, the sign of the filtered signal depends on the phase between the discriminator and the TTL signal controlling the switch [4]

1. Create the circuit sketched in Fig. 3.17(a) on a circuit board and test it by varying the phase between the modulated output signal and the TTL signal provided by a function generator.

3.5 Further reading

P. Horowitz et al., *The art of electronics* [DOI]

U. Tietze et al., *Halbleiterschaltungstechnik* [DOI]

[4] Datasheets for the operational amplifier see appendix Fig. 7.24, data sheet for the switch see appendix Fig. 7.23.

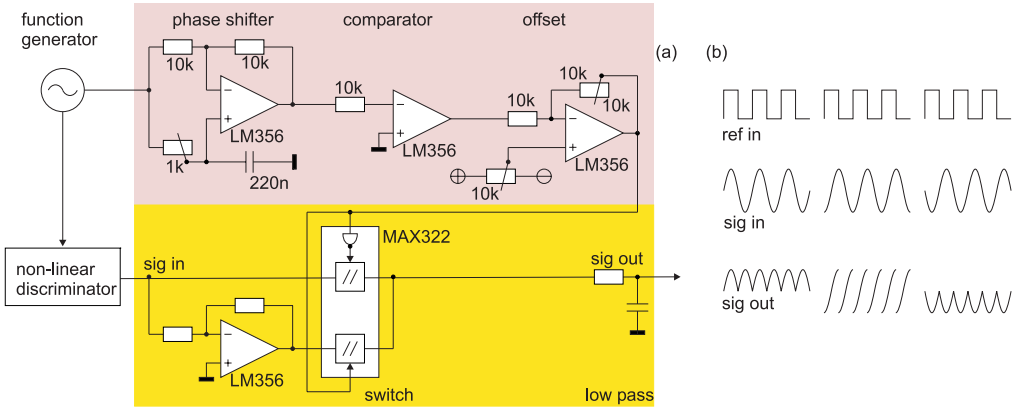

Figure 3.17: (a) Principal scheme of a lock-in amplifier. (b) Mode of operation.

Chapter 4

Quantum optics and optical interferometry

The objective of this chapter is to introduce the basics of optical *interferometry*. We will see, how to match the light modes in optical cavities and fibers, and to phase-match the wavefronts of two laser beams in order to detect their frequency beating with a photodetector. Furthermore, he will learn how to handle essential tools of *quantum electronics*, such as a piezo-electric transducer, an electro-optic modulator, and an acousto-optic modulator, used in interferometry, as discussed in Secs. 4.4.1 to 4.4. Interferometers have versatile applications such as 1. for the detection of very small length variations (as for example caused by gravitational waves), 2. as vibration and inertial sensors, or in 3. the transmission of information (radio).

4.1 Introduction to interferometry

4.1.1 Beam splitter in $\mathcal{S}$-representation

The essential component of any interferometer is the (non-polarizing) *beam splitter*.

We consider a classical lossless beam splitter with electric fields incident at both its inputs. The two output fields E_c and E_d are linearly related to the inputs through

$$\begin{pmatrix} \mathcal{E}_c \\ \mathcal{E}_d \end{pmatrix} = \begin{pmatrix} t_{ac} & r_{bc} \\ r_{ad} & t_{bd} \end{pmatrix} \begin{pmatrix} \mathcal{E}_a \\ \mathcal{E}_b \end{pmatrix} , \tag{4.1}$$

where the 2×2 element is the beam splitter matrix. r and t are the reflectance and transmittance along a particular path through the beam splitter, that path being indicated by the subscripts.

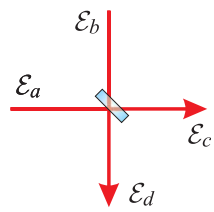

Figure 4.1: Beam splitter.

Assuming the beam splitter removes no energy from the light beams, the total output energy can be equated with the total input energy, reading

$$|\mathcal{E}_c|^2 + |\mathcal{E}_d|^2 = |t_{ac}\mathcal{E}_a + r_{bc}\mathcal{E}_b|^2 + |r_{ad}\mathcal{E}_a + t_{bd}\mathcal{E}_b|^2 = |\mathcal{E}_a|^2 + |\mathcal{E}_b|^2 \ . \tag{4.2}$$

Factorizing the expression in the center we obtain terms in $|\mathcal{E}_a|^2$, $|\mathcal{E}_b|^2$, $|\mathcal{E}_a\mathcal{E}_b^*|$, and $|\mathcal{E}_a^*\mathcal{E}_b|^2$. Comparing with the terms in the right-hand side expression we find that the equation can only be true for any field amplitudes, if the following relationships between reflectance and transmittance are satisfied,

$$\boxed{|t_{ac}|^2 + |r_{ad}|^2 = 1 = |t_{bd}|^2 + |r_{bc}|^2 \quad \text{and} \quad t_{ac}r_{bc}^* + r_{ad}t_{bd}^* = 0} \ . \tag{4.3}$$

We write each r and t as a complex number having an amplitude and phase factor accounting for possible phase shifts of a beam as it reflects or transmits at the beam splitting surface. From the second equation (4.3) we obtain,

$$t_{ac}r_{bc}^* + t_{bd}^*r_{ad} = |t_{ac}||r_{bc}|e^{\imath(\phi_{ac}-\phi_{bc})} + |t_{bd}||r_{ad}|e^{\imath(\phi_{ad}-\phi_{bd})} = 0 \ . \tag{4.4}$$

This expression can only be true if,

$$\phi_{ad} - \phi_{bd} + \phi_{bc} - \phi_{ac} = \pi \qquad \text{and} \qquad \frac{|r_{bc}|}{|t_{bd}|} = \frac{|r_{ad}|}{|t_{ac}|} \ . \tag{4.5}$$

Comparing the second equation (4.5) with the first two equations (4.3) we conclude,

$$|r_{ac}| = |r_{bd}| \equiv \sqrt{R} \qquad \text{and} \qquad |t_{ad}| = |t_{bc}| \equiv \sqrt{T} \ , \tag{4.6}$$

where we defined the reflection and the transmission of the beam splitter. It follows that

$$\boxed{R + T = 1} \ . \tag{4.7}$$

Without loss of generality, we may set $\phi_{bd} \equiv 0$, so that $\phi_{ac} = \phi_{ad} - \phi_{bc} - \pi$. Then,

$$\mathcal{S} = \begin{pmatrix} t_{ac} & r_{bc} \\ r_{ad} & t_{bd} \end{pmatrix} = \begin{pmatrix} -\sqrt{T}e^{\imath(\phi_{ad}-\phi_{bc})} & \sqrt{R}e^{\imath\phi_{bc}} \\ \sqrt{R}e^{\imath\phi_{ad}} & \sqrt{T} \end{pmatrix} \ . \tag{4.8}$$

Until, now the calculations were totally general, so that the above results hold for any type of beam splitting device. Let us now give a few concrete examples.

Example 5 (*Beam splitters*): For beam splitting at dielectric interfaces in particular we know that the electric field amplitude does not suffer phase shifts upon transmission, $\phi_{ac} \equiv 0$, implying $\phi_{ad} - \phi_{bc} = \pi$. Hence,

$$\mathcal{S} = \begin{pmatrix} \sqrt{T} & \sqrt{R}e^{\imath\phi_{bc}} \\ \sqrt{R}e^{\imath(\phi_{bc}+\pi)} & \sqrt{T} \end{pmatrix} \ . \tag{4.9}$$

Thus, the two off-diagonal elements are 180° out of phase. For the situation depicted in Fig. 4.1 one of the reflections occurs at an optical more dilute medium. For this reflection the phase shift is 0. But the other reflection occurs at an optical denser medium and therefore suffers a 180° phase shift. With this constraints the matrix describing a lossless beam splitter reads,

$$\boxed{\begin{pmatrix} \mathcal{E}_c \\ \mathcal{E}_d \end{pmatrix} = \begin{pmatrix} \sqrt{T} & \sqrt{R} \\ -\sqrt{R} & \sqrt{T} \end{pmatrix} \begin{pmatrix} \mathcal{E}_a \\ \mathcal{E}_b \end{pmatrix}} \ . \tag{4.10}$$

4.1.2 Piezo-electric actuator

The piezo-electricity effect describes the reciprocal action between mechanical pressure (from Greek: piézein - press) and electrical voltage in solids. It is based on the phenomenon that occurs in the regular deformation of certain piezoelectric materials: at the surface occur displacements of electric charges creating microscopic dipoles inside the unit cells. The sum over all the unit cells of the crystal leads to a macroscopically measurable electrical voltage. The deformation should be directed, which means, that the pressure is not applied from all sides on the crystal, but for example only on opposite sides.

On the other hand, by applying an electric voltage, a crystal (or piezo-ceramic element) may be deformed. Like any other solid body, piezo-electric crystals can execute mechanical vibrations. In a *piezo-electric actuator* (or piezo transducer PZT), these vibrations can be electrically excited. The frequency of the vibrations depend only on the speed of sound (which is a constant of the material) and the dimensions of the actuator. Therefore, actuators are also suitable for realizing oscillators (for example, quartz crystals). The piezo-electric effect can only occur in non-conductive materials (e.g., lead titanate zirconate).

When a voltage is applied to the piezo-ceramic in the direction of polarization, we observe an expansion in this direction and a perpendicular contraction. Depending on the employed material and the coefficient for piezo-electric strain d, stretches up to $\Delta l/l = 0.15\%$ can be obtained:

$$\Delta l = d\mathcal{E}l_0 \ , \tag{4.11}$$

where l_0 is the length of the actuator and $E = U/l_0$ the amplitude of the electric field. The elongation effect is therefore proportional to the field strength and the overall length of the actuator. To achieve large stretches with manageable electrical voltages, actuator discs are often stacked (mechanical circuit in series and electric circuit in parallel).

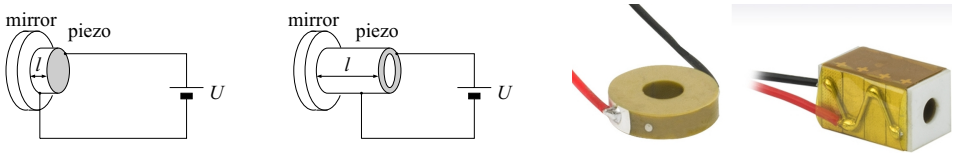

Figure 4.2: (Left) Scheme of mirrors mounted on a piezo actuator having the shape of a disc or a ring. (Right) Photos of a ring piezo and a piezo stack.

Negative voltages with respect to the orientation of the discs cause a contraction. However, negative voltages can also cause a change in the polarization state of the piezo and should therefore be avoided! In electrical circuits, piezoelectric actuators introduce a capacitance with a relative dielectric constant between 600 and 5000 and an internal resistance of about 10^8 Ω depending on the material. See Exc. 4.1.10.1.

4.1.3 Michelson and Mach-Zehnder interferometer

Interferometry is a technique exploiting the interference of waves coherently split and recombined by beam splitters. Sufficiently stable interferometers allow to visualize

variations of the path lengths of two or more partial waves following different pathways as an alteration of constructive and destructive interference.

The two most common types of interferometers are the *Michelson interferometer* and the *Mach-Zehnder interferometer* are depicted in Fig. 4.3. The advantages of the Michelson interferometer are an easy alignment and the need of only one beamsplitter. The advantage of the Mach-Zehnder interferometer is a direct optical access to both output ports of the interferometer. The following treatment applies to both types.

The field amplitude of a laser beam, $\mathcal{E}_i$, with frequency, $\omega = ck$, is divided by a beam splitter (reflectivity $\sqrt{R}$) into a transmitted $\mathcal{E}_t$ and a reflected beam $\mathcal{E}_r$,

$$\mathcal{E}_r = \sqrt{R_1}\mathcal{E}_i \qquad \text{and} \qquad \mathcal{E}_t = \sqrt{1-R_1}\mathcal{E}_i \ , \tag{4.12}$$

where we disregard possible phase-shifts upon reflection at optically dilute interface. The energy is obviously conserved, $|\mathcal{E}_r|^2 + |\mathcal{E}_t|^2 = \mathcal{E}_i^2$.

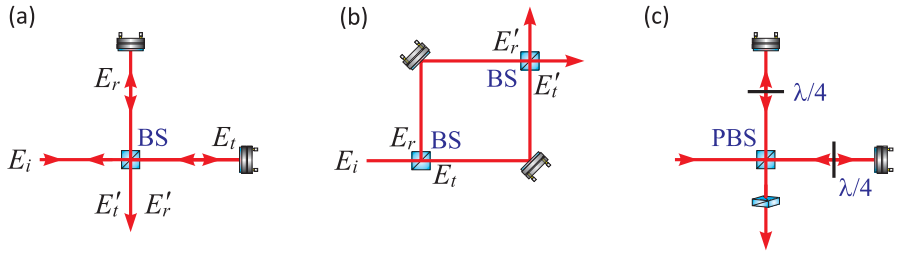

Figure 4.3: Principle of a two-beam interferometer: (a) Michelson interferometer and (b) Mach-Zehnder interferometer using non-polarizing beamsplitters. (c) Michelson interferometer using a polarizing beamsplitter.

We consider the Mach-Zehnder interferometer sketched in Fig. 4.3 with one arm of length L_r, which can be varied by a piezo, and the other arm of length L_t,

$$\mathcal{E}_r' = \mathcal{E}_r e^{2\imath k L_r} \qquad \text{and} \qquad \mathcal{E}_t' = \mathcal{E}_t e^{2\imath k L_t} \ . \tag{4.13}$$

The beams are recombined on a second beam splitter and sent to a photodetector, whose signal is,

$$\begin{aligned} I &\propto |\sqrt{R_2}\mathcal{E}_r' + \sqrt{1-R_2}\mathcal{E}_t'|^2 \\ &= |\sqrt{R_2}\sqrt{R_1}e^{2\imath k L_r} + \sqrt{1-R_2}\sqrt{1-R_1}e^{2\imath k L_t}|^2 \mathcal{E}_i^2 \ . \end{aligned} \tag{4.14}$$

Hence,

$$I \propto R_2 R_1 + (1-R_2)(1-R_1) + 2\sqrt{R_2}\sqrt{R_1}\sqrt{1-R_2}\sqrt{1-R_1}\cos[2k(L_t - L_r)] \ . \tag{4.15}$$

For reflectivities of $R_1 = R_2 = 50\%$, we get,

$$\boxed{I \propto \tfrac{1}{2} + \tfrac{1}{2}\cos[2k(L_t - L_r)]} \ . \tag{4.16}$$

It is important to realize that, while superpositions of light field amplitudes in the same mode interfere, *superpositions of light field amplitudes in different modes*

do not. For example, the superposition of two plane waves with equal frequency and polarization interferes,

$$\left|\begin{pmatrix}\mathcal{E}_1+\mathcal{E}_2\\0\end{pmatrix}\right|^2 = |\mathcal{E}_1+\mathcal{E}_2|^2 \ , \tag{4.17}$$

while the superposition of two plane waves with equal frequency but different polarizations does not,

$$\left|\begin{pmatrix}\mathcal{E}_1\\0\end{pmatrix}+\begin{pmatrix}0\\\mathcal{E}_2\end{pmatrix}\right|^2 = |\mathcal{E}_1|^2+|\mathcal{E}_2|^2 \ . \tag{4.18}$$

Solve the Excs. 4.1.10.2 to 4.1.10.4.

4.1.4 Coherence and spectrum of a light field

We have seen above that interferometers probe the electric field amplitude rather than the intensity. For this reason, they are suited to measure the first-order correlation function $g^{(1)}(\tau)$ and the emission spectrum, which are defined by,

$$g^{(1)}(\tau) \equiv \frac{\langle \mathcal{E}^-(t)\mathcal{E}^+(t+\tau)\rangle}{\langle \mathcal{E}^-(t)\mathcal{E}^+(t)\rangle} \qquad \text{and} \qquad S_\mathcal{E}(\omega) \equiv \mathcal{F}[g^{(1)}(\tau)] \ . \tag{4.19}$$

As an example, Fig. 4.4 shows the aurocorrelation function and spectrum of a simultaneously amplitude- and phase-modulated laser beam, $\mathcal{E}(t) = (1+n\cos\omega_n t)e^{\imath m \sin\omega_m t}$.

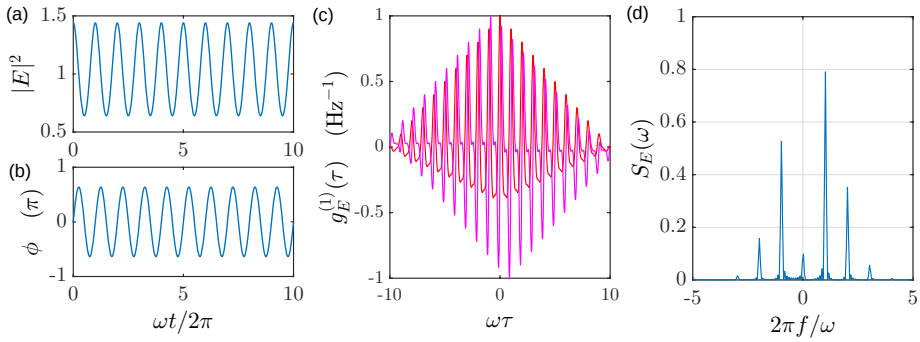

Figure 4.4: (code) (a) Amplitude and (b) phase of the electric field, with $n = 0.2$, $m = 1$, and $\omega_n = \omega_m = (2\pi)\ 1\,\mathrm{Hz}$. (c) Aurocorrelation function and (d) spectrum of the light field.

4.1.5 Birefringent interferometer

A *birefringent interferometer* or *Lyot filter* consists of one or more birefringent crystals mounted onto a rotation frame between two polarizers. Let n_o and $n_e = n_o + \Delta n$ be the refractive indices of the normal and the extraordinary axis, respectively. The corresponding Jones matrix is then,

$$\mathcal{M} = \begin{pmatrix}1&0\\0&0\end{pmatrix}\begin{pmatrix}\cos\phi&\sin\phi\\-\sin\phi&\cos\phi\end{pmatrix}\begin{pmatrix}e^{\imath k_0 L}&0\\0&e^{\imath k_e L}\end{pmatrix}\begin{pmatrix}\cos\phi&-\sin\phi\\\sin\phi&\cos\phi\end{pmatrix}\begin{pmatrix}1&0\\0&0\end{pmatrix} \ , \tag{4.20}$$

Such that,

$$\begin{pmatrix} \mathcal{E}_{out} \\ 0 \end{pmatrix} = \mathcal{M} \begin{pmatrix} \mathcal{E}_{in} \\ 0 \end{pmatrix} = \begin{pmatrix} \left(e^{\imath k_0 L} \cos^2\phi + e^{\imath k_e L} \sin^2\phi\right) \mathcal{E}_{in} \\ 0 \end{pmatrix} . \tag{4.21}$$

By trigonometric transformations it is possible to show, that the transmission $T \equiv |\mathcal{E}_{out}/\mathcal{E}_{in}|^2$ is,

$$\boxed{T(\lambda,\phi) = |e^{\imath k_0 L} \cos^2\phi + e^{\imath k_e L} \sin^2\phi|^2 = 1 - \sin^2 2\phi \sin^2 \tfrac{\pi L \Delta n}{\lambda}} . \tag{4.22}$$

For $\phi = 45°$ the transmission becomes simply,

$$T(\lambda, \tfrac{\pi}{4}) = \cos^2 \tfrac{\pi L \Delta n}{\lambda} . \tag{4.23}$$

In practice Lyot filters are often used, placed under the Brewster angle inside ring cavity lasers, as frequency selective elements. Frequently, birefringent plates of different thicknesses are stacked,

$$T(\lambda) = T_1(\lambda) T_2(\lambda) , \tag{4.24}$$

in order to increase the frequency selectivity. Furthermore, when the axis of the birefringent plates are rotated by fixed angles $\Delta\alpha$ with respect to each other,

$$T(\lambda, \alpha) = T_1(\lambda, \alpha) T_2(\lambda, \alpha + \Delta\alpha) , \tag{4.25}$$

the frequency of maximum transmission can be tuned by simply rotating the stack as a whole by an angle α. See 4.1.10.5.

A Lyot filter can be considered an interferometer, because it splits and recombines the polarization vector of a light beam in two parts following the ordinary and the extraordinary axis of the birefringent crystal. This is somewhat analogous to the Michelson interferometer depicted in Fig. 4.3(c).

4.1.6 Optical resonators

Optical cavities consist of an arrangement of mirrors reflecting the light beams in such a way, that they form a closed path. Since light that entered the cavity is performing there many round trips before it is transmitted again or absorbed, the light power is considerably enhanced, i.e. cavities can store light.

Light which is to resonate in the cavity must satisfy the boundary condition, that the mirror surfaces coincide with standing wave nodes. Therefore, in a cavity with length L only a discrete spectrum of wavelengths $N\frac{\lambda}{2} = L$ can be resonantly amplified, where N is a natural number. Because of this property, cavity are often used as frequency filters or optical spectrum analyzers: Only frequencies $\nu = N\delta_{fsr}$ are transmitted, where

$$\boxed{\delta_{fsr} = c/2L} \tag{4.26}$$

is the free spectral range of the cavity.

Cavities are characterized on one hand by their geometry, i.e. the curvature and the distance of their mirrors, and on the other hand by their finesse, which is given by the reflectivity of their mirrors. Let us first study the finesse. Regarding the cavity

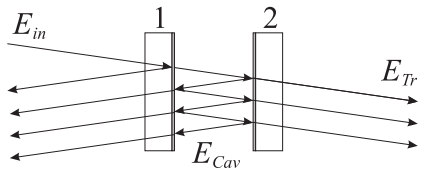

Figure 4.5: Multiple interference in an optical cavity.

as a multipass interferometer [25], we can derive expressions for the reflected and transmitted intensity as a function of frequency [1]. The so-called *Airy formula* for transmission and reflection are,

$$\frac{\mathcal{E}_{refl}}{\mathcal{E}_{in}} = r_1 - \frac{t_1^2 r_2 e^{2\imath kL}}{1 - r_1 r_2 e^{2\imath kL}} \qquad \text{and} \qquad \frac{\mathcal{E}_{trns}}{\mathcal{E}_{in}} = \frac{t_1 t_2 e^{\imath kL}}{1 - r_1 r_2 e^{2\imath kL}} \ . \tag{4.27}$$

In terms of intensity, assuming identical mirrors, $r_1 = r_2 = \sqrt{R}$ and $t_1 = t_2 = \sqrt{T}$, and neglecting possible absorptive losses, $A = 1 - R - T = 0$,

$$\boxed{\frac{I_{refl}}{I_{in}} = \frac{(\frac{2F}{\pi})^2 \sin^2 \frac{\Delta}{2\delta_{fsr}}}{1 + (\frac{2F}{\pi})^2 \sin^2 \frac{\Delta}{2\delta_{fsr}}} \qquad \text{and} \qquad \frac{I_{trns}}{I_{in}} = \frac{1}{1 + (\frac{2F}{\pi})^2 \sin^2 \frac{\Delta}{2\delta_{fsr}}}} \ , \tag{4.28}$$

where R is the reflectivity of a mirror and $\delta = 4\pi L/\lambda = 2\pi\nu/\delta_{fsr}$. The transmission curve of a cavity has a finite transmission bandwidth $\Delta\nu$, which depends on the reflectivity of the mirrors. The finesse of a cavity is defined by

$$\boxed{F \equiv \frac{2\pi\delta_{fsr}}{\kappa} = \frac{\pi\sqrt{R}}{1 - R}} \ . \tag{4.29}$$

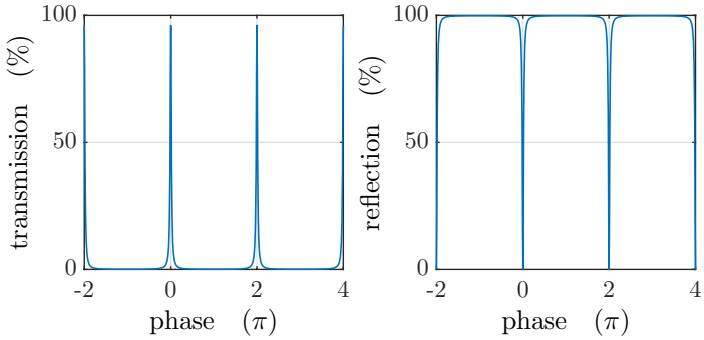

Figure 4.6: (code) Transmission and reflection through a resonator.

Note that factors others than the finite reflectivity may degrade the finesse of a cavity. For example, an imperfect mirror flatness (commonly specified as λ/F_{surf})

[1] See script on *Electrodynamics* (2023), Exc. 7.3.6.16.

reduces the finesse to [25],

$$F_{tot} = \left(\frac{1}{F} + \frac{1}{F_{surf}} \right)^{-1} . \tag{4.30}$$

.

The geometry of a cavity must satisfy certain conditions, in order to be stable [47]. Besides the main longitudinal modes a cavity possesses transverse modes of the order TEM_{mn}, whose frequencies are given by [2],

$$\nu/\delta_{fsr} = (q+1) + \frac{m+n+1}{\pi} \arccos \sqrt{\left(1 - \frac{L}{\rho_1}\right)\left(1 - \frac{L}{\rho_2}\right)} . \tag{4.31}$$

A *confocal cavity* with degenerate transverse modes, $\rho_1 = \rho_2 = L$, is particularly suited as optical spectrum analyzer.

The diameter of the beam waist in the cavity is,

$$w_0 = \sqrt[4]{\left(\frac{\lambda}{\pi}\right)^2 \frac{L(\rho_1 - L)(\rho_2 - L)(\rho_1 + \rho_2 - L)}{(\rho_1 + \rho_2 - 2L)^2}} . \tag{4.32}$$

For an optimal coupling of the light into the cavity the Gaussian laser beam must be matched to the cavity's geometry of the cavity, i.e. diameter and divergence of the laser beam must be adapted to the cavity mode with a suitable arrangement of lenses [26, 47]. See Excs. 4.1.10.6 to 4.1.10.11.

4.1.7 Dielectric mirrors and filters

Dielectric mirrors and filters are multiple beam interferometers in a similar sense as Fabry-Pérot cavities. They consist of stacks of thin dielectric layers with alternating refraction indices [3].

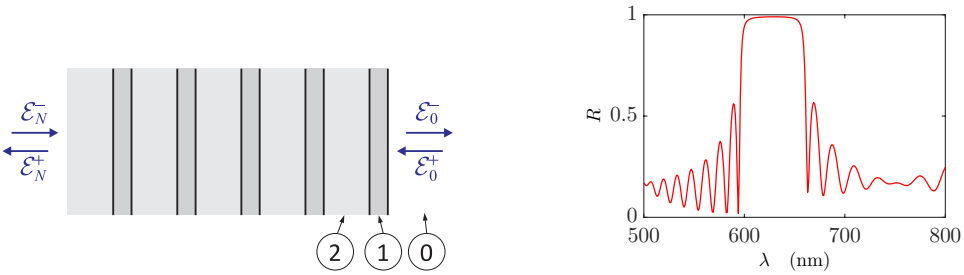

Figure 4.7: (code) Reflection by a high reflecting mirror made of 10 layers with $n_1 = 2.4$ and $\Delta z_1 = 80\,\mathrm{nm}$ alternating with 10 layers with $n_2 = 1.5$ and $\Delta z_2 = 500\,\mathrm{nm}$. The absorption coefficient for each layer is supposed to be $\alpha = 0.2\%$. The beam impinges from vacuum, $n_0 = 1$.

Reflections of $R = 99.999\%$ can be reached which, applied of superpolished mirrors, allow for the construction of cavities with finesse $F > 300000$. On the other

[2] See script on *Electrodynamics* (2023), Sec. 7.4.2.2.
[3] See script on *Electrodynamics* (2023), Sec. 7.1.7.

anti-reflection coatings can be applied to surfaces reducing their reflections to below $R = 0.1\%$. See Excs. 4.1.10.12 and 4.1.10.13 [26, 50].

4.1.8 Optical fibers

An *optical fiber* is a waveguide in which light is guided by internal total reflection. The total reflection occurs between layers with different refractive indices called *fiber core* and *fiber cladding*. The core is the central region of the optical fiber where the light is guided. In order to create guiding conditions, the refractive index of the core must be higher than the one of the cladding. The cladding diameter is typically 8 to 10 times the *mode field diameter* (MFD) of the fundamental mode. In general, MFD is greater than the physical diameter of the fiber core, which means that some optical power is always guided by the fiber cladding as an evanescent wave.

The *cut-off wavelength* λ_{co} of an optical fiber is the wavelength above which a guided mode of a waveguide ceases to exist. For wavelength longer than λ_{co} an optical fiber becomes single-mode. At wavelengths shorter than λ_{co} several optical modes may propagate and the fiber becomes multi-mode. The cut-off wavelength is directly related to the core diameter of the fiber $\lambda_{co} \propto \emptyset$. For

$$\frac{\lambda}{2} < \emptyset < \lambda \qquad \text{or equivalently} \qquad \emptyset < \lambda < 2\emptyset \tag{4.33}$$

the fiber is single-mode. For $\lambda > 2\emptyset$ no guided mode exists and for $\emptyset > \lambda$ the fiber becomes multimode.

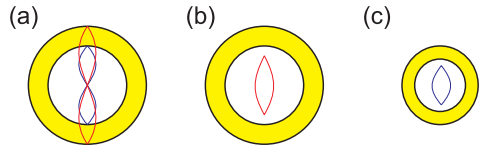

Figure 4.8: Mono-mode waveguiding by optical fibers.

The *numerical aperture* is a measure of the acceptance angle of the fiber. It is very important because it determines how strongly a fiber guides light, and so how resistant it is to bend-induced losses. The numerical aperture can be defined by the acceptance angle of the fiber, though as this is highly diverging in space it is rather complicated to reach a simple definition. It is most convenient to define the NA in terms of the relative indices of core and cladding glass forming the fiber waveguide:

$$NA = \sin\tfrac{\theta_a}{2} = \sqrt{n_{core}^2 - n_{clad}^2} \simeq \sqrt{2n_{core}^2 \delta n}\ , \tag{4.34}$$

where δn is the index difference between the core and cladding. An optical fiber with 'high' numerical aperture will confine light more strongly in the core, and so support guidance further above cut-off. This attribute has two important effects: (a) it will be single-mode over a greater range of wavelengths than is possible with a fiber with a 'low' numerical aperture fiber and (b) it will still guide a single-mode when coiled or bent to a smaller diameter.

4.1.8.1 Multi-mode, mono-mode, and polarization maintaining fibers

Many types of fibers are currently available for a large variety of applications.

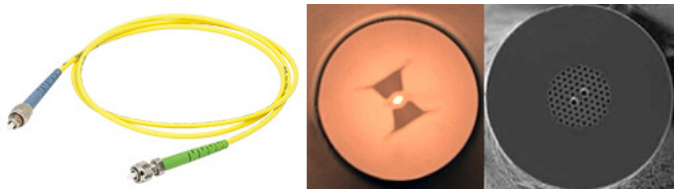

Figure 4.9: (Left) Fiber patch cord, (center) cross section of a bow-tie polarization maintaining fiber, and (right) cross section of a photonic crystal fiber.

4.1.9 Laser gyroscope and the Sagnac effect

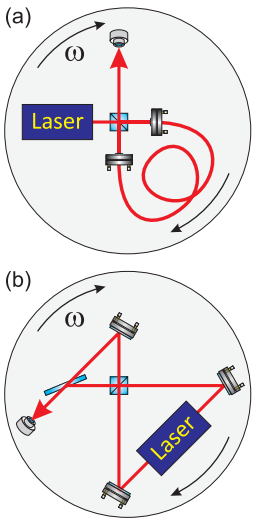

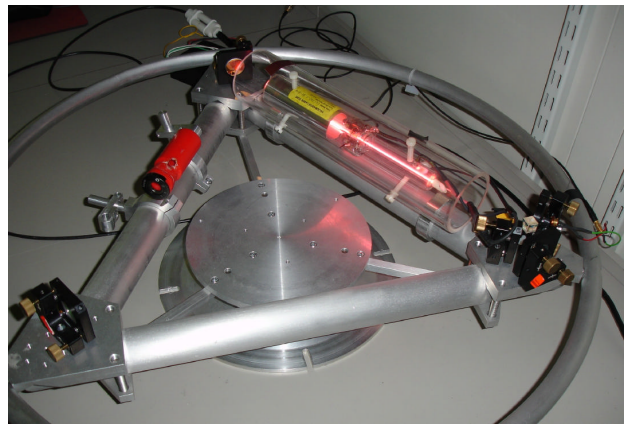

Figure 4.10: (a) Principle scheme of a fiber-based Sagnac interferometer. (b,c) Laser gyroscope realized with a HeNe gain tube.

Gyroscopes are based on the *Sagnac effect*. They are based on a ring cavity mounted on a rotating stage, as shown in Fig. 4.10(a). Let us, for simplicity first consider a circular path for the light beam (e.g. a fiber-based ring cavity) rotating at an angular velocity Ω. Then the time needed for the light beam to travel in either one of the two directions is,

$$t_\pm = \frac{(2\pi \pm \Omega t_\pm)r}{c} = \frac{2\pi r}{c \mp \Omega r} \ , \tag{4.35}$$

that is,

$$\Delta t \equiv t_+ - t_- = \frac{4\pi r^2 \Omega}{c^2 - \Omega^2 r^2} \simeq \frac{4\pi r^2 \Omega}{c^2} \equiv \frac{4A\Omega}{c^2} \ , \tag{4.36}$$

where A is the area enclosed by the path. This formula can be generalized to arbitrary paths.

For example, assuming an interferometer with $A = 1\,\mathrm{m}^2$ at rest in an Earth-based system, $\Omega \simeq 2\pi/24\,\mathrm{h}$, the time difference for light propagating along the two directions

is $\Delta t \approx 3 \cdot 10^{-21}$ s and the path difference $\Delta L = c\Delta t \approx 100$ fm. The frequency shift is,

$$\boxed{\Delta v = k(v_+ - v_-) = k(2\Omega r) = \frac{\sqrt{4\pi A}\Omega}{\lambda}}\,, \tag{4.37}$$

yielding for the given example of an Earth-based interferometer $\Delta\nu \approx 400$ Hz.

4.1.10 Exercises

4.1.10.1 Ex: Characterizing a piezo actuator

In order to characterize a recently purchased piezo actuator (Thorlabs, TA0505D024W) a Scientific Initiation student sets up a Michelson interferometer driven by a HeNe laser beam. Scanning the voltage applied to the piezo through the entire permitted range, he observes 8.8 oscillations of the interference fringes. What is the piezo displacement per volt?

4.1.10.2 Ex: Michelson interferometer

The figure 4.11 shows a Michelson interferometer containing in one arm an airtight 5 cm long cell with glass windows. Light with wavelength $\lambda = 500$ nm is used. After the cell has been evacuated, the interference pattern shifts by 60 fringes. Use this information to calculate the refractive index of air at atmospheric pressure. With what accuracy can you determine the refractive index with this method?

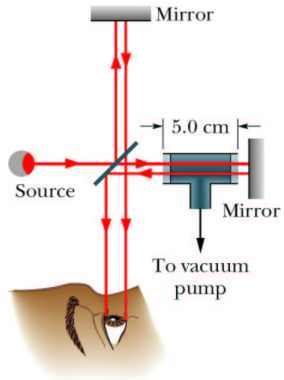

Figure 4.11:

4.1.10.3 Ex: Michelson interferometer

Assume that a signal-to-noise ratio of 50 has been achieved in measuring the fringe pattern of a Michelson interferometer with one continuously moving mirror. Estimate the minimum path length ΔL that the mirror has to travel in order to reach an accuracy of $\Delta\lambda = 10^{-4}$ nm in the measurement of a laser wavelength at $\lambda = 600$ nm.

4.1.10.4 Ex: Rotating the polarization with a Mach-Zehnder interferometer

Using the Jones matrix formalism demonstrate how to use the Mach-Zehnder interferometer setup sketched in the figure to rotate the polarization of a linearly polarized laser beam in an electronically controlled way using a piezo actuator mounted in ones of the interferometer arms.

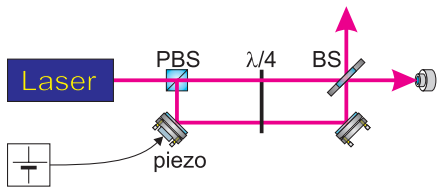

Figure 4.12:

4.1.10.5 Ex: Lyot filter

Consider a Lyot filter with two plates ($L_1 = 1\,\text{mm}$ and $L_2 = 4\,\text{mm}$) with the refraction indices $n_o = 1.40$ in the fast axis and $n_e = 1.45$ in the slow axis.
a. Calculate the transmission peaks of the Lyot filter as a function of λ for the rotation angle $\phi = 45°$.
b. Determine the transmitted intensity $I(\phi)$ as a function of the rotation angle ϕ for a fixed wavelength λ. What is the contrast of the transmitted intensity for arbitrary values of λ if the absorption losses are 2%?

4.1.10.6 Ex: Wedge-shaped etalon

A beam of light of wavelength $\lambda = 683\,\text{nm}$ with large diameter is incident perpendicularly on the first of two quadratic plates. Each plate has the edge length 120 mm; at the left edge the plates touch each other, at the right edge they are separated by a wire of $d_w = 0.048\,\text{mm}$ in diameter. The air between the plates acts as a thin layer.
a. How many interference fringes does an observer see from above this arrangement?
b. Now suppose that the incident light be white. Will the interference pattern at the far left be bright or dark?
c. Starting from the left edge there will be a series of interference minima, whose position depend on the wavelength of the light. For what light color (blue or red) will the minimum be closer to the edge?

4.1.10.7 Ex: Fabry-Perot interferometer

The dielectric coatings of each plate of a Fabry-Perot interferometer have the following specifications: $R = 98\%$, $A = 0.3\%$. The flatness of the surfaces is $\lambda/100$ at $\lambda = 500\,\text{nm}$.
a. Estimate the finesse from (4.27) and (4.30), the maximum transmission, and the spectral resolution of the FPI for a plate separation of 5 mm.

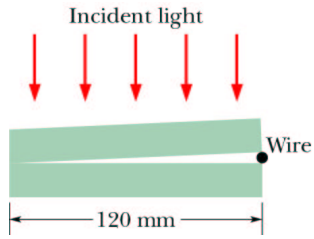

Figure 4.13:

b. Show that, for a given absorption, the transmitted intensity decreases with increasing reflectivity. Explain why. **Note:** A trade-off between high finesse and high transmission at a given absorption $A > 0$, called *impedance matching*, is reached by maximizing the intracavity intensity. For a symmetric cavity, it can be shown that impedance matching is reached for $A = T$.

4.1.10.8 Ex: Confocal and concentric cavities

a. Calculate the spectrum of longitudinal and transverse modes for (i) a confocal cavity ($\rho_a = \rho_b = L$) and (ii) a concentric cavity ($\rho_a = \rho_v = L/2$). Interpret the results.
b. Assuming radii of curvature $\rho_a = \rho_b = 5$ cm and a finesse of $F = 500$ for the cavity, how precise must the length of the cavity be adjusted in order to observe only longitudinal modes in the transmission spectrum?

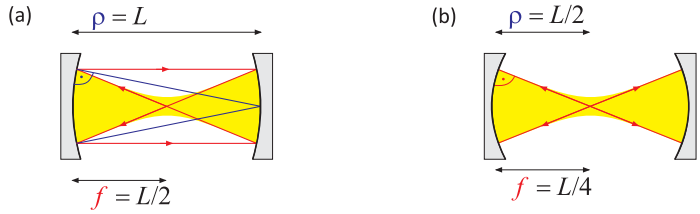

Figure 4.14: (a) Confocal cavity and (b) concentric cavity.

4.1.10.9 Ex: Thermal drift of a laser cavity

Estimate the frequency drift of a laser oscillating at $\lambda = 500\,\text{nm}$ because of thermal expansion of the resonator at a temperature drift of $1°\,\text{C/h}$, when the resonator mirrors are mounted on distance-holder rods a. made of invar and b. made of fused quartz.

4.1.10.10 Ex: Stability of a supercavity

Consider a non-confocal optical cavity of 10 cm length whose spacer is made of (i) aluminum, (ii) stainless steel, (iii) invar steel, (iv) fused quartz, (v) Zerodur, and (vi) ULE. The cavity is maintained at constant temperature with a precision of

0.001 C. What maximum drift do you estimate for its resonance frequency at 633 nm?

4.1.10.11 Ex: Fabry-Perot interferometer as optical spectrum analyzer

A confocal FPI shall be used as optical spectrum analyzer, with a free spectral range of $\delta_{fsr} = 3\,\mathrm{GHz}$. Calculate the mirror separation L and the finesse that is necessary to resolve spectral features in the laser output within $\Delta\nu = 10\,\mathrm{MHz}$. What is the minimum reflectivity R of the mirrors, if the surface finesse is $F_S = 500$?

4.1.10.12 Ex: Interference and colors filters

Strontium atoms resonantly driven by two lasers at 461 nm and 689 nm emit fluorescence light at both wavelengths. Because the red transition is 5000 times narrower than the blue one, the red fluorescence is much weaker and difficult to detect. Find a suitable low-pass filter in the Thorlabs® catalogue suppressing the blue light sufficiently to be sure that any fluorescence recorded after the filter must be resulting from the red transition. What signal ratios can you achieve with a single filter? Consider interference filters as well as color filters.

4.1.10.13 Ex: Interference filter

An interference filter shall be designed with peak transmission at $\lambda = 550\,\mathrm{nm}$ and a bandwidth of 5 nm. Estimate the reflectivity R of the dielectric coatings and the thickness of the etalon, if no further transmission maximum is allowed between 350 and 750 nm.

4.1.10.14 Ex: Cut-off wavelength of a single-mode fiber

You want to transport 461 nm light via a polarization maintaining single-mode fiber. How do you need to choose the cut-off wavelength of the fiber? Assuming a 50% coupling efficiency, how much power can you get through the 5 nm long fiber? Choose a model from the Thorlabs catalog and justify your choice.

4.1.10.15 Ex: Exc Numerical aperture of a fiber

Calculate the numerical aperture of a step-index fiber with core refraction index n_{core} and cladding refraction index $n_{cladding}$ considering the scheme 4.15.

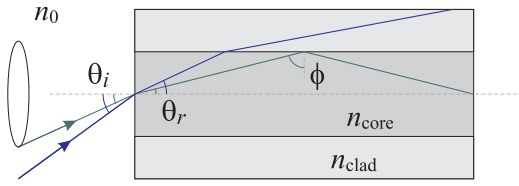

Figure 4.15:

4.1.10.16 Ex: Tuning by tilting an etalon

a. It is a common method to tune an etalon (or dielectric mirror or waveplate) to a certain transmission wavelength by tilting it as a whole with respect to the optical axis (without changing its intrinsic alignment. Does the tilt increase or decrease the wavelengths of the transmission peaks? Justify your answer. What is the implication for a dielectric mirror to be used under a non-normal angle of incidence?
b. A narrow band interference filter consisting of a glas plate coated on both surfaces has the following characteristics: thickness $L = 0.5\,\text{mm}$, refractive index $n_{rfr} = 1.45$, central wavelength $\lambda_{eff} = 706\,\text{nm}$, and bandwidth $\Delta\lambda = 0.3\,\text{nm}$. Considering the filter as Fabry-Pérot etalon, calculate its free spectral range, its finesse, and the reflectivity of its surfaces.
c. Assuming that the filter of part (b) can be tilted from normal incidence up to an angle $\theta_{max} = 35°$, how far will the center frequency shift. Prepare a graph showing λ_{eff} as a function of θ.

4.1.10.17 Ex: Double MZI as a model for Coherent Back-Scattering

Consider the setup shown in Fig. 4.16 and calculate the signal observed on the photodetector for arbitrary phase shifts ϕ and arbitrary rotation angles α by the $\lambda/2$-waveplate.

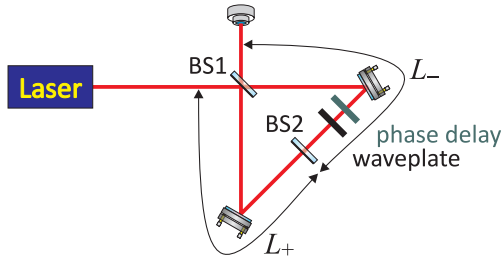

Figure 4.16: Double Mach-Zehnder interferometer.

4.1.11 *Experiment: Mach-Zehnder interferometer*

The Mach-Zehnder interferometer and the Michelson interferometer are the two most common two-beam interferometers. For the realization of the following project prior knowledge of 1. Gaussian beams (see Sec. 2.2), 2. photodetectors (see Sec. 3.2.1), and 3. piezo-electric transducers (see Sec. 4.1.2) is required.

1. Set up a Mach-Zehnder interferometer with a piezo in one of the arms according to Fig. 4.3(a). Optimize the phase matching of the two beams onto a photodetector and the rotation of the $\lambda/2$-waveplates until you obtain visible interference patterns.

2. Vary the length of one arm of the interferometer using the piezo. Measure the contrast of the interference fringes and discuss from which parameters it depends and how it can be maximized.

3. Rotate the first $\lambda/2$-waveplate (behind the laser). What do you observe? Explain the observation!

4. Remove the PBS in front of the photodetector. What do you observe? Explain the observation!

5. If a piezo is used, vary the voltage applied to the piezo-electric actuator and measure the voltage expansion coefficient d.

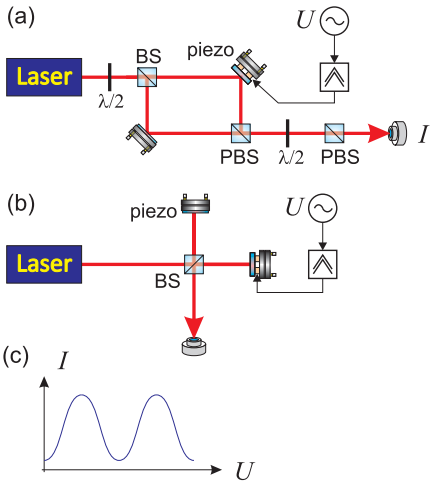

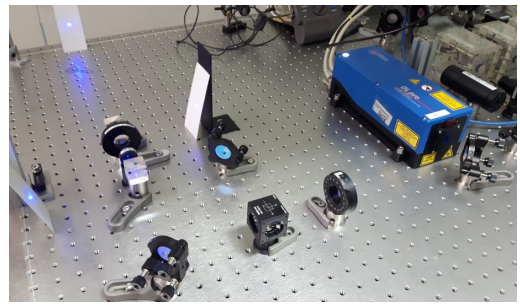

Figure 4.17: Setup for (a) a Mach-Zehnder interferometer or (b) a Michelson interferometer. (BS) non-polarizing beamsplitter, (PBS) polarizing beamsplitter. (c) Signal on the photodetector as a function of the length variation of an arm of the interferometer.

4.1.12 *Experiment: Fabry-Pérot cavity*

A Fabry-Pérot cavity is a typical multi-beam interferometer.

1. Set up a Fabry-Pérot cavity according to Fig. 4.18 and mode-match a laser beam into the cavity. Scan the cavity length using a piezo and observe the transmitted spectrum on an oscilloscope. What do you observe?

2. If an ECDL is used, vary the current and the temperature of the laser diode. What do you observe? Vary the frequency of the diode laser by scanning the piezo transducer of the laser cavity. Observe the mode spectrum of the laser in the transmission signal of the cavity. Measure its free spectral range, the transmission linewidth, and the finesse of the cavity.

Optical cavities are frequently used as *optical spectrum analyzers*. For this application, it is helpful to simplify the intrinsic mode spectrum of the cavity by using a confocal design, where all transerse modes are degenerated. We will now set up an optical cavity and characterize it by its free spectral range and its finesse. Then we will analyze its mode spectrum and modify its geometry to make it confocal.

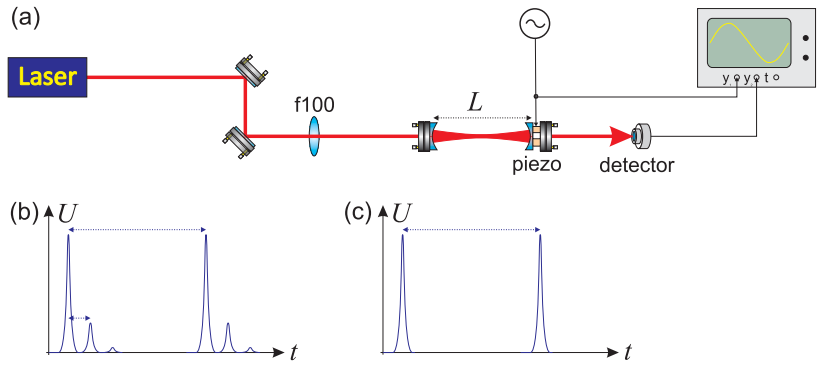

Figure 4.18: (a) Setup for aligning a confocal resonator. (b) Transmission spectrum of the cavity for non-confocal alignment. (c) Same as (b) but for the case of confocal alignment.

1. Couple a laser beam into a cavity as shown in Fig. 4.18. The cavity provided by this tinker course consists of a plane incoupler ($\rho_1 = \infty$, $R_1 = 98\%$) and a high reflector ($\rho_2 = 25\,\text{mm}$, $R_2 = 99.8\%$). Position the mirror at a distance L, where the cavity is stable. Calculate the free spectral range, the finesse, the diameter of the beam waist.

2. Optimize the phase-matching of the laser beam to the cavity. In order to do this, (a) measure the diameter of the diode laser beam, (b) determine the lens which can be used to focus down to the beam waist of the cavity. How does the transmission spectrum change upon the beam matching?

4.1.13 *Experiment: Fizeau interferometer*

A *Fizeau interferometer* is a device allowing to analyze the rugosity of surfaces.

1. Set up a Fizeau interferometer according to Fig. 4.18.

4.1.14 *Experiment: Coupling light into an optical fiber*

Coupling a laser beam into an optical fiber is a delicate task, requiring a good collimation optics and full control over the 6 degrees of freedom defining a laser beam: horizontal and vertical position, horizontal and vertical tilt, beam diameter and divergence.

1. Redirect the light of a HeNe laser via two adjustable mirrors into a fiber collimator in such a way that the beam is not deviated from the optical axis by the collimator.

2. Now connect (a) a multimode fiber and (b) a single mode fiber to the collimator. Optimize the coupling by walking the laser beam and by adjusting the focus of the fiber collimator. What differences do you observe for multi- and single mode fibers?

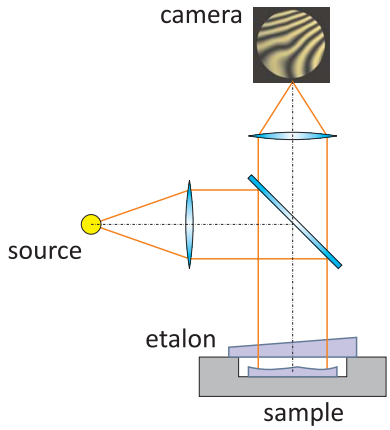

Figure 4.19: Principle of operation of a Fizeau interferometer.

4.2 Conventional light sources and lasers

For the first half of the 20-th century these assumptions matched the available light sources, usually incandescent, arc or plasma discharge lamps. After the invention of the laser in 1958, single mode and pulsed lasers quickly replaced the lamps as a source for optical excitation. These new light sources initiated a revolution in optical science, the consequence of which continue to reverberate through modern sciences and applied technologies. The characteristics of laser sources are far superior to the old lamps in all respects. They are intense, collimated, spectrally narrow and phase coherent. The laser gave rise to a multitude of new spectroscopic techniques and new disciplines, such as quantum electronics, the study of statistical properties of light in quantum optics, optical cooling and trapping of microscopic particles, the control of chemical reactivity, and new technologies for imaging and high resolution microscopy. The impact the laser had on technology is only comparable to that of to the invention of the transistor. See also (watch talk).

The laser produces light through an optical quantum amplification process based on the stimulated emission of electromagnetic radiation. The term 'laser' is an acronym for 'Light Amplification by Stimulated Emission of Radiation'. A laser differs from other light sources in that it emits *coherent* light. Its spatial coherence allows the light to be focused on a very tiny spot, where the concentration of energy is sufficient for applications such as laser cutting and lithography. The spatial coherence also allows it to collimate a laser beam over large distances, that is, the light forms a concentrated beam propagating in a straight line. Lasers can also have a very high temporal coherence, which corresponds to a very narrow spectrum, that is, lasers usually emit a single very well defined color of light. The extreme temporal coherence can be used to produce pulses of light as short as a femtosecond. In addition, laser light is polarized.

In 1917, Albert Einstein established the theoretical foundations of the laser in an article 'Zur Quantentheorie der Strahlung' through a rederivation of Max Planck's radiation law. He proposed a mechanism explaining how light is absorbed and emitted from atoms. The fundamental ingredient is that the photon can be emitted in two

different ways, by spontaneous emission, an indeterministic process that occurs without physical reason, or by stimulated emission. This latter emission process occurs because of stimulation by light, which is already present in the system and represents the fundamental mechanism of the laser. In the following decade German and American researchers experimentally confirmed the phenomena of stimulated emission and negative absorption, that is, gain. In 1950, Alfred Kastler (French physicist and Nobel Prize in Physics of 1966) proposed the method of optical pumping, confirmed experimentally two years later by other French physicists.

In 1953, Charles Townes produced the first microwave amplifier called *maser*, a device that operates similarly to the laser but amplifies microwave radiation instead of visible or infrared radiation. However, Townes' maser was unable to emit light continuously. In 1955, in the Soviet Union, Nikolay Basov and Aleksandr Prokhorov solved the problem of continuous operation using atoms with more than two energy levels. These level systems were able to sustain a permanent population inversion of an energetic level decaying to a less energetic system by releasing light via stimulated emission. Despite the fact that several prominent physicists, including Niels Bohr, John von Neumann, and Isidor Rabi, argued that the maser violates Heisenberg's uncertainty principle and therefore could not work, in 1964, Charles Townes, Nikolay Basov and Aleksandr Prokhorov shared the Nobel Prize in Physics for fundamental work in the field of quantum electronics that led to the realization of oscillators and amplifiers based on the maser principle.

In 1957, Charles Townes and Arthur Schawlow, from the Bell labs, began to seriously study feasibility of an 'optical maser'. In 1958, the Bell labs submitted a patent proposing a scheme for optical radiation, and Schawlow and Townes presented a scientific paper. Simultaneously, at the Columbia University, the PhD student Gordon Gould was working on the energy levels of excited thallium. In 1957-8, Gould and independently Prokhorov, Schawlow and Townes proposed the use of an open resonator, which later became an essential component of the laser. Gould also proposed several possible applications for a laser, such as spectrometry, interferometry, the radar, and nuclear fusion. He continued to develop the idea, and filed a patent application in April 1959. The United States Patent Office dismissed his application, and granted a patent to the Bell Labs in 1960. Gould won his first minor patent in 1977 after a 28-year fight, and it took him until 1987 to win his first significant process in the struggle, when a federal judge ordered the United States Patent Office to issue to Gould patents for optical pumping and the invention of a laser based on the principle of electrical gas discharge.

It was Theodore Maiman, who on May 16, 1960, operated the first working laser at the Hughes Research Laboratories, Malibu, California, evincing several other research teams, including the ones of Townes at Columbia University, of Schawlow at Bell Labs, and Gould at the company TRG (Technical Research Group). Maiman's laser used a synthetic solid-state ruby crystal pumped by a flash lamp to produce red laser light at 694 nm wavelength; however, the device was only capable of pulsed operation due to its three-level pumping scheme. Later in 1960, the first gas laser was built, using a helium-neon mixture, which was capable of continuous operation in the infrared spectrum. Basov and Javan proposed the concept of a semiconductor laser diode. In 1962, the first laser diode device, made of gallium arsenide, was realized emitting near-infrared light. Nowadays, laser diodes are available in various spectral regimes

up to the UV.

Figure 4.20: First suggested application in 1964 of a (left) HeNe laser and (right) a diode laser.

Interestingly, despite many attempts, it has not yet been possible to manufacture yellow or green laser diodes.

4.2.1 Features and operation of lasers

To understand how a laser operates, we consider the process of absorption and emission of light by an atom. Following Bohr's model an absorbed photon raises an electron from a lower orbit to a higher orbit, and when the electron returns back to the ground state, it re-emits a photon in an arbitrary direction.

When we illuminate a sample of N atoms, N_1 atoms of which are in the ground state, by a radiation field, the absorption rate depends on the field intensity $I(\nu)$ and a constant B_{12}, which is characteristic for the transition,

$$R_{abs} \propto B_{12} I(\nu) N_1 \ . \tag{4.38}$$

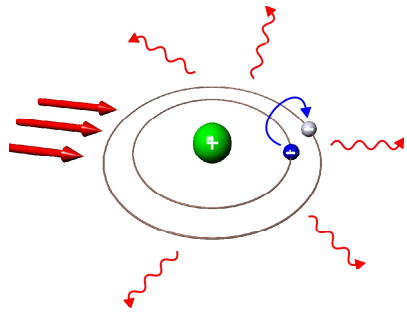

Figure 4.21: Bohr's model of photon absorption.

The emission rate depends on the number of atoms N_2 in the excited state, such that,

$$R_{sp} \propto A_{21} N_2 \ . \tag{4.39}$$

As the excited state has more energy, it can decay by itself (i.e. spontaneously) to a lower energy state. Einstein's brilliant idea now was to postulate a third process, which he called stimulated emission,

$$R_{st} \propto B_{21} I(\nu) N_2 \ . \tag{4.40}$$

In this process, an incident photon stimulates an excited atom to transfer the electron to a lower orbit. The released energy is then used to form a second photon, which is in all respects identical to the first. This process is necessary to ensure that, in thermal equilibrium, the population of the states follows Boltzmann's law.

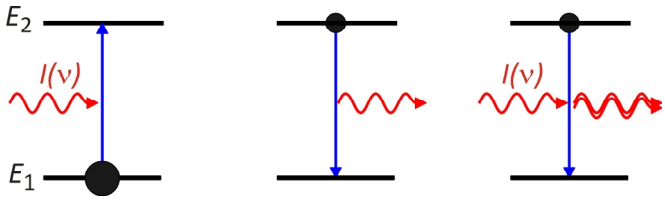

Figure 4.22: Einstein's model of absorption and spontaneous and stimulated emission.

Obviously, absorption decreases the intensity of a light beam crossing the atomic sample, while stimulated emission amplifies it. In order to amplify incident light, the gain in intensity must overcome the losses. Therefore, we need the absorption processes to be less frequent than the stimulated emission processes, i.e. the number of atoms in the excited state N_2 must exceed the number of atoms in the ground state $N_1 < N_2$.

We can easily write the rate equation,

$$\frac{dN_2}{dt} = -A_{21} N_2 - B_{21} I(\nu) N_2 + B_{21} I(\nu) N_1 = -\frac{dN_1}{dt} \ , \tag{4.41}$$

with $N = N_1 + N_2$. It is easy to solve this equation. The result is,

$$N_2 = \frac{I(\nu) B_{21} N}{A + 2 B_{21} I(\nu)} [1 - e^{-(A_{21} + 2 B_{21} I(\nu)) t}] < N_1 \ . \tag{4.42}$$

The graphical representation 4.23 shows the temporal behavior of the populations N_1 (in green in the figure) and N_2 (in blue), reaching a state of equilibrium after a certain time. By increasing the intensity of the incident light, we observe that the curves approach each other but never cross. That is, in a two-level system, we always get $N_1 > N_2$ and the populations are never inverted. Therefore, amplification of light as in the laser does not happen.

Fortunately, we can resort to a trick by inserting a third level. Ensuring that the decay rate of the (metastable) state E_3 is much slower than the optical pumping to this state via the driven transition $E_1 \to E_2$ followed by a rapid decay $E_2 \to E_3$, we can reach the situation $N_3 > N_1$. Now it is possible to amplify light, which is resonant with the transition $E_2 \to E_3$.

What are the minimum requirements for the realization of a laser? The first condition is that the *pumping cycle is irreversible* to ensure that the processes of

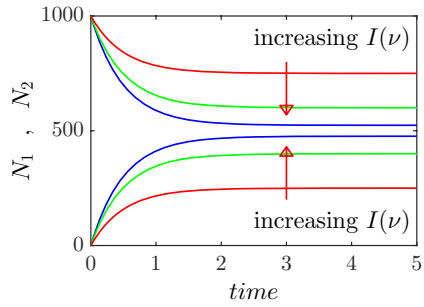

Figure 4.23: (code) Impossibility of achieving inversion in a two-level system.

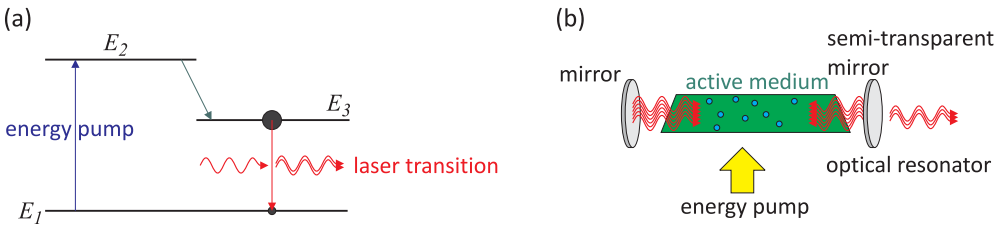

Figure 4.24: Basics of a laser: (a) Level system and (b) principle scheme.

stimulated emission and absorption do not compensate. Spontaneous emission is irreversible and can be incorporated into a three-level system.

The second condition is the existence of a *stimulated emission process*, because we want the amplified photon to be an exact copy of the incident photon.

The third requirement is a *feedback mechanism* that synchronizes the amplification processes by different atoms in a disordered environment, such as a gas. Mirrors are ideal because they increase the effective gain path, i.e. the distance within which inverted atoms can amplify light. Also, the mirrors define the phase of the light wave, since the standing wave formed by the counterpropagating light fields must have nodes on the surfaces of the mirrors.

4.2.1.1 Threshold condition

According to the *Lambert-Beer law* the intensity of a monochromatic laser beam evolves, on its way through a gas of two-level atoms with energies $E_2 - E_1 = \hbar\omega_0$ like,

$$I(z,\nu) = I(0,\nu)e^{-\alpha(\nu)z} \ , \tag{4.43}$$

where the frequency-dependent absorption coefficient,

$$\boxed{\alpha(\nu) = [N_1 - \tfrac{g_1}{g_2}N_2]\sigma(\nu)} \ , \tag{4.44}$$

is determined by the absorption cross section $\sigma(\nu)$ for the transition and by the inversion,

$$\Delta N \equiv \tfrac{g_1}{g_2}N_2 - N_1 \ , \tag{4.45}$$

which determines whether stimulated emission prevails or absorption: For $\Delta N > 0$, the absorption coefficient $\alpha(\nu)$ becomes negative and the incident wave is amplified instead of attenuated [25].

If the active medium is placed between two mirrors [Fig. 4.24(b)], the wave is reflected back and forth, and traverses the amplifying medium many times, which increases the total amplification. With the length L of the active medium the total gain factor per single round-trip without losses is,

$$G(\nu) = \frac{I(\nu, 2L)}{I(\nu, 0)} = e^{-2\alpha(\nu)L} \ . \tag{4.46}$$

A mirror with reflectivity R reflects only the fraction R of the incident intensity. The wave therefore suffers at each reflection a fractional reflection loss of $(1 - R)$. Furthermore, absorption in the windows of the cell containing the active medium, diffraction by apertures, and scattering due to dust particles in the beam path or due to imperfect surfaces introduce additional losses. When we summarize all these losses by a loss coefficient γ, which gives the fractional energy loss $\Delta W/W$ per round-trip time T, the intensity I decreases without an active medium per round-trip as,

$$I(2d, \nu) = I(0, \nu)e^{-\gamma} \ . \tag{4.47}$$

Including the amplification by the active medium with length L, we obtain for the intensity after a single round-trip through the resonator with length d, which may be larger than L:

$$I(2d, \nu) = I(0, \nu)e^{-2\alpha(\nu)L-\gamma} \ . \tag{4.48}$$

The wave is amplified if the gain overcomes the losses per round-trip. This implies that,

$$-2L\alpha(\nu) = 2L\Delta N\sigma(\nu) > \gamma \ , \tag{4.49}$$

which yields the threshold condition for the population difference,

$$\Delta N > \Delta N_{thr} = \frac{\gamma}{2L\sigma(\nu)} \ . \tag{4.50}$$

If the inverted population difference ΔN of the active medium is larger than ΔN_{thr}, a wave that is reflected back and forth between the mirrors will be amplified in spite of losses, therefore its intensity will increase.

The wave is initiated by spontaneous emission from the excited atoms in the active medium. Those spontaneously emitted photons that travel into the right direction (namely, parallel to the resonator axis) have the longest path through the active medium and therefore the greater chance of creating new photons by induced emission. Above the threshold they induce a photon avalanche, which grows until the depletion of the population inversion by stimulated emission just compensates the repopulation by the pump. Under steady-state conditions the inversion decreases to the threshold value ΔN_{thr}, the saturated net gain is zero, and the laser intensity limits itself to a finite value I_L. This laser intensity is determined by the pump power, the losses γ, and the gain coefficient $\alpha(\nu)$.

The frequency dependence of the gain coefficient $\alpha(\nu)$ is related to the line profile $g(\nu - \nu_0)$ of the amplifying transition. Without saturation effects (i.e. for small

intensities), $\alpha(\nu)$ directly reflects this line shape, for homogeneous as well as for inhomogeneous profiles. According to (4.44) and we obtain with the Einstein coefficient B_{ik},

$$\alpha(\nu) = \Delta N \sigma(\nu) = -\Delta N (h\nu/c) B_{12}(\nu - \nu_0) \ , \tag{4.51}$$

which shows that the amplification is largest at the line center ν_0. For high intensities, saturation of the inversion occurs, which is different for homogeneous and for inhomogeneous line profiles.

The loss factor γ also depends on the frequency ν because the resonator losses are strongly dependent on ν. The frequency spectrum of the laser therefore depends on a number of parameters.

4.2.1.2 Applications of lasers in industry and fundamental research

Among their many applications, lasers are nowadays used in compact disc players, laser printers, and bar code scanners, optical fibers and optical communication, laser surgery and skin treatments, welding, cutting and machining, military devices, distance and velocity measurements, projectors, laser pointers, etc..

In fundamental research (in particular on atomic gases, metamaterials, etc.), the laser plays elementary roles in the areas of photonics, quantum computers, metrology, frequency combs, and atomic clocks (laser-based clocks are up to 1000 times more stable than the best state-of-the-art microwave clocks).

We all know that light is a wave. With the invention of the laser we found a process and a device to make this light coherent. On the other hand, since de Broglie's assertion we know that *matter is a wave, as well.* Is it conceivable to construct a matter laser? Yes, it is! The first coherent matter wave was in fact observed in 1995. This state of matter, also called Bose-Einstein condensate, was predicted by Bose and Einstein in 1924. To create a Bose-Einstein condensate, we need, similarly to the laser, that the matter waves interfere constructively in a way that they amplify each other. For this, the Broglie wavelength of the particles, which constitute the matter, must be longer than the distance between them. Assuming a typical average distance on the order of μm, this corresponds to an average velocity of the particles of mm/s or a temperature of some 100 nK.

4.2.2 HeNe laser

HeNe lasers are gas lasers, whose gain medium consists of a mixture of 90% helium and 10% neon at a total pressure of about 1 Torr excited by a small electrical discharge. The most widely used transition wavelength is at 632.8 nm.

Fig. 4.25(a) shows the principle scheme of a commercial HeNe laser. The distance between the high-reflecting mirror (R_{hr}) and the output coupler (R_{oc}) determines the free spectral range δ_{fsr}. Typically, a HeNe laser operates on two or three longitudinal modes separated by δ_{fsr}. As illustrated in Fig. 4.25(b), the numbers of lasing modes above threshold depends on the ratio of gain-to-loss. Fig. 4.25(c) shows the optical pumping scheme to reach inversion on three of the lasing transitions at 632.8 nm, 1.15 μm, and 3.39 μm.

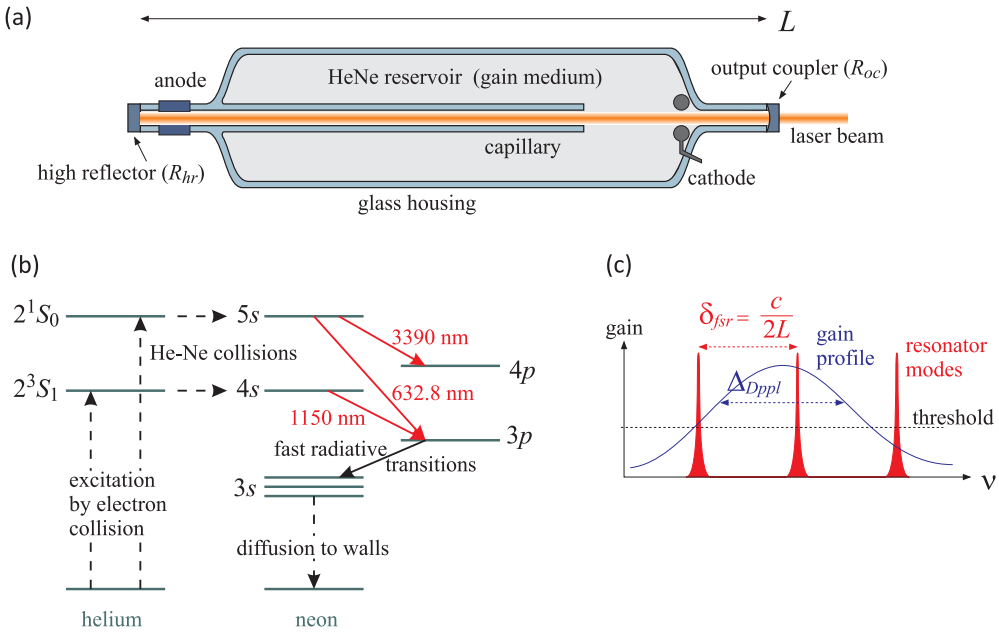

Figure 4.25: (a) Construction scheme of a HeNe laser. (b) Gain and emission profile. (c) Optical pumping scheme.

4.2.3 Diode laser

A laser diode is electrically a *pin*-diode. The active region of the laser diode is in the intrinsic (i) region, and the carriers (electrons and holes) are pumped into that depletion region from the n- and p-doped regions respectively. The depletion region, devoid of any charge carriers, forms as a result of the difference in electrical potential between n- and p-type semiconductors wherever they are in physical contact. Unlike a regular diode, the goal for a laser diode is to recombine all carriers in the i region, and produce light.

Figure 4.26: (Left) Laser diode with protective housing removed, e.g. using a can opener. (Right) Laser diode collimator.

4.2.3.1 Generation of light

Electrons and holes present in the same region may recombine or 'annihilate' by spontaneous emission of photons with energy equal to the difference between the electron's original state and hole's state (see Fig. 3.10). This is in contrast to a conventional semiconductor junction diode, where the energy released from the recombination is carried away as phonons, i.e. lattice vibrations. Spontaneous emission below the lasing threshold is the operating mode of an LED. While spontaneous emission is necessary to initiate laser oscillation, it contributes to reduce the efficiency of a laser operating above threshold.

One condition for lasing is that, in the absence of stimulated emission, electrons and holes may coexist in proximity to one another without recombining immediately. For typical diode laser materials the 'upper-state lifetime' or 'recombination time' is on the order of a nanosecond. A nearby photon with energy equal to the recombination energy can cause recombination by stimulated emission. This generates another photon of the same frequency, polarization, and phase, traveling in the same direction as the first photon. In this way stimulated emission will cause gain for an optical wave in the injection region, and the gain increases as the number of electrons and holes injected across the junction increases.

4.2.3.2 Optical cavity and laser modes

As in other lasers, the gain region needs to be surrounded by an optical cavity providing optical feedback. In its simplest form, a laser diode is made in the shape of a narrow optical waveguide on a the surface of a crystal. The two ends of the crystal are cleaved to form perfectly smooth, parallel edges, forming a Fabry-Pérot resonator. Emitted photons will travel along the waveguide, be amplified by stimulated emission and reflected several times from each end face before exiting. If the losses due to absorption and incomplete reflection from the end facets are smaller than the gain, the diode begins to 'lase'.

Important properties of laser diodes are determined by the geometry of the optical cavity. If the waveguide is thick compared to the wavelength of the light, it can support higher-order transverse optical modes. The laser is then called 'multi-mode'. These transversely multi-mode lasers are adequate for application where high power is needed, for example, in printing, activating chemicals, or pumping other types of lasers.

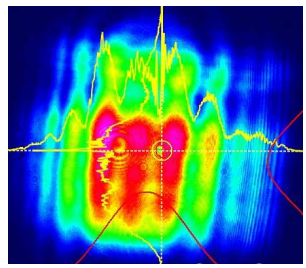

Figure 4.27: Typical beam profile of a multimode laser diode (Thorlabs, L450P1600MM.

For applications requesting small focused beams the waveguide must be made narrow, on the order of the optical wavelength, such that only a single transverse mode is supported, and one ends up with a diffraction-limited beam. Such single spatial mode devices are used for optical storage, laser pointers, and fiber optics. Note that these lasers may still support multiple longitudinal modes, and thus can lase simultaneously at multiple wavelengths. The wavelength emitted is a function of the band-gap of the semiconductor material and the modes of the optical cavity. In general, the maximum gain will occur for photons with energy slightly above the band-gap energy, and the modes nearest the peak of the gain curve will lase most strongly. The width of the gain curve will determine the number of additional 'side modes' that may also lase, depending on the operating conditions. Single spatial mode lasers that can support multiple longitudinal modes are called Fabry-Pérot (FP) lasers. A FP laser will lase at multiple cavity modes within the gain bandwidth of the lasing medium. The number of lasing modes in an FP laser is usually unstable, and can fluctuate due to changes in current or temperature.

Single spatial mode diode lasers can be designed so as to operate on a single longitudinal mode. These single frequency diode lasers exhibit a high degree of stability, and are used in spectroscopy and metrology, and as frequency references. Single frequency diode lasers are classed as either distributed feedback (DFB) lasers or distributed Bragg reflector (DBR) lasers.

Due to diffraction, the beam diverges (expands) rapidly after leaving the chip, typically at 30 degrees vertically by 10 degrees laterally. A lens must be used in order to form a collimated beam like that produced by a laser pointer. If a circular beam is required, cylindrical lenses and other optics are used. For single spatial mode lasers, using symmetrical lenses, the collimated beam ends up being elliptical in shape, due to the difference in the vertical and lateral divergences.

4.2.3.3 Distributed Bragg reflector lasers and distributed feedback lasers

The simple diode described above has been heavily modified in recent years to accommodate modern technology, resulting in a variety of types of laser diodes. One example is the distributed Bragg reflector laser (DBR). It consists of a monolithic single frequency laser diode, characterized by an optical cavity consisting of an electrically or optically pumped gain region between two mirrors to provide feedback. One of the mirrors is a broadband reflector and the other mirror is wavelength selective so that gain is favored on a single longitudinal mode, resulting in lasing at a single resonant frequency. The broadband mirror is usually coated with a low reflectivity coating to allow emission. The wavelength selective mirror is a periodically structured diffraction grating with high reflectivity. The diffraction grating is etched into the semiconductor within a non-pumped, or passive region of the cavity.

A distributed feedback laser (DFB) is a monolithic single frequency laser diode with a diffraction grating etched close to the *pn*-junction of the diode aiming at stabilizing the lasing wavelength. This grating acts like an optical filter, causing a single wavelength to be fed back to the gain region and lase. Since the grating provides the feedback that is required for lasing, reflection from the facets is not required. Thus, at least one facet of a DFB is anti-reflection coated. The DFB laser has a stable wavelength that is set during manufacturing by the pitch of the grating,

and can only be tuned slightly with temperature. DFB lasers are widely used in optical communication applications, where a precise and stable wavelength is critical.

4.2.3.4 ECDL

An *extended-cavity diode laser* (*ECDL*) is an optical setup based on a laser diode chip, which typically has one end anti-reflection (AR) coated, and the laser resonator is completed with a collimating lens and a mirror, as shown in Fig. 4.28(a). The extended external laser resonator introduces various new features and options: Compared to a standard laser diode, the longer resonator increases the damping time of the intracavity light according to Eq. (4.29), and thus allows for lower phase noise and a smaller emission linewidth (in single-frequency operation). Furthermore, it opens the way for inserting frequency-selective optical components into the extended laser resonator, such as narrow-band Fabry-Pérot etalons or diffraction gratings, which can further *reduce the linewidth* and even allow to *tune and control the frequency* of the laser.

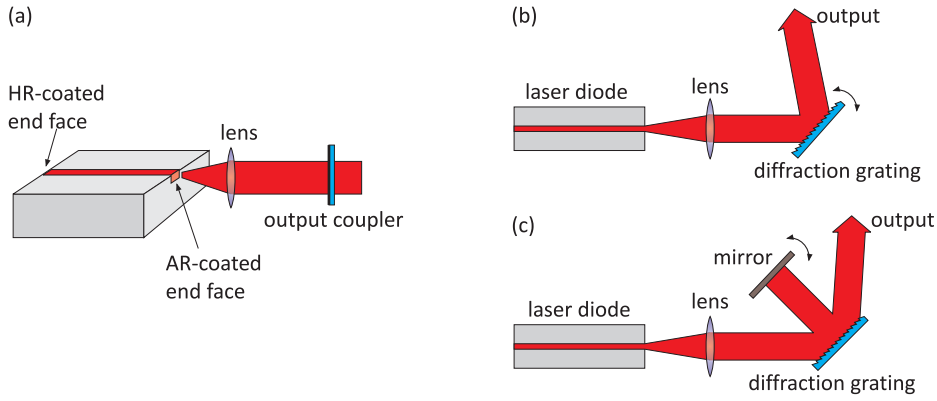

Figure 4.28: (a) ECDL with an AR-coated laser diode and an external mirror. (b) Littrow configuration. (c) Littmann configuration.

Tunable ECDLs based on diffraction grating as the wavelength-selective element are also called grating-stabilized diode lasers. The common Littrow configuration Fig. 4.28(b) generates optical feedback to the laser diode chip by retro-reflecting the first-order diffracted beam from the grating. The emission wavelength can be tuned by slightly tilting the diffraction grating. A disadvantage of this configuration is, that the tilt also changes the direction of the output beam, which is inconvenient for many applications.

In the Littman-Metcalf configuration Fig. 4.28(c), the grating angle is held fixed, and an additional mirror is used to reflect the first-order beam back into the laser diode. The wavelength can be tuned by rotating that mirror. This configuration offers a fixed direction of the output beam, and also tends to exhibit a smaller linewidth, as the wavelength selectivity is stronger, because the wavelength-dependent diffraction occurs twice per resonator round trip. A disadvantage is that the zero-order reflection of the beam reflected by the tuning mirror is lost, so that the output power is lower than that of a Littrow laser.

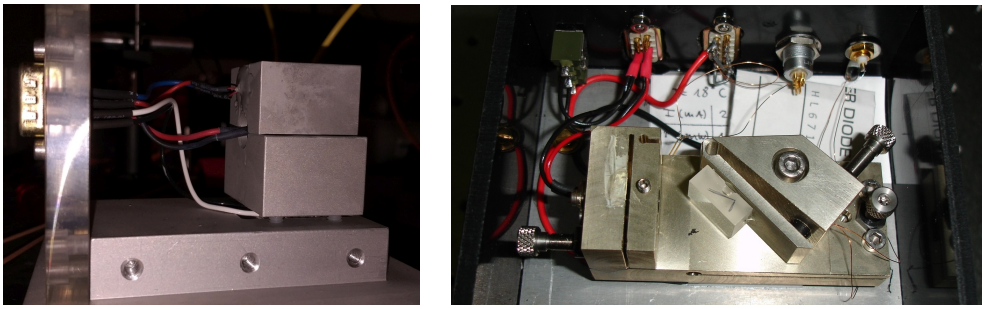

Figure 4.29: (Left) Side view of a 'free-running' laser diode mounted in a collimator (Thorlabs, LT110P-B) clamped in an aluminum block cooled by a Peltier element (Thorlabs, TEC3-6) and whose temperature is measured by a thermistor (Thorlabs, TH10K). (Right) Top view of a home-built ECDL laser in Littrow configuration. The diode collimator is clamped into the left mount. a holographic grating (Newport, 10HG2000-475-1) is glued to the right mount, whose angle can be adjusted mechanically and via a piezo. The whole setup is cooled by a Peltier element mounted on the bottom of the base plate.

New concepts have recently become popular, such as the so-called *cat-eye laser* [7, 36, 10], where the frequency-selective element is an extremely narrow-band (0.3 nm) optical filter [4].

By adjusting the tilt angle of a grating or a narrow-band filter by means of a piezo an extremely fine tuning of the emission frequency is possible, while coarse tuning of the frequency over a range of several nanometers is typically achieved by changing the temperature and the laser current. Typical linewidths of free-running ECDLs are well below 5 MHz. Controlling the laser temperature, current, and piezo voltage by active feedback circuits (e.g. within a Pound-Drever-Hall servo electronics) emission bandwidths in the milliHertz range have been achieved, which corresponds to quality factors of the laser oscillator of up to 10^{18}.

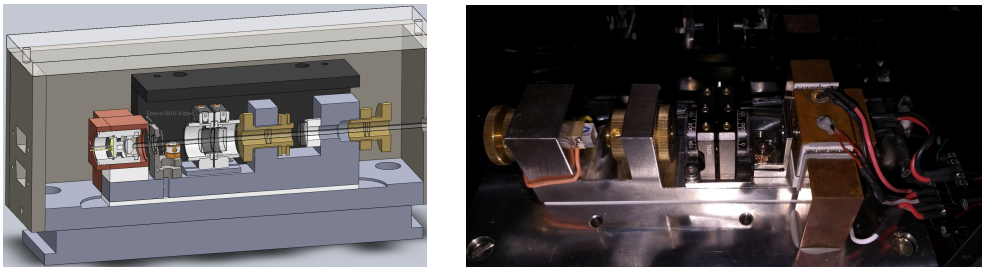

Figure 4.30: (Left) Construction plan of a home-built ECDL lasers in cat-eye configuration. (Right) Side view of the cat-eye laser.

In comparison to other laser types, a *diode laser* exhibits, the advantage of a very small size and a compact design. They are, in general, easy to handle and can be

[4] Available from Semrock or Laseroptik.

controlled conveniently via current and temperature. However, they also have the disadvantage of a large beam divergence and a broad emission spectrum. The beam divergence can be compensated by a collimation optics in front of the laser diode.

The temperature has an impact on the band structure of the *pn*-transition of the laser diode and hence on the frequency. Therefore, it is stabilized via a Peltier element, which is mounted underneath the laser diode holder. The degree of freedom is used for tuning the laser frequency in wide steps.

4.2.3.5 Pulsed diode lasers

Diode lasers can be used for generating ultrashort pulses either with various techniques of mode locking or with gain switching. Typically, pulses with durations between 0.5 and 5 ps and pulse repetition rates between 1 GHz and hundreds of giga-Hertz are generated with mode locking. In extreme cases, the repetition rate can even be above 1 THz. The main application of ultrafast diode lasers is in optical fiber communications systems, where such lasers function as pulse sources of fast data transmitters or for all-optical signal processing.

Common techniques for mode locking of diode lasers are active ore passive mode locking. Active mode locking can be accomplished with an optical modulator in the laser resonator. This is usually either an electro-absorption modulator in the form of an unpumped region with some modulated voltage, or an amplifying section where the drive current is modulated. Passive mode locking relies on a saturable absorber in the resonator. This can simply be an unpumped section of the device. It is common to apply an electrical bias for adjusting the absorber properties. However, the recovery time of that kind of absorber is fairly long. Shorter recovery times are achieved e.g. by implanting nitrogen (N^+ or N_2^+) ions from one facet. This introduces crystal defects, where carriers can recombine. The absorber is often placed at a resonator end, but it can also be placed somewhere within the resonator so that different pulses can meet in the absorber (colliding pulse mode locking).

For pulse repetition rates roughly below 10 GHz, an external cavity setup is usually required, as a monolithic device would become too long. The extended cavity may be an ECDL setup. Another technical approach is to incorporate the semiconductor chip into a ring laser resonator made of optical single-mode fiber. In the latter case, the resonator is typically much longer, and allows the use of fiber-optic components. The semiconductor device may then be a fiber-coupled semiconductor optical amplifier (SOA).

External-cavity lasers have various advantages: The pulse repetition rate can be chosen in a wide range, and can easily be tuned e.g. by moving the end mirror, or with a fiber resonator by stretching a piece of fiber with a piezo transducer. It is possible to insert an optical filter for fixing the emission wavelength, or use a diffraction grating as the end mirror (Littrow configuration; see the article on external-cavity diode lasers). Even for higher pulse repetition rates, where harmonic mode locking is required, external-cavity devices can be advantageous, because they have a potential for lower laser noise, e.g. in the form of timing jitter. Therefore, mode-locked external-cavity diode lasers sometimes compete with mode-locked fiber lasers in areas where monolithic laser diodes would not be suitable. On the other hand, a monolithic setup with fundamental mode locking can be very compact, much cheaper to manufacture,

and can exhibit very robust pulse emission.

On the other hand, mode-locked diode lasers are subject to various limitations, which do not allow them to reach the full performance potential of, e.g., mode-locked fiber lasers: The pulse energy is fairly limited often far below 1 pJ. Average output powers are often below 1 mW. Due to the short upper-state lifetime, ultrafast semiconductor lasers are generally not suitable for lower repetition rates of e.g. well below 1 GHz, except with synchronous pumping. Although the gain bandwidth of semiconductors would be compatible with pulse durations of a few tens of femtoseconds, the pulse durations achieved are usually much longer at least hundreds of femtoseconds, and often picoseconds. The pulse formation dynamics are relatively complicated, e.g. due to nonlinear phase changes associated with gain saturation, and difficult to optimize. The pulse quality is normally not as good as e.g. for mode-locked fiber lasers. In particular, there are often additional satellite pulses, caused e.g. by imperfections of the anti-reflection coating. Also, the pulses are often chirped, i.e. they are not bandwidth-limited. The timing jitter and the noise of other pulse parameters are higher than for other mode-locked lasers. This is partly a consequence of the low power level.

4.2.3.6 Tapered amplifiers and injection locking

Other ways to amplify a the power of a laser without altering its coherence properties are using a *tapered amplifier* or via *injection locking* also called *master-slave locking* [16, 52] (see Fig. 4.31).

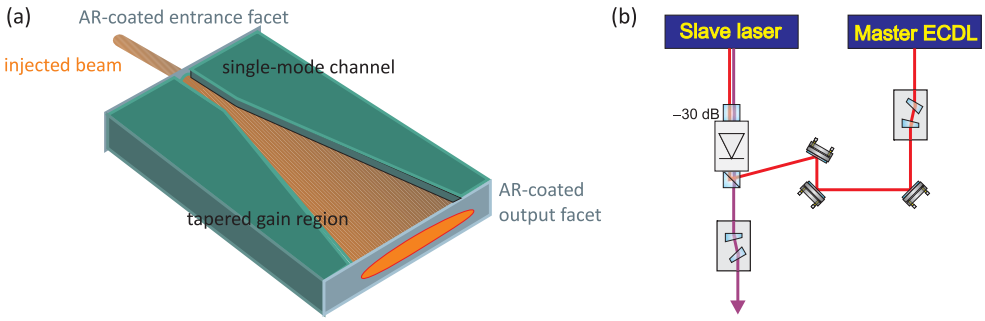

Figure 4.31: (a) Tapered amplifiers are available e.g. from Eagleyard. (b) Principle of injection locking.

The description presented here uses semi-classical laser rate equations [51]. Assuming that the master and the slave laser field are given by, respectively,

$$E_{inj} = A_{inj} e^{-\imath\omega_{inj}t} e^{\imath\phi_{inj}(t)} \quad \text{and} \quad E = A e^{-\imath\omega_s t} e^{\imath\phi_s(t)} \,, \tag{4.52}$$

The phase difference between the both fields is denoted by $\phi(t) = \phi_s(t) - \phi_m(t)$. Now, Considering the semi-classical laser rate equations we can describe the impact of the

master laser field in the slave laser,

$$\begin{aligned}\frac{dA(t)}{dt} &= \frac{1}{2}g[N(t)-N_{th}]A(t)+\kappa A_{inj}\cos\phi(t) \\ \frac{d\phi(t)}{dt} &= \frac{\alpha}{2}[N(t)-N_{th}]-\kappa\frac{A_{inj}}{A(t)}\sin\phi(t)-\Delta\omega \\ \frac{dN(t)}{dt} &= J-\gamma_N N(t)-[\gamma_p+g[N(t)-N_{th}]A(t)^2\ ,\end{aligned} \tag{4.53}$$

where $A(t)$ is the field amplitude normalized as $A^2(t)=S(t)$, and $S(t)$ is the photon number. $N(t)$ is the number of carriers in the slave laser, and the other parameters are g laser gain coefficient, N_{th} threshold carrier number, κ coupling coefficient, α linewidth enhancement factor, γ_p photon decay rate, N carrier recombination rate, J pump current normalized by electron charge, $\Delta\omega$ frequency difference between the master and the free running slave $\omega_m-\omega_s$. The parameter κ describes the rate at which the photons of the master laser enter into the slave laser cavity and is given in terms of the cavity quality factor,

$$\kappa=\frac{\omega_s}{2Q}\ . \tag{4.54}$$

From the steady state solutions of above equations, we can obtain the frequency locking range,

$$-\kappa\sqrt{(1+\alpha^2)}\sqrt{\frac{P_{inj}}{P_s}}<\Delta\omega<\kappa\sqrt{\frac{P_{inj}}{P_s}}\ , \tag{4.55}$$

where P_{inj}/P_s is the master laser fraction power used for the injection locking and P_s is the power of slave laser. From equation 4.25 we can see that the locking range is determined by the amplitude ratio between the fields and by the cavity quality factor since $\kappa\propto Q^{-1}$. Therefore, lasers with low Q are easier to lock. On the other hand, this leads to increased laser linewidth that reduces the phase noise performance of the injection locking systems. For higher injection ratio P_{inj}/P_s also results in a large locking range, which also makes the lock easier to achieve.

4.2.4 Exercises

4.2.4.1 Ex: Conventional light sources and lasers

Compare the properties of an incandescent light and a laser.

4.2.4.2 Ex: Threshold inversion for lasing 1

Calculate the necessary threshold inversion of a gas laser transition at $\lambda=500\,\text{nm}$ with the transition probability $A_{ik}=5{\cdot}10^7\,\text{s}^{-1}$ and a homogeneous linewidth $\Delta\nu_{hom}=20\,\text{MHz}$. The active length is $L=20\,\text{cm}$ and the resonator losses per round-trip are $\gamma=5\%$.

4.2.4.3 Ex: Threshold inversion for lasing 2

A laser medium has a Doppler-broadened gain profile of halfwidth $\delta\nu=2\,\text{GHz}$ and central wavelength $\lambda=633\,\text{nm}$. The homogeneous width is 50 MHz, and the transition

probability $A_{ik} = 10^8\,\mathrm{s}^{-1}$. Assume that one of the resonator modes ($L = 40\,\mathrm{cm}$) coincides with the center frequency ν_0 of the gain profile. What is the threshold inversion for the central mode, and at which inversion does oscillation start on the two adjacent longitudinal modes if the resonator losses are 10%?

4.2.4.4 Ex: Mode pulling in an active resonator

The frequency of a passive resonator mode ($L = 15\,\mathrm{cm}$) lies $0.5\Delta\nu_D$ away from the center of the Gaussian gain profile of a gas laser at $\lambda = 632.8\,\mathrm{nm}$. Estimate the mode pulling if the cavity resonance width is 2 MHz and $\Delta\nu_D = 1\,\mathrm{GHz}$.

4.2.4.5 Ex: Spatial hole-burning

Assume a laser transition with a homogeneous width of 100 MHz, while the inhomogeneous width of the gain profile is 1 GHz. The resonator length is $d = 200\,\mathrm{cm}$ and the active medium with length $L \ll d$ is placed $a = 20\,\mathrm{cm}$ from one end mirror. Estimate the spacing of the spatial hole-burning modes. How many modes can oscillate simultaneously if the unsaturated gain at the line center exceeds the losses by 10%?

4.2.4.6 Ex: Optimizing the transmission of laser output mirrors

Estimate the optimum transmission of the laser output mirror if the unsaturated gain per round trip is 2 and the internal resonator losses are 10%.

4.2.4.7 Ex: Mode selection in a HeNe laser

A HeNe laser with an unsaturated gain of $G(\nu_0) = 1.3$ per round trip at the center of the Gaussian gain profile with halfwidth $\Delta\nu_D = 1.5\,\mathrm{GHz}$ has a resonator length of $d = 50\,\mathrm{cm}$ and total losses of 4%. Single-mode operation at ν_0 is achieved with a coated tilted etalon inside the resonator. Design the optimum combination of etalon thickness and finesse.

4.2.4.8 Ex: Mode hopping in a HeNe laser

A single-mode HeNe laser with resonator length $L = 15\,\mathrm{cm}$ is tuned by moving a resonator mirror mounted on a piezo. Estimate the maximum tuning range before a mode hop will occur, assuming an unsaturated gain of 10% at the line center and resonator losses of 3%. What voltage has to be applied to the piezo (expansion 1 nm/V) for this tuning range?

4.2.4.9 Ex: Mode selection with an intracavity etalon

Mode selection in an argon laser is often accomplished with an intracavity etalon. What is the frequency drift of the transmission maximum
a. for a solid fused quartz etalon with thickness $d = 1\,\mathrm{cm}$ due to a temperature change of 2° C?
b. For an air-space etalon with $d = 1\,\mathrm{cm}$ due to an air pressure change of 4 mbar?
c. Estimate the average time between two mode hopes (cavity length $L = 100\,\mathrm{cm}$) for a temperature drift of 1° C/h or a pressure drift of 2 mbar/h.

4.2.4.10 Ex: Frequency and intensity noise of a laser

A single-mode laser is frequency stabilized onto the slope of the transmission maximum of an external reference Fabry-Perot interferometer made of invar with a free spectral range of 8 GHz. Estimate the frequency stability of the laser
a. against temperature drifts, if the FPI is temperature stabilized within 0.01°C,
b. against acoustic vibrations of the mirror distance L in the FPI with amplitudes of 100 nm.
c. Assume that the intensity fluctuations are compensated to 1% by a difference amplifier. Which frequency fluctuations are still caused by the residual intensity fluctuations, if a FPI with a free spectral range of 10 GHz and a finesse of 50 is used for frequency stabilization at the slope of the FPI transmission peak?

4.2.5 *Experiment: Analyzing the mode structure of a HeNe laser*

Here we will analyze the mode structure of a HeNe laser via (i) an optical spectrum analyzer and (ii) a radiofrequency spectrum analyzer. We will also try to unravel the polarization of the laser light.

1. Couple the light of a HeNe laser simultaneously into an optical spectrum analyzer and a radiofrequency spectrum analyzer. What do you observe when you slightly heat the laser housing? Calculate from your observations the length of the laser cavity.

2. Pass the light through a $\lambda/4$-plate and then through a polarizing beam splitter. What do you observe in the two output ports of the PBS?

4.2.6 *Experiment: Adjusting the threshold of an ECDL laser*

Here we will construct a diode laser in Littmann configuration.

1. Take a laser diode, a Peltier cooler, a thermistor, a piezo transducer, and a diffraction grating. Put everything together.

2. Optimize the threshold. Analyze the emission spectrum with an optical spectrum analyzer.

4.3 Introduction to optical phase and frequency modulation

4.3.1 Acousto-optic modulator

The *acousto-optic modulator AOM* permits fast frequency and amplitude variations of a laser beam. Because it does not incorporate mechanical parts, it works without fatigue. AOMs are used, for instance, in laser printers, where the gray tone of a pixel can be adjusted via the intensity of the laser beam, while its position (rows and

columns) is varied by a rotating mirror and the drum propagating the paper sheet. In quantum optics labs they are frequently used for fast (down to μs) switching on and off, intensity control, and super-fine frequency-tuning of laser beams. The angular deflection of the first-order diffracted beam upon frequency tuning, which is often perceived as an inconvenience, can be circumvented by double-passage through the AOM.

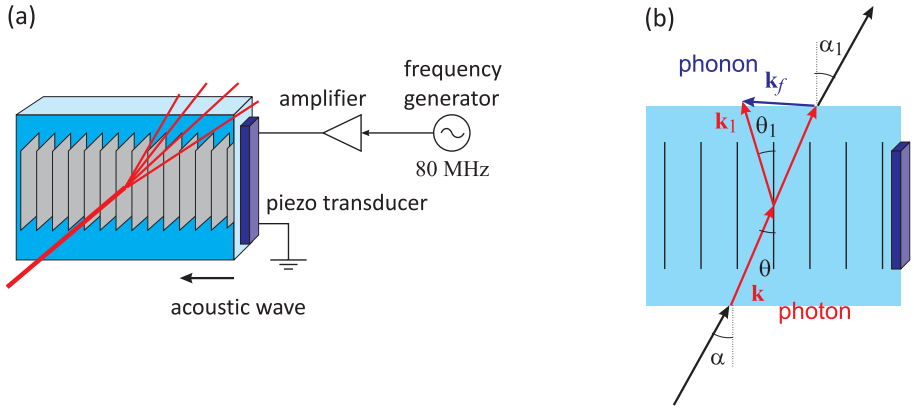

Figure 4.32: (a) Principle of the acousto-optic modulator. (b) Scheme of the diffraction in an acousto-optic modulator: A photon with wavevector k is scattered by a phonon with wavevector k_1 resulting in a photon with wavevector k_f.

The acousto-optic modulator consists of a piece of crystal (or glass) excited by an acoustic wave with frequency f produced by a piezo-electric transducer (see Sec. 4.3.1) mounted perpendicularly to propagation direction of the laser beam. The sound waves propagate through the crystal as density fluctuations periodically changing the refraction index n. The incident light is diffracted through Brillouin scattering at the spatial modulation of the refraction index. In a wave picture, the process can be interpreted as Bragg scattering of a light wave (with its wavelength inside the crystal $\lambda_n = 2\pi/k_n = c/n\nu$) from a density grating. c/n is the propagation velocity of light inside the crystal. Since phonons (with their wavelength $\lambda_f = 2\pi/k_f = c_f/f$, where c_f is the sound velocity in the crystal) are quantized and can only be emitted and absorbed entirely, the frequency of the first-order diffraction is $\nu_1 = \nu + f$. In case of an ideal adjustment of the Bragg angle, the *Bragg condition* results in $\theta_1 = \theta$ (see Fig. 4.32),

$$\sin\theta = \frac{k_f}{2k} = \frac{f\lambda_n}{2c_f} \ . \tag{4.56}$$

Since the laser beam is refracted when it enters the crystal, the relation between the incidence and exit angle is given by *Snell's law*, $\sin\alpha = n\sin\theta$. With this, the Bragg condition can be written,

$$\boxed{\sin\alpha = \frac{f\lambda}{2c_f}} \ . \tag{4.57}$$

The angle between the 0^{th} and the 1^{st} order is, hence, 2α.

In a corpuscular picture, the process can be understood as a *four-wave mixing* (*4WM*) between photons and phonons. The deflection of the laser beam is a consequence of momentum, $\mathbf{k}_1 = \mathbf{k} + \mathbf{k}_f$. The frequency shift corresponds exactly to the Doppler shift induced by the Brillouin scattering (absorption and reemission of a phonon in reverse direction), and we obtain a relationship that is equivalent to the Bragg condition,

$$f = \nu_1 - \nu = 2\nu \frac{c_f \sin\theta}{c/n} \ . \tag{4.58}$$

From the Bragg condition, knowing the deflection angle and the (fixed) frequency shift, we can calculate the sound velocity. A typical value is $c_f \simeq 4200$ m/s [5]

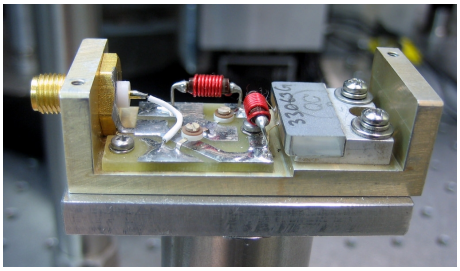

Figure 4.33: Image of an AOM without cover.

An AOM works best (highest diffraction efficiency in to the first Bragg order, which may reach more than 90%) at a specific radiofrequency, which typically is located somewhere in the range $f = 40...800$ MHz, the most common one being 80 MHz. Deviations from this 'center frequency' are possible within a range of typical ±10% of the center frequency.

4.3.2 Electro-optic modulator

An *electro-optic modulator* is an optical device with which, by an applied voltage, the phase, frequency, amplitude or direction of a light beam can be modulated. Modulation bandwidths in the GHz regime are possible. In the simplest case, the EOM consists of a crystal (e.g., lithium niobate), whose refractive index depends on the amplitude of the local electric field. That is, when a lithium niobate crystal is exposed to an electric field the speed of light propagation is reduced. One can thus control the phase of a light beam at the output of a crystal by inserting it into a plate capacitor and applying a voltage. The phase shift of the light depends linearly on the applied voltage.

EOMs are often used to generate sidebands in a monochromatic laser beam. They are also used as *Pockels cell*, i.e., as a voltage-controlled phase-plate. The Pockels

[5] The result (4.58) can be derived from conservations laws for energy $\omega_1 = \omega + \omega_f$ and momentum $\mathbf{k}_1 = \mathbf{k} + \mathbf{k}_f$. Defining $\omega \equiv 2\pi\nu$, $\omega_1 \equiv 2\pi\nu_1$ and $\omega_f \equiv 2\pi f$ we find,

$$\frac{\omega_f^2}{c_f} = \mathbf{k}_f^2 = (\mathbf{k}_1 - \mathbf{k})^2 = k_1^2 + k^2 - 2\mathbf{k}_1 \cdot \mathbf{k} = \frac{\omega_1^2}{c_n^2} + \frac{\omega^2}{c_n^2} - \frac{2\omega\omega_1}{c_n^2}\cos(2\theta) \simeq \frac{4\omega\omega_1}{c_n^2}\sin^2\theta \ .$$

With $\omega_1 \simeq \omega$ we reproduce the result [81, 82].

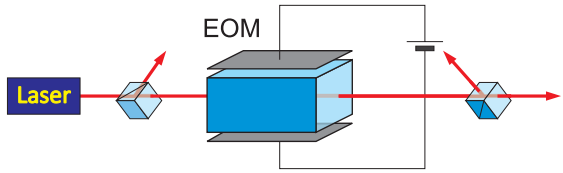

Figure 4.34: Electro optic modulator.

effect produces in a medium a *birefringence*, which depends linearly on the applied electric field. This is in contrast to the *Kerr effect*, in which the birefringence depends in a quadratic form of the electric field.

Suppose the optically inactive axis is x. In this case, the influence of EOM on the polarization of a laser beam is described by

$$\mathcal{M}_{EOM}(\theta) = \begin{pmatrix} 1 & 0 \\ 0 & e^{\imath\theta} \end{pmatrix} . \tag{4.59}$$

For operation as a Pockels cell, the EOM is inserted between two crossed polarizers oriented, e.g., along the x and y axis. The EOM itself is rotated by an angle ϕ,

$$\begin{aligned} \mathcal{M}_{Pockels}(\theta,\phi) &= \begin{pmatrix} 0 & 0 \\ 0 & 1 \end{pmatrix} \begin{pmatrix} \cos\phi & \sin\phi \\ -\sin\phi & \cos\phi \end{pmatrix} \begin{pmatrix} 1 & 0 \\ 0 & e^{\imath\theta} \end{pmatrix} \begin{pmatrix} \cos\phi & -\sin\phi \\ \sin\phi & \cos\phi \end{pmatrix} \begin{pmatrix} 1 & 0 \\ 0 & 0 \end{pmatrix} \\ &= 2\imath e^{\imath\theta/2} \sin\tfrac{\theta}{2} \sin\phi\cos\phi \begin{pmatrix} 0 & 0 \\ 1 & 0 \end{pmatrix} , \end{aligned} \tag{4.60}$$

For $\phi = \pi/4$ we get,

$$\mathcal{M}_{Pockels}(\theta, \tfrac{\pi}{4}) = \imath e^{\imath\theta/2} \sin\tfrac{\theta}{2} \begin{pmatrix} 0 & 0 \\ 1 & 0 \end{pmatrix} . \tag{4.61}$$

That is, an incident beam of light, $\mathbf{E} = E\hat{\mathbf{e}}_x$, linearly polarized in x-direction is rotated into the y-direction and, depending on the phase shift θ, it is completely blocked or transmitted through the Pockels cell [see Fig. 4.35(a)],

$$I_{tr} = I_0 \sin^2\tfrac{\theta}{2} . \tag{4.62}$$

4.3.3 Optical phase modulation

The frequency and the phase of a laser beam can be influenced and modulated similarly to radiofrequency signals. We can therefore use the calculation of Sec. 3.3.1 completely, only changing the carrier frequency to be the frequency of the light: The Fourier expansion of a complex-valued periodic function $s(x)$ into a series is defined as,

$$s_N(x) = \sum_{k=-N}^{N} c_k e^{\imath kx} \qquad \text{where} \qquad c_k = \frac{1}{2\pi}\int_{2\pi} s(x) e^{-\imath kx} dx . \tag{4.63}$$

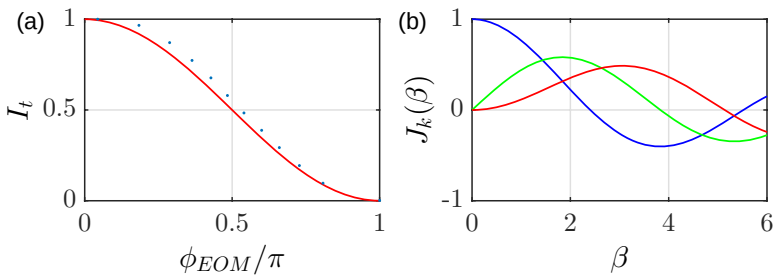

Figure 4.35: (code) (a) Effect of a Pockels cell. The solid line was calculated with the Eq. (4.60), the dotted was measured experimentally. (b) Lowest-order Bessel functions.

Applying this to the modulated phase shift factor $s(\Omega t) = e^{\imath\theta(t)}$ with $\theta(t) \equiv \beta \sin \Omega t$, we get,

$$s_N(\Omega t) = \sum_{k=-\infty}^{\infty} c_k e^{\imath k \Omega t} \qquad \text{where} \qquad c_k = \frac{1}{2\pi} \int_{-\pi}^{\pi} e^{\imath\beta \sin \Omega t} e^{-\imath k \Omega t} d\Omega t \ , \tag{4.64}$$

but the Fourier coefficients are nothing else than the integral definition of the k-th order Bessel function,

$$J_k(\beta) \equiv \frac{1}{2\pi} \int_{-\pi}^{\pi} e^{\imath(\beta \sin \tau - k\tau)} d\tau \ , \tag{4.65}$$

where $J_{-k}(\beta) = -J_k(\beta)$. Hence, we may write the electric field,

$$\boxed{\begin{aligned} E(t) &= e^{\imath[kz - \omega t + \imath\theta(t)]} = e^{\imath(kz-\omega t)} \sum_{k=-\infty}^{\infty} J_k(\beta) e^{\imath k \Omega t} \\ &\simeq J_0(\beta) e^{\imath\omega t} + J_1(\beta) e^{\imath\omega t + \imath\Omega t} + J_{-1}(\beta) e^{\imath\omega t - \imath\Omega t} \end{aligned}} \ . \tag{4.66}$$

For small modulation indices β only the lowest-order Bessel function contribute noticeable amplitudes, as illustrated in Fig. 4.35(b).

The interpretation of this is, that *phase modulation* imprints sidebands onto a monochromatic laser beam. These sidebands are independent modes which can be resolved, e.g. with an optical spectrum analyzer, as illustrated in Fig. 4.36.

Technically the phase can be modulated by means of an electro-optical modulator, as shown in Fig. 4.37(b). Alternatively, one may apply a periodic modulation of the current which controls a diode laser, as shown in Fig. 4.37(a), which can be done e.g. by inductive coupling using a *bias-T*.

From (4.66) we immediately see that phase modulation remains invisible for a photodetector measuring $|E(t)|^2$. Imagine, however, that the light passes through a frequency-selective absorber, as illustrated in Fig. 4.37(b), such that the sidebands suffer unequal losses. Then the photodetector will record (apart from a constant offset) a signal oscillating at the frequency Ω,

$$\begin{aligned} |E(t)|^2 &= \left| J_0(\beta) e^{\imath\omega t} + a J_1(\beta) e^{\imath\omega t + \imath\Omega t} + b J_{-1}(\beta) e^{\imath\omega t - \imath\Omega t} \right|^2 \\ &= J_0(\beta)^2 + (a+b) J_1(\beta)^2 + (a-b) J_0(\beta) J_1(\beta) 2 \cos \Omega t + \dots \ . \end{aligned} \tag{4.67}$$

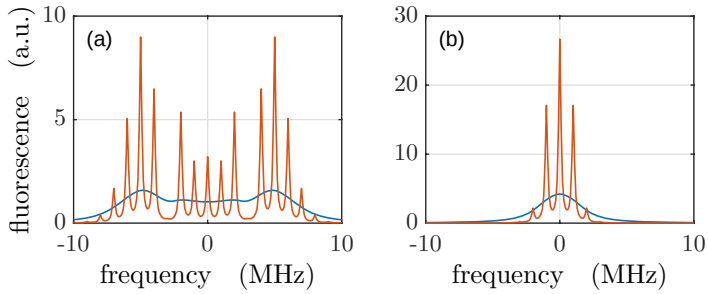

Figure 4.36: (code) Phase modulation sidebands with high (left) and low (right) modulation index resolved by a narrow (red) or broad (blue) filter.

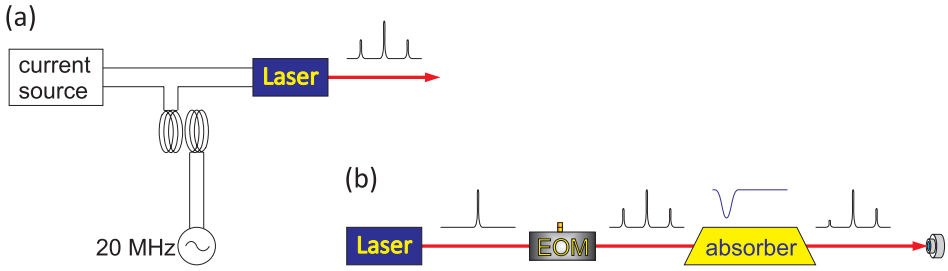

Figure 4.37: (a) Scheme for phase modulation of a diode laser by modulating the drive current. (b) Phase modulation with an external EOM followed by frequency-selective absorption of the lower sideband.

This idea is at the heart of powerful spectroscopic techniques, such as *frequency modulation spectroscopy*, *modulation transfer spectroscopy*, and the *Pound-Drever-Hall* frequency stabilization technique.

4.3.4 Exercises

4.3.4.1 Ex: Response time of an AOM

A beam of light at 689 nm focused to a waist of 100 µm passes through the crystal of an 80 MHz AOM, characterized by a sound velocity of $c_s = 4200\,\mathrm{m/s}$.
a. By how much the first diffraction order is deflected by the AOM? Regarding the beam divergence of the Gaussian beam, will it be possible to spatially separate the diffraction orders?
b. An experimentalist ramps the driving frequency between 70 and 90 MHz by means of a voltage-controlled oscillator. What is the range of diffraction angles covered?
c. Estimating the response time of the AOM by the time that the traveling sound wave needs to cover a distance corresponding to the focus of the light beam, how fast can the experimentalist switch off the light beam by suddenly interrupting the driving signal? What is the modulation bandwidth of the AOM?
d. The light beam passes through the AOM at a distance of $d = 2\,\mathrm{mm}$ from the piezo transducer generating the sound wave. How will this fact limit response time?

4.3.4.2 Ex: Intensity stabilization with a Pockels cell

Assume that the output power of a laser shows random fluctuations of about 5%. Intensity stabilization is accomplished by a Pockels cell with a halfwave voltage of 600 V. Estimate the ac output voltage of the amplifier driving the Pockels cell that is necessary to stabilize the transmitted intensity if the Pockels cell is operated around the maximum slope of the transmission curve.

4.3.4.3 Ex: Generating sidebands with an EOM

An EOM (e.g. Thorlabs, EO-PM-NR-C1) characterized by a half-wave voltage of $U_{hwv} = 230\,\mathrm{V}$ at 689 nm is to be used to generate optical sidebands at 20 MHz.
a. Estimate numerically, how much voltage amplitude at what frequency a frequency generator must provide in order to generate optical sidebands having half the light power as the carrier?
b. How high must the finesse of a 5 cm confocal Fabry-Pérot spectrum analyzer be in order to resolve the sidebands.

4.3.4.4 Ex: Reflection of a phase-modulated signal from an optical cavity

A phase-modulated light beam (modulation frequency $f = 20\,\mathrm{MHz}$) is reflected from an optical cavity and recorded by a fast photodetector, whose bandwidth is larger than f. Using the Airy formulae for the electric field of a light beam reflected from a cavity (4.27) calculate the reflection spectrum, that is, the intensity of reflected light as a function of detuning $\Delta = \omega - \omega_c$, where ω is the frequency of the light and ω_c a resonant frequency of the cavity. What frequency components does the photodetector signal contain.

4.3.5 *Experiment: Characterizing an AOM*

Fig. 4.38 illustrates the setup, use, and test of an AOM. It is recommended familiarizing with the operation principle of a *voltage-controlled oscillator* (*VCO*) (see Sec. 3.3.1) and a voltage-controlled *variable attenuator*. We will also learn how to use a spectrum analyzer [6].

1. Optimize a diffraction efficiency of the AOM. What are the impacts of the Bragg angle, the radiofrequency power, and the laser beam diameter.

2. Measure the deflection angle as a function of the applied radiofrequency. Based on this result, calculate the sound velocity in the crystal.

3. Measure the diffraction efficiency as a function of the applied radiofrequency power at a fixed Bragg angle. Repeat the measurement optimizing the Bragg angle for every value of the radiofrequency.

4. Reduce the radiofrequency power using the variable voltage-controlled attenuator. Determine the diffraction efficiency as a function of radiofrequency power.

[6] Data sheet for the VCO see appendix Fig. 7.16,
data sheet for the AOM see appendix Fig. 7.20

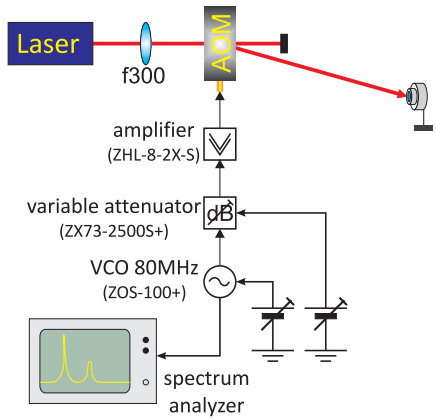

Figure 4.38: Setup for testing an acousto-optic modulator.

See Fig. 4.39.

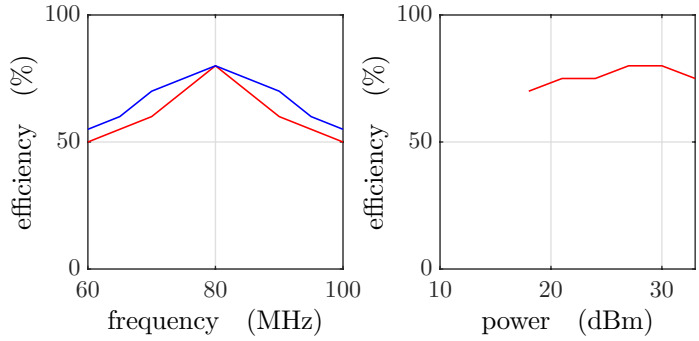

Figure 4.39: Example of measured efficiency curves.

4.3.6 *Experiment: EOM in a Mach-Zehnder interferometer*

Here we will learn to operate an EOM as Pockels cell and as phase modulator.

1. Align a laser beam through an electro-optic modulator. Supply a voltage between 0 V and 500 V to the EOM. Test its operation by beating the ordinary with the extraordinary beam. Modulate the supply voltage at a low frequency.
2. Set up a Mach-Zehnder interferometer by phase-matching the exit beam of the EOM with a part of the input beam.
3. The interferometer provides a mean to convert a phase modulation into an amplitude modulation. Describe this feature theoretically using the Eqs. (3.12) and (3.13).
4. Use the EOM as a Pockels cell. Rotate the EOM by 45° around the optical axis. Probe the polarization of the outgoing beam with a polarization filter.

5. Modulate the EOM and show that the light acquires sidebands.

4.3.7 *Experiment: Creating sidebands with an EOM*

EOMs can be used to generate optical sidebands [7].

1. Apply the required voltages to a VCO (MiniCircuits, ZOS100), until it generates a variable frequency between 40 and 60 MHz. Attenuate the power with a variable attenuator up to −20 dBm. Check the amplitude and frequency with a spectrum analyzer.
2. Add a bias-T to the power supply of a laser diode. Observe the transmission spectrum of a Fabry-Pérot cavity for various frequencies and modulation amplitudes. Determine the modulation index. Use the known distance of the sidebands to estimate the finesse of the Fabry-Pérot cavity.

4.4 Radiofrequency techniques and the transfer of information

It often happens that information is coded within a frequency band corresponding to wavelengths which are not easily transported to other locations. For example, audio frequencies (speech or music), ones they are converted to electromagnetic vibrations, correspond to wavelengths of hundreds of kilometers. Such waves are very difficult to radiate and are subject to diffraction.

For this reason, audio frequencies are often used to *modulate* so-called carriers, which in turn are chosen in frequency ranges which are easy to radiate by antennas. This is the basic idea of the radio, where the carrier frequencies are typically chosen in the MHz regime. But information can as well be encoded into laser beams, as illustrated in Fig. 4.40.

4.4.1 Measurement of a frequency beat

Interferometry is always based on the splitting and recombination of a wave, e.g., a laser beam or a matter wave. The recombination of laser beams is always a little technical challenge, as it requires a perfect phase matching of the Gaussian laser modes. Let us consider two plane waves $\mathcal{E}_1 = Ae^{\imath\omega_1 t}$ and $\mathcal{E}_2 = Ae^{\imath\omega_2 t}$ impinging on a photodiode. We suppose that they are phase-matched, such that their wavevectors are parallel. The photodiode then generates a *beat signal*,

$$\boxed{I = |\mathcal{E}_1 + \mathcal{E}_2|^2 = AB[2 + 2\cos(\omega_1 - \omega_2)t]} \,. \tag{4.68}$$

In practice, laser beams are usually not plane waves, but have a finite diameter and radius of curvature. In order to get a high contrast signal, a good phase-matching of the beams is important in order to obtain a strong photodiode signal.

[7] Datasheet for the VCO see appendix Fig. 7.16,
data sheet for the power divider see appendix Fig. 7.18,
data sheet for the mixer see appendix Fig. 7.19

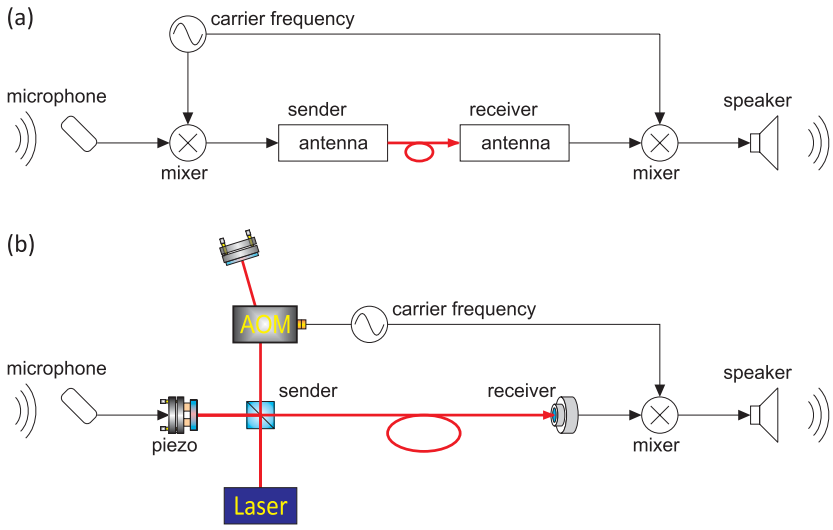

Figure 4.40: Analogy between radio transmission (a) and heterodyne techniques with a laser (b).

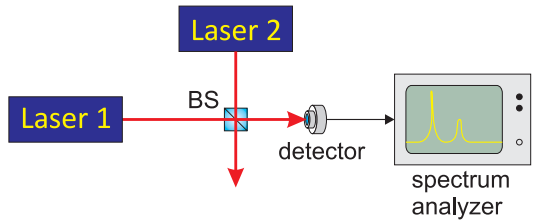

Figure 4.41: Principle of a beat frequency measurement.

4.4.2 Homodyne method

For the *homodyne method* the field amplitude of a laser beam, E_i, with frequency, $\omega = ck$, is divided by a beam splitter (reflectivity $R = |\eta|^2 \simeq 50\%$) into a reference beam (reflection at an optically dilute medium) and a probe beam, exactly as we have done for the Michelson interferometer in Sec. 4.1.3, when we obtained the formula (4.16) [8],

$$I \propto 1 + \cos[k(L_t - L_r)] \; . \tag{4.69}$$

However, we will now modulate the path length of one interferometer arm, e.g. using an EOM, $L_r = L_r(t)$. The modulation can, but does not need to be sinusoidal. In fact it may be an arbitrary radiofrequency signal, e.g. generated by acoustic sound. Restricting to small modulation amplitudes, $kL_r \ll \pi$, and choosing the length of the interferometer arms such that,

$$\boxed{I(t) \propto \sin kL_r \simeq kL_r(t)} \; , \tag{4.70}$$

[8] Here, we call $L_{t,r}$ the total length of the interferometer arm (back and forth for Michelson, one-way for Mach-Zehnder).

we see, that the photodetector signal will reproduce the modulation signal. In other words, we encoded information on a laser beam, which carries it (e.g. through an optical fiber) to another place.

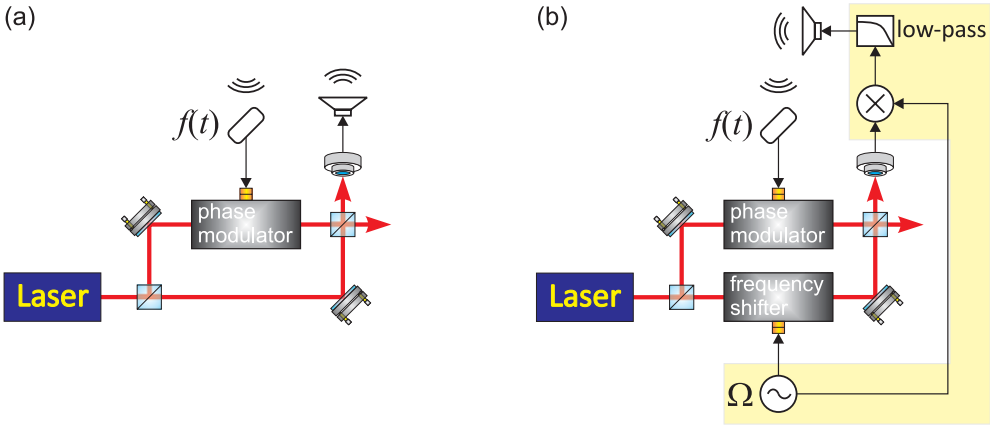

Figure 4.42: Principle scheme of the (a) homodyning and (b) heterodyning technique at the example of a Mach-Zehnder interferometer. The components in the yellow area of (b) constitute a Lock-In amplifier.

4.4.3 Heterodyne method

The *heterodyne method* is similar to the homodyne one, except that the probe beam is frequency-shifted (e.g., by the passage through an AOM operated at frequency Ω),

$$\mathcal{E}'_t = \mathcal{E}_t e^{\imath k L_t + \imath \Omega t} \ . \tag{4.71}$$

The photodetector signal generated by the beams after their recombination at the beam splitter is,

$$\begin{aligned} I &\propto \left|(1-\eta)\mathcal{E}_r e^{\imath k L_r} + \eta \mathcal{E}_t e^{\imath k L_t + \imath \Omega t}\right|^2 \\ &= \left|-(1-\eta)\eta \mathcal{E}_i e^{\imath k L_r} + \eta(1-\eta)\mathcal{E}_i e^{\imath k L_t + \imath \Omega t}\right|^2 \\ &= |(1-\eta)\eta \mathcal{E}_i|^2 \left|-e^{2\imath k L_r} + e^{\imath k L_t + \imath \Omega t}\right|^2 \ . \end{aligned} \tag{4.72}$$

This signal is now demodulated with the AOM frequency,

$$I e^{\imath \Omega t} \propto \left|-e^{\imath k L_r} + e^{\imath k L_t + \imath \Omega t}\right|^2 e^{i\Omega t} = e^{2\imath \Omega t} - e^{\imath k (L_t - L_r) + 2\imath \Omega t} - e^{-\imath k (L_t - L_r)} \ . \tag{4.73}$$

A low-pass filter cuts all ac-components of the signal,

$$\boxed{I_{filtered}(t) \propto -e^{-\imath k (L_t - L_r)} \simeq -1 + \imath k [L_t - L_r(t)]} \ , \tag{4.74}$$

for small signal amplitudes $L_r(t)$.

4.4.4 Measuring the quadrature components of an electric field

Photodetectors measure intensities $I \propto |\vec{\mathcal{E}}|^2$. Sometimes, however, we are interested in the electric field itself, for example, when we want to get the correlation function $g^{(1)}(\tau)$ and the spectrum $S_{\mathcal{E}}(\omega)$ of a signal. A frequently used procedure consists in beating the signal of interest with a frequency-shifted local oscillator and demodulating the *quadrature components* of the beat signal.

Let us consider a signal of interest $\mathcal{E}_{sig}(t) = |\mathcal{E}_{sig}|e^{\imath\phi(t)}$ with information encoded in the temporal behavior of the phase $\phi(t)$. The first step consists in beating this signal on a photodetector with a frequency-shifted local oscillator $\mathcal{E}_{lo}(t) = |\mathcal{E}_{lo}|e^{\imath\omega_{lo}t}$, yielding a photocurrent,

$$S \propto |\mathcal{E}_{sig} + \mathcal{E}_{lo}|^2 = |\mathcal{E}_{sig}|^2 + |\mathcal{E}_{lo}|^2 + 2|\mathcal{E}_{lo}||\mathcal{E}_{sig}| \cos[\omega_{lo}t - \phi(t)] \ . \tag{4.75}$$

Now, demodulating this signal simultaneously with the local oscillator frequencies $\cos\omega_{lo}t$ and $\sin\omega_{lo}t$, we get,

$$\begin{aligned} U_c &= S\cos\omega_{lo}t = |\mathcal{E}_{lo}||\mathcal{E}_{sig}|\cos\phi(t) + \text{oscillating terms} \\ U_s &= S\sin\omega_{lo}t = |\mathcal{E}_{lo}||\mathcal{E}_{sig}|\sin\phi(t) + \text{oscillating terms} \ , \end{aligned} \tag{4.76}$$

where the oscillating terms can be removed by a low-pass filtering. Finally, we calculate,

$$|\mathcal{E}_{sig}| = \frac{\sqrt{U_c^2 + U_s^2}}{|E_{lo}|} \qquad \text{and} \qquad \tan\phi(t) = \frac{U_s}{U_c} \ , \tag{4.77}$$

and obtain the electric field via,

$$\boxed{\mathcal{E}_{sig} = |\mathcal{E}_{sig}|e^{\imath\phi(t)} = \frac{\sqrt{U_c^2 + U_s^2}}{|\mathcal{E}_{lo}|} e^{\imath \arctan\frac{U_s}{U_c}}} \ . \tag{4.78}$$

4.4.5 Exercises

4.4.5.1 Ex: Pound-Drever-Hall signal

Consider the photodetector signal of Exc. 4.3.4.4. What signal do you observe when demodulating the signal with an oscillation of frequency f? Calculate the derivative of the signal close to resonance; from which parameters does the slope depend, and how must you choose the modulation index to maximize it?

4.4.6 *Experiment: Beating two lasers*

In this exercise, we will ...

1. Take two independent lasers operating at nearly the same frequency (within $\sim 1\,\text{GHz}$) and overlap them at a (non-polarizing) beam splitter.
2. Focus one of the ports of the beam splitter on a photodetector with large band width ($\sim 1\,\text{GHz}$).
3. Analyze the beat signal on a spectrum analyzer.
4. Focus a helium-neon laser onto a fast photodetector and determine the free spectral range of the laser resonator.

4.4.7 *Experiment: Homo- and heterodyning with a Michelson interferometer*

In this exercise, we will ...

1. Set up a Michelson interferometer.

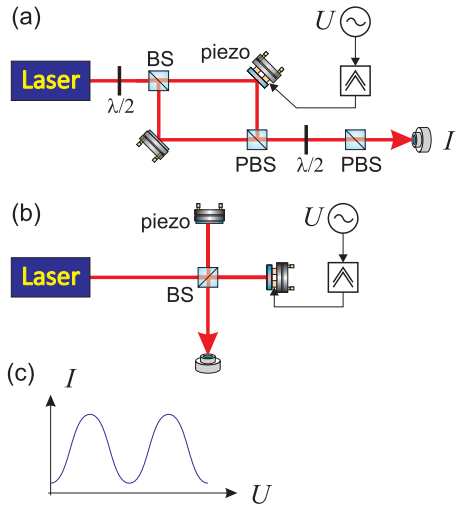

Figure 4.43: Homo- and heterodyning with a Michelson interferometer.

4.5 Further reading

C.J. Buczek et al., *Laser injection locking* [DOI]

Zhixin Liu et al., *Optical Injection Locking: From Principle to Applications* [DOI]

H. Kogelnik et al., *Laser Beams and Resonators* [DOI]

A. Yariv, *Quantum Electronics* [DOI]

A. Yariv et al., *Optical waves in crystals* [DOI]

W. Demtröder, *Atoms, Molecules and Photons: An Introduction to Atomic- Molecular- and Quantum Physics* [DOI]

W. Lichten, *Precise Wavelength Measurements and Optical Phase Shifts: I. General Theory* [DOI]

W.W. Chow, *The ring laser gyro* [DOI]

Chapter 5

Optical spectroscopy

Modern 'optics' is to be understood as 'physics of light-matter interaction' in the optical energy regime. In this sense, this area of physics comprises quantum optics, photonics, atomic physics, and atom optics. Since the invention of the laser the field of optics has seen a huge technological progress leading to the development of extremely powerful and precise tool for investigating and manipulating matter. The femtosecond laser, the frequency comb, atomic interferometers and clocks, and Bose-Einstein condensation are just a few examples.

Spectroscopy is the art of taking and interpreting spectra, i.e. frequency-dependent response functions. The variety of spectroscopic techniques is so overwhelming that a survey is hopeless. As the course also aims at familiarizing the student with applications, a major part of this course will concentrate on techniques employed and available in quantum optics labs. These techniques are mostly oriented toward ultra-high resolution spectroscopy and techniques of manipulating the motion of atoms.

In Sec. 5.1 to 5.4.3, we will try various spectroscopic techniques applied to atomic or cavity resonances.

5.1 Spectrometer and monochromator

Typical dispersive devices are *prisms* and *gratings*.

- lateral displacement as a function of λ
- spectral resolving power $R = |\lambda/\Delta\lambda| = |\nu/\Delta\nu|$
- Rayleigh criterion

5.1.1 Prism spectrometer

For a symmetrical arrangement ($\alpha_1 = \alpha_2 = \alpha$) it is easy to see from Fig. 5.1 that, $\beta = \frac{1}{2}\epsilon$ and $\theta = 2(\alpha - \beta)$. Snell's law the yields,

$$n = \frac{\sin\alpha}{\sin\beta} = \frac{\sin\frac{1}{2}(\theta+\epsilon)}{\sin\frac{1}{2}\epsilon} \ . \tag{5.1}$$

Hence,

$$\frac{dn}{d\theta} = \frac{1}{2}\frac{\cos\frac{1}{2}(\theta+\epsilon)}{\sin\frac{1}{2}\epsilon} \ , \tag{5.2}$$

or

$$\frac{d\theta}{dn} = \frac{\sin\frac{1}{2}\epsilon}{1 - n^2 \sin\frac{1}{2}\epsilon} \ . \tag{5.3}$$

The angular dispersion is therefore,

$$\frac{d\theta}{d\lambda} = \frac{\sin\frac{1}{2}\epsilon}{1 - n^2 \sin\frac{1}{2}\epsilon} \frac{dn}{d\lambda} \ . \tag{5.4}$$

The spectral dispersion of typical transparent materials is on the order of $-dn/d\lambda \approx 10^{-4}$.

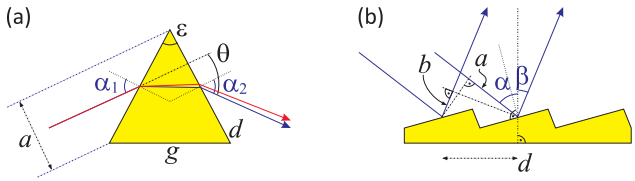

Figure 5.1: Illustration of (a) the prism spectrometer and (b) the grating spectrometer.

Example 6 (*Prism spectrometer*): We calculate the angular dispersion for an equilateral prism ($\sin\frac{1}{2}\epsilon = 0.5$) made of BK7 for two superposed wavelength $\lambda_1 = 461\,\text{nm}$ ($n_{\lambda_1} = 1.5243$) and $\lambda_2 = 633\,\text{nm}$ (with $n_{\lambda_2} = 1.5151$) to be,

$$d\theta = \frac{1}{\sqrt{1 - (n/2)^2}} dn \approx 0.8^\circ \ .$$

The resolving power can be calculated, once we have expressed the limiting aperture $a = d\cos\alpha$ where $d = g/(2\sin\frac{\epsilon}{2})$,

$$\left|\frac{\lambda}{\Delta\lambda}\right| = a\frac{d\theta}{d\lambda} = \frac{g\cos\alpha}{1 - n^2\sin\frac{1}{2}\epsilon}\frac{dn}{d\lambda} = g\frac{dn}{d\lambda} \ . \tag{5.5}$$

Solve Exc. 2.2.3.14.

5.1.2 Grating spectrometer

Destructive interference occurs for,

$$\Delta s = m\lambda = a - b = d\sin\alpha - d\sin\beta \ . \tag{5.6}$$

Frequently used is the so-called *Littrow configuration* for which $\alpha = -\beta$.

The grating represents a multiple beam interferometer, because the beams reflected from every groove of the grating are phase-shifted by amounts (setting $\alpha = 0$,

$$\delta = \tfrac{2\pi}{\lambda}\Delta s = -2\pi\frac{d}{\lambda}\sin\beta \ . \tag{5.7}$$

The sum of the reflections from N grooves of an incident plane wave $E_{in} = E_0 e^{\imath(\mathbf{k}\cdot\mathbf{r}-\omega t}$ is therefore,

$$\mathcal{E}_r = \sqrt{R}\mathcal{E}_0 \sum_{m=0}^{N} e^{\imath \mathbf{k}_r\cdot\mathbf{r}-\omega t} e^{im\delta} = \sqrt{R}E_0 e^{\imath \mathbf{k}_r\cdot\mathbf{r}-\omega t} \frac{1-e^{\imath N\delta}}{1-e^{\imath\delta}} \ . \tag{5.8}$$

Consequently, the intensity is,

$$I_r = RI_0 \frac{\sin^2 \frac{N}{2}\delta}{\sin^2 \frac{1}{2}\delta} \ . \tag{5.9}$$

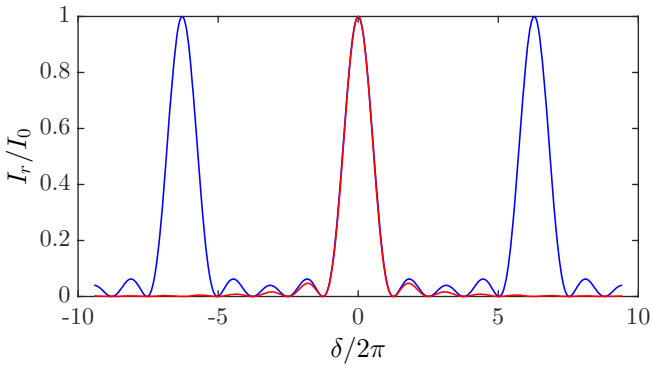

Figure 5.2: (code) Reflection curve of a diffraction grating.

The angular dispersion is, using Eqs. (5.7) and (5.6),

$$\frac{d\beta}{d\lambda} = \left(\frac{d\lambda}{d\beta}\right)^{-1} = -\frac{m}{d\cos\beta} = -\frac{\sin\alpha - \sin\beta}{\lambda\cos\beta} \ . \tag{5.10}$$

The resolving power is,

$$\left|\frac{\lambda}{\Delta\lambda}\right| = \frac{Nd(\sin\alpha - \sin\beta)}{\lambda} = mN \ . \tag{5.11}$$

Solve Exc. 5.1.3.1, 5.1.3.2, and 5.1.3.3.

5.1.3 Exercises

5.1.3.1 Ex: Resolution of a grating spectrometer

Calculate the spectral resolution of a grating spectrometer with an entrance slit width of 10 µm, focal lengths $f_1 = f_2 = 2$ m of the mirrors M1 and M2, a grating with 1800 grooves/mm and an angle of incidence $\alpha = 45°$. What is the useful minimum slit width if the size of grating is $100 \times 100\,\mathrm{mm}^2$?

5.1.3.2 Ex: Grating spectrometer

The spectrometer in Exc. 5.1.3.1 shall be used in first order for a wavelength range around 500 nm. What is the optimum blaze angle, if the geometry of the spectrometer allows an angle of incidence α about 20°?

5.1.3.3 Ex: Littrow grating

Calculate the number of grooves/mm for a Littrow grating for a 25° incidence at $\lambda = 488\,\text{nm}$ (i.e., the first diffraction order is being reflected back into the incident beam at an angle $\alpha = 25°$ to the grating normal).

5.1.3.4 Ex: Combining spectrometers

A fluorescence spectrum shall be measured with a spectral resolution of 10^{-2} nm. The experimenter decides to use a crossed arrangement of grating spectrometer (linear dispersion: 0.5 nm/mm) and FPI of Exc. 4.1.10.7. Estimate the optimum combination of spectrometer slit width and FPI plate separation.

5.1.4 *Experiment: Separating bichromatic light by prisms and gratings*

In this experiment we will study the dispersive power of a prism and a grating.

1. Combine the beams of a helium-neon laser and a laser at 461 nm via a beam-splitter. Pass this combination through a prism and quantify the dispersion.
2. Calculate the minimum angle between the two beams.
3. Shine the combination onto a reflection grating and quantify the dispersion.

5.1.5 *Experiment: Thorlabs optical spectrum analyzer*

CCS175, characterization, Thorlabs ® tour.

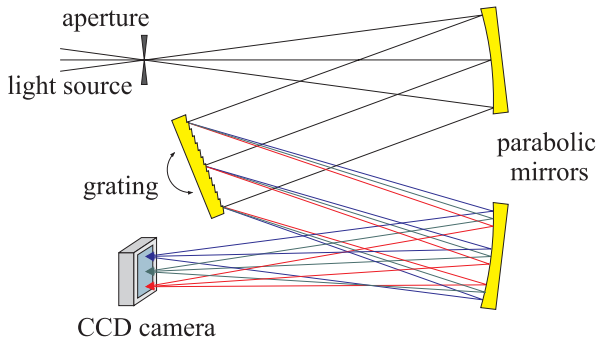

Figure 5.3: Principle of operation of a Czerny-Turner monochromator.

Czerny-Turner CCD spectrometer

1. Irradiate light on OSA and observe the spectrum.

5.1.6 *Experiment: HighFinesse wavemeter*

Wavemeters measure the wavelength of monochromatic light sources by interference. One type of wavemeter is based on a Michelson interferometer, where the length of one interferometer arm is uniformly increased while the interference fringes are counted. Counting the fringes of a known reference laser simultaneously and comparing the counts of the unknown and the reference laser, the wavelength of the unknown laser can be determined with high precision (down to 2 MHz resolution).

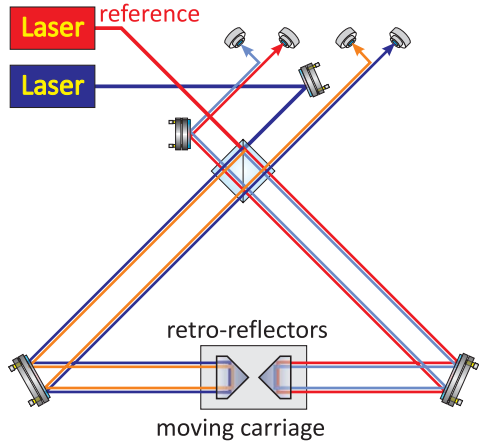

Figure 5.4: Principle of operation of a Michelson-type wavemeter.

1. HighFinesse WSU30, characterization.

5.2 Fluorescence, excitation, and absorption spectroscopy

Depending on the information we want to extract from a sample and on the available instrumentation various types of spectroscopic techniques are possible, which will be discussed on the following sections.

5.2.1 Classification of spectroscopic methods

It is important to distinguish *fluorescence spectra* from *excitation spectra*: Fluorescence spectra are taken by processing the light emitted from a radiator in a monochromator. That is, the light is shone onto a spectral band filter, which only transmits a narrow fraction of the fluorescence spectrum. The power of the transmitted light is measured with a detector. Upon changing the center frequency of the band filter,

different components of the fluorescence spectrum are measured, thus yielding a curve $u(\nu)$, which represents the spectral energy density of the radiator [see Fig. 5.5(a,d)].

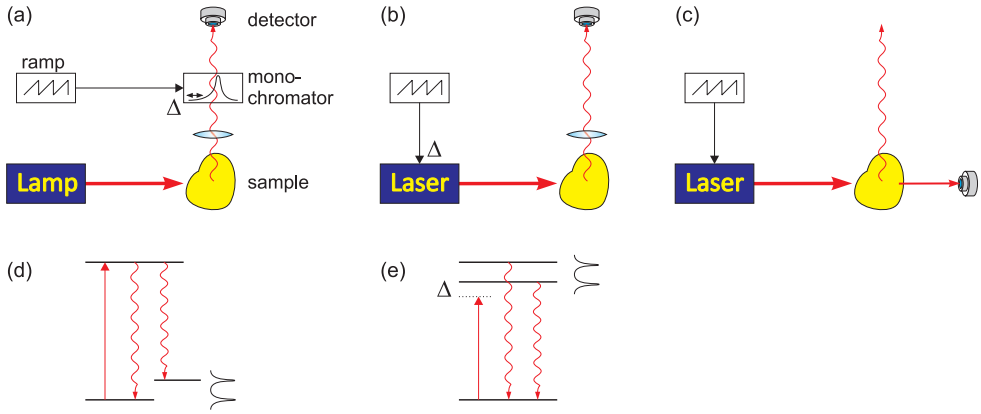

Figure 5.5: (a) Taking a fluorescence spectrum, (b) an excitation spectrum, and (c) an absorption spectrum. Typical level schemes for (d) fluorescence spectroscopy and (e) excitation or absorption spectroscopy.

In contrast to fluorescence spectroscopy, excitation or absorption spectra are taken by varying the frequency of the light exciting a sample. The reemitted light is then measured by a detector without discriminating its frequency components. Obviously, both method yield very different information about the scatterer [see Fig. 5.5(b,c,e)]. Depending on whether the scattered of the transmitted light is detected, we speak of excitation and absorption spectroscopy.

5.2.2 Saturated absorption spectroscopy

One of the most popular spectroscopic technique is *saturation spectroscopy*, as it is simple, robust, and allows to avoid Doppler-broadening. There are, however, many

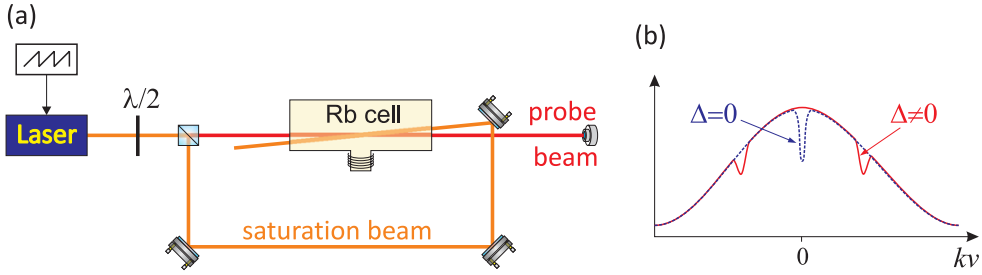

Figure 5.6: (a) Experimental scheme for saturated absorption spectroscopy. (b) Spectral hole burning by the counter-propagating saturation and probe beams for (red) detuned and (blue) resonant light.

possible implementations of saturation spectroscopy, f.ex. *frequency modulation spectroscopy* or *modulation transfer spectroscopy*, which we will present in the following.

5.2.2.1 Calculation of the Lamb-dip

The scheme known as *Lamb-dip spectroscopy* and which is illustrated in Fig. 5.6(a), consists in a cell filled with a gas [for example, atomic rubidium whose resonance frequency is $\omega_0 = ck = 2\pi c/780\,\text{nm}$ and decay rate is $\Gamma = (2\pi)\ 6\,\text{MHz}$] and two laser beams with the same frequency ω, but propagating in opposite directions. One is called the saturating beam, the other probe beam.

The basic idea is that, if the laser frequency is detuned from resonance, $\omega \neq \omega_0$, the counter-propagating beams will interact with different velocity classes (i.e. atomic velocities projected on the optical axis, $v = \mathbf{v}\cdot\hat{\mathbf{e}}_\mathbf{k}$), which results in two distinct 'holes' in the excitation profile [red curve in Fig. 5.6(b)]. Only for resonant light, $\omega = \omega_0$, will the counter-propagating beams interact with the same velocity class (i.e. atomic velocities with $v = 0$). The 'holes' in the excitation profile then overlap thus leading to a deeper depression called Lamb-dip [blue curve in Fig. 5.6(b)].

For a quantitative description of the Lamb-dip we consider Maxwell's one-dimensional and normalized velocity distribution,

$$\rho(v)dv = \sqrt{\frac{m}{2\pi k_B T}} e^{-mv^2/2k_B T} dv \ . \tag{5.12}$$

As an example, we consider a gas at $T = 300\,\text{K}$ temperature, where the partial pressure of rubidium is about $P = 10^{-1}\,\text{mbar}$, such that the particle density is,

$$n(T) = \frac{P}{k_B T} \ . \tag{5.13}$$

We also assume a cell length of $L = 10\,\text{cm}$.

The probe laser intensity is below saturation, such that the optical cross section for an atom moving with velocity v, is,

$$\sigma(v) = \frac{6\pi}{k^2} \frac{\Gamma^2}{4(\omega - \omega_0 - kv)^2 + \Gamma^2} \ , \tag{5.14}$$

where we considered the fact that the atoms moving with the velocity v along the optical axis perceive the probe laser beam as Doppler-shifted by an amount kv.

The saturating laser now has high intensity. Let us suppose here, $\Omega \equiv 10\Gamma$, where Ω is the Rabi frequency caused by the saturating laser. In this way, it creates a population of N_e atoms in the excited state. Since this population is missing in the ground state, $N_g = N - N_e$, the absorption is reduced for the probe beam by a factor,

$$\frac{N_e}{N} = \frac{\Omega^2}{4(\omega - \omega_0 + kv)^2 + 2\Omega^2 + \Gamma^2} \ . \tag{5.15}$$

In contrast to (5.14), we now have to consider saturation broadening.

We will now calculate the spectrum of the optical density for the probe laser, $O_D(\omega)$, and the light intensity transmitted through the cell, $\frac{I}{I_0} = e^{-O_D}$, according to the Lambert-Beer law.

The optical density with Doppler broadening is,

$$O_D(T,\omega) = Ln(T) \int_{-\infty}^{\infty} \tfrac{N_g - N_e}{N} \sigma(v)\rho(v)dv \tag{5.16}$$

$$= L\frac{P}{k_B T}\sqrt{\frac{m}{2\pi k_B T}}\frac{6\pi}{k^2}\int_{-\infty}^{\infty}\left(1 - \frac{2\Omega^2}{4(\Delta + kv)^2 + 2\Omega^2 + \Gamma^2}\right)\frac{\Gamma^2}{4(\Delta - kv)^2 + \Gamma^2} e^{-mv^2/2k_B T} dv \ ,$$

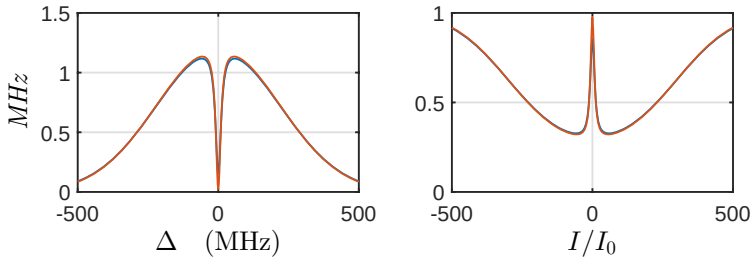

Figure 5.7: (code) (a) Optical density and (b) absorption. (Blue) Integral formula and (green) approximation for high temperature and high saturation.

with $\Delta \equiv \omega - \omega_0$ and substituting $N_g - N_e = N - 2N_e$. The widths of the three distribution functions are, respectively,

$$\begin{aligned} \delta\nu_{sat} &= \sqrt{\tfrac{1}{2}\Omega^2 + \tfrac{1}{4}\Gamma^2} \approx (2\pi)\ 68\,\text{MHz} && \text{for the saturating beam} \\ \delta\nu_{Dpp} &= k\sqrt{\tfrac{k_B T}{m}} \approx (2\pi)\ 217\,\text{MHz} && \text{for the Doppler broadening} \\ \delta\nu_{prb} &= \tfrac{1}{2}\Gamma \approx (2\pi)\ 3\,\text{MHz} && \text{for the probe beam} \end{aligned} \tag{5.17}$$

where $\bar{v} = \sqrt{k_B T/m}$ is the mean atomic velocity (or the *rms* width) of Maxwell's distribution. Since the spectral width of the probe laser spectrum is much smaller, we can replace it by a δ-function,

$$\frac{\Gamma^2}{4(\Delta - kv)^2 + \Gamma^2} \longrightarrow \frac{\pi\Gamma}{2}\delta(\Delta - kv)\ , \tag{5.18}$$

which gives,

$$\begin{aligned} O_D(T,\omega) \simeq L\frac{P}{k_B T}\sqrt{\frac{m}{2\pi k_B T}}\frac{6\pi}{k^3}\int_{-\infty}^{\infty}\left(1 - \frac{2\Omega^2}{4(\Delta+kv)^2 + 2\Omega^2 + \Gamma^2}\right)\times \\ \times \frac{\pi\Gamma}{2}\delta(\Delta - kv)e^{-mv^2/2k_B T}dkv \\ = L\frac{P}{k_B T}\sqrt{\frac{m}{2\pi k_B T}}\frac{6\pi}{k^3}\frac{\pi\Gamma}{2}\left(1 - \frac{2\Omega^2}{8\Delta^2 + 2\Omega^2 + \Gamma^2}\right)e^{-m(\Delta/k)^2/2k_B T}\ . \end{aligned} \tag{5.19}$$

The *Lamb dip* is the narrow (Doppler-free) feature in the center of the the spectrum exhibited in Fig. 5.7. Lamb-dip spectra are commonly serve as frequency references for laser frequency stabilization schemes.

5.2.3 Frequency modulation and modulation transfer spectroscopy

Variations of the saturation spectroscopic idea are the *frequency modulation spectroscopy* (FMS) and the *modulation transfer spectroscopy* (MTS). The basic scheme of those techniques is shown in Fig. 5.8. As in saturation spectroscopy, two counterpropagating beams interact with the same atoms of a molecular gas, but now one

of the beams is frequency-modulated (e.g. using an electro-optic modulator). In the FMS configuration, the probe beam is modulated, and the sidebands are discriminated at the spectral feature generated by the saturation beam in a very similar way as for the Pound-Drever-Hall technique. The profile of the FMS signal is calculated in Exc. 5.2.4.3 [49, 13, 38, 73, 46, 18, 29, 72, 70, 40, 55].

In the MTS configuration, the saturation beam is modulated, and the sidebands are transferred to the probe beam via nonlinear four-wave mixing processes. In both cases, the sidebands are demodulated with the local oscillator frequency driving the EOM.

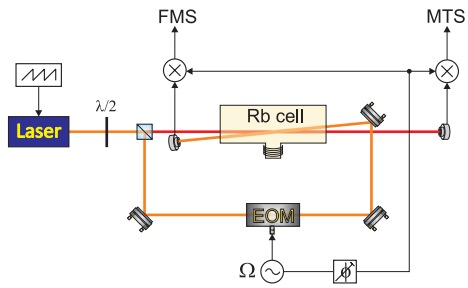

Figure 5.8: Schemes of frequency-modulation and modulation transfer spectroscopy.

The advantages of both techniques is, that they generate dispersive Doppler-free lineshapes. The FMS signal appears as a sharp feature on top of a large Doppler background (similarly to the Lamb-dip). In contrast, the MTS signal is free from Doppler background. The MTS signal recorded by the photodetector is given by,

$$I(\Delta) = \sum_{a,b} \frac{\mu_{ab}^2}{\gamma_j + \imath\delta} \left(\frac{1}{\gamma_{ab} + \imath(\Delta + \delta/2)} - \frac{1}{\gamma_{ab} + \imath(\Delta + \delta)} + \frac{1}{\gamma_{ab} - \imath(\Delta - \delta)} - \frac{1}{\gamma_{ab} - \imath(\Delta - \delta/2)} \right) , \tag{5.20}$$

where a and b denote the lower and upper levels, μ_{ab}^2 is the electric dipole moment, γ_{ab} is the optical relaxation rate, γ_j is the decay of the energy level j of the molecule, and δ is the modulation frequency. Behind the mixer we see the electric signal,

$$S(\Delta, \vartheta) = \mathrm{Re}\left[I(\Delta) e^{-\imath\varphi} \right] , \tag{5.21}$$

where ϑ is the demodulation phase [54]. The curves are shown in Fig. 5.8.

Example 7 (*Modulation transfer spectroscopy*): Modulation transfer spectroscopy is caused by four-wave mixing (4WM) processes, which have the general form $P(\omega + \Omega) = \chi^{(3)}(\omega + \Omega) E_s(\omega_s) E_p(\omega_s) E_s^*(\omega_s - \Omega)$, or similar. When the beams ω and ω_s are counter-propagating, and the atoms are moving, their resonances shift toward $\omega \mp \mathbf{k} \cdot \mathbf{v}$, respectively in the atomic rest system. Resonant enhancement of 4WM occurs, when one of the intermediate levels coincides with

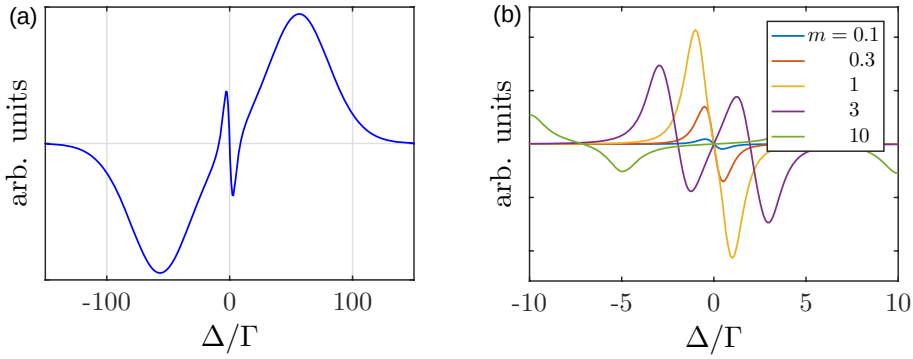

Figure 5.9: (code) (a) Calculated FMS signals and (b) MTS signals as a function of detuning for various modulation indices.

ω_0:

$$\omega - \mathbf{k}\cdot\mathbf{v} = \omega_0$$
$$(\omega - \mathbf{k}\cdot\mathbf{v}) - (\omega + \mathbf{k}\cdot\mathbf{v} - \Omega) = 0$$
$$(\omega - \mathbf{k}\cdot\mathbf{v}) - (\omega + \mathbf{k}\cdot\mathbf{v} - \Omega) + (\omega + \mathbf{k}\cdot\mathbf{v}) = \omega_0$$
$$(\omega - \mathbf{k}\cdot\mathbf{v}) - (\omega + \mathbf{k}\cdot\mathbf{v} - \Omega) + (\omega + \mathbf{k}\cdot\mathbf{v}) - (\omega - \mathbf{k}\cdot\mathbf{v} + \Omega) = 0\ .$$

Assuming $\omega = \omega_s = \omega - 0$, these resonances reduced to,

$$\mathbf{k}\cdot\mathbf{v} = 0, \pm\Omega\ ,$$

and similarly for the other 4WM processes. This means, that the saturation beam burns holes in the velocity distribution at $\mathbf{k}\cdot\mathbf{v} = 0, \pm\frac{1}{2}\Omega, \pm\Omega$, which modulate the probe beam.

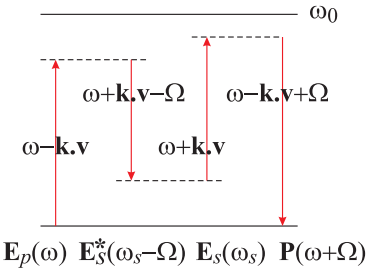

Figure 5.10: Levels involved in 4WM upon MTS.

5.2.4 Exercises

5.2.4.1 Ex: Width of the absorption band

The resonator of a dye laser with a large emission bandwidth additionally contains an absorbing (dense) gas. The absorption spectrum of the gas is Lorentzian with a width

of 3 GHz, and the absorption coefficient has, in the middle of the absorption line (at 600 nm), the value of 0.2. What are the maximum and minimum relative spectral distances $\Delta f/\Delta f_0$ of the axial modes within the spectral range of the absorption, compared to the distances Δf_0 of the empty resonator?

5.2.4.2 Ex: Lorentz and Gaussian profiles

At which detuning is a Doppler-broadened line dominated by Lorentzian profile of the transition?

5.2.4.3 Ex: Frequency-modulation spectroscopy

Calculate the FMS spectrum for a rubidium gas (describing the atoms as a two-level system) under the conditions specified in Sec. 5.2.2 and assuming a modulation frequency of $f = 10\,\text{MHz}$ and a modulation index of $\beta = 1$.

5.2.5 *Experiment: Rubidium Lamb-dips*

In this exercise, we will spectroscopically identify the various lines of the rubidium D_2-transition of the isotopes ^{87}Rb and ^{85}Rb. The hyperfine splittings of the ground and excited states are reproduced in Fig. 5.11.

1. Set up the optics for a Lamb-dip spectroscopy as shown in Fig. 5.11.

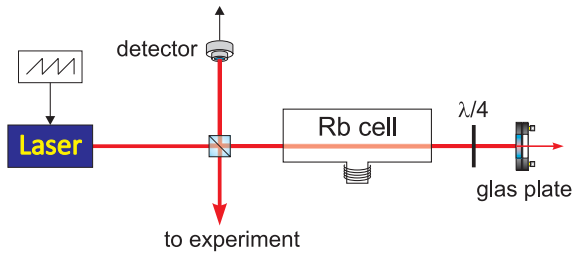

Figure 5.11: Saturation spectroscopy.

2. Fig. 5.12 shows a typical spectrum recorded with a rubidium gas cell. Find an interpretation for the various lines of the spectrum.

5.3 Polarization spectroscopy

The *Hänsch-Couillaud technique* uses the *birefringence* of certain materials, devices, or gases.

5.3.1 Birefringent cavity

We consider a birefringent cavity exhibiting slightly different path lengths for two axis that we will call, respectively, *ordinary* and *extraordinary*. Fig. 5.13(a) shows the

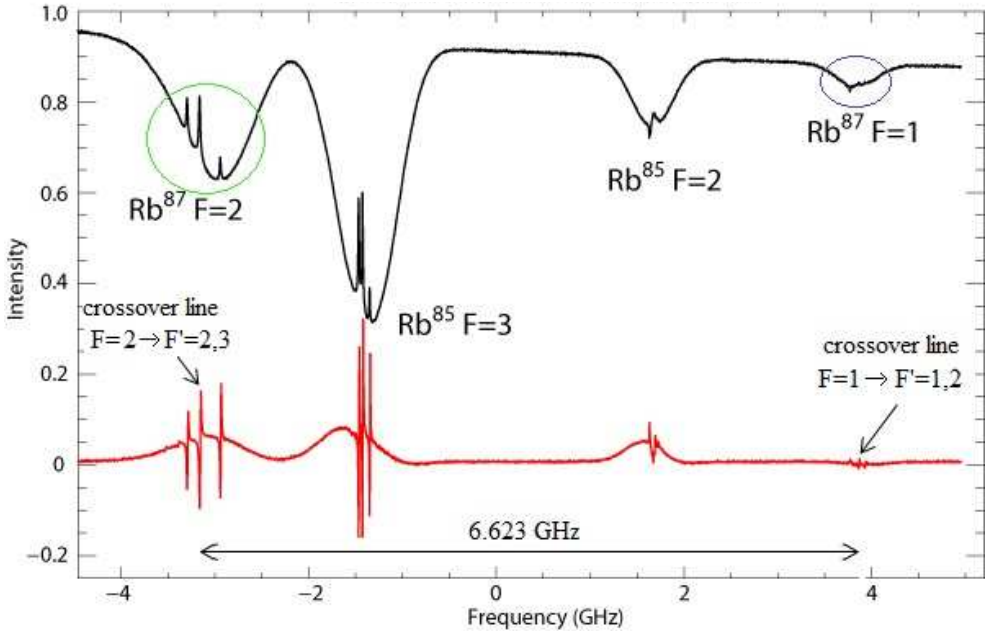

Figure 5.12: (Black) Lamb-dip spectroscopy of a rubidium gas (natural isotope mixture of ^{85}Rb and ^{87}Rb) showing the hyperfine structure transitions of the D2-line. (Red) Derivative of the spectrum in (a).

optical setup. The detector signals may be calculated via a concatenation of the Jones matrices for a $\lambda/2$-plate, the transmissive response of the cavity, another $\lambda/2$-plate, and finally a polarizing beam splitter,

$$\begin{pmatrix} E_o \\ E_e \end{pmatrix} = M \begin{pmatrix} 1 \\ 0 \end{pmatrix} \qquad with \tag{5.22}$$

$$M \equiv \begin{pmatrix} \cos\beta & \sin\beta \\ -\sin\beta & \cos\beta \end{pmatrix} \begin{pmatrix} \frac{T}{1-Re^{2ik_oL}} & 0 \\ 0 & \frac{T}{1-Re^{2ik_eL}} \end{pmatrix} \begin{pmatrix} \cos\alpha & \sin\alpha \\ -\sin\alpha & \cos\alpha \end{pmatrix} . \tag{5.23}$$

For the particular polarization angles $\alpha = \frac{\pi}{4}$ and $\beta = 0$, we derive the difference of the photodetector signals,

$$\Delta I = |E_o|^2 - |E_e|^2 = \frac{T^2}{2}\left[\frac{1}{1-R^2-2R\cos 2k_oL} - \frac{1}{1-R^2-2R\cos 2k_eL}\right] . \tag{5.24}$$

As Fig. 5.13(b) demonstrates, the spectra corresponding to the axis, obtained by ramping the laser frequency are slightly shifted with respect to each other. Their subtraction leads to a dispersive lineshape that suits for laser locking purposes in the so-called *Hänsch-Couillaud* stabilization.

5.3.2 *Experiment: Birefringence of a ring cavity*

Birefringence automatically occurs in a ring cavities. In this exercise, we will analyze the birefringence observed in reflection of a such a ring cavity. In a *ring cavity*, the

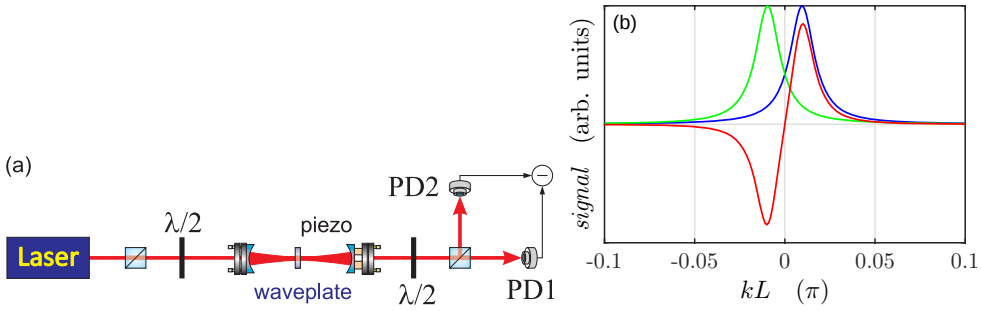

Figure 5.13: (code) (a) Generating a Hänsch-Couillaud error signal by transmission of a birefringent linear cavity. (b) Signals recorded by the two photodetectors (blue and green) and their difference (red).

resonance frequencies of the s-polarized and the p-polarized modes are slightly shifted from one another due to the different penetration depth of the s- and p-polarized light modes into the layers of the dielectric mirrors. For a moderate finesse of the cavity (say $\mathcal{F} = 2000$), the modes actually overlap. This leads to a birefringence used in the

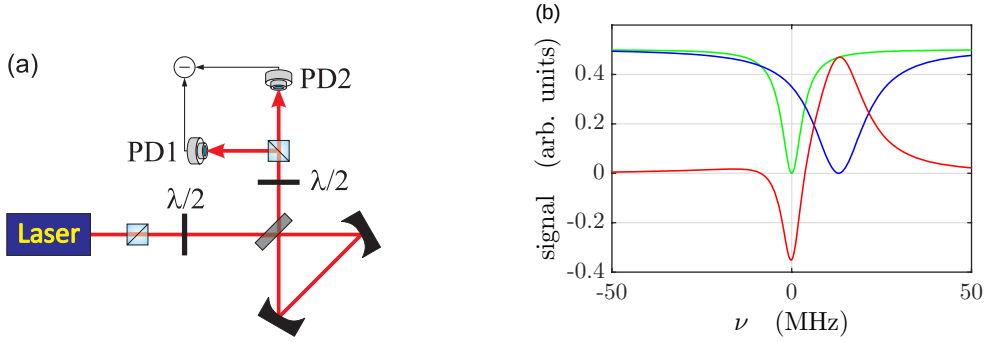

Figure 5.14: (code) (a) Generating a Hänsch-Couillaud error signal by (a) reflection from a ring cavity and (b) transmission of a linear cavity containing a Brewster plate. (b) Signals recorded by the two photodetectors (blue and green) and their difference (red). (a) Reflection signals $|E_s|^2$ and $|E_p|^2$ from a birefringent cavity with $\delta_{fsr} = 8.2\,\mathrm{GHz}$, $\varphi_s = 0$, $R_{hr,s} = 99.97\%$, $R_{ic,s} = 99.74\%$, $F_s = \pi(R_{hr,s}^2 R_{ic,s})^{1/6}/[1-(R_{hr,s}^2 R_{ic,s})^{1/3}]$, $\varphi_p = 0.01$, $R_{hr,p} = 99.92\%$, $R_{ic,p} = 99.34\%$, and $F_p = \pi(R_{hr,p}^2 R_{ic,p})^{1/6}/[1-(R_{hr,p}^2 R_{ic,p})^{1/3}]$. (b) Difference $|E_s|^2 - |E_p|^2$.

famous Hänsch-Couillaud locking scheme. The detector signal in the scheme shown in the figure may calculated via a concatenation of the Jones matrices for a $\lambda/2$-plate, the reflective response of the ring cavity, another $\lambda/2$-plate, and finally a polarizing

beam splitter,

$$\begin{pmatrix} E_s \\ E_p \end{pmatrix} = M \begin{pmatrix} 1 \\ 0 \end{pmatrix} \quad with \tag{5.25}$$

$$M \equiv \begin{pmatrix} \cos\beta & \sin\beta \\ -\sin\beta & \cos\beta \end{pmatrix} \begin{pmatrix} \frac{1-e^{-2\pi\imath\omega/\delta_{fsr}+\imath\phi_s}}{1-R_s e^{-2\pi\imath\omega/\delta+\imath\phi_s}} & 0 \\ 0 & \frac{1-e^{-2\pi\imath\omega/\delta_{fsr}+\imath\phi_p}}{1-R_p e^{-2\pi\imath\omega/\delta+\imath\phi_p}} \end{pmatrix} \begin{pmatrix} \cos\alpha & \sin\alpha \\ -\sin\alpha & \cos\alpha \end{pmatrix}.$$

Calculating $|E_s|^2$ and $|E_p|^2$ as a function of the laser frequency ω reproduces the curves plotted in Fig. 5.14(a).

1. x

5.4 Other spectroscopic techniques

5.4.1 Mode-locked femtosecond laser

Mode-locking is a technique in optics by which a laser can be made to produce pulses of light of extremely short duration, down to the order of femtoseconds. The basis of the technique is to induce a fixed-phase relationship between the longitudinal modes of the laser's resonant cavity. Constructive interference between these modes can cause the laser light to be produced as a train of pulses.

In a simple laser, each of these cavity modes amplified within the bandwidth of the gain medium oscillates independently, with no fixed relationship between each other. The individual phase of the light waves in each mode is not fixed, and may vary randomly due to such things as thermal changes in materials of the laser. In lasers with only a few oscillating modes, interference between the modes can cause beating effects in the laser output, leading to fluctuations in intensity; in lasers with many thousands of modes, these interference effects tend to average to a near-constant output intensity.

If instead of oscillating independently, each mode operates with a fixed phase relation to the other modes. Instead of a random or constant output intensity, the modes of the laser will periodically constructively interfere with one another, producing an intense burst or pulse of light. Such a laser is said to be *mode-locked* or *phase-locked*. These pulses occur separated in time by $\tau = 2L/c$, where τ is the laser cavity round trip time and corresponds to the cavity's inverse free spectral range.

5.4.1.1 Active mode-locking

The most common active mode-locking technique places a standing wave electro-optic modulator (EOM) into the laser cavity. When driven with a sinusoidal electrical signal, this produces an amplitude modulation of the light in the cavity. Considering this in the frequency domain, if a mode has optical frequency ν, and is amplitude-modulated at a frequency f, the resulting signal has sidebands at optical frequencies $\nu \pm f$. The modulation frequency is now chosen to coincide with the cavity's free spectral range, $f = \delta_{fsr}$, and since the sidebands are driven in-phase, the central mode and the adjacent modes will be phase-locked together. Further operation of the

modulator on the sidebands produces phase-locking of the $\nu \pm 2f$ modes, and so on until all modes in the gain bandwidth are locked.

This process can also be considered in the time domain. The amplitude modulator acts as a weak 'shutter' to the light bouncing between the mirrors of the cavity, attenuating the light when it is 'closed', and letting it through when it is 'open'. If the modulation rate f is synchronized to the cavity round-trip time τ, then a single pulse of light will bounce back and forth in the cavity. The actual strength of the modulation does not have to be large; a modulator that attenuates 1% of the light when 'closed' will mode-lock a laser, since the same part of the light is repeatedly attenuated as it traverses the cavity.

Related to this amplitude modulation (AM), active mode-locking is frequency modulation (FM) mode-locking, which uses a modulator device based on the acousto-optic effect. This device, when placed in a laser cavity and driven with an electrical signal, induces a small, sinusoidally varying frequency shift in the light passing through it. If the frequency of modulation is matched to the round-trip time of the cavity, then some light in the cavity sees repeated upshifts in frequency, and some repeated downshifts. After many repetitions, the upshifted and downshifted light is swept out of the gain bandwidth of the laser. The only light which is unaffected is that which passes through the modulator when the induced frequency shift is zero, which forms a narrow pulse of light.

The third method of active mode-locking is synchronous mode-locking, or synchronous pumping. In this, the pump source (energy source) for the laser is itself modulated, effectively turning the laser on and off to produce pulses.

5.4.1.2 Passive mode-locking

Passive mode-locking techniques are those that do not require a signal external to the laser to produce pulses. Rather, they use the light in the cavity to cause a change in some intracavity element, which will then itself produce a change in the intracavity light. A commonly used device to achieve this is a saturable absorber.

A saturable absorber is an optical device that exhibits an intensity-dependent transmission. For passive mode-locking, ideally a saturable absorber will selectively absorb low-intensity light, and transmit light which is of sufficiently high intensity. When placed in a laser cavity, a saturable absorber will attenuate low-intensity constant wave light (pulse wings). However, because of the somewhat random intensity fluctuations experienced by an un-mode-locked laser, any random, intense spike will be transmitted preferentially by the saturable absorber. As the light in the cavity oscillates, this process repeats, leading to the selective amplification of the high-intensity spikes, and the absorption of the low-intensity light. After many round trips, this leads to a train of pulses and mode-locking of the laser.

Considering this in the frequency domain, if a mode has optical frequency ν, and is amplitude-modulated at a frequency nf, the resulting signal has sidebands at optical frequencies $\nu \pm nf$ and enables much stronger mode-locking for shorter pulses and more stability than active mode-locking, but has startup problems.

Saturable absorbers are commonly liquid organic dyes, but they can also be made from doped crystals and semiconductors. Semiconductor absorbers tend to exhibit very fast response times ($\sim$100 fs), which is one of the factors that determines the

final duration of the pulses in a passively mode-locked laser. In a colliding-pulse mode-locked laser the absorber steepens the leading edge while the lasing medium steepens the trailing edge of the pulse.

There are also passive mode-locking schemes that do not rely on materials that directly display an intensity dependent absorption. In these methods, nonlinear optical effects in intracavity components are used to provide a method of selectively amplifying high-intensity light in the cavity, and attenuation of low-intensity light. One of the most successful schemes is called Kerr-lens mode-locking (KLM), also sometimes called 'self mode-locking'. This uses a nonlinear optical process, the optical Kerr effect, which results in high-intensity light being focussed differently from low-intensity light. By careful arrangement of an aperture in the laser cavity, this effect can be exploited to produce the equivalent of an ultra-fast response time saturable absorber.

5.4.2 Frequency comb

In optics, a frequency comb is a laser source whose spectrum consists of a series of discrete, equally spaced frequency lines. Frequency combs can be generated by a number of mechanisms, including periodic modulation (in amplitude and/or phase) of a continuous-wave laser, four-wave mixing in nonlinear media, or stabilization of the pulse train generated by a mode-locked laser. The invention of the *frequency comb* represents a breakthrough in ultrahigh resolution spectroscopy, which was honored with the Nobel price attributed to Theodor Hänsch in 2005 [83, 45, 41, 42, 62, 1, 76].

The frequency domain representation of a perfect frequency comb is a series of delta functions spaced according to,

$$f_n = f_{ceo} + n f_{rep} \ , \tag{5.26}$$

where n is an integer, f_{rep} is the comb tooth spacing (equal to the mode-locked laser's repetition rate or, alternatively, the modulation frequency), and f_{ceo} is the carrier offset frequency, which is less than f_{rep}. Combs spanning an octave in frequency (i.e., a factor of two) can be used to directly measure (and correct for drifts in) f_{ceo}. Thus, octave-spanning combs can be used to steer a piezoelectric mirror within a carrier-envelope phase-correcting feedback loop. Any mechanism by which the combs' two degrees of freedom (f_{rep} and f_{ceo}) are stabilized generates a comb that is useful for mapping optical frequencies into the radio frequency for the direct measurement of optical frequency.

5.4.2.1 Spectrum of a frequency comb

The field emitted by a pulsed laser characterized by its pump laser frequency ν, the *repetition rate* f_{rep}, and the pulse width T, can be given as a temporal sequence of Gaussian shaped pulses. The repetition is mathematically described as a convolution of the Gaussian profile with a sum of temporal δ-functions displaced in time,

$$\boxed{E(t) = \cos 2\pi\nu t \left(\sum_n \delta(t - \tfrac{n}{f_{rep}}) \star e^{-t^2/T^2} \right) = \cos 2\pi\nu t \sum_n e^{-(t-\frac{n}{f_{rep}})^2/T^2}} \ . \tag{5.27}$$

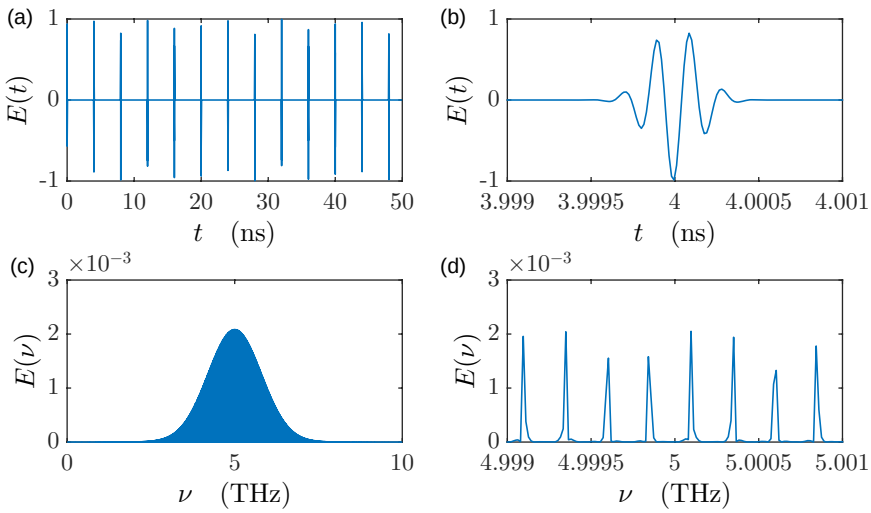

Figure 5.15: (code) Pulse train (a,b) and spectrum (b,c).

The carrier under each pulse is phase-shifted with respect to the adjacent pulse, except when the laser is mode-locked, that is, when,

$$\cos 2\pi\nu t = \cos 2\pi\nu(t + \tfrac{1}{f_{rep}}) \ . \tag{5.28}$$

The Fourier transform of the laser field (5.27) is,

$$\begin{aligned} \mathcal{F}[E(t)] &= \int_{-\infty}^{\infty} e^{-\imath\omega t} \cos 2\pi\nu t \sum_n e^{-(t-n/f_{rep})^2/T^2} dt \\ &= \tfrac{1}{2} \sum_n \int_{-\infty}^{\infty} e^{-\imath(\omega-2\pi\nu)t} e^{-(t-n/f_{rep})^2/T^2} dt \ , \end{aligned} \tag{5.29}$$

where neglect negative frequency components. Using the rules,

$$\mathcal{F}[f(t)e^{\imath\Omega t}] = \int_{-\infty}^{\infty} e^{-\imath\omega t} f(t) e^{\imath\Omega t} dt = (\mathcal{F}f)(\omega - \Omega) \tag{5.30}$$

$$\text{and} \qquad \mathcal{F}[f(t-T)] = \int_{-\infty}^{\infty} e^{-\imath\omega t} f(t-T) dt = e^{-\imath\omega T}(\mathcal{F}f)(\omega)$$

$$\text{and} \qquad \mathcal{F}[e^{-t^2/T^2}] = \int_{-\infty}^{\infty} e^{-\imath\omega t} e^{-t^2/T^2} dt = T\sqrt{\pi} e^{-T^2\omega^2/4}$$

we get,

$$E(\omega) = \mathcal{F}[E(t)] = \tfrac{1}{2} T\sqrt{\pi} e^{-T^2(\omega-2\pi\nu)^2/4} \sum_n e^{-\imath(\omega-2\pi\nu)n/f_{rep}} \ . \tag{5.31}$$

We now write the pump laser frequency as,

$$\nu \equiv m f_{rep} + f_{ceo} \ , \tag{5.32}$$

where we set $m \in \mathbb{N}$ and call $|f_{ceo}| < f_{rep}$ the *carrier envelope offset*. We also express the Fourier frequency by,

$$\omega \equiv 2\pi(\eta f_{rep} + f_{ceo}) \ , \tag{5.33}$$

firstly *without* specifying that η be an integer number. The spectrum is,

$$|E(\omega)|^2 = \tfrac{1}{4}\pi T e^{-T^2(\omega-2\pi\nu)^2/2} \left| \sum_n e^{-2\pi i n(\eta-m)} \right|^2 \ , \tag{5.34}$$

which only gives contributions for,

$$\eta = \frac{\omega - 2\pi f_{ceo}}{2\pi f_{rep}} \in \mathbb{N} \ . \tag{5.35}$$

I.e. the spectrum of comb frequencies is,

$$\boxed{|E(\omega)|^2 = \tfrac{1}{4}\pi T e^{-T^2(\omega-2\pi\nu)^2/2} \sum_n \delta[\omega - (n f_{rep} + f_{ceo})]} \ . \tag{5.36}$$

The δ-function comes from the fact that the sum of (5.35) over many oscillations $e^{-2\pi i n(\eta-m)}$ vanishes by destructive interference, except when they are *in phase*, which is just the case when $\omega = n f_{rep} + f_{ceo}$.

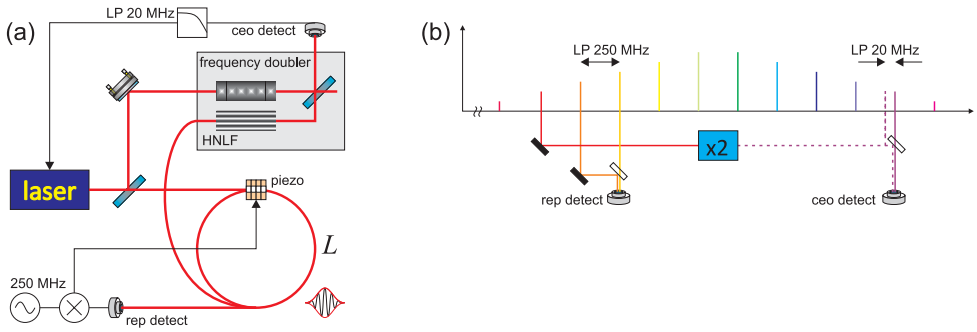

Figure 5.16: (a) Scheme and (b) operation principle of a frequency comb with control of the repetition rate and the carrier envelope offset.

5.4.2.2 Mode-locking of a frequency comb

From Eq. (5.28) we see that *mode-locking* is achieved when,

$$\frac{\nu}{f_{rep}} = m + \frac{f_{ceo}}{f_{rep}} \in \mathbb{N} \ , \tag{5.37}$$

which implies $f_{ceo} = 0$. Eq. (5.36) then becomes,

$$|E(\omega)|^2 = \frac{\pi T}{4} e^{-T^2(\omega-2\pi\nu)^2/2} \sum_n \delta(\omega - n f_{rep}) \ , \tag{5.38}$$

which means that all comb frequencies are locked.

5.4.2.3 Referencing radio and optical frequencies

In a frequency comb f_{rep} is easy to measure, as one just has to filter the beat of the comb light with a low pass filter cutting off frequency components higher than f_{rep}, as illustrated in Fig. 5.16. In contrast, measuring f_{ceo} is more complicated. Unless we have an octave spanning frequency comb, i.e. there are two frequencies in the comb,

$$\nu_1 = m_1 f_{rep} + f_{ceo} \qquad \text{and} \qquad \nu_2 = m_2 f_{rep} + f_{ceo} \ , \tag{5.39}$$

such that $\nu_2 = 2\nu_1 + \Delta\nu$ with $|\Delta\nu| < |f_{ceo}|$, i.e. $m_2 = 2m_1$. We get,

$$m_2 f_{rep} + f_{ceo} = 2m_1 f_{rep} + 2f_{ceo} + \Delta\nu \ , \tag{5.40}$$

or,

$$f_{ceo} = -\Delta\nu \ . \tag{5.41}$$

5.4.2.4 Dual comb spectroscopy

Optical sensors are based on the interaction of light with matter and are often implemented like some kind of spectrometer. The ideal sensor should detect a given substance with great sensitivity, identify it (especially in the presence of many other substances or a noisy background) and quantify it. Add to these features the ability to perform measurements in real time, if possible remotely, in a compact and easy-to-use assembly at affordable price, and we have an absolutely non-trivial problem. Broadband sources allow to detect multiple substances, but have limitations in resolution, calibration or acquisition time. Monochromatic sources allow good resolution, but in general have limitations on tunability and spectral coverage. The sensitivity can be increased by increasing the optical path of interaction, requiring multi-pass cells or resonant optical cavities, which augment the complexity of the setup. Finally, the detection method places limits on the acquisition rate and also on the sensitivity. Particularly the Fourier transform spectroscopy uses broadband incoherent light sources and the time of acquisition and resolution are limited by the speed of translation of a mechanical stage, as well as the range of its displacement. Here, the use of optical frequency combs replacing the incoherent sources, combined with *dual comb spectroscopy*, brings important advantages [78, 39].

5.4.3 Multi-photon spectroscopy

5.4.4 Raman spectroscopy

Raman spectroscopy is a spectroscopic technique typically used to determine vibrational modes of molecules, although rotational and other low-frequency modes of systems may also be observed. Raman spectroscopy is commonly used in chemistry to provide a structural fingerprint by which molecules can be identified. Raman spectroscopy relies upon inelastic scattering of photons, known as Raman scattering. A source of monochromatic light, usually from a laser in the visible, near infrared, or near ultraviolet range is used, although X-rays can also be used. The laser light interacts with molecular vibrations, phonons or other excitations in the system, resulting in the energy of the laser photons being shifted up or down. The shift in energy

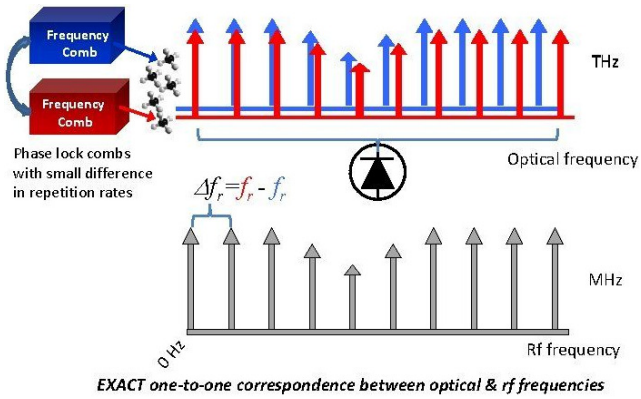

Figure 5.17: Principle of dual comb spectroscopy.

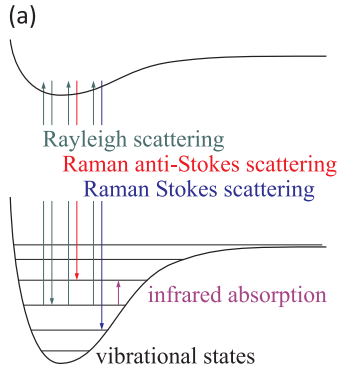

Figure 5.18: Energy-level diagram showing the states involved in Raman spectra.

gives information about the vibrational modes in the system. Infrared spectroscopy typically yields similar, complementary, information.

Typically, a sample is illuminated with a laser beam. Electromagnetic radiation from the illuminated spot is collected with a lens and sent through a monochromator. Elastic scattered radiation at the wavelength corresponding to the laser line (Rayleigh scattering) is filtered out by either a notch filter, edge pass filter, or a band pass filter, while the rest of the collected light is dispersed onto a detector.

Spontaneous Raman scattering is typically very weak; as a result, for many years the main difficulty in collecting Raman spectra was separating the weak inelastically scattered light from the intense Rayleigh scattered laser light (referred to as 'laser rejection'). Historically, Raman spectrometers used holographic gratings and multiple dispersion stages to achieve a high degree of laser rejection. In the past, photomultipliers were the detectors of choice for dispersive Raman setups, which resulted in long acquisition times. However, modern instrumentation almost universally employs notch or edge filters for laser rejection. Dispersive single-stage spectrographs, for example Czerny-Turner (CT) monochromators (see Sec. 5.1.5), paired with CCD detectors are common.

The name 'Raman spectroscopy' typically refers to vibrational Raman using laser wavelengths which are not absorbed by the sample. Raman spectroscopy is used in chemistry to identify molecules and study chemical bonding and intramolecular bonds. Because vibrational frequencies are specific to a molecule's chemical bonds and symmetry (the fingerprint region of organic molecules is in the wavenumber range $500 - 1500\,\mathrm{cm}^{-1}$, Raman provides a fingerprint to identify molecules.

In solid-state physics, Raman spectroscopy is used to characterize materials, measure temperature, and find the crystallographic orientation of a sample. As with single molecules, a solid material can be identified by characteristic phonon modes. Information on the population of a phonon mode is given by the ratio of the Stokes and anti-Stokes intensity of the spontaneous Raman signal. Raman spectroscopy can also be used to observe other low frequency excitations of a solid, such as plasmons, magnons, and superconducting gap excitations. Distributed temperature sensing (DTS) uses the Raman-shifted backscatter from laser pulses to determine the temperature along optical fibers.

5.4.5 Time-resolved spectroscopy

pump-probe spectroscopy

5.5 Further reading

G.C. Bjorklund, *Frequency-Modulation Spectroscopy: A new Method for Measuring Weak Absorptions and Dispersions* [DOI]

J.L. Hall et al., *Optical Heterodyne Saturation Spectroscopy* [DOI]

J.J. Snyder et al., [DOI]

R.K. Kaj et al., *High-Frequency Optically Heterodyned Saturation Spectroscopy via Resonant Degenerate Four-Wave Mixing* [DOI]

G. Camy et al., *Heterodyne Saturation Spectroscopy through Frequency Modulatiof the Saturating Beam* [DOI]

M. Ducloy et al., *Theory of Degenerate Four-Wave Mixing in Resonant Doppler-Broadened Media II* [DOI]

J.H. Shirley, *Modulation Transfer Processes in Optical Heterodyne Saturation Spectroscopy* [DOI]

A. Schenzle et al., *Phase Modulation Laser Spectroscopy* [DOI]

L. Hollberg et al., *Measurement of the shift of Rydberg energy levels incuded by blackbody radiation* [DOI]

L.S. Ma et al., *Optical Heterodyne Spectroscopy Enhanced by an External Optical Cavity: Toward Improved Working Standards* [DOI]

L.S. Ma et al., *Spectroscopy of Te2 with Modulation Transfer Reference Lines for Precision Spectroscopy in Yb* [DOI]

Chapter 6

Locking circuits

In a laboratory we are often confronted with the need to control the value of a physical parameter, f.ex., room temperature, currents and voltages, or the frequency and intensity of laser beams. The physical discipline dealing with the fundamental concepts of this field is called *control theory* and its application to development of automatic control systems is called *control engineering*.

In this chapter, after a brief introduction into *control theory*, we will design and construct a few automatic control systems, which are common in quantum optics labs.

6.1 Introduction to control theory

The minimum ingredients of a control system are 1. a *sensor* measuring the actual value of the parameter to be controlled (e.g., a thermometer), 2. an *actuator* capable of correcting the value (e.g., a heater or cooler), and 3. a suitable *controller* (*servo system*) linking sensor and actuator thus providing a feedback.

The controller comprises a *comparator* comparing the measured value with a reference and delivers the difference to a controller, which may be implemented electronically by proportional control, *PID control*, bistable hysteretic control, or programmable logic control. Older controller units have been mechanical, as in a carburetor. Finally, the value computed by the controller is delivered to an actuator, which manipulates and changes a variable in the controlled system (or *plant*).

6.1.1 Open- and closed-loop control

Fundamentally, there are two types of control loop: *open loop* control, and *closed loop* (feedback) control.

In open loop control, the control action from the controller is independent of the 'process output' (or 'controlled process variable'). An example of this is a central heating boiler controlled only by a timer, so that heat is applied for a constant time, regardless of the temperature of the building. The control action is the switching on/off of the boiler. The process output is the building temperature.

In closed loop control, the control action from the controller is dependent on the process output. In the case of the boiler analogy, this would include a thermostat to monitor the building temperature, and thereby feed back a signal to ensure the controller maintains the building at the temperature set on the thermostat. A closed loop controller therefore has a feedback loop which ensures the controller exerts a

control action to give a process output the same as the 'reference input' or 'set point'. For this reason, closed loop controllers are also called feedback controllers.

The definition of a closed loop control system is *a control system capable of canceling the deviation of a system variable from a reference value by means of a feedback signal computed from a measured value of the variable and used to act on the system in a controlled way* [74]. Automatic feedback control has revolutionized all areas of human activities.

To overcome the limitations of the open-loop controller, control theory introduces *feedback*. A closed-loop controller uses feedback to control states or outputs of a dynamical system. Its name comes from the information path in the system: process inputs (e.g. voltage applied to an electric motor) have an effect on the process outputs (e.g. speed or torque of the motor), which is measured with sensors and processed by the controller; the result (the control signal) is 'fed back' as input to the process, closing the loop.

Closed-loop controllers have the following advantages over open-loop controllers:

- disturbance rejection (such as hills in the cruise control example above)
- guaranteed performance even with model uncertainties, when the model structure does not match perfectly the real process and the model parameters are not exact
- unstable processes can be stabilized
- reduced sensitivity to parameter variations
- improved reference tracking performance

In some systems, closed-loop and open-loop control are used simultaneously. In such systems, the open-loop control is termed feedforward and serves to further improve reference tracking performance.

6.1.1.1 Closed-loop transfer function

Due to noise the variables of the system become time-dependent. The output of the system $y(t)$ is fed back through a sensor measurement F to a comparison with the reference value $r(t)$. The controller C then takes the error $e(t)$ (difference) between the reference and the output to change the inputs $u(t)$ to the system under control P. This is shown in the figure. This kind of controller is a closed-loop controller or feedback controller. We will restrain here to *single-input-single-output control* systems (SISO) disregarding the possibility of having multiple and interdependent inputs and outputs.

If we assume the controller C, the plant P, and the sensor F are linear and time-invariant (i.e. elements of their transfer function $C(s)$, $P(s)$, and $F(s)$ do not depend on time), the systems above can be analyzed using the Laplace transform on the variables, $U(s) = \mathcal{L}u(t)$, $Y(s) = \mathcal{L}y(t)$, and $R(s) = \mathcal{L}r(t)$. Here,

$$s \equiv \imath f \tag{6.1}$$

is an abbreviation for the imaginary Fourier frequency component f of the noise. In the following sections we will, however, characterize the transfer functions in terms

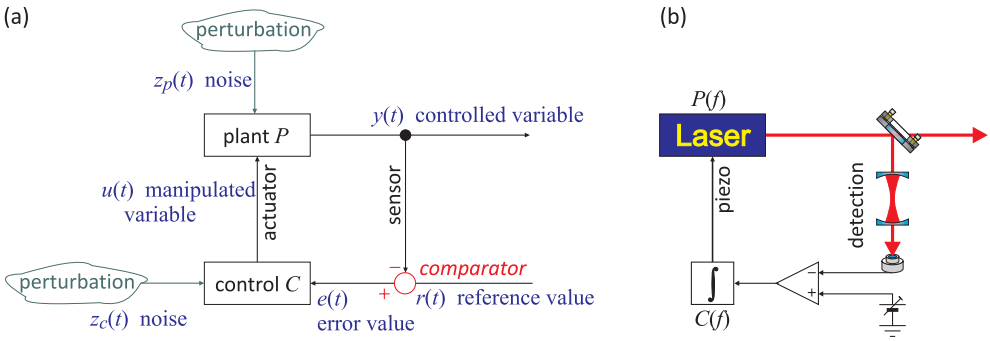

Figure 6.1: (a) General schematic diagram of a feedback loop. (b) Possible implementation for the frequency stabilization of a laser to a cavity resonance,

of real Fourier frequencies. The theoretical foundation of Linear Time-Independent (LTI) systems is outsourced to Sec. 7.2.

For a control to work, it needs to know in which direction to act and when the control point is reached. Therefore, each control needs a slope (*discriminator*) crossing zero. This can be implemented by comparing the signal $Y(f)$ delivered by the detector (for simplicity assumed to be frequency-independent) with a reference signal R. The error signal $E(f) = R(f) - Y(f)$ is then processed by a controller C, and the control signal $U(f)$ is passed, via an actuator (for simplicity assumed to be frequency-independent), to the controlled device P. The controlled device (and obviously all other components of the circuit) are subject to perturbations Z. The transfer functions form a closed control circuit described by the following relations:

$$Y(f) = P(f)U(f) \quad \text{and} \quad U(f) = C(f)E(f) \quad \text{and} \quad E(f) = R(f) - Y(f)\ . \tag{6.2}$$

Solving the system of equations (6.2) for $Y(f)$ in terms of $R(f)$ gives,

$$\boxed{Y(f) = \frac{P(f)C(f)}{1 + P(f)C(f)}\ R(f) \equiv H(f)R(f)}\ . \tag{6.3}$$

$H(s)$ is referred to as the closed-loop transfer function of the system. The numerator $V(f) \equiv P(f)C(f)$ is called the *forward gain* (*open-loop gain*) from R to Y, and the denominator is one plus the gain in going around the feedback loop, the so-called *loop gain*. If $|P(f)C(f)| \gg 1$, i.e. it has a large norm with each value of f, and then $Y(f) \simeq R(f)$ and the output closely tracks the reference input.

6.1.1.2 Noise reduction via feedback circuits

We have seen that the idea of *locking*, whether mechanical or electronic, is to bring a given physical signal Y to a predetermined value R and lock it there, which is the role of the control circuit or *regulator*. Now, considering a possible perturbation of the plant (see Fig. 6.1) by noise Z_p and also of the regulator by noise Z_c, the result (6.3) must be generalized,

$$Y(f) = \frac{P(f)C(f)}{1 + P(f)C(f)}R(f) + \frac{P(f)C(f)}{1 + P(f)C(f)}Z_c(f) + \frac{1}{1 + P(f)C(f)}Z_p(f)\ , \tag{6.4}$$

or,

$$\boxed{Y(f) = \frac{1}{1+V(f)^{-1}}[R(f)+Z_c(f)] + \frac{1}{1+V(f)}Z_p(f)} \,. \tag{6.5}$$

This shows that, provided the open loop gain is high enough, perturbations affecting the plant can be efficiently be neutralized. In contrast, noise entering via the control cannot be suppressed, and this fact is independent on the chosen controller transfer function: *Perturbations entering between the measurement point and the input of the regulator are not eliminated*! Consequently, the detector (which generally works with very low signals) should not introduce or let penetrate noise, because this affects the variable to be controlled: Any variation of the steering variable at the regulator will be transmitted 1 to 1.

In the following, we will discuss the most common controller called PID-servo.

6.1.2 PID feedback control

A *PID controller* continuously calculates an error value $e(t)$ as the difference between a desired setpoint and a measured process variable and applies a correction based on proportional, integral, and derivative terms. PID is an acronym for Proportional-Integral-Derivative, referring to the three terms operating on the error signal to produce a control signal.

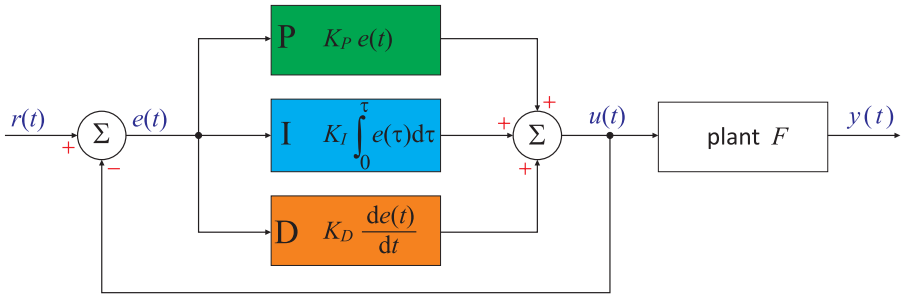

Figure 6.2: A block diagram of a PID controller in a feedback loop, $r(t)$ is the desired process value or 'set point', and $y(t)$ is the measured process value. A proportional-integral-derivative controller (PID controller) is a control loop feedback mechanism control technique widely used in control systems.

The theoretical understanding and application dates from the 1920s, and they are implemented in nearly all analogue control systems; originally in mechanical controllers, and then using discrete electronics and latterly in industrial process computers. The PID controller is probably the most-used feedback control design.

If $u(t)$ is the control signal sent to the system, $y(t)$ is the measured output and $r(t)$ is the desired output, and tracking error $e(t) = r(t) - y(t)$, a PID controller has the general form,

$$\boxed{u(t) = K_P e(t) + K_I \int e(\tau)d\tau + K_D \frac{de(t)}{dt}} \,. \tag{6.6}$$

The desired closed loop dynamics is obtained by adjusting the three parameters K_P, K_P, and K_I, often iteratively by 'tuning' and without specific knowledge of a plant model. Stability can often be ensured using only the proportional term. The integral term permits the rejection of a step disturbance (often a striking specification in process control). The derivative term is used to provide damping or shaping of the response [1].

Applying Laplace transformation results in the transformed PID controller equation,

$$\boxed{U(f) = \left(K_P + K_I \frac{1}{\imath f} + K_D \imath f\right) E(f) \equiv C(f)E(f)} \,, \tag{6.7}$$

defining the PID controller transfer function $C(f)$.

From equations (6.6) or (6.7) we immediately see that the PID transfer functions can readily be implement in electronic circuits using resistors (P), capacitors (I), and inductances (D).

Example 8 (*Comparing servo controllers*): We now assume a low-pass behavior for the plant,

$$P(f) = \frac{1}{1 + \imath f/f_c} \,,$$

and analyze the feedback circuit for four cases.

- The first one is that of a proportional servo, $C(f) = K_P$. Then, Eq. (6.5) reads,

$$Y = \frac{K_P}{1 + \imath f/f_c + K_P}(R + Z_c) + \frac{1 + \imath f/f_c}{1 + \imath f/f_c + K_P} Z_p$$
$$\begin{cases} \stackrel{s\to 0}{\longrightarrow} \frac{K_P}{1+K_P}(R + Z_c) + \frac{1}{1+K_P} Z_p \\ \stackrel{s\to\infty}{\longrightarrow} \frac{K_P f_c}{\imath f}(R + Z_c) + Z_p \end{cases} .$$

  We see that, for limited open-loop gain, noise affecting the plant Z_p is not eliminated at low frequencies. Additionally, at high frequencies, the gain for the error signal R drops like -6dB/oct.

- The second case is that of an integral servo $C(f) = K_I/\imath f$. Then Eq. (6.5) reads,

$$Y = \frac{K_I/\imath f}{1 + \imath f/f_c + K_I/\imath f}(R + Z_c) + \frac{1 + \imath f/f_c}{1 + \imath f/f_c + K_I/\imath f} Z_p$$
$$\begin{cases} \stackrel{f\to 0}{\longrightarrow} R + Z_c + \frac{\imath f}{K_I} Z_p \\ \stackrel{\to\infty}{\longrightarrow} \frac{K_I f_c}{(\imath f)^2}(R + Z_c) + Z_p \end{cases} .$$

  Apparently, the noise Z_p is now eliminated at low frequencies. However, the gain for R drops even faster at high frequencies.

[1] PID controllers are the most well established class of control systems: however, they cannot be used in several more complicated cases, especially if MIMO systems are considered.

- The third case is that of a PI-servo, $C(f) = K_P + K_I/\imath f$. Then Eq. (6.5) reads,

$$Y = \frac{K_P + K_I/\imath f}{1 + \imath f/f_c + K_P + K_I/\imath f}(R + Z_c) + \frac{1 + \imath f/f_c}{1 + \imath f/f_c + K_P + K_I/\imath f} Z_p$$
$$\begin{cases} \stackrel{f\to 0}{\longrightarrow} R + Z_c + \frac{\imath f}{K_I} Z_p \\ \stackrel{f\to\infty}{\longrightarrow} \frac{f_c K_P}{\imath f}(R + Z_c) + Z_p \end{cases},$$

  which represents a viable compromise, since it has the same low-frequency behavior as the I-servo, but at high frequencies the gain for R drops only like -6dB/oct.

- Finally, the forth case is that of a PID-servo, $C(f) = K_D \imath f + K_P + K_I/\imath f$. Then Eq. (6.5) reads,

$$Y = \frac{K_D \imath f + K_P + K_I/\imath f}{1 + \imath f/f_c + K_D \imath f + K_P + K_I/\imath f}(R + Z_c) + \frac{1 + \imath f/f_c}{1 + K_D \imath f + K_P + K_I/\imath f} Z_p$$
$$\begin{cases} \stackrel{f\to 0}{\longrightarrow} R + Z_c + \frac{\imath f}{K_I} Z_p \\ \stackrel{f\to\infty}{\longrightarrow} \frac{1}{1+1/f_c K_d}(R + Z_c) + \frac{1}{f_c K_D} Z_p \end{cases}.$$

  The low-frequency behavior remains still the same, but at high frequencies the gain for R stays constant.

A time domain analysis shows that P regulators have little phase lag, but the controlled variable can not be zeroed. On the other hand, I regulators have finite control bandwidth, but the controlled variable can be zeroed. PI regulators (parallel circuit of P and I regulators) have a reaction time $T_n = K_P/K_I$; that is, the jump response is advanced by T_n in comparison to the regulator I.

In the time domain we can summarize that regulators

- D are characterized by the absence of memory, but they are very fast,
- P have no idea of the strength of their impact,
- I increase their impact in time until the error disappears.

For practical PID controllers, a pure differentiator is neither physically realizable nor desirable due to amplification of noise and resonant modes in the system. Therefore, a phase-lead compensator type approach is used instead, or a differentiator with low-pass roll-off [43, 33, 34, 77]. See Excs. 6.2.3.1 and 6.2.3.2.

Like any real system, the controlled device behaves as a low-pass for manipulations or perturbations at high frequency. In other words, the device can only respond to external perturbations with finite speed. This delay of the response leads to a phase shift that can reverse the sign of the error signal $E(f)$ and transform a negative feedback into a positive feedback. Now, in the case that there are high frequency perturbations, for which the amplification of the closed control circuit is > 1, these perturbations can be amplified to form oscillations. These oscillations, which occur at the bandwidth of the closed loop gain are called *servo oscillations*.

Fig. 6.3 illustrates the necessity of optimizing the gain and the frequency response of the servo circuit: A proportional servo simply providing a frequency-independent gain $C(f) = K_P$ will lead to a forward gain $R(f) \propto P(f)$ exhibiting a low-pass behavior, i.e. a phase-shift $\phi = -\pi/2$ transforming negative to positive feedback. The gain at the frequency where this happens need to be lower than 1, otherwise the feedback servo will generate servo-oscillations, i.e. it will oscillate at the lowest Fourier frequencies where noise is amplified. A PI-servo alleviates this problem by a phase shift in opposite direction.

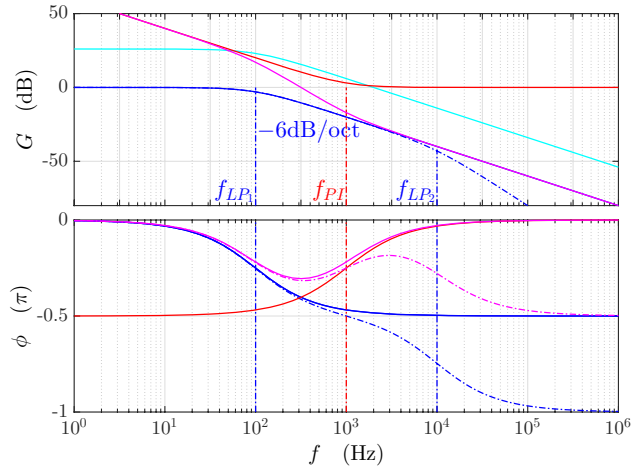

Figure 6.3: (code) Bode diagram for a plant subject to low-pass behavior and for a PI-servo. (blue solid) Low-pass filter with 100 Hz bandwidth; (blue dash-dotted) another low-pass filter at 100 kHz; (cyan) same as blue, but amplified by 20 dB; (red) PI-servo; (magenta) open-loop amplification.

6.1.3 Noise transfer in feedback loops

In order to develop a model for noise transfer we must understand what noise is and how it can be measured. This is not a simple task and we therefore outsourced a proper discussion to Sec. 7.3. Here, we will only use the information that noise affecting a signal $y(t)$ is quantified by a *spectral noise density* defined as the Fourier transform of the signal's autocorrelation function (7.59),

$$S_y(f) \equiv \mathcal{F}[\overline{y^*(t)y(t+\tau)}] \; . \tag{6.8}$$

Now, we can see how noise is transmitted through an LTI device $P(f)$:

$$\boxed{Y(f) = P(f)X(f) \quad \Rightarrow \quad S_y(f) = |P(f)|^2 S_x(f)} \; . \tag{6.9}$$

This result can be applied to our formula (6.5) describing a feedback loop,

$$\boxed{S_y(f) = \left|\frac{1}{1+V(f)^{-1}}\right|^2 S_c(f) + \left|\frac{1}{1+V(f)}\right|^2 S_p(f)} \; . \tag{6.10}$$

This formula describes how a servo control shapes the noise spectrum of a feedback-controlled variable $y(t)$.

Example 9 (*Noise reduction by feedback*): As an example, let us study the control circuit for stabilizing a laser to a cavity mode depicted in Fig. 6.1(b) using the following additional background information: The laser frequency ω be perturbed by $1/f$ noise described by the power spectral density,

$$S_p(f) \equiv 2 \cdot 10^{-24}/f \ .$$

This noise enters the feedback loop via the fluctuations $z_p(t)$ depicted in

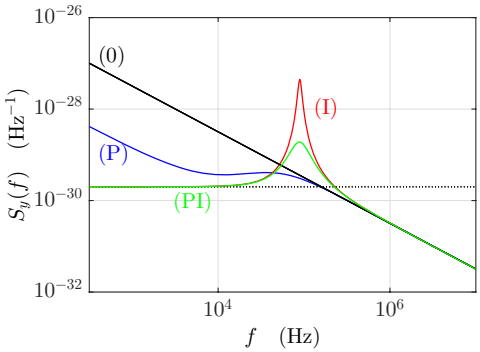

Figure 6.4: (code) Spectral density of frequency fluctuations of the servo system exhibited in Fig. 6.2. Shown is the spectral noise density $S_y(f)$ of the laser light for 4 different feedback gain curves: (black solid) no feedback control $C(f) = 0$, (blue) P-regulator with $C(f) = 4$, (red) I-regulator with $C(f) = 5 \cdot 10^6/\imath f$, and (green) PI-regulator $C(f) = 4 + 5 \cdot 10^6/\imath f$.

Fig. 6.1(a). The black solid line in Fig. 6.4 traces the noise spectrum $S_p(f)$, which is also the noise expected for the laser without feedback loop. Furthermore the optical cavity, which constitutes the essential part of the regulator, is itself afflicted by acoustic noise and thermal drifts which, for simplicity, we describe by a white Fourier frequency spectrum given by,

$$S_c(f) \equiv 2 \cdot 10^{-30}\,\mathrm{Hz}^{-1} \ ,$$

and represented by the black dotted line in Fig. 6.4. As we have seen, servos systems always have a finite bandwidth beyond which noise is fully coupled to the system. For example in laser frequency locks, the weakest point of a servo chain is often the small bandwidth of a piezo transducer used to correct the length of the laser cavity. We describe this behavior by a low-pass filter for the transfer function of the laser,

$$P(f) = \frac{1}{1 + \imath f/f_c}$$

with a bandwidth of $f_c = 10\,\mathrm{kHz}$.
Fig. 6.4 demonstrates how the $1/f$ noise $S_p(f)$ can be efficiently suppressed at frequencies below the low-pass filter cut-off f_c to a value limited by the white noise $S_c(f)$ entering through the regulator. As predicted by the formula (6.10), the suppression of the noise $S_p(f)$becomes all the better, as the open-loop gain

$V(f)$ gets higher. However, with the amplification of the controller, also the gain of the closed control circuit increases, and this necessarily causes phase shifts, which lead to (servo-)oscillations in the circuit appearing as a strong peak of strong noise around a certain Fourier frequency f_{bw} characterizing the bandwidth of the closed loop servo system. Note that high-frequency noise, to which the cavity might be subject, is not coupled to the laser, because it is filtered by the low-pass filter $P(f)$ to the same extend as the error signal itself.

The next example, exhibited in Fig. 6.5, shows the experimental characterization of a dye laser locked via the Pound-Drever-Hall technique (see Sec. 6.3.3) to an optical cavity.

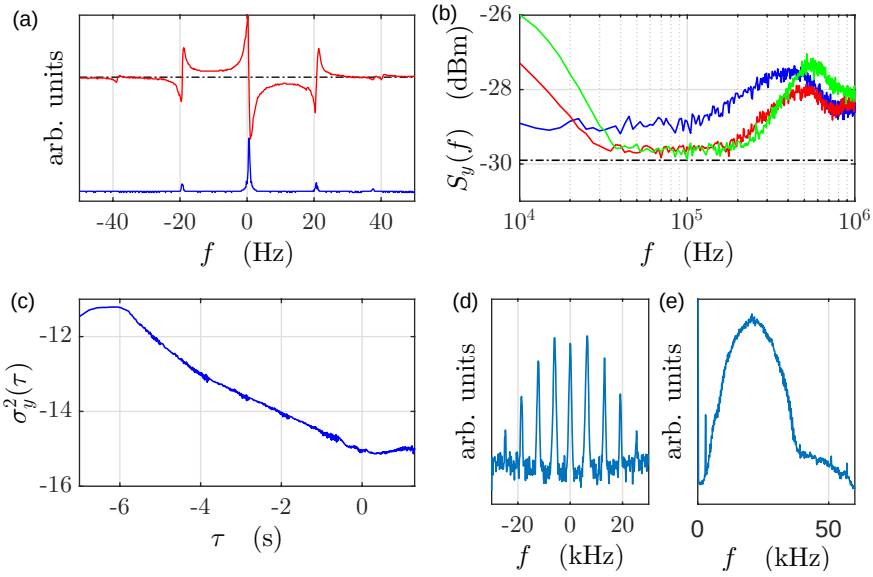

Figure 6.5: Characterization of a Pound-Drever-Hall stabilization of a dye laser. (a) PDH error signal (red) and cavity transmission signal (blue), (b) spectral density of frequency fluctuations, (c) Allan variance. (d-e) Beat signals of Mach-Zehnder interferometers. In (d) one interferometer arm is passed through an optical fiber attached to a piezo transducer to which a sinusoidal 5 kHz modulation of is applied. This demonstrates the sensitivity of optical fibers to acoustic noise. In (e) one interferometer arm is send to another optical table and back. This demonstrates how mechanical vibrations of optical components in the beam path can broaden the spectrum of a laser field.

6.2 Amplitude stabilization circuits

6.2.1 Laser intensity stabilization with an AOM

The light emitted from lasers is generally subject to *frequency fluctuations* and *intensity fluctuations*, which are unacceptable for many applications. In this section we will construct an *intensity stabilization* for a laser beam.

One way of stabilizing the light intensity of a laser beam consists in using the an acousto-optic modulator, as shown in Fig. 6.6. The first Bragg diffraction order (see Sec. 4.3.1) is focused onto a photodiode. Intensity fluctuations of the light recorded by the photodiode are converted into voltage fluctuations, processed by an electronic circuit fed back to the AOM. The intensity of light diffracted into the first order can be controlled via the power of the radiofrequency alimenting the AOM. The control circuit can now be conceived such as to neutralize the intensity fluctuations recorded by the photodiode.

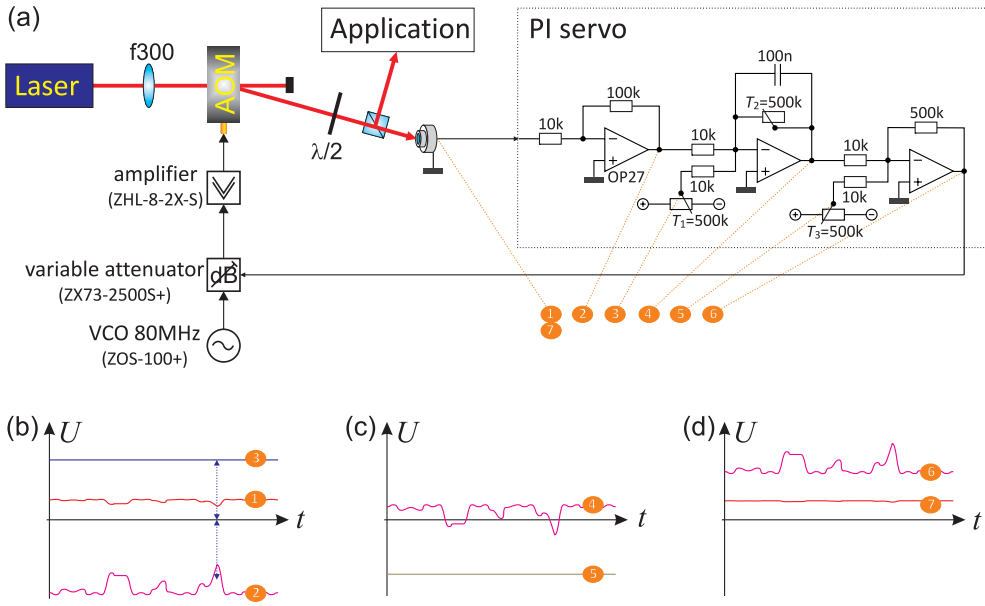

Figure 6.6: (a) Layout of the intensity control. The variable attenuator controls the amplitude of the radiofrequency driving the AOM: low voltage (0 V) increases the attenuation, high voltage (+16 V) reduces it. The sketched control circuit realizes a negative feedback, when the photodetector produces a positive signal. (b-d) Signals recorded at the test points of the circuits shown in (a). See text for explanations.

6.2.1.1 Operation principle and adjustment procedure

The idea of the intensity stabilization is illustrated in Fig. 6.6(b-d): The laser intensity scattered into the first diffraction order is recorded by a photodiode (test point 1 in the figure). The signal is then amplified (and inverted) by a first OpAmp (test point 2). The trimmer T_1 (test point 3) is now adjusted to a positive voltage compensating the DC part of the signal (2), i.e., the sum (2+3) after being inverted and amplified by the second OpAmp (test point 4), should be around zero DC. The signal (2+3) is called *error signal*, since it is this signal which tells us in which direction the control circuits has to work to counteract the power fluctuation. In the present design, the second OpAmp also incorporates the PI servo (see Sec. 6.1), which can be adjusted via the amplification of the trimmer T_2 and the capacity C.

It is now important to realize, that the variable attenuator works best around a given control voltage, which is provided by adding via the trimmer T_3 (test point 5) and a third OpAmp an appropriate offset. Furthermore, we note that variable attenuator reduces its attenuation with increasing control voltage. Thus, the control signal (test point 6) works to enhance the efficiency of the AOM, when the photodiode signals a power drop, and vice versa. As a result, the light power in the first diffraction order is stabilized, however, at a level inferior to the unstabilized power [77, 34].

The trimmers of the servo circuits can be adjusted using the following procedure:

1. Observe the light intensity and its fluctuations at test point (1), set test point (4) to ground (e.g. short-circuiting the trimmer T_2), and adjust trimmer T_3 until the light intensity level is at bit lower than the lowest fluctuations.
2. Reconnect test point (4) to the circuit and adjust trimmer T_1 until the voltage at test point (4) cancels to zero.

6.2.2 PI servo for a current stabilization

Many applications in quantum optics require very stable high currents, for instance, in coils generating magnetic field for atomic trapping potentials. Here, we will construct a *PI servo* to para realize a *current stabilization*.

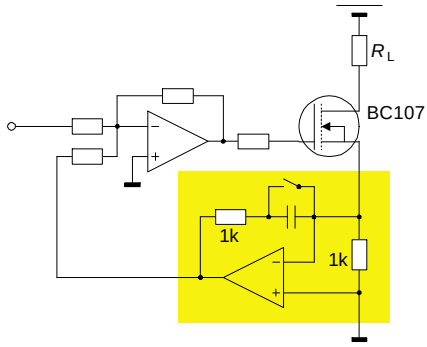

Figure 6.7: Current stabilization.

6.2.3 Exercises

6.2.3.1 Ex: Integrator

Determine the transfer function of the circuit depicted in Fig. 6.8. What kind of control circuit is it?

6.2.3.2 Ex: PID controller

Consider the PID controller transfer function in series,

$$C(f) = K\left(1 + \frac{1}{\imath f T_I}\right)(1 + \imath f T_D) \ ,$$

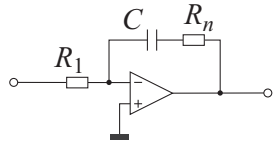

Figure 6.8:

a first-order low-pass filter in the feedback loop,

$$F(f) = \frac{1}{1 + \imath f T_F} \ ,$$

and a linear actuator with low-pass behavior,

$$P(f) = \frac{A}{1 + \imath f T_P} \ .$$

How do you have to choose the various time constants in order to let the closed-loop transfer function be $H(f) = 1$.

6.2.4 *Experiment: Development of an intensity stabilization*

We will now set up up an intensity stabilization. For the realization of the project prior knowledge of 1. photodetectors (see Sec. 3.2.1), 2. acousto-optic modulators (AOM) (see Sec. 4.3.1), 3. electronic circuits (see Sec. 3.1.3), and 4. control circuits (see Sec. 6.1) is required.

1. Realize the optical setup illustrated in Fig. 6.6. Optimize the alignment of the AOM (in particular, the focus and the Bragg angle) in order to maximize the efficiency of the AOM. Take care not to saturate the photodiode, if necessary adapt the load resistance (see Sec. 3.1.). Study the data sheet of the variable attenuator.

2. Derive and plot the transfer function for ac-signals of the electronic circuit. What kind of control circuit is it?

3. Set up the electronic circuit exhibited in Fig. 6.6. Test it by observing the signals at the six test points marked in the circuit diagram. Understand and interprete the roles of the three adjustable parameters: input offset, amplification, and output offset.

4. Incorporate the servo circuit into the optical setup as shown in Fig. 6.6. How to make sure the circuit is operating properly? [2].

[2] Datasheet for the VCO see appendix Fig. 7.16,
data sheet for the variable attenuator see appendix Fig. 7.17,
data sheet for the amplifier see appendix Fig. 7.15.

6.2.5 *Experiment: PI servo for a current stabilization*

How to control high currents? How to dramatically increase the switching speed despite inductive loads and eddy currents?

1. Connect a resistive charge to a voltage source. Insert a *MOSFET* into the circuit and a small resistor. Control the gate of the MOSFET with a voltage and measure the current of the circuit via the voltage drop at the small resistor as a function of the gate voltage.

2. Now control the gate voltage via the voltage measured at the small resistor and measure again the dependency voltage-to-current.

6.3 Frequency stabilization circuits

Although lasers are often monochromatic, they generally have a poor intrinsic frequency stability, that is, the frequency of the light field $E(t) = \sin \omega t$ drifts in time, $\omega = \omega(t)$ on a time scale, which is slow in comparison to the oscillation period $1/\omega$. The reasons for these drifts are typically acoustic noise or thermal drifts to which the laser device is subject and which are difficult to avoid.

Often it is much easier to guarantee the mechanical and thermal stability of a passive device exhibiting resonances, such as an optical cavity. Furthermore, nature provides intrinsically stable resonances, such as narrow atomic transitions. These resonances can be used to actively stabilize the frequency of lasers via feedback servo circuits. In the following sections we will present a few common techniques.

6.3.1 Side-of-fringe stabilization to/of a Fabry-Pérot cavity

Resonances are generally characterized by peaked profiles symmetrically centered about a resonance frequency ω_0. Excited by a laser field of frequency ω, they respond by an oscillation whose amplitude depends on the detuning $\omega - \omega_0$. Unfortunately, the amplitude of the response signal does not tell us, whether the detuning is positive or negative. We have to invent techniques allowing us to extract this information from the response signal and to generate a true error signal.

One of these techniques is the *side-of-fringe stabilization* technique illustrated in Fig. 6.9. Here, the laser tuned to one side of the optical resonance such that, when the laser frequency drifts, the response signal increases or decreases correspondingly. Technically, this is achieved by comparing (i.e. subtracting) the response signal with a stable reference signal.

6.3.2 Lock-in method for frequency stabilizing to/of a cavity

One method of stabilizing a laser on a resonator consists in modulating the frequency slightly and then demodulating the transmission signal of the resonator at the same frequency. This is the so-called *lock-in method*. Frequency modulation of the laser beam can be done by modulating the laser diode feed current, the piezo of the extended laser cavity or using an AOM. Fig. 6.10 shows the layout of the optical assembly.

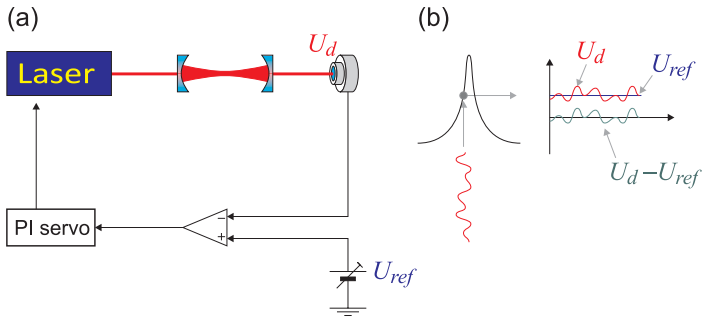

Figure 6.9: (a) Frequency stabilization to a cavity using the side-of-fringe method. (b) The laser is tuned to rising (or falling) slope of a transmission curve of a Fabry-Pérot cavity. The error signal is compared with reference voltage.

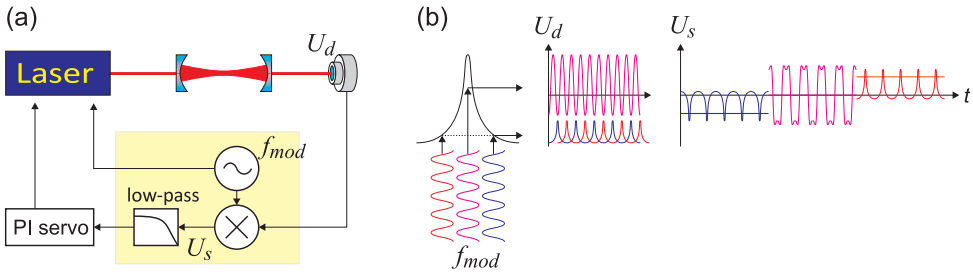

Figure 6.10: (a) Frequency stabilization to a cavity using the lock-in method. (b) Frequency-modulated signals applied to a resonance suffer a period doubling, when the signal frequency is close to resonance. By demodulating the signals discriminated at the resonance profile, we obtain, after averaging over a period, a DC voltage that is proportional to the frequency detuning. The yellow area denotes the components constituting the lock-in amplifier.

The principle of control through modulation is explained in Fig. 6.10(a). A laser beam passes twice (round-trip) through an *acousto-optic modulator* fed by a radiofrequency voltage with modulated frequency, $\omega(t) = \omega_c + M \cos ft$. Here, the modulation frequency is much lower than its amplitude (or frequency excursion), $f \ll M$. The laser beam is now injected into an optical cavity and the frequency of the laser tuned near a resonance of the cavity. The dependence of the transmission on the frequency is described in good approximation of the *Airy formula* by a Lorentzian,

$$I(\omega) = \frac{\gamma^2}{4(\omega - \omega_0)^2 + \gamma^2} \ . \tag{6.11}$$

The signal transmitted through the cavity [see Fig. 6.10(b)],

$$U_d(t) = I(\omega(t)) = \frac{\gamma^2}{4\left(\omega_c + M\cos ft - \omega_0\right)^2 + \gamma^2} \ , \tag{6.12}$$

is demodulated by a lock-in amplifier [see Fig. 6.10(c)],

$$U_s(t) = U_d(t)\cos(ft + \phi) \ , \tag{6.13}$$

integrated with a locking electronics [see Fig. 6.10(d)]

$$\bar{U}_s(t) = \frac{1}{T}\int_0^T U_s(t)dt \ . \tag{6.14}$$

and used to control the piezo of the laser's extended cavity.

6.3.3 Pound-Drever-Hall stabilization

When the frequency of a carrier wave ω is modulated by a frequency Ω [3], the spectrum consists of sidebands the frequencies and phases of which can be calculated from an expansion of the wave in Bessel functions. Let N be the modulation excursion and $J_k(x)$ the Bessel function of the order k. Higher-order sidebands $k > 1$ are usually dropped in the calculation,

$$e^{\imath(\omega t + N\sin\Omega t)} = e^{\imath\omega t}[-J_1(N)e^{\imath\Omega t} + J_0(N) + J_1(N)e^{-\imath\Omega t}] \ . \tag{6.15}$$

From the latter expression, it can be seen that the spectrum of sidebands is formed

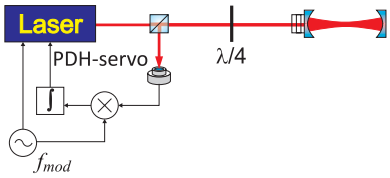

Figure 6.11: Frequency stabilization to a cavity using the Pound-Drever-Hall method.

by the frequencies ω and $\omega \pm \Omega$. A resonator responds to a field of incident light $E_0(\omega)$ oscillating with frequency ω by reflecting the field (R: reflectivity of mirrors, δ_{fsr}: free spectral range)

$$E_r(\omega) = E_0(\omega)\sqrt{R}\frac{1 - e^{-\imath\omega/\delta_{fsr}}}{1 - R\ e^{-\imath\omega/\delta_{fsr}}} \ , \tag{6.16}$$

where the amplitude and the phase of the reflected light field follow from the relation $E_r(\omega) = |E_r(\omega)|e^{\imath\phi(\omega)}$. Obviously the field of the reflected light is strong only, when the laser frequency is close to one mode of the resonator (when ω/δ is an integer number). By inserting Eq. (6.16) into Eq. (6.15), we obtain the response of the resonator to a field containing sidebands as a function of the frequency of light ω, of the modulation frequency Ω, and of the cavity finesse,

$$\begin{aligned} |E_{tot}|^2 &= |e^{\imath\omega t}[J_1(N)E_r(\omega+\Omega)e^{\imath\Omega t} + J_0(N)E_r(\omega) - J_1(N)E_r(\omega-\Omega)e^{-\imath\Omega t}]|^2 \\ &= J_0(N)J_1(N)E_r(\omega+\Omega)e^{\imath\Omega t} + J_0(N)J_1(N)E_r^*(\omega-\Omega)e^{\imath\Omega t} + ... + c.c. \ . \end{aligned} \tag{6.17}$$

The contributions of the reflected field to the current in the photodetector, $|E_r|^2$, oscillating with frequency Ω and extracted by the alternating current $e^{-i\Omega t + i\theta}$ (θ is

[3] Remember that we specify all frequencies except the free spectral range δ_{fsr} in radians.

an arbitrarily chosen phase angle), are

$$S_{PDH} = |E_{tot}|^2 e^{-i\Omega t + i\theta} \tag{6.18}$$
$$= J_0(N)J_1(N)\mathfrak{Re}\ \{e^{\imath\theta}[E_r^*(\omega)E_r(\omega+\Omega) - E_r(\omega)E_r^*(\omega-\Omega)]\} + \ldots\ .$$

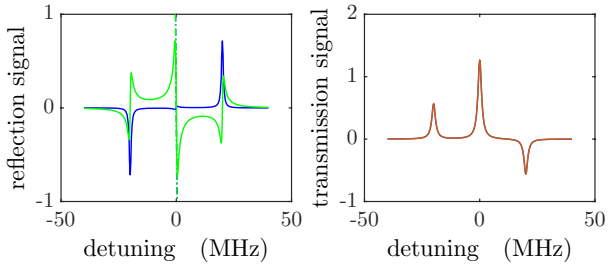

Figure 6.12: (code) (Left) Pound-Drever-Hall reflection signal for $\theta = 0, \pi/2$. (Right) Transmission signal.

By a suitable choice of the modulation index, the pre-factor containing Bessel functions (and therefore the signal amplitude) can be maximized. That is the case, for $M \simeq 1.1$ (see Exc. 4.4.5.1). Each of the two parts of the summation in the above equation is the result of a beating of the carrier $E_r(\omega)$ with one of the sidebands $E_r(\omega \pm \Omega)$. Only those optical sidebands being close to a mode of the resonator provide, along with the radiofrequency sidebands, contributions to the reflection signal

The dependence of the reflection signal S_{PDH} on the frequency ω is shown in Fig. 6.12(a). The antisymmetric shape and the zero-crossing slope are ideal for use as a discriminator generating an *error signal* for a frequency stabilization. This method is called *Pound-Drever-Hall method*.

6.3.4 Phase stabilization of standing waves

For the stabilization of the phase of a standing wave one can use the following scheme. It is similar to the homodyne method used with the Michelson interferometer with the difference that laser beam separation and recombination are done at different beam splitters.

6.3.5 Frequency-offset locking with phase-locked loops

Many application in spectroscopy require two stable lasers emitting at different but well-defined and tunable frequencies. Examples are stimulated Raman transitions, or the spectroscopy of atoms interacting with optical cavities [17]. In the following we will discuss and compare different approaches to locking one laser to another laser using a phase-locked loop (PLL). See also (watch talk).

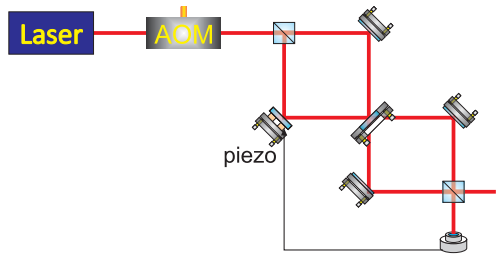

Figure 6.13: Phase stabilization.

6.3.5.1 VCO and mixing

In a *phase-locked loop* one tries to synchronize a self-sustained oscillator, in general realized by a VCO, with a local oscillator. The VCO generates an ac-voltage U_{rf}, whose frequency is tuned via a dc-control-voltage U_{ct} around a center frequency ω_0, as shown in Fig. 6.14(a). It can be modeled by,

$$\boxed{U_{rf}(t) = 2B\cos\phi(t) \qquad \text{with} \qquad \frac{d\phi}{dt} = \omega_0 + KU_{ct}(t)} \; . \tag{6.19}$$

The local oscillator produces an ac-voltage, $U_{lo}(t) = A\sin\phi_{lo}(t)$. A mixer multiplies both signals,

$$U_d(t) = AB\left(\sin[\phi_{lo}(t) - \phi(t)] + \sin[\phi_{lo}(t) + \phi(t)]\right) \; . \tag{6.20}$$

See also Exc. 6.3.7.1.

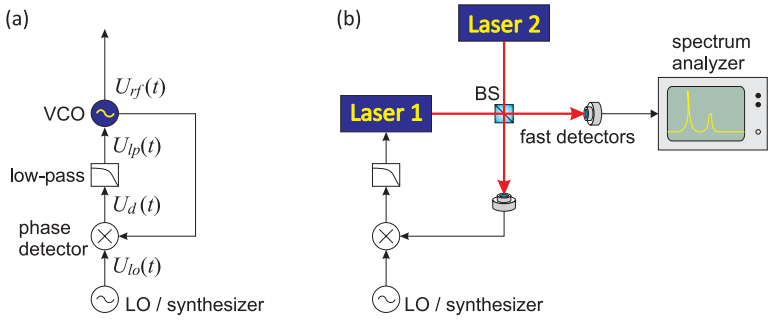

Figure 6.14: (a) PLL to lock a VCO to a reference oscillator LO. (b) PLL to lock the difference frequency of two lasers to a LO.

6.3.5.2 Low-pass filtering

The multiplied signal U_d contains all information about frequency deviations of the VCO from the LO. To extract them, we *low-pass filter* this signal, cutting off all high frequency components, i.e. apply the filter transfer function,

$$F(f) = (1 + sRC)^{-1} \; . \tag{6.21}$$

The signal of the filter is $U_{lp}(f) \equiv F(f)U_d(f)$. In time domain, which is obtained by a Laplace transform, $F(t) = (RC)^{-1}\theta(t)e^{-t/RC}$, such that

$$U_{lp}(t) = F \star U_d(t) = \int_{-\infty}^{\infty} F(t-\tau)U_d(\tau)d\tau = \frac{e^{-t/RC}}{RC}\int_{-\infty}^{t} e^{\tau/RC}U_d(\tau)d\tau \ . \quad (6.22)$$

The derivative is obviously,

$$\frac{dU_{lp}}{dt} + \frac{U_{lp}}{RC} = \frac{U_d(t)}{RC} = \frac{AB}{RC}\sin\left[\phi_{lo}(t) - \phi(t)\right] \ , \quad (6.23)$$

inserting the above expression for U_d. Note, that we would have obtained the same result using control theory (see Sec. 6.1).

6.3.5.3 Phase synchronization

The phase synchronization servo is closed by setting $U_{ct} = U_{lp}$. Thus we may substitute $U_{lp}(t)$ and define $\psi \equiv \phi - \phi_{lo}$,

$$\frac{d^2\psi}{dt^2} + \frac{1}{RC}\frac{d\psi}{dt} + \frac{KAB}{RC}\sin\psi = -\frac{d^2\phi_{lo}}{dt^2} - \frac{1}{RC}\left(\frac{d\phi_{lo}}{dt} - \omega_0\right) \ . \quad (6.24)$$

In most cases the LO frequency varies slowly, so that we may assume $\dot{\phi_{lo}} = \omega_{lo}$,

$$\frac{d^2\psi}{dt^2} + \frac{1}{RC}\frac{d\psi}{dt} + \frac{KAB}{RC}\sin\psi = -\frac{1}{RC}\left(\omega_{lo} - \omega_0\right) \ . \quad (6.25)$$

Hence, a PLL generates a signal $U_{rf}(t)$ having approximately the same (time-dependent) frequency as the local oscillator $U_{lo}(t)$. The equation is identical to that of an overdamped rotator or a resistively shunted Josephson junction [64].

We observe that the PLL is locking to servo oscillations. The spectrum of signal produced by the VCO exhibits sidebands as soon as the loop is closed. Their amplitude depends on the gain, their frequency varies with the offset voltage controlling the VCO.

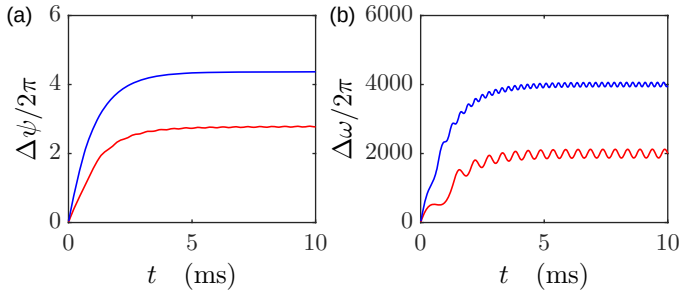

Figure 6.15: (code) Simulation of (a) the phase and (b) frequency difference in a PLL for (red) $\omega_{lo} - \omega_0 = (2\pi)$ 2 kHz and (blue) 4 kHz.

6.3.6 Frequency-offset locking using transfer cavities

Sometimes we want to take a ultra-high resolution spectrum in a frequency region, where there is no reference frequency available nearby. By nearby we mean frequency regimes which can be reached by PLLs based on frequency beats on fast photodetectors, as studied in Sec. 6.3.5. A possible method consists in the use of an optical *transfer cavity*.

Here, a reference laser stabilized to a known frequency ω_{ref}, e.g. via a saturation spectroscopy to an atomic transition, is used to lock a piezo-tunable optical cavity (called transfer cavity), as shown in Fig. 6.16. The cavity in turn is used to lock the spectroscopy laser $\omega_{blu-las}$, e.g. via the Pound-Drever-Hall method.

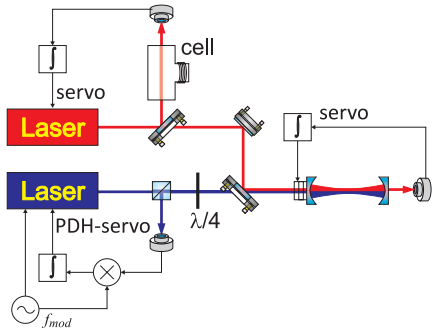

Figure 6.16: Schematic view of a transfer cavity locking system involving three cascaded servo systems for (i) the stabilization of the reference laser to a known frequency; (ii) of the transfer cavity to the reference laser, and (iii) of the spectroscopy laser to the transfer cavity.

Two issues need to be considered when using the transfer cavity scheme:

- The scheme does not permit tuning of the spectroscopy laser; this feature must be included using, e.g. AOMs (see Sec. 4.3.1) of PLL offset locks (see Sec. 6.3.5).
- The use of piezo in the transfer cavity is incompatible with its high-level thermal and mechanical stabilization. This means that special care must be taken in the design of the reference laser in order to avoid degradation of the stability of the transfer cavity via the servo lock.

The whole locking scheme consists of three cascaded servo loops (see Fig. 6.16). To model the transfer of stability from the reference to the spectroscopy laser, we write down the following relations,

$$\begin{aligned} \omega_{red-las} &= H_{sat}(f)\omega_{ref} \\ N_{red-trns}\delta_{fsr} &= H_{trns}(f)\omega_{red-las} \\ \omega_{blu-las} &= H_{pdh}(f)N_{blu-trans}\delta_{fsr} \ . \end{aligned} \tag{6.26}$$

In the absence of noise or for perfect servos, $H_x \to 1$, we get,

$$\omega_{blu-las} = \frac{N_{blu-trans}}{N_{red-trans}}\omega_{red-las} \ . \tag{6.27}$$

We assume specific transfer functions for the closed-loop gains of the three servos and describe the impact of noise by adding frequency deviations $\Delta\omega$ entering at various points.

6.3.7 Exercises

6.3.7.1 Ex: Schemes for laser tuning

Discuss the two PLL-setups shown in Fig. 6.17.

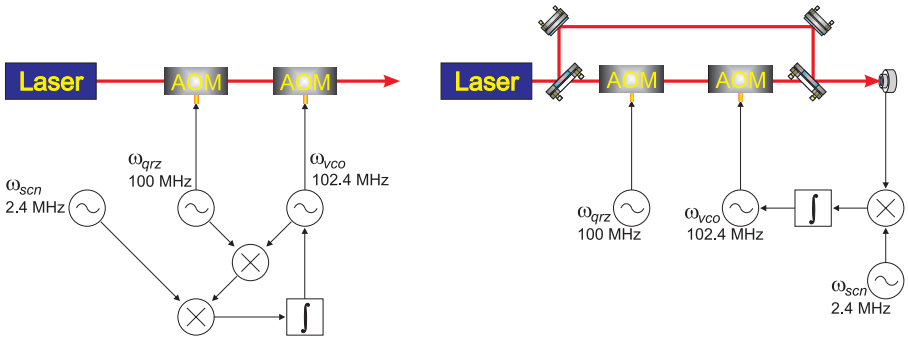

Figure 6.17: Two schemes for laser tuning.

6.3.8 *Experiment: Stabilizing a laser to a cavity*

Here is, how we are going to stabilize a laser to a cavity:

1. Stabilize a helium-neon laser to a Fabry-Pérot cavity, generating a frequency modulation by modulating the laser diode current or the piezo of the extended cavity. Choose a modulation frequency in the range of $f \simeq 1\,\text{kHz}$ and a modulation amplitude in the range of $M \simeq 5$ MHz. Adjust the reference voltage of the control electronics until the error signal is symmetrical.

2. If you do not have a lock-in amplifier available, construct one following the project Sec. 3.4.3.

3. Now, do the opposite, stabilizing the optical cavity to the laser frequency using the resonator piezo as control element.

4. Vary the optical setup now modulating the frequency using an AOM (see Fig. 6.18).

6.3.9 *Experiment: Pound-Drever-Hall locking*

Now we will stabilize a laser to a cavity using the Pound-Drever-Hall technique [14, 28]:

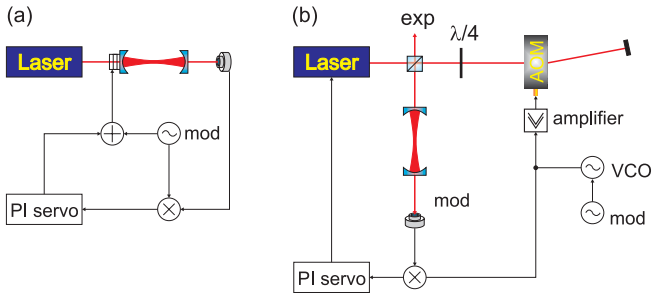

Figure 6.18: Variations on the same theme: (a) Frequency stabilization of a cavity to a laser frequency using the lock-in method. This method is often used for spectral filtering of a laser beam by a transmission etalon. (b) Frequency stabilization of a laser to a cavity using an AOM. The advantage of using an AOM compared to the scheme shown in Fig. 6.10 is, that only the beam injected into the cavity is modulated, but not the beam used for the main experiment.

1. Consider the reflected signal. To do this, separate the beam injected into the resonator from the reflected beam by means of a $\lambda/4$ waveplate and a polarizing beam splitter.

2. Now analyze the reflected signal with a fast photodetector at a spectrum analyzer.

3. Demodulate the signal with the modulation frequency. Vary the length of the cables. Optimize the slope of the error signal by a suitable choice of frequency and modulation excursion [4].

6.4 Further reading

6.4.1 on frequency noise description

D.W. Allan, *Statistics of atomic frequency standards* [DOI]

J.A. Barnes et al., *Characterization of frequency stability* [DOI]

J.L. Stewart, *The power spectrum of a carrier frequency modulated by Gaussian noise* [DOI]

D.S. Elliott et al., *Extracavity laser band-shape and bandwidth modification* [DOI]

L.S. Cutler, *Some Aspects of the Theorv and Measurement of Frequency Fluctuations in Frequency Standards* [DOI]

D.B. Sullivan et al., *Characterization of Clocks and Oscillators* [ISBN]

[4] Datasheet for the VCO see appendix Fig. 7.16,
data sheet for the power splitter see appendix Fig. 7.18,
data sheet for the mixer see appendix Fig. 7.19.

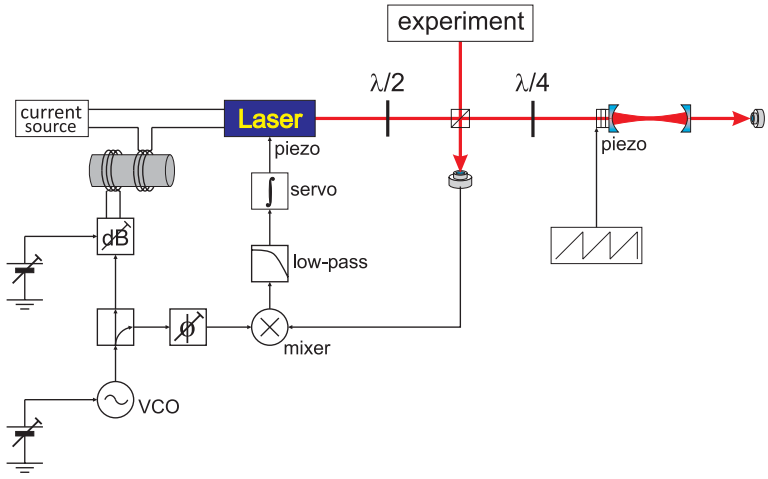

Figure 6.19: Setup of a frequency regulator following Pound-Drever-Hall. VCO: Voltage-Controlled Oscillator, LT: power splitter, dB: variable attenuator, LP: low-pass filter.

G. Di Domenico et al., *Simple approach to the relation between laser frequency noise and laser line shape* [DOI]

J. Appel et al., *A versatile digital GHz phase lock for external cavity diode lasers* [DOI]

L. Ricci et al., *A compact grating-stabilized diode laser system for atomic physics* [DOI]

G. Ritt et al., *Laser frequency offset locking using a side of filter technique* [DOI]

A.S. Arnold et al., *A simple extended-cavity diode laser* [DOI]

E.C. Cook et al., *High passive-stability diode-laser design for use in atomic-physics experiments* [DOI]

C.J. Hawthorn et al., *Littrow configuration tunable external cavity diode laser with fixed direction output beam* [DOI]

Huanqian Loh et al., *Influence of grating parameters on the linewidths of external-cavity diode lasers* [DOI]

Y. Shimada et al., *A simplified 461-nm laser system using blue laser diodes and a hollow cathode lamp for laser cooling of Sr* [DOI]

R.J. Steed, *Derivations of the Phase Noise Spectra of Lasers and of Lasers Passing Through Interferometers* [ISBN]

6.4.2 on laser stabilization

J. Alnis et al., *Stable diode lasers for hydrogen precision spectroscopy* [DOI]

J. Alnis et al., *Subhertz linewidth diode lasers by stabilization to vibrationally and thermally compensated ultralow-expansion glass Fabry-Pérot cavities* [DOI]

L. Couturier et al., *Laser frequency stabilization using a commercial wavelength meter* [DOI]

K. Huang et al., *Microcontroller-based locking in optics experiments* [DOI]

Shun Wu et al., *Direct fiber comb stabilization to a gas-filled hollow-core photonic crystal fiber* [DOI]

Y.N. Zhao et al., *Sub-Hertz frequency stabilization of a commercial diode laser* [DOI]

R.W.P. Drever et al., *Laser Phase and Frequency Stabilization Using an Optical Resonator* [DOI]

D. Budker et al., *Obtaining frequency markers of variable separation with a spherical mirror Fabry-Perot interferometer* [DOI]

6.4.3 on control theory

U. Tietze et al., *Halbleiterschaltungstechnik* [ISBN]

O. Föllinger et al., *Regelungstechnik: Einführung in die Methoden und ihre Anwendung* [ISBN]

Chapter 7

Appendices to 'Instrumentation of a Quantum Optics Lab'

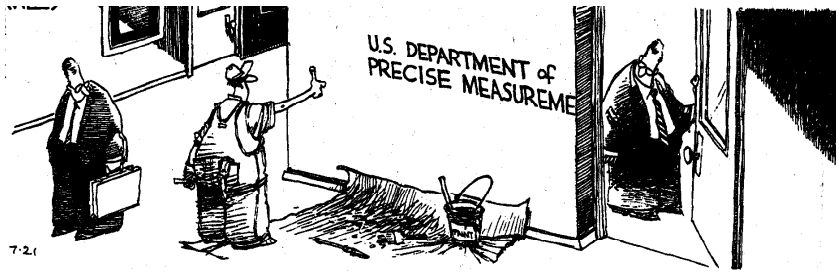

Figure 7.1: At the National Institute for Standards and Technology (NIST).

7.1 Calculating the uncertainty of measured quantities

7.1.1 Mean value and standard deviation

Mean value and *standard deviation* are defined by,

$$\bar{x} \equiv \frac{1}{N}\sum_k x_k \qquad \text{and} \qquad \sigma_{\bar{x}} \equiv \sqrt{\frac{1}{N-1}\sum_k (x_k - \bar{x})^2}\ . \tag{7.1}$$

The standard deviation can be weighed by a confidence parameter,

$$\bar{x} \equiv \frac{\sum_k w_k x_k}{\sum_k w_k} \qquad \text{and} \qquad \sigma_{\bar{x}} \equiv \frac{1}{\sqrt{\sum_k w_k}} \tag{7.2}$$

Weighing by individual standard deviation,

$$w_k \equiv \frac{1}{\sigma_k^2} \qquad \text{for} \qquad \sigma_k = \sigma_0 \tag{7.3}$$

gives,

$$\bar{x} \equiv \frac{\sum_k \frac{x_k}{\sigma_k^2}}{\sum_k \frac{1}{\sigma_k^2}} = \sigma_{\bar{x}}^2 \sum_k \frac{x_k}{\sigma_k^2} \overset{\sigma_k=\sigma_0}{\longrightarrow} \frac{1}{N}\sum_k x_k \quad \text{with} \quad \sigma_{\bar{x}} \equiv \frac{1}{\sqrt{\sum_k \frac{1}{\sigma_k^2}}} \overset{\sigma_k=\sigma_0}{\longrightarrow} \frac{\sigma_0}{\sqrt{N}} \tag{7.4}$$

or,

$$\hat{\sigma}_{\bar{x}} \equiv \sigma_{\bar{x}}\chi_v \overset{\sigma_k=\sigma_0}{\longrightarrow} \sqrt{\frac{1}{N-1}\sum_k (x_k - \bar{x})^2} \tag{7.5}$$

$$\chi_v = \sqrt{\frac{1}{N-1}\sum_k \frac{(x_k-\bar{x})^2}{\sigma_i^2}} \; .$$

From error propagation

$$\Delta\bar{x} \equiv \sqrt{\frac{1}{N}\sum_k \Delta x_k^2} \; . \tag{7.6}$$

7.1.1.1 χ^2-fit

The χ^2-fit of a constant of a function $y = f(x)$ to a measured data set (x_k, y_k) is,

$$\chi^2 = \frac{1}{N(N-1)}\sum_k [f(x_k) - y_k]^2 \; . \tag{7.7}$$

The above formula suggest that, increasing the number of measurements $N \to \infty$ we could pull the error to zero. This, however, is NOT TRUE. If the standard deviation is smaller than the precision Δ of the measurement tool, the error will be limited by Δ,

$$\bar{y} \pm \max(\sigma, \Delta) \; . \tag{7.8}$$

7.1.2 Error propagation

The *error propagation* for a function $f(x_1, x_2, ..)$ is given by,

$$\Delta f = \sqrt{\left(\frac{\partial f}{\partial x_1}\right)^2 \Delta x_1^2 + \left(\frac{\partial f}{\partial x_2}\right)^2 \Delta x_2^2 + ...} < \left|\frac{\partial f}{\partial x_1}\right| \Delta x_1 + \left|\frac{\partial f}{\partial x_2}\right| \Delta x_2 + ... \; . \tag{7.9}$$

Calculations can often be simplified by noting that the four fundamental operations, $f = x_1 \pm x_2$, $f = x_1 x_2$, and $f = \frac{x_1}{x_2}$ allow us to simply add the relative errors,

$$\frac{\Delta f}{f} = \frac{\Delta x_1}{x_1} + \frac{\Delta x_2}{x_2} \; . \tag{7.10}$$

Alternatively, we may use the following quick rules,

$$\begin{array}{rrcrl}
sum: & f \pm \Delta f = & (x \pm \Delta x) + (y \pm \Delta y) & = & (x+y) \quad \pm (\Delta x + \Delta y) \\
subtraction: & f \pm \Delta f = & (x \pm \Delta x) - (y \pm \Delta y) & = & (x-y) \quad \pm (\Delta x + \Delta y) \\
multiplication: & f \pm \Delta f = & (x \pm \Delta x)\cdot(y \pm \Delta y) & = & (x\cdot y) \quad \pm (x\Delta y + y\Delta x) \\
division: & f \pm \Delta f = & \frac{x\pm\Delta x}{y\pm\Delta y} & = & \frac{x}{y} \quad \pm \frac{1}{y^2}(x\Delta y + y\Delta x) \\
power: & f \pm \Delta f = & (x \pm \Delta x)^n & = & x^n \quad \pm n x^{n-1}\Delta x
\end{array} \; . \tag{7.11}$$

Example 10 (*Error propagation*): Let us study the following example,

$$f = \frac{x_1}{x_2 + a}$$
$$\Longrightarrow \Delta f = f\frac{\Delta x_1}{x_1} + f\frac{\Delta(x_2+a)}{x_2+a} = f\frac{\Delta x_1}{x_1} + f\frac{\Delta x_2}{x_2+a} \ .$$

7.1.3 Fitting a curve

We start defining the following prescription to calculate mean values,

$$\bar{x} \equiv \frac{1}{N}\sum_{k=1}^{N} x_k \quad , \quad \overline{xy} \equiv \frac{1}{N}\sum_{k=1}^{N} x_k y_k \ . \tag{7.12}$$

For a *fit* of a *linear curve* $f(x) = ax + b$ to a data set $\{x_k, y_k\}_{k\in[1,N]}$, we calculate ,

$$\boxed{f(x) = ax + b \quad , \quad a = \frac{\overline{xy} - \overline{x}\ \overline{y}}{\overline{x^2} - \overline{x}^2} = \frac{\overline{(x-\bar{x})y}}{\overline{(x-\bar{x})^2}} \quad , \quad b = \frac{\overline{y}\ \overline{x^2} - \overline{xy}\ \overline{x}}{\overline{x^2} - \overline{x}^2} = \overline{y} - a\overline{x}} \ . \tag{7.13}$$

The uncertainties are obtained via,

$$\Delta y = \sqrt{\frac{N}{N-2}\overline{(ax+b-y)^2}} \quad , \quad \Delta a = \Delta y\sqrt{\frac{1}{N\ (\overline{x^2} - \overline{x}^2)}} = \frac{\Delta y}{\sqrt{N\ \overline{x-\bar{x}}}} \tag{7.14}$$
$$, \quad \Delta b = \Delta y\sqrt{\frac{\overline{x^2}}{N\ \overline{x^2} - \overline{x}^2}} = \Delta y\sqrt{\frac{\overline{x^2}}{N\ \overline{x-\bar{x}}}} \ .$$

To fit an *exponential curve* $f(x) = \beta e^{\alpha x}$, we simply convert the data set $\{x_k, v_k\} \equiv \{x_k, \lg y_k\}$, calculate the mean values of the decadal logarithm using the recipe (7.12), and fit a linear curve $\tilde{f}(x) = \lg f(x) = \frac{\alpha}{\ln 10}x + \lg\beta \equiv ax + b$ in a semi-logarithmic scale to the data set $\{x_k, v_k\}$. This gives,

$$\boxed{f(x) = \beta e^{\alpha x} \quad , \quad \frac{\alpha}{\ln 10} = a = \frac{\overline{x\lg y} - \overline{x}\ \overline{\lg y}}{\overline{x^2} - \overline{x}^2} \quad , \quad \lg\beta = b = \frac{\overline{\lg y}\ \overline{x^2} - \overline{x\lg y}\ \overline{x}}{\overline{x^2} - \overline{x}^2}} \ . \tag{7.15}$$

To fit a *power law curve* $f(x) = \beta x^\alpha$, we simply convert the data set $\{u_k, v_k\} \equiv \{\lg x_k, \lg y_k\}$, calculate the mean values of the decadal logarithm using the recipe (7.12), and fit the linear curve $\tilde{f}(x) = \lg f(x) = \alpha\lg x + \lg\beta \equiv ax + b$ in a double-logarithmic scale to the data set $\{u_k, v_k\}$. This gives,

$$\boxed{f(x) = \beta x^\alpha \quad , \quad \alpha = a = \frac{\overline{\lg x\lg y} - \overline{\lg x}\ \overline{\lg y}}{\overline{\lg x^2} - \overline{\lg x}^2} \quad , \quad \lg\beta = b = \frac{\overline{\lg y}\ \overline{\lg x^2} - \overline{\lg x\lg y}\ \overline{\lg x}}{\overline{\lg x^2} - \overline{\lg x}^2}} \ . \tag{7.16}$$

7.1.4 Probability density

Consider a function $P(x)$ having the meaning of a *probability* depending on a variable $x \in [-\infty, \infty]$. The *probability density* $\rho(x)$ is defined as its derivative, $\rho(x) = P'(x)$, such that,

$$P(x) = \int_{-\infty}^{\infty} \rho(t)dt \qquad \text{with} \qquad P(-\infty) = 0 \qquad \text{and} \qquad P(\infty) = 1 \ . \tag{7.17}$$

Every probability must have the same likeliness, i.e.,

$$P(x) = \zeta_n \ , \tag{7.18}$$

where $\zeta_n \in [0, 1]$ is a uniformly distributed *random variable*. In order to numerically generate a *stochastic distribution*, we have to invert the distribution function, i.e. when ζ_n is generated by a computer, then

$$\boxed{x_n = P^{-1}(\zeta_n)} \tag{7.19}$$

is the distribution of the random variable x_n. In other words, a histogram of x_n reproduces the probability density $\rho(x)$.

Let us, for example, consider the Boltzmann distribution,

$$P(x) \equiv 1 - e^{-\beta x} \ . \tag{7.20}$$

Probing the probability with a random number, as in (7.18), we obtain the random variable via (7.19),

$$x_n = P^{-1}(\zeta_n) = -\frac{1}{\beta} \ln(1 - \zeta_n) \ . \tag{7.21}$$

The histogram of this random variable x_n can directly be compared with the probability density $\rho(x)$ given by,

$$\rho(x) = P'(x) = \beta e^{-\beta x} \ . \tag{7.22}$$

This is illustrated in Fig. 7.2(a).

Example 11 (*Probability density of a Gaussian distribution*): Another example is the *error function* given by,

$$\mathrm{erf}(x) \equiv \frac{2}{\sqrt{\pi}} \int_0^x e^{-t^2} dt \ .$$

By define the probability function,

$$P(x) \equiv \frac{1}{2}[\mathrm{erf}(x) - \mathrm{erf}(-\infty)] = \frac{1}{\sqrt{\pi}} \int_{-\infty}^x e^{-t^2} dt \ .$$

Probing the probability with a random number, as in (7.18), we obtain the random variable via (7.19),

$$x_n = P^{-1}(\zeta_n) = \mathrm{erf}^{-1}(2\zeta_n - 1) \ .$$

The histogram of this random variable x_n can directly be compared with the probability density $\rho(x)$, which is nothing else than the Gauss function,

$$\rho(x) = P'(x) = \frac{1}{\sqrt{\pi}} e^{-x^2} = 2\mathrm{erf}'(x) \ .$$

This is illustrated in Fig. 7.2(b).

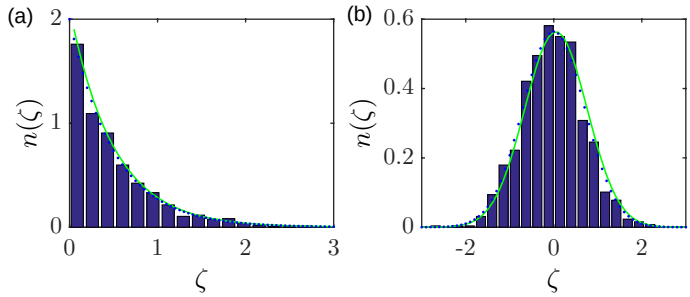

Figure 7.2: (code) (a) Boltzmann distribution simulated by random numbers (histogram). The numerical derivative of this distribution is shown as a blue dotted line, and the probability density as a green solid line. (b) Error function probability distribution simulated by random numbers (histogram). The numerical derivative of the error function is shown as a blue dotted line, and the Gauss function as a green solid line.

7.2 Deepening control theory

The variation of a physical quantity (e.g., a voltage or a temperature) in time is called *signal*. In a specific environment or technical device, such a variation may cause other physical quantities to change as well. For example, the rise in temperature of an optical cavity may modify its length and its resonance frequency, while the inverse is not true. This feature is illustrated by a block diagram as shown in Fig. 7.3, where $x(t)$ denotes the variation of a physical quantity (called *input*) that causes the variation of another quantity $y(t)$ (called *output*). The precise way how $y(t)$ depends on $x(t)$ depends on the particularities of the device, which is labeled by a symbol $\mathcal{T}$ called transfer function. $\mathcal{T}$ is in fact an operator acting on functions and transforming input signals into output signals.

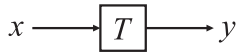

Figure 7.3: Transfer and modification of a time-dependent signal.

While we have described above the transfer of (time-varying) signals, the same feature can be treated in frequency domain via Fourier or Laplace-transforms. This script is not the right place to recapitulate the mathematics of these transforms, and we will restrict ourselves to reproducing some on the most fundamental results, as we may need them in the following.

7.2.1 Analysis techniques - frequency domain and time domain

Mathematical techniques for analyzing and designing control systems fall into two different categories:

Frequency domain: In this type the values of the state variables, the mathematical variables representing the system's input, output and feedback are represented

as functions of frequency. The input signal and the system's transfer function are converted from time functions to functions of frequency by a transform such as the Fourier transform, Laplace transform, or Z transform. The advantage of this technique is that it results in a simplification of the mathematics; the differential equations that represent the system are replaced by algebraic equations in the frequency domain which are much simpler to solve. However, frequency domain techniques can only be used with linear systems, as mentioned above.

Time-domain state space representation: In this type the values of the state variables are represented as functions of time. With this model the system being analyzed is represented by one or more differential equations. Since frequency domain techniques are limited to linear systems, time domain is widely used to analyze real-world nonlinear systems. Although these are more difficult to solve, modern computer simulation techniques such as simulation languages have made their analysis routine.

In contrast to the frequency domain analysis of the classical control theory, modern control theory utilizes the time-domain state space representation, a mathematical model of a physical system as a set of input, output and state variables related by first-order differential equations. To abstract from the number of inputs, outputs and states, the variables are expressed as vectors and the differential and algebraic equations are written in matrix form (the latter only being possible when the dynamical system is linear). The state space representation (also known as the 'time-domain approach') provides a convenient and compact way to model and analyze systems with multiple inputs and outputs. With inputs and outputs, we would otherwise have to write down Laplace transforms to encode all the information about a system. Unlike the frequency domain approach, the use of the state-space representation is not limited to systems with linear components and zero initial conditions. 'State space' refers to the space whose axes are the state variables. The state of the system can be represented as a point within that space.

7.2.1.1 Signal transfer through LTI systems without delay

For an operator $\mathcal{T}$ transforming a temporal signal $x(t)$ into a signal $y(t)$,

$$y(t) = \mathcal{T}x(t) \ , \tag{7.23}$$

to be *linear* and time-independent, we require,

$$\begin{aligned} \mathcal{T}[\alpha x_1(t) + \beta x_2(t)] &= \alpha \mathcal{T}[x_1(t)] + \beta \mathcal{T}[x_2(t)] \\ \mathcal{T}[x(t-\tau)] &= \mathcal{T}[x(t)] \star \delta(t-\tau) \ , \end{aligned} \tag{7.24}$$

where the $\star$ denotes a convolution,

$$(f \star g)(t) = \int_{-\infty}^{\infty} f(\tau) g(t-\tau) d\tau \ . \tag{7.25}$$

Such system are called *Linear Time-Independent LTI* systems [1].

[1] To be more general, also the derivative and integral of the output signal must be included (see later sections).

7.2.1.2 Laplace transform

We define the *Laplace transform* $\mathcal{L}$ as a linear operator acting on a signal $x(t)$ defined through,

$$\mathcal{L}... \equiv \int_{-\infty}^{0} ...e^{st}d\tau \ . \tag{7.26}$$

The frequency variable is denoted by the imaginary quantity $s = \imath f$. The question is now, what is the meaning of the Laplace operator?

To answer this question, we start introducing the pulse response $h(t)$ via

$$h(t) = \mathcal{T}[\delta(t)] \tag{7.27}$$

as the reaction of a system $\mathcal{T}$ to a pulse $\delta(t)$. Now, it is easy to see, that the operator $\mathcal{P}$ defined as,

$$\mathcal{P}... \equiv h(t) \star ... \ , \tag{7.28}$$

and which describes the convolution of an arbitrary input signal with the pulse response, satisfies the above linearity condition. Now calculating,

$$\mathcal{P}e^{st} = h(t) \star e^{st} = \int_{-\infty}^{0} h(\tau)e^{s(t-\tau)}d\tau = \mathcal{L}[h(t)] \cdot e^{st} = (\mathcal{L}h)(s) \cdot e^{st} \ , \tag{7.29}$$

we find that the functions e^{st} are eigenfunctions of the operator $\mathcal{P}$ with the eigenvalues $\mathcal{L}[h(t)]$, which are just the Laplace transforms of the pulse response.

We can now expand arbitrary functions $x(t)\theta(t)$ in a Laplace series and obtain,

$$\mathcal{L}[h(t) \star x(t)] = \int_{-\infty}^{0} h(t) \star e^{st} \ x(t)dt = (\mathcal{L}h)(s) \int_{-\infty}^{0} e^{st}x(t)dt = (\mathcal{L}h)(s) \cdot (\mathcal{L}x)(s) \ . \tag{7.30}$$

The convolution on the left-hand side is in time domain, while the product on the right-hand side is in frequency domain.

7.2.1.3 Pulse and jump response from a transfer function

The transmission of a signal by an element of a control loop can be described in the temporal or spectral domain [34, 35, 56], and we can switch from one representation to another via Laplace transformation. Operators of LTI systems $\mathcal{T}$ are represented by products with spectral functions in frequency-domain, $\tilde{F}(s) \cdot ... = (\mathcal{L}F)(s) \cdot ...$ or convolutions with time-varying functions in time-domain, $F(t) \star ...$,

$$\begin{aligned} y(t) &= \mathcal{T}x(t) \\ &\overset{Laplace}{\longrightarrow} \tilde{y}(s) = \tilde{F}(s) \cdot \tilde{x}(s) \\ &\overset{inverse\ Laplace}{\longrightarrow} y(t) = F(t) \star x(t) \ . \end{aligned} \tag{7.31}$$

In practice, the function $\tilde{F}(f)$ can be determined by feeding a sinusoidal signal with amplitude $x(s)$ into the system, measuring $y(s)$ (which is a complex number) [2],

[2] From now on, we will drop the tilde $\sim$ on transfer functions and amplitudes, when it is clear that we are in frequency-domain.

and calculating

$$F(s) = \frac{y(s)}{x(s)} \ . \tag{7.32}$$

The transitory behavior $F(t)$ can in practice be extracted via an adequate choice of the test function, f.ex., the response to a pulse:

$$\begin{aligned} x(t) &= \delta(t) \\ \overset{Laplace}{\longrightarrow} \quad y(s) &= F(s) \\ \overset{inverse\ Laplace}{\longrightarrow} \quad y(t) &= F(t) \ , \end{aligned} \tag{7.33}$$

or to a sudden jump:

$$\begin{aligned} x(t) &= \theta(t) \\ \overset{Laplace}{\longrightarrow} \quad y(s) &= F(s)/s \\ \overset{inverse\ Laplace}{\longrightarrow} \quad y(t) &= \int_0^t F(\tau) d\tau \ . \end{aligned} \tag{7.34}$$

Here, $\theta(t)$ denotes the Heavyside function, which is 1 for $t > 0$ and 0 else. The time-dependent function, which describes the pulse response is often used as a symbol for a specific control loop element.

The pulse response works in a similar way as the Green's function procedure: Wanting to know how a loop control element F transforms a given input signal $x(t)$ into an output signal $y(t)$, i.e., $y(t) = F(t) \star x(t)$, we produce a rapid pulse leading to the output,

$$y_\delta(t) = F(t) \star \delta(t) = F(t) \ . \tag{7.35}$$

Now, once we know $F(t)$, the response to arbitrary input signals can be computed via,

$$y(t) = y_\delta(t) \star x(t) \ . \tag{7.36}$$

7.2.1.4 Bode diagram and polar diagram

The *Bode diagram* illustrates the transfer function in the spectral domain on a bilogarithmic scale separating the amplitude spectrum from the phase spectrum [see Fig. 7.4(a-b)]. Frequency regions, where $|F(s)|$ or $\varphi(s)$ vary particularly strongly are nicely emphasized in the polar representation [see Fig. 7.4(c-d)].

For LTI systems $F(s)$ is always a rational function and can, hence, be represented by its poles and zeros in the complex plane,

$$F(s) = A \frac{(s-a_1)(s-a_2)...(s-a_n)}{(s-b_1)(s-b_2)...(s-b_n)} \ . \tag{7.37}$$

With this, $F(s)$ is analytical and conform, i.e., multiple curves in the s-plane are represented in an isogonal way in the $F(s)$-plane. In order to avoid that the eigenfunctions e^{st} oscillate and diverge, it is necessary that all the poles and zeros are in the left halfplane.

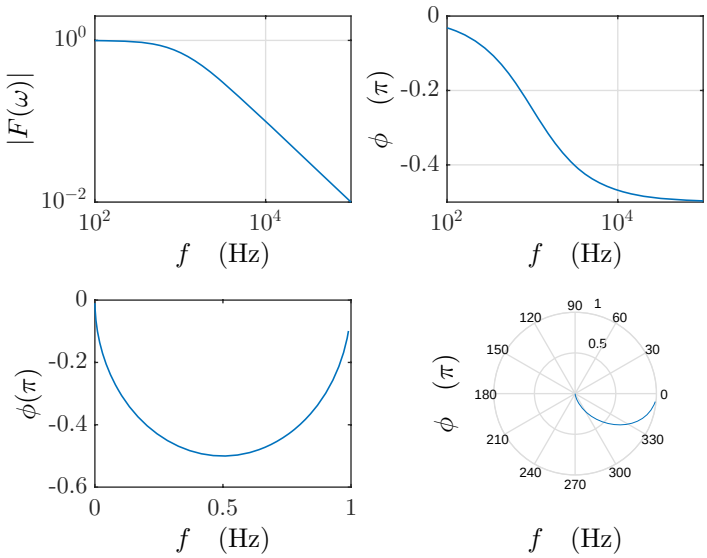

Figure 7.4: (code) Bode diagram.

7.2.2 Algebra of transfer circuits

A technical realization of a signal transfer circuit is illustrated by a signal flux diagram, which itself corresponds to the formalism of linear operators. As shown in Fig. 7.5, signals can be

- (a) added $(f_1 + f_2)(t) \equiv f_1(t) + f_2(t)$,
- (b) multiplied $(f_1 \cdot f_2)(t) \equiv f_1(t) \cdot f_2(t)$,
- (c) combined $f_1(t) = f_2(t)$,
- (d) transformed $f_2(t) = F[f_1](t) \equiv F(f_1(t))$,
- (e) connected in parallel $(F_1 + F_2)[f(t)] \equiv F_1[f(t)] + F_2[f(t)]$,
- (f) connected in series $(F_1 \circ F_2)[f(t)] \equiv F_1[F_2[f(t)]]$,

Mathematically, the functions $f(t)$ form a *vector space* and the operators $F[f]$ a *ring*. The linear operators generally are defined implicitly by a system of differential equations. The particular case of linear systems is considerably simpler. The general circuit shown in Fig. 7.5(g) corresponds to the differential equation,

$$0 = F[x_1, .., x_k, \partial_t x_1, .., \partial_t x_k, y_1, .., y_j] \ . \tag{7.38}$$

The linearity $F[\lambda f_1 + \mu f_2] = \lambda F[f_1] + \mu F[f_2]$ warrants that this equation becomes,

$$0 = [1 + \partial_t + ... + \int dt + ...]y_k = [1 + \partial_t + ... + \int dt + ...]x_j \ . \tag{7.39}$$

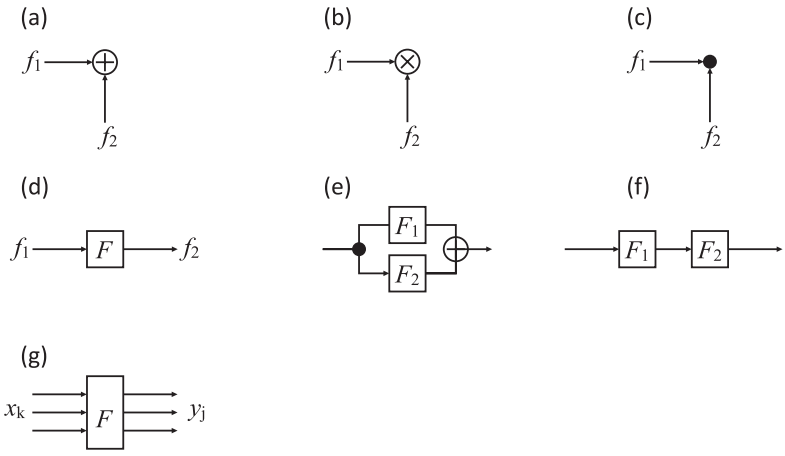

Figure 7.5: LTI circuits.

Note that the multiplication, the derivation, and the integration are linear operators in the same sense as the Fourier and the Laplace transformation.

Linear differential equations can be Laplace transformed. The corresponding transfer function is,

$$F(s) = F(-\delta + \imath\omega) \equiv \frac{\mathcal{L}y(t)}{\mathcal{L}x(t)} \ . \tag{7.40}$$

In the Laplace-transformed space the operations multiplication, derivation, and integration are all replaced by multiplications:

$$\mathcal{L}[\lambda + \partial_t + ... + \int dt + ...] = \lambda + s + ... + \frac{1}{s} \ . \tag{7.41}$$

With this, the control loop elements and the additive nodes can be used to completely represent a control circuit.

The characteristic responses of components are frequently non-linear (e.g. transistor). For small signal amplitudes, these response functions, and also multiplication points (e.g. mixers) can be linearized by Taylor expansion up to first order,

$$\begin{aligned} y_0 + \Delta y &= F[x_{01} + \Delta x_1, ..., x_{0k} + \Delta x_k] \\ &= F[x_{01}, ..., x_{0k}] + \left(\frac{\partial F}{\partial x_1}\right)_0 \Delta x_1 + ... + \left(\frac{\partial F}{\partial x_k}\right)_0 \Delta x_k \ , \end{aligned} \tag{7.42}$$

with $y_0 = 0 = F[x_{01}, ..., x_{0k}]$ giving,

$$\Delta y = \left(\frac{\partial F}{\partial x_1}\right)_0 \Delta x_1 + ... + \left(\frac{\partial F}{\partial x_k}\right)_0 \Delta x_k \ . \tag{7.43}$$

For example for a multiplication point,

$$\Delta y = K_1 \Delta x_1 + K_2 \Delta x_2 \ . \tag{7.44}$$

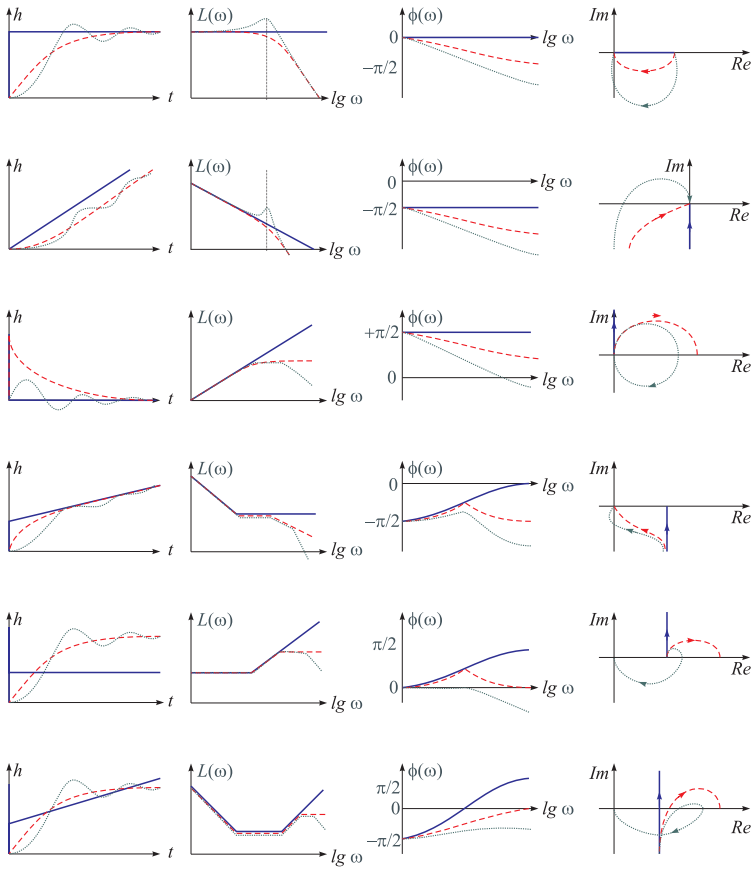

Figure 7.6: Transfer function $h(t) = \frac{y(t)}{x_w}$, Bode diagram amplitude $L(\omega) = 20 \lg |F_R|$ and phase $\varphi = \arctan \frac{\Im \mathfrak{m} \ F_R}{\Re \mathfrak{e} \ F_R}$, and polar representation $F(i\omega) = \Re \mathfrak{e} \ F_R + i \Im \mathfrak{m} \ F_R$ of the most common regulators. With delay time (—), $T_2 = T_1 = 0$, first order with delay time (- - -), $T_2 = 0 \neq T_1$, and second order $(\cdots)$, $T_2 \neq 0 \neq T_1$. From top to bottom, the diagrams show the regulators P, I, D, PI, PD, and PID, described by the equations (7.45) and (7.46).

7.2.2.1 Regulators

For many circuits, it is sufficient to restrict to combinations of resistive (proportional), capacitive (integral), and inductive (differential) circuits. Then, the general case of a control regulator is that of a $PID - T_1 ... T_n$-element, meaning that:

$$T_2^2 \ddot{y} + T_1 \dot{y} + y = K_D \dot{x} + K_P x + K_I \int dt x = K_P \left(x + T_v \dot{x} + \frac{1}{T_n} \int dt x \right) \ , \quad (7.45)$$

corresponding to the transfer function,

$$F(s) = \frac{K_D s + K_P + K_I / s}{1 + T_1 s + T_2^2 s^2} = \frac{(1 + T_v s + 1/T_n s)}{1 + T_1 s + T_2^2 s^2} \ . \quad (7.46)$$

In literature, two notations are used for the constants. They are linked via: $K_D \equiv K_P T_v$ and $K_I \equiv K_P / T_n$. The stationary behavior is obtained setting the delays to

zero: $T_n \equiv 0$.

Example 12 (*PID regulators*): For example, for a *proportional regulator*, we have,

$$y = K_P x_w \qquad \text{and} \qquad F_R = K_P \ , \tag{7.47}$$

for an *integral regulator* with time delay T_1, we have,

$$T_1 \dot{y} + y = K_I \int x_w dt \qquad \text{and} \qquad F_R = \frac{K_I}{s(1+sT_1)} \ , \tag{7.48}$$

or for a *PID regulator* without delay, we have,

$$y = K_P x_w + K_D \dot{x}_w + K_I \int x_w dt \qquad \text{and} \qquad F_R = K_P + \frac{K_I}{s} + K_D s \ . \tag{7.49}$$

Since there are three basic operations (multiplication with 1, s and $1/s$), in the end, all rational circuit elements can be reduced to an addition and concatenation of proportional $F(s) = K_P$, integral $F(s) = K_I/s$, and differentials elements, $F(s) = K_D s$. In particular, $PID{-}T_1 ... T_n$ circuits can be constructed by putting in parallel P, I, and D regulators concatenated with delay elements T_1. The possibility of feedback opens other possibilities [see Fig. 7.7(a)].

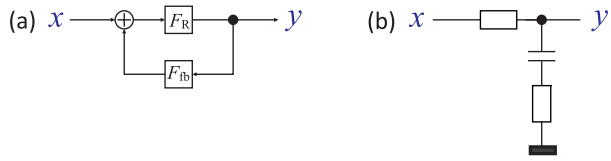

Figure 7.7: (a) Circuit with feedback, (b) low-pass filter circuit.

Example 13 (*Low-pass filter and time delays*): We consider the example of a low-pass filter exhibited in Fig. 7.7(b) and described by the equation,

$$F(\imath\omega) = \frac{R + \imath\omega L + 1/\imath\omega C}{R_i + R + \imath\omega L + 1/\imath\omega C} \ . \tag{7.50}$$

I.e., we have a $PID - T_1 T_2$ circuit.
Another example, is the dead time circuit,

$$y(t) = x(t - T_t) \quad \text{and} \quad F(s) = e^{-sT_t} \ . \tag{7.51}$$

We have,

$$F(\imath\omega) = e^{-\imath\omega T_t} F_0 \quad \text{and} \quad |F(\imath\omega)| = F_0 \quad \text{and} \quad \varphi(\imath\omega) = -\omega T_t \ . \tag{7.52}$$

Hence, dead time circuits produce phase shifts, which are proportional to the dead time interval T_t.

7.2.2.2 Heuristic rules for the Bode diagram

Any deviation of the amplitude spectrum from $n \cdot 6$dB/octave to $(n+1) \cdot 6$dB/octave causes a retardation in the phase spectrum of 90°. At the cut-off frequency, where the inclination changes its behavior, the phase shift is just 45°. A deviation to higher/lower inclinations shifts the phase by ±90°. (This does not hold for some phase-shifting circuits).

7.2.2.3 Transfer function of feedback circuits

Fig. 7.7 shows the idea underlying the feedback,

$$F(s) = \frac{1}{1/F_R - F_{fb}} \ . \tag{7.53}$$

For example, for $F_R = 1/T_1 s$ and $F_{fb} = -1$ we have,

$$F(s) = \frac{1}{1 + T_1 s} \ , \tag{7.54}$$

which corresponds to a delay element (or high-pass filter).

For F_r being a proportional element, we say that the feedback rigid, for F_r being differential, the feedback is anticipating, and for F_r being integral, the feedback is delaying.

7.2.3 Stability of feedback circuits

As discussed above, the transfer function of the feedback circuit is,

$$H(s) = \frac{F(s)}{1 + F(s)F_{fb}(s)} \ . \tag{7.55}$$

The *open loop gain* is $V(s) = F(s)F_{fb}(s)$. The circuit is stable, when for all the eigenfunctions e^{st}, that do not decay with $Re\ s \geq 0$, the transfer function of the feedback circuit is finite, $H(s) < \infty$.

An equivalent criterion is the *Nyquist criterion*: *The curve $V(i\omega)$ to $\omega \in [0; \infty[$ must always bypass the point of instability at $Re\ s = -1$ leaving it on the left side. That is, considering negative frequencies, the curve should not circle this point.* Fig. 7.9 shows an example.

7.2.4 Further topics in control theory

7.2.4.1 Nonlinear control theory

Linear control theory applies to systems made of devices which obey the superposition principle, which means roughly that the output is proportional to the input. They are governed by linear differential equations. A major subclass is systems which in addition have parameters which do not change with time, called linear time invariant (LTI) systems. These systems are amenable to powerful frequency domain mathematical techniques of great generality, such as the Laplace transform, Fourier transform, Z transform, Bode plot, root locus, and Nyquist stability criterion. These lead to a description of the system using terms like bandwidth, frequency response, eigenvalues, gain, resonant frequencies, poles, and zeros, which give solutions for system response and design techniques for most systems of interest.

Nonlinear control theory covers a wider class of systems that do not obey the superposition principle, and applies to more real-world systems, because all real control systems are nonlinear. These systems are often governed by nonlinear differential equations. If only solutions near a stable point are of interest, nonlinear systems can often be linearized by approximating them by a linear system using perturbation theory, and linear techniques can be used.

P-servo with rigid feedback	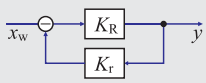	*P*	$K_P = \frac{K_R}{1+K_r K_R} \xrightarrow{K_P \to \infty} \frac{1}{K_r}$
P-servo with yielding feedback	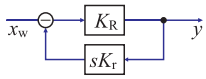	*P*-T_1	$K_P = K_R \;,\; T_1 = K_R K_r$ for $K_R \ll \infty$
		I	$K_I = K_r^{-1}$ for $K_R \to \infty$
P-servo with yielding feedback	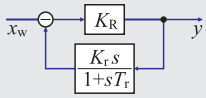	*PD*-T_1	$K_P = K_R \;,\; T_v = T_r \;,\; T_1 = T_r + K_r K_R$ for $K_R \ll \infty$
		PI	$K_P = T_r/K_r \;,\; T_n = T_r$ for $K_R \to \infty$
P-servo with delayed feedback	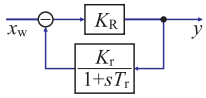	*PD*-T_1	$K_P = \frac{K_R}{1+K_r K_R} \;,\; T_v = T_r \;,\; T_1 = \frac{T_r}{1+K_r K_R}$ for $K_R \ll \infty$
		PD	$K_P = 1/K_r \;,\; T_v = T_r$ for $K_R \to \infty$
P-servo with delayed yielding feedback	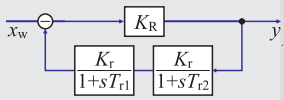	*PID*	$K_P = \frac{T_{r1}+T_{r2}}{K_{r1}K_{r2}} \;,\; T_v = \frac{T_{r1}T_{r2}}{T_{r1}+T_{r2}} \;,\; T_n = T_{r1}+T_{r2}$ for $K_R \to \infty$
P-servo with two delay circuits in the feedback	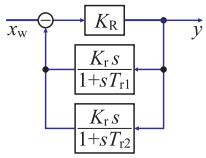	*PID*	$K_P = \frac{T_{r1}+T_{r2}}{K_{r1}(T_{r1}-T_{r2})} \;,\; T_v = \frac{T_{r1}T_{r2}}{T_{r1}+T_{r2}} \;,\; T_n = T_{r1}+T_{r2}$ for $K_R \to \infty$ and $T_{r1} > T_{r2}$
I-servo with rigid feedback	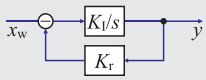	*P*-T_1	$K_P = \frac{1}{K_r} \;,\; T_1 = \frac{1}{K_I K_r}$
I-servo with yielding feedback	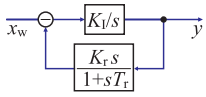	*PI*-T_1	$K_P = \frac{K_I T_r}{1+K_I K_r} \;,\; T_n = T_r \;,\; T_1 = \frac{T_r}{1+K_I K_r}$

Figure 7.8: Some examples for feedback regulators. The columns show from left to right: the nomenclature, the circuit diagram, the behavior, and the constants of the LTI system.

7.2.4.2 MIMO control systems

In this script we restrict to *single-input single-output control systems* (*SISO*), which is the simplest and most common type, in which one output is controlled by one control signal. Examples are the temperature control or an audio system, in which the control input is the input audio signal and the output is the sound waves from the speaker.

In contrast, *multiple-input multiple-output control systems* (*MIMO*) are found in more complicated systems. For example, modern large telescopes such as the Keck and MMT have mirrors composed of many separate segments each controlled by an actuator. The shape of the entire mirror is constantly adjusted by a MIMO active optics control system using input from multiple sensors at the focal plane, to compensate for changes in the mirror shape due to thermal expansion, contraction, stresses as it is rotated and distortion of the wavefront due to turbulence in the atmosphere.

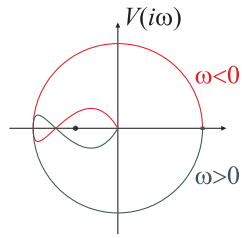

Figure 7.9: Illustration of the Nyquist criterion.

Another example are ultra-stable laser systems stabilized by combinations of fast actuators with low dynamic range and slow actuators with large dynamic range.

7.2.5 Exercises

7.2.5.1 Ex: Step response

Calculate the step response of a low-pass filter using the Laplace transform formalism.

7.3 Characterization of stability

The quality factor of a resonance measured with an oscillator in its function as a measuring apparatus for the resonance frequency is named *precision*. The precision also includes the perturbations to which the controlled oscillator is exposed and can be understood as the standard deviation of the frequency realized by the standard. The temporal or spectral behavior of precision, i.e. the stability can e.g. measured directly by comparing similar but independent standards. The reciprocal of the spread of the frequency realizations of an ensemble of similar standards is called *reproducibility*. The term reproducibility is also used to compare the frequencies of an individual standard before and after readjustment of all its technical parameters.

The *accuracy* is defined as the degree of agreement between the frequency realized by the standard and the defined standard frequency, i.e. the frequency that would be displayed in the fault-free ideal case [3]. The accuracy is always less than the quality of the resonance and the certainty of it center frequency. It includes the precision and limits the reproducibility [3]. The fact that the accuracy is related to the ideal case of absent errors implies that it cannot be measured directly. It must be inferred indirectly through model assumptions regarding the measuring apparatus estimating the probability for presumed or possible errors. We then speak of the *uncertainty* of the measured value [20].

The temporal or spectral behavior of *accuracy* is called *stability*. It is measurable and is quantified in the frequency domain by the *spectral density of fluctuations* and in the time domain best by the *Allan variance*. The noise is now the physical phenomenon that manifests itself as a deviation from the optimal stability.

[3]For example, when a measurement apparatus for the constant π provided the value $x = 3.141\ 59\ (12)$, then the accuracy is $x - \pi$ and the precision 0.000 12.

The stability that an ideal frequency standard can achieve in principle is proportional to quality factor of the resonance $\omega/(\Delta\omega_{nat}+\Delta\omega_{broaden})$ and the signal-to-noise ratio of the control signal S/N. Hence, the stability can be optimized by choosing atomic transitions with small spontaneous decay rates $\Delta\omega_{nat}$. Appropriate techniques for the experimental preparation of the resonance limit the influence of line broadening mechanisms $\Delta\omega$. According to the Fourier theorem, the resolution of narrow lines requires long observation times. Now, the control signal of a feedback regulator can only be determined after a whole observation period. This means that the apparatus already must have an intrinsic stability good enough that the frequency does not leave the control range during a period of observation. Furthermore, a better signal-to-noise ratio can improve the precision with which the line center of the resonance can be determined.

Ultimately, the most promising way to increase the accuracy of a frequency standard seems to be to choose the highest possible transition frequencies ω, provided that the oscillations can still be counted electronically, or be linked in a phase-coherent way to oscillators generating countable oscillations, e.g. using frequency combs. The requirement of phase coherence at optical frequencies puts the laser in the focus of interest in metrology.

7.3.1 Quantifying frequency fluctuations

The following sections deal with perturbation-induced fluctuations of the laser frequency, i.e. frequency noise. To characterize the behavior of an oscillator (especially when used as a frequency standard), it is necessary to introduce some concepts that allow the quantitative description of the noise. The most important are reproducibility, stability, spectral density of fluctuations, Allan variance, and emission bandwidth. The basic work on this has been carried out at the National Bureau of Standards (NBS) in Boulder, Co, USA [2, 3, 8, 23].

7.3.1.1 Stability in the frequency domain, spectral fluctuation density

The instantaneous amplitude of an oscillator, e.g. the electric field of a laser radiation, can be written,

$$\mathcal{E}(t) = \mathcal{E}_0(t)e^{\imath\phi(t)} \ . \tag{7.56}$$

noise afflicts phase and amplitude. In the following we will neglect amplitude noise, $\mathcal{E}_0(t) = \mathcal{E}_0$, and if the frequency fluctuations only deviate slightly from a mean value, $\omega_0 \gg |\dot{\varphi}(t)|$, we may write,

$$\phi(t) \equiv \omega_0 t + \varphi(t) \ . \tag{7.57}$$

In the following, we will often consider normalized frequency fluctuations,

$$y(t) = \dot{\varphi}(t)/\omega_0 \ . \tag{7.58}$$

When measuring stability, one must differentiate between *deterministic fluctuations* and *stochastic noise*. Deterministic fluctuations are usually due to inadequate control of equipment parameters. They generate systematic errors and slow drifts $y_{sys}(t)$ which, if one recognizes them as such in time domain measurements (measure for sufficiently long times!), can be subtracted and disregarded. Stochastic noise,

however, is stationary:

$$\overline{y_{sto}(t)} = \overline{y(t) - y_{sys}(t)} = 0 \qquad \text{defining} \qquad \overline{y(t)} \equiv \lim_{T\to\infty} \frac{1}{T} \int_0^T y(t)dt \tag{7.59}$$

as the time average. In the following only stationary stochastic fluctuations are considered.

Let us take a look at the *autocorrelation function* of the phase defined as,

$$\boxed{R_y(\tau) \equiv \overline{y^*(t)y(t+\tau)} = \lim_{T\to\infty} \frac{1}{T} \int_0^T y^*(t)y(t+\tau)\rangle d\tau} \tag{7.60}$$

and the *spectral density of phase fluctuations* which, according to the *Wiener-Khintchine theorem*, can be obtained as the Fourier transform of the autocorrelation function,

$$\boxed{S_y(f) \equiv \mathcal{F}R_y(\tau) = \int_{-\infty}^{\infty} R_y(\tau)e^{-2\pi\imath f\tau}d\tau} \ . \tag{7.61}$$

The normalized density of frequency fluctuations $S_y(f)$ is a spectral quantity with the unit 1/Hz. Frequency and phase fluctuations are linked by:

$$S_{\dot{x}}(f) = f^2 S_x(f) \ , \tag{7.62}$$

as will be shown in Exc. 7.3.3.1. Also,

$$S_{ax}(f) = a^2 S_x(f) \ , \tag{7.63}$$

If the integral of the spectral fluctuation density is finite it corresponds, according to the definition (7.62), to the noise power or the mean square deviation of a measured variable:

$$\int_0^{\infty} S_y(f)df = R_y(0) = \overline{|y(t)|^2} < \infty \ . \tag{7.64}$$

7.3.1.2 Model of noise

Measurements seem to confirm today that stochastic fluctuations in frequency standards can be traced back to a few additive noise processes with different physical origins and different frequency responses [2]:

$$\boxed{S_y(f) = \sum_{\beta=-2}^{2} h_\beta f^\beta} \ . \tag{7.65}$$

The table below lists the most common ones.

This noise model is based on the assumption that the noise processes it describes operate in all Fourier frequency ranges, which violates the requirement (7.64). The dilemma does not arise in experiment, since the integration over an unlimited Fourier frequency range is not a realistic concept in that each measurement only takes a finite time τ, so that very low frequencies below a cut-off frequency $f_{min} = 2\pi/\tau$ are not

noise type	$S_x(f)$	$S_y(f)$	$\sigma_y^2(\tau)$
white phase noise	h_2	$h_2 f^2$	$\propto \frac{h_2}{\tau^2}$
flicker phase noise	$h_1 f^{-1}$	$h_1 f^1$	$\propto \frac{h_1}{\tau^2}$
white frequency noise	$h_0 f^{-2}$	$h_0 f^0$	$\frac{h_0}{2\tau}$
flicker frequency noise	$h_{-1} f^{-3}$	$h_{-1} f^{-1}$	$h_{-1} 2 \ln 2$
random walk frequency drifts	$h_{-2} f^{-4}$	$h_{-2} f^{-2}$	$h_{-2} \frac{(2\pi)^2}{6} \tau$

Table 7.1: *Spectral fluctuation density and Allan-variance for common noise processes [8].*

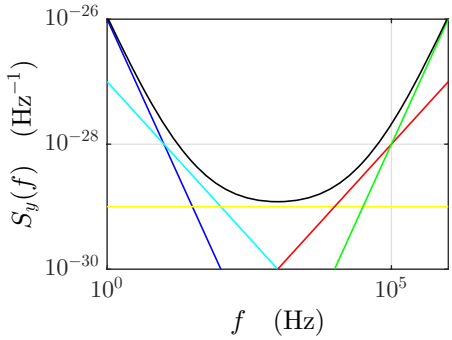

Figure 7.10: Noise model according to (7.65).

perceived. In addition, every real data acquisition system has a low-pass behavior with a cut-off frequency f_{max}, so that high frequencies also do not contribute to the integral. These bandwidth constraints enforce the condition (7.64) for the five noise processes assumed by (7.65) [48]. The measure for the noise power in any case has the form: $\int_{f_{min}}^{f_{max}} S_y(f) df$.

7.3.1.3 Description of stability in the time domain, Allan variance

Temporal frequency fluctuations of an oscillator can be measured by *discriminating the frequency fluctuations at the dispersive profile of a resonance* (or error signal) and convert it into voltage fluctuations. It is just the curve exhibited by a spectrum analyzer to which the error signal is fed, as illustrated by the left setup of Fig. 7.12.

Like any physical quantity, frequency fluctuations can only be measured as an average over an *integration time interval* τ imposed by the measuring apparatus. The k-th measurement of the quantity y at the time t_k results in the measured value:

$$y_k(\tau) = \frac{1}{\tau} \int_{t_k}^{t_k+\tau} y(t) dt \ . \tag{7.66}$$

Assuming that the dead time of the measuring apparatus is negligible (if necessary, technical precautions must be taken to meet this requirement approximately), the

variance of stochastic noise can be expressed as follows:

$$\sigma_y^2(\tau) = \frac{1}{N-1}\sum_{k=1}^{N} y_k^2 \qquad \text{where} \qquad \overline{y_k} = 0 \ . \tag{7.67}$$

The variance is a direct measure of the stability of an oscillator in time domain. It is measured from a discrimination of the error signal in a similar way as the fluctuation density $S_y(f)$. However, as illustrated by the left setup of Fig. 7.12, the discriminated signal is recorded in time domain, e.g. by an oscilloscope.

The variance can be linked to the spectral density of frequency fluctuations in frequency domain by Fourier transformation. With the Heaviside step function Θ the following relationship can be given [23, 2, 6],

$$\sigma_y^2(\tau) = \int_0^\infty S_y(f)|\mathcal{F}\zeta_1(f)|^2 df \qquad \text{where} \qquad \zeta_1(t) = \frac{1}{\tau}\Theta_{[-\tau,0]}(t) \ , \tag{7.68}$$

is the area-normalized jump function, which models the duration of the integration time τ. Its Fourier-transform is the transfer function of the equivalent filter.

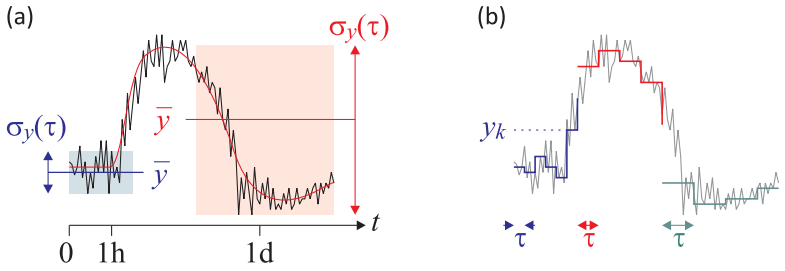

Figure 7.11: (a) Noise can exhibit very different short and long time behavior. (b) Any measurement needs a minimum integration time.

It turns out that the variance for $1/f$ noise and for stochastic drifts ($1/f^2$ noise) diverges at the lower limit, i.e. this variance is not useful for practical applications. The divergence comes from the fact that for longer and longer measurements ($N \to \infty$), respectively, smaller and smaller Fourier frequencies ($f \to 0$), longer and longer periodic fluctuations can be identified as such, while for shorter measurements they appear as linear drifts. One way out is to calculate the variance for a limited number k of measurement data and to average the variances of M of such data sets of length k. This variance converges for a larger number of noise processes. This so-called pair variance ($k = 2$) or *Allan variance* is widely used:

$$\boxed{\sigma_y^2(\tau) = \frac{1}{2M}\sum_{j=1}^{M}(y_{2j} - y_{2j-1})^2} \ . \tag{7.69}$$

Like the normal variance, the Allan variance can also be related to the spectral density of frequency fluctuations:

$$\sigma_y^2(\tau) = \int_0^\infty S_y(f)|\mathcal{F}\zeta_2(f)|^2 df \qquad \text{where} \qquad \zeta_2(t) \equiv \tfrac{1}{\sqrt{2}}[\zeta_1(t) - \zeta_1(-t)] \ . \tag{7.70}$$

The Fourier transforms of the step functions $\zeta_1(t)$ and $\zeta_2(t)$ will be calculated in Exc. 7.3.3.2, as well as the variances for white noise.

7.3.2 Power spectral density

It is important not to confuse the spectral density of frequency fluctuations with the power spectral density of the oscillator defined via the *autocorrelation function of the field amplitude* [4],

$$\boxed{R_{\mathcal{E}}(\tau) \equiv \langle \mathcal{E}^*(t)\mathcal{E}(t+\tau)\rangle = \mathcal{E}_0^2 \langle e^{\imath[\phi(t+\tau)-\phi(t)]}\rangle = \mathcal{E}_0^2 e^{\imath\omega_0\tau}\langle e^{\imath[\varphi(t+\tau)-\varphi(t)]}\rangle} \ , \tag{7.71}$$

as its Fourier transform,

$$\boxed{S_{\mathcal{E}}(\omega) = \mathcal{F}R_{\mathcal{E}}(\tau)} \ . \tag{7.72}$$

The power spectral density is typically measured as the beat frequency of two independent oscillators. It is just the curve exhibited by a spectrum analyzer to which the beat signal is fed, as illustrated in the right setup of Fig. 7.12.

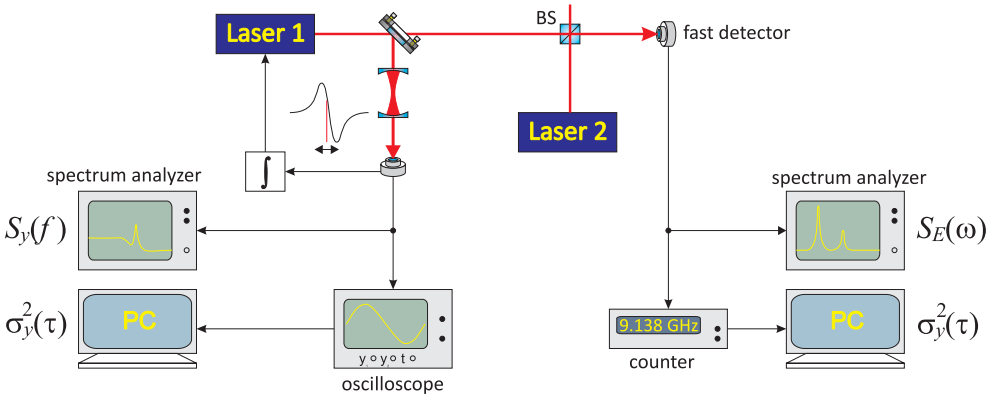

Figure 7.12: (left) Setup for measuring the spectral density of frequency fluctuations $S_y(f)$ and the Allan variance $\sigma_y^2(\tau)$ of laser 1 discriminating it at the slope of transmission signal of an optical cavity. (right) The power spectral density $S_{\mathcal{E}}(\omega)$ can be found as the beat signal between two lasers and either be exhibited on a spectrum analyzer $S_{\mathcal{E}}(\omega)$ or counted and processed to an Allan variance $\sigma_y^2(\tau)$.

The beat spectrum is the convolution of the emission bandwidth of the two oscillators,

$$S_{\mathcal{E}}(\omega) = S_{\mathcal{E},laser1}(\omega) * S_{\mathcal{E},laser2}(\omega) \ . \tag{7.73}$$

In particular, for the case that we have good reasons to believe that one laser is much narrower than the other, the power spectral density $S_{\mathcal{E}}(\omega)$ will reflect the emission spectrum of just the broader laser. Note that the power spectral density derived

[4] Note that the *first-order coherence* is just the normalized autocorrelation,

$$g^{(1)}(\tau) \equiv \frac{\langle \mathcal{E}^*(t)\mathcal{E}(t+\tau)\rangle}{\langle \mathcal{E}^*(t)\mathcal{E}(t)\rangle} = \frac{R_{\mathcal{E}}(\tau)}{R_{\mathcal{E}}(0)} \ .$$

.

from a beat of two independent (uncorrelated) oscillators gives us information on their true emission bandwidths, which is relevant e.g. for resolving narrow atomic transitions. On the other hand, the stability measures $S_y(f)$ and $\sigma_y^2(\tau)$ derived from a discriminated error signal (left setup in Fig. 7.12) only tell us the stability of an oscillator with respect to the reference from which the error signal was derived, e.g. the transmission slope of an optical cavity.

7.3.2.1 Spectral noise power density in the case of white noise

The spectral noise power density $S_{\mathcal{E}}(\omega)$ of the field $\mathcal{E}(t)$ of an oscillator can, in the case of white frequency noise, be related to the spectral density of its frequency fluctuations. In the case of a laser oscillator, the half-width half maximum of the spectral noise power density, i.e. the emission bandwidth, is often specified. We will, in the following, derive the emission spectrum for the case of white Gaussian noise [75, 32, 27].

In Exc. 7.3.3.3 we show that for a *Gaussian noise process* holds [24, 32],

$$\left\langle e^{-\imath[\varphi(t)-\varphi(t+\tau)]} \right\rangle = e^{-\left\langle[\varphi(t)-\varphi(t+\tau)]^2\right\rangle/2} \,. \tag{7.74}$$

Now we set $\varphi(t) = \omega_0 \int_0^t y(t')dt'$ using (7.58) and obtain,

$$\begin{aligned} \left\langle[\varphi(t)-\varphi(t+\tau)]^2\right\rangle &= \left\langle \omega_0^2 \left[\int_0^\tau y(t')dt'\right]^2 \right\rangle = \omega_0^2 \int_0^\tau \int_0^\tau \langle y(t')y(t'')\rangle \, dt'dt'' \\ &= \omega_0^2 \int_0^\tau \int_0^\tau R_y(t'-t'')dt'dt'' = 2\omega_0^2 \int_0^\tau (\tau - t) R_y(t)dt \,. \end{aligned} \tag{7.75}$$

Using (7.61), we now substitute the autocorrelation function by its Fourier transform, the spectral fluctuation density, $R_y(t) = \int_0^\infty S_y(f) e^{2\pi\imath f t} df$:

$$\begin{aligned} \left\langle[\varphi(t)-\varphi(t+\tau)]^2\right\rangle &= 2\omega_0^2 \int_0^\infty S_y(f) \int_0^\tau (\tau - t) e^{2\pi\imath f t} dt df \\ &= 2\omega_0^2 \int_0^\infty S_y(f) \left(\frac{\sin \pi f \tau}{2\pi f}\right)^2 df + \text{imaginary part} \,. \end{aligned} \tag{7.76}$$

We neglect the imaginary part.

For Markovian white noise the phase fluctuations are δ-distributed, which means,

$$R_y \equiv \langle y^*(t) y(t+\tau)\rangle = h_0 \delta(\tau) \qquad \text{and} \qquad S_y(f) = h_0 = const. \tag{7.77}$$

I.e. the so-called *white noise* is characterized by a constant spectral density of phase fluctuations. Carrying on the calculation (7.76) for the case of white frequency noise we get,

$$\left\langle[\varphi(t)-\varphi(t+\tau)]^2\right\rangle = \frac{h_0\omega_0^2|\tau|}{\pi} \int_0^\infty \left(\frac{\sin x}{x}\right)^2 dx = \frac{h_0\omega_0^2|\tau|}{2} \,. \tag{7.78}$$

With this result, we can undertake to calculate the autocorrelation function of the field amplitude (7.71),

$$R_{\mathcal{E}}(\tau) = \mathcal{E}_0^2 e^{\omega_0 \tau} e^{-h_0\omega_0^2|\tau|/2} \,. \tag{7.79}$$

The resulting *power spectral density* (7.72) is [5]:

$$\boxed{S_{\mathcal{E}}(\omega) = \mathcal{E}_0^2 \int_{-\infty}^{\infty} R_{\mathcal{E}}(\tau) e^{-\imath(\omega-\omega_0)\tau} d\tau = \frac{2h_0\omega_0^2}{4\Delta^2 + (h_0\omega_0^2/2)^2}} \,, \tag{7.80}$$

where $\Delta \equiv \omega - \omega_0$ is the deviation of the oscillator frequency from the center frequency ω_0. Thus, the the emission spectrum for the case of white Gaussian noise is a Lorentzian profile with the *laser emission bandwidth*,

$$\boxed{\beta = \tfrac{1}{2} h_0 \omega_0^2} \,. \tag{7.81}$$

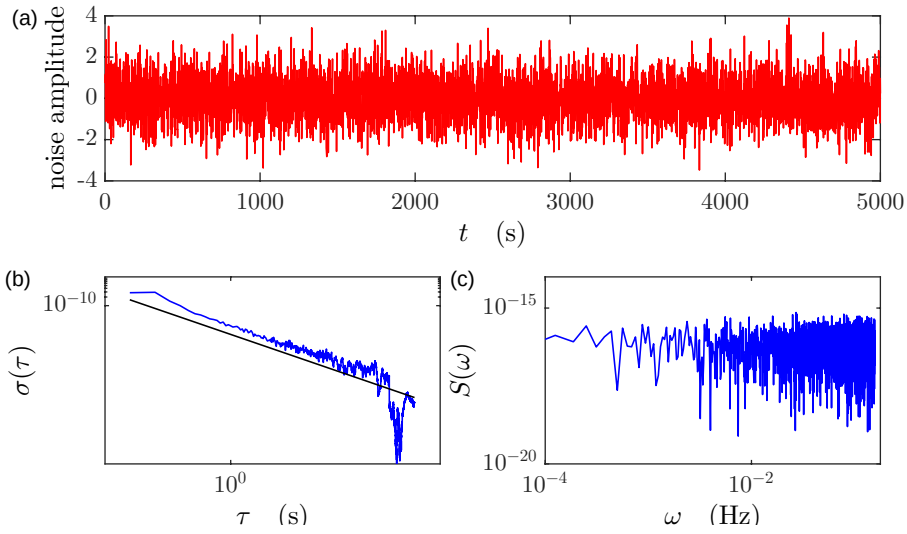

Figure 7.13: (code) Allan variance (b) and spectral density of frequency fluctuations (c) calculated from a randomly generated data set (a).

The Lorentz shape of the emission profile of an oscillator or a resonance always indicates white noise of the underlying frequency fluctuation density. In this sense, the Lorentz form of the natural broadening of an atomic resonance can also be traced back to the white noise of the vacuum fluctuations. Here, the emission bandwidth has to be replaced by the natural linewidth. The Allan variance in this case is:

$$\sigma_y^2(\tau) = \frac{h_0}{2\tau} = \frac{1}{Q^2}\frac{1}{\Gamma}\frac{1}{\tau} \,. \tag{7.82}$$

with the linewidth (FWHM) $\Gamma = h_0\omega_0^2/2$ and $Q = \omega_0/\Gamma$ and indicates the maximum achievable stability for a frequency standard that is coupled to the resonance ω_0.

[5] Using $\mathcal{F}[e^{-a|x|}] = \int_{-\infty}^{\infty} e^{-a|t|} e^{-\imath\omega t} dt = \frac{2a}{a^2+\omega^2}$.

7.3.2.2 Spectral noise power density in case of periodic phase perturbation

The momentary deflection of the oscillator can be described in the case of a harmonic phase disturbance by equation (7.60) with the additional condition: $\phi(t) = N \sin \Omega t$. The frequency fluctuation density and the Allan variance are obtained in this case:

$$S_y(f) = \left(\frac{fN}{2\omega_0}\right)^2 \delta(f-\Omega) \qquad \text{resp.} \qquad \sigma_y^2(\tau) = \left(\frac{\Omega N}{2\omega_0}\right)^2 \frac{\sin^2 \Omega\tau/2}{\Omega\tau/2} \ . \tag{7.83}$$

The spectral noise power density consists of a discrete spectrum of sidebands, the number and height of which is given by the modulation index N:

$$\boxed{S_{\mathcal{E}}(\omega) = \sum_{n=-\infty}^{\infty} |J_n(N)|^2 \delta(\omega - \omega_0 - \Omega)} \ . \tag{7.84}$$

A full width at half maximum of the spectral noise power density cannot be specified. However, as a measure of the emission bandwidth of the oscillator, the frequency spacing of the sideband of the highest order can be understood, the height of which corresponds to at least half the height of the carrier frequency ω_0.

7.3.3 Exercises

7.3.3.1 Ex: Spectral density of frequency fluctuations

Prove the relationship $S_{\dot{x}}(f) = f^2 S_x(f)$.

7.3.3.2 Ex: Allan variance for white noise

a. Calculate the Fourier transform of step function $\zeta_1(t)$ and the one-point variance for white noise from its definition (7.68).
b. Repeat the calculation for the step function $\zeta_2(t)$ and the Allan variance as defined in (7.70).

7.3.3.3 Ex: Gaussian noise process

Prove the relationship (7.75) for a *Gaussian noise process* characterized by,

$$\frac{\langle A^{2n}\rangle}{(2n)!} = \frac{\langle A^2\rangle^n}{2^n n!} \qquad \text{and} \qquad \langle A^{2n-1}\rangle = 0 \ .$$

7.4 Data sheets

The following pages contain the data sheets of the main components used in this course.

HL6722G

AlGaInP Laser Diode

opnext
Powered by HITACHI

ODE-208-220E (Z)

Rev.5
Mar. 2005

Description

The HL6722G is a 0.67 µm band AlGaInP index-guided laser diode with a multi-quantum well (MQW) structure. It is suitable as a light source for bercode scanner, and various other types of optical equipment. Hermetic sealing of the package assures high reliability.

Features

- Visible light output at wavelengths up to 680 nm
- Single longitudinal mode
- Continuous operating output: 5 mW CW
- Low voltage operation: 2.7 V Max
- Low current operation: 32 mA Typ
- Built-in monitor photodiode

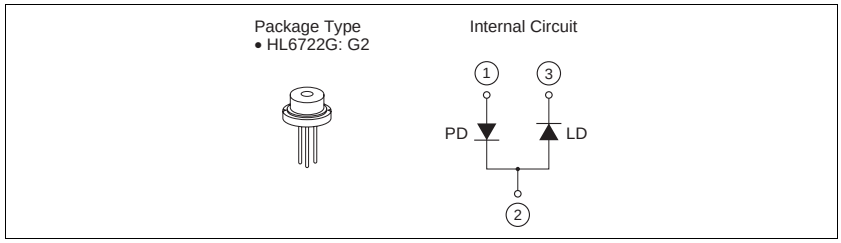

opnext
Powered by HITACHI

Figure 7.14: Data sheet for the diode laser from Thorlabs, model Hitachi HL6722G.

Coaxial

Amplifier

ZHL-2-8

50Ω Medium High Power 10 to 1000 MHz

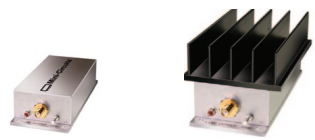

ZHL-2-8X ZHL-2-8

SMA version shown

Features

- wideband, 10 to 1000 MHz
- high IP3, +38 dBm typ.
- medium high power, 29 dBm min.

Applications

- VHF/UHF
- test equipment
- cellular
- instrumentation
- laboratory

CASE STYLE: T34

Connectors	Model	Price	Qty.
BNC	ZHL-2-8	$525.00 ea.	(1-9)
BNC	ZHL-2-8X	$515.00 ea.	(1-9)
SMA	ZHL-2-8-S	$535.00 ea.	(1-9)
SMA	ZHL-2-8X-S	$525.00 ea.	(1-9)

Electrical Specifications

MODEL NO.	FREQ. (MHz)		GAIN (dB)			MAXIMUM POWER OUTPUT (dBm)		DYNAMIC RANGE		VSWR (:1) Max.		DC POWER	
	f_L	f_U	Min.	Typ.	Flatness Max.	(1 dB Compr.) Min.	Input (no damage)	NF (dB) Typ.	IP3 (dBm) Typ.	In	Out	Volt (V) Nom.	Current (A) Max.
ZHL-2-8	10	1000	31	35	±1.0	+29	+5	10.0	+38	2.0	2.0	24	0.6
ZHL-2-8X*	10	1000	31	35	±1.0	+29	+5	10.0	+38	2.0	2.0	24	0.6

* Heat sink not included
Open load is not recommended, potentially can cause damage.
With no load derate max input power by 20 dB

To order without heat sink, add suffix X to model number. Alternative heat sinking and heat removal must be provided by the user to limit maximum temperature to 65°C, in order to ensure proper performance. For reference, this requires thermal resistance of user's external heat sink to be 1.35°C/W Max.

Maximum Ratings

Operating Temperature	-20°C to 65°C
Storage Temperature	-55°C to 100°C
DC Voltage	+25V Max.

Permanent damage may occur if any of these limits are exceeded.

Outline Drawing

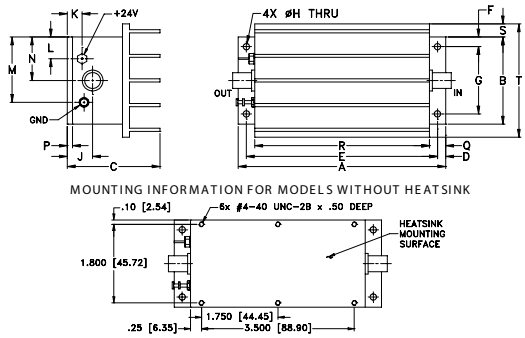

Figure 7.15: Data sheet for the rf-amplifier from MiniCircuits, model ZHL-2-8.

Coaxial

Voltage Controlled Oscillator ZOS-100+

Dual Output 50 to 100 MHz

Features
- octave bandwidth
- linear tuning, 4.5 MHz/V typ.
- excellent harmonic suppression, -29 dBc typ.
- rugged shielded case
- protected by US Patent, 6,943,629

Applications
- auxiliary output freq. monitoring
- load insensitive source

CASE STYLE: BR386

Connectors	Model	Price	Qty.
SMA	ZOS-100+	$119.95	(1-9)

+ RoHS compliant in accordance with EU Directive (2002/95/EC)

The +Suffix has been added in order to identify RoHS Compliance. See our web site for RoHS Compliance methodologies and qualifications.

Electrical Specifications

FREQUENCY (MHz)		POWER OUTPUT (dBm) Typ.		TUNING VOLTAGE (V)		PHASE NOISE (dBc/Hz) SSB at offset frequencies: Typ.			PULLING (MHz) pk-pk (open/short)	PUSHING (MHz/V)	TUNING SENSITIVITY (MHz/V)	HARMONICS (dBc)		3 dB MODULATION BANDWIDTH (MHz)	DC OPERATING POWER	
Min.	Max.	Main	Aux.	Min.	Max.	10 kHz	100 kHz	1 MHz	Typ.	Typ.	Typ.	Typ.	Max.	Typ.	Vcc (volts)	Current (mA) Max.
50	100	+9	-12	1	16	-111	-131	-143	0.026	0.25	4.5	-29	-20	0.1	12	140

Maximum Ratings

Operating Temperature	-55°C to 85°C
Storage Temperature	-55°C to 100°C
Absolute Max. Supply Voltage (Vcc)	+16V
Absolute Max. Tuning Voltage (Vtune)	+18V

all specifications: 50 ohm system
Permanent damage may occur if any of these limits are exceeded.

electrical schematic

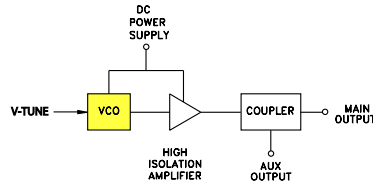

Outline Drawing

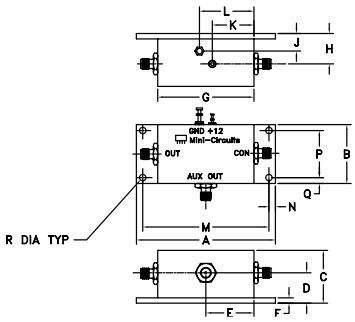

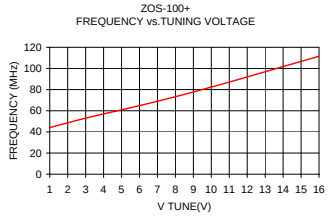

Outline Dimensions (inch / mm)

A	B	C	D	E	F	G	H	J	K	L	M	N	P	Q	R	wt
3.25	1.38	1.25	.71	1.13	.125	2.25	.71	.41	.98	1.28	2.950	.15	1.100	.14	.150	grams
82.55	35.05	31.75	18.03	28.70	3.18	57.15	18.03	10.41	24.89	32.51	74.93	3.81	27.94	3.56	3.81	180

Figure 7.16: Data sheet for the Voltage-Controlled Oscillator (VCO) from Minicircuits, model ZOS-100+.

Coaxial

Voltage Variable Attenuator

ZX73-2500+

50Ω 10 to 2500 MHz

FEMALE SMA shown

CASE STYLE: GD958

Maximum Ratings

Operating Temperature	-55°C to 85°C
Storage Temperature	-55°C to 85°C
Absolute Max. Supply Voltage (V+)	12V
Absolute Max. Control Voltage (Vcrtl)	20V
Absolute Max. RF Input Level	+20 dBm

Permanent damage may occur if any of these limits are exceeded.

Features

- Broadband, 10-2500 MHz
- IP3, +43 dBm typ.
- 40 dB attenuation @ 1500 MHz
- Good VSWR at in /out ports over attenuation range
- No external bias and RF matching network required
- Shielded case
- Protected by US Patent 6,790,049

Applications

- Variable gain amplifier
- Power level control
- Feed-forward amplifiers
- ALC circuits

SMA INPUT	SMA Connectors OUTPUT	Model	Price	Qty.	Case
FEMALE	FEMALE	ZX73-2500-S+	$49.95	(1-9)	GD958
MALE	FEMALE	ZX73-2500M-S+	$49.95	(1-9)	GD1163

+ RoHS compliant in accordance with EU Directive (2002/95/EC)

The +Suffix has been added in order to identify RoHS Compliance. See our web site for RoHS Compliance methodologies and qualifications.

Outline Drawing (GD958)

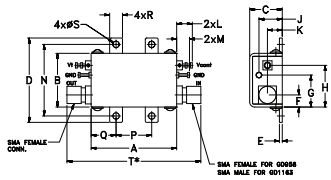

Outline Dimensions (inch / mm)

A	B	C	D	E	F	G	H	J
1.20	**.75**	**.46**	**1.18**	**.04**	**.17**	**.45**	**.59**	**.33**
30.48	19.05	11.68	29.97	1.02	4.32	11.43	14.99	8.38

K	L	M	N	P	Q	R	S	T	wt.
.21	**.22**	**.18**	**1.00**	**.50**	**.35**	**.18**	**.106**	**1.88**	**grams**
5.33	5.59	4.57	25.40	12.70	8.89	4.57	2.69	47.75	35.0

Note:

* T dimension is 2.05 inch (52.07 mm) for GD1163 Case Style.

Electrical Specifications (T_{AMB}= 25°C)

FREQ. (MHz)		MIN. INSERTION LOSS, dB (+15V)		MAX. ATTENUATION dB (0V)		INPUT POWER (dBm)	CONTROL Voltage (V)	CONTROL Current (mA)	IP3 (dBm)	RETURN LOSS[1] (dB)	POWER SUPPLY Voltage (V)	POWER SUPPLY Current (mA)
Min.	Max.	Typ.	Max.	Typ.	Min.	Max.		Max.	Typ.	Typ.		Max.
10	500	3.0	4.6	55	41	+20	0 - 17	30	43	20	+3 to +5	5
500	1500	3.3	5.0	40	30	+20	0 - 17	30	43	20	+3 to +5	5
1500	2500	4.0	6.2	37	25	+20	0 - 17	30	44	20	+3 to +5	5

Notes:
Rise/Fall time: 14μSec/25μSec Typ.
Switching Time, turn on/off: 14μSec/25μSec Typ.
[1] Improved R. Loss in/out performance can be achieved at certain frequencies by choosing a V+ between +3V to +5V

Equivalent Schematic

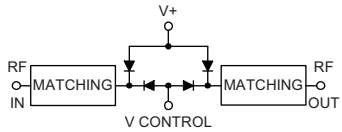

ZX73-2500+
TYPICAL ATTENUATION AT 1000MHz

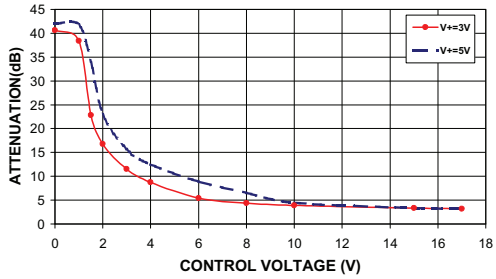

Figure 7.17: Data sheet for the voltage-controlled variable attenuator from Minicircuits, model ZX73-2500+.

Plug-In

Power Splitter/Combiner

PSC-2-1+
PSC-2-1

2 Way-0° 50Ω 0.1 to 400 MHz

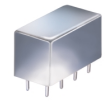

CASE STYLE: A01
PRICE: $14.20 ea. QTY. (1-9)

+ RoHS compliant in accordance with EU Directive (2002/95/EC)

The +Suffix identifies RoHS Compliance. See our web site for RoHS Compliance methodologies and qualifications.

Maximum Ratings

Operating Temperature	-55°C to 100°C
Storage Temperature	-55°C to 100°C
Power Input (as a splitter)	1W max.
Internal Dissipation	0.125W max.

Pin Connections

SUM PORT	1
PORT 1	5
PORT 2	6
GROUND	2,3,4,7,8
CASE GROUND	2,3,4,7,8

Features

- wideband, 0.1 to 400 MHz
- low insertion loss, 0.4 dB typ.
- rugged welded construction

Applications

- VHF/UHF
- federal & defense communications

Outline Drawing

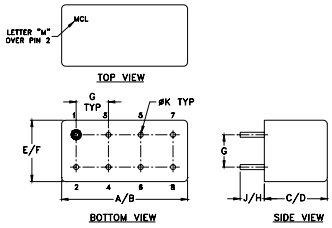

Outline Dimensions (inch / mm)

A	B	C	D	E	F
.770	.800	.385	.400	.370	.400
19.56	20.32	9.78	10.16	9.40	10.16
G	H	J	K		wt
.200	.20	.14	.031		grams
5.08	5.08	3.56	0.79		5.2

Electrical Specifications

FREQ. RANGE (MHz)	ISOLATION (dB)						INSERTION LOSS (dB) ABOVE 3.0 dB						PHASE UNBALANCE (Degrees)			AMPLITUDE UNBALANCE (dB)		
	L		M		U		L		M		U		L	M	U	L	M	U
f_L-f_U	Typ.	Min	Typ.	Min	Typ.	Min	Typ.	Max.	Typ.	Max.	Typ.	Max.	Max.	Max.	Max.	Max.	Max.	Max.
0.1-400	20	15	25	20	25	20	0.2	0.6	0.4	0.75	0.6	1.0	2.0	3.0	4.0	0.15	0.2	0.3

L = low range [f_L to 10 f_L] M = mid range [10 f_L to f_U/2] U= upper range [f_U/2 to f_U]

Typical Performance Data

Frequency (MHz)	Insertion Loss (dB)		Amplitude Unbalance (dB)	Isolation (dB)	Phase Unbalance (deg.)	VSWR S	VSWR 1	VSWR 2
	S-1	S-2						
0.10	3.23	3.23	0.00	24.82	0.01	1.16	1.37	1.37
5.00	3.14	3.14	0.00	35.64	0.01	1.10	1.11	1.11
20.00	3.18	3.17	0.00	35.33	0.03	1.11	1.10	1.10
40.00	3.18	3.18	0.00	34.39	0.02	1.12	1.10	1.10
60.00	3.22	3.22	0.00	33.16	0.02	1.12	1.09	1.09
80.00	3.24	3.24	0.00	31.85	0.04	1.13	1.09	1.09
100.00	3.24	3.24	0.00	30.68	0.05	1.13	1.09	1.09
150.00	3.28	3.27	0.00	28.37	0.04	1.14	1.08	1.08
175.00	3.31	3.30	0.01	27.46	0.07	1.14	1.07	1.07
200.00	3.32	3.31	0.01	26.72	0.05	1.15	1.07	1.07
225.00	3.32	3.31	0.01	26.14	0.02	1.15	1.06	1.06
250.00	3.37	3.36	0.01	25.65	0.05	1.15	1.06	1.06
300.00	3.41	3.38	0.03	24.88	0.10	1.15	1.06	1.06
350.00	3.47	3.44	0.03	24.40	0.06	1.16	1.08	1.07
400.00	3.50	3.46	0.04	23.86	0.05	1.18	1.10	1.09

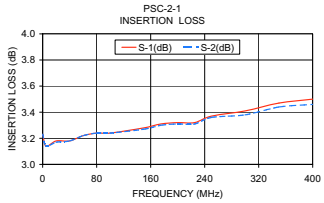

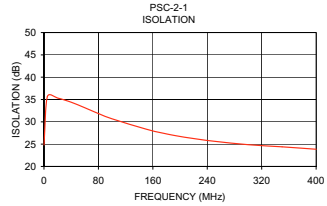

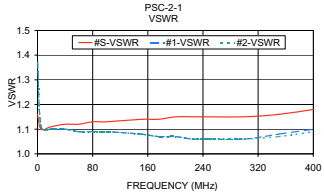

electrical schematic

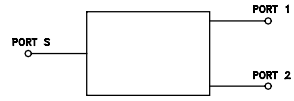

Mini-Circuits®
ISO 9001 ISO 14001 CERTIFIED

ALL NEW minicircuits.com

P.O. Box 350166, Brooklyn, New York 11235-0003 (718) 934-4500 Fax (718) 332-4661 For detailed performance specs & shopping online see Mini-Circuits web site

The Design Engineers Search Engine Provides ACTUAL Data Instantly From MINI-CIRCUITS At: www.minicircuits.com

RF/IF MICROWAVE COMPONENTS

REV. A
M98898
PSC-2-1
HY/TD/CP
070202

Figure 7.18: Data sheet for the power divider from Minicircuits, model PSC-2-1.

Plug-In

Frequency Mixer

SRA-2CM+

Level 7 (LO Power +7 dBm) 5 to 1000 MHz

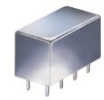

CASE STYLE: A01
PRICE: $18.20 ea. QTY (1-9)

+ RoHS compliant in accordance with EU Directive (2002/95/EC)

The +Suffix has been added in order to identify RoHS Compliance. See our web site for RoHS Compliance methodologies and qualifications.

Maximum Ratings

Operating Temperature	-55°C to 100°C
Storage Temperature	-55°C to 100°C
RF Power	50mW
IF Current	40mA

Features

- excellent conversion loss, 5.27 dB typ.
- good L-R isolation, 35 dB typ. L-I isolation, 30 dB typ.
- rugged welded construction
- hermetic

Applications

- VHF/UHF
- cellular
- defense & federal communications
- ISM/GSM

Pin Connections

LO	8
RF	1
IF	3,4^
GROUND	2,5,6,7
CASE GROUND	2,5,6,7

^ *pins must be connected together externally*

Outline Drawing

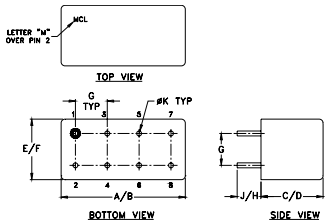

Outline Dimensions (inch / mm)

A	B	C	D	E	F
.770	.800	.385	.400	.370	.400
19.56	20.32	9.78	10.16	9.40	10.16
G	H	J	K		wt
.200	.20	.14	.031		grams
5.08	5.08	3.56	0.79		5.2

Electrical Specifications

FREQUENCY (MHz)		CONVERSION LOSS (dB)				LO-RF ISOLATION (dB)						LO-IF ISOLATION (dB)					
		Mid-Band m			Total Range	L		M		U		L		M		U	
LO/RF f_L-f_U	IF	$\bar{X}$	σ	Max.	Max.	Typ.	Min.	Typ.	Min.	Typ.	Min.	Typ.	Min.	Typ.	Min.	Typ.	Min.
5-1000	DC-1000	5.27	.04	7.0	8.5	60	50	35	30	30	25	50	45	30	25	25	20

1 dB COMP.: +1 dBm typ.

L = low range [f_L to 10 f_L] m= mid band [2f_L to f_U/2] M = mid range [10 f_L to f_U/2] U = upper range [f_U/2 to f_U]

Typical Performance Data

Frequency (MHz)		Conversion Loss (dB)	Isolation L-R (dB)	Isolation L-I (dB)	VSWR RF Port (:1)	VSWR LO Port (:1)
		LO	LO	LO	LO	LO
RF	LO	+7dBm	+7dBm	+7dBm	+7dBm	+7dBm
5.00	35.00	7.36	67.00	67.00	5.03	4.09
38.13	68.13	5.59	54.82	53.34	1.40	3.04
71.27	41.27	5.30	49.15	48.13	1.31	2.99
137.53	107.53	5.33	46.10	45.22	1.27	2.83
200.00	170.00	5.35	42.68	41.91	1.24	2.82
236.93	206.93	5.27	41.09	40.29	1.24	2.72
303.20	273.20	5.28	39.42	38.94	1.24	2.76
336.33	306.33	5.42	39.72	36.88	1.26	2.77
402.60	372.60	5.63	38.13	35.49	1.30	2.85
468.86	438.86	5.62	37.15	35.09	1.37	2.84
535.13	505.13	5.87	35.49	32.57	1.45	2.97
568.26	538.26	6.01	35.26	31.27	1.50	2.96
634.53	604.53	6.17	36.03	29.46	1.61	3.10
700.79	670.79	6.68	38.00	30.29	1.70	3.21
767.06	737.06	6.49	38.00	29.92	1.85	3.09
800.19	770.19	6.11	39.26	28.34	2.01	3.03
833.33	803.33	6.37	39.87	27.52	2.08	3.08
899.59	869.59	6.80	40.23	26.99	2.32	3.39
965.86	935.86	6.86	42.61	25.65	2.53	3.58
1000.00	969.00	7.10	44.90	24.17	2.76	3.76

Electrical Schematic

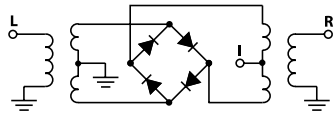

Figure 7.19: Data sheet for the mixer from Minicircuits, model SRA-2CM+.

SPECIFICATIONS				
AO Medium				TeO2
Acoustic Velocity				4.2 mm/µs
Active Aperture*	2.5	mm 'L' X	1	mm 'H'
Center Frequency (Fc)				80 MHz
RF Bandwidth	20 MHz @	-10 dB	Return Loss	
Input Impedance				50 Ohms Nominal
VSWR @ Fc				1.3 :1 Max
Wavelength				442-633 nm
Insertion Loss				4 % Max
Reflectivity per Surface				1 % Max
Anti-Reflection Coating				MIL-C-48497
Optical Power Density				250 W/mm^2
Contrast Ratio				1000 :1 Min
Polarization			90 ° To Mounting Plane	

PERFORMANCE VS WAVELENGTH				
Wavelength (nm)	**442**	**488**	**515**	**633**
Saturation RF Power (W)	0.27	0.33	0.36	0.55
Bragg Angle (mr)	4.2	4.6	4.9	6
Beam Separation (mr)	8.4	9.2	9.8	12

PERFORMANCE VS BEAM DIAMETER			
Beam Diameter (µm)	**200**	**300**	**500**
at Wavelength (nm)	633	633	633
Diffraction Efficiency (%)	80	83	85
Rise Time (nsec)	34	49	80
	15.9	10.6	6.3
	10	5	1

Figure 7.20: Data sheet for the acousto-optic modulator (AOM) from Crystal Technologies, model AOMO 3080-120.

Silicon PIN Photodiodes - Large Area, Fast Response Time – 400 nm to 1100 nm

The FFD series devices are high-quality, large-area, high-speed, N-type Si PIN photodiodes in hermetically sealed TO packages designed for the 400 nm to 1100 nm wavelength range. The FND-100Q has a quartz window to enhance UV responsivity.

Preamplifiers

Preamplifier modules incorporating these photodiodes are available on a custom basis.

Si PINs – Large Area, Fast Response

Typical Characteristics @ T = 22º C

Part #	Standard Package	Photo Sens. Diam. (mm)	Resp. @ 900 nm (A/W)	Dark Current Id (nA)	Spect. Noise Curr. Dens. In (fW/√Hz)	Cap. @ 100 kHz Cd (pF)	Response Time tr (ns)	NEP @ 900 nm (fW/√Hz)	Bias Volt (V)
FFD-040B	Y	1	0.58	1	18	1.8	2	31	15
FFD-100	B	2.5	0.58	2	25	8.5	3.5	44	15
FFD-200	C3	5.1	0.58	4	36	30	5	62	15
FND-100Q	B	2.5	0.58	10	60	8.5	2	100	90

Typical Applications

Laser detection systems, fast pulse detection, instrumentation, and high-speed switching.

Figure 7.21: Data sheet for the photo diode from Perkin Elmers FDD100.

Detectors

Silicon Epitaxial PIN Photodiodes - High Speed – 400 nm to 1100 nm

The C30736 series of high-speed epitaxial silicon PIN photodetectors provide fast response and good quantum efficiency in the spectral range between 400 nm and 1100 nm. These devices are optimized for high-speed, high volume and low cost applications. Standard sizes include 0.25 mm, 0.5 mm, 1.0 mm, 1.5 x 1.5 mm, and custom sizes can be accomodated depending on volume required. Available in plastic surface mount packages and in chip form.

Silicon Epitaxial PIN Photodiodes

Typical Characteristics @ T = 22º C

Part #	Standard Package	Photo Sens. Diam. (mm)	Resp. @ 870 nm (A/W)	Dark Current @2V Id (nA)	Spect. Noise Curr. Dens. In (fW/√Hz)	Cap. @ 100 kHz Cd (pF)	Response Time tr (ns)	NEP @ 870 nm (fW/√Hz)	Bias Volt (V)
C30736-1	Chip form	0.20	0.55	0.05	6	0.75	0.3	11	2
C30736-2	Chip form	0.50	0.55	0.10	10	1.5	0.5	18	2
C30736-3	Chip form	1.5 x 1.5	0.55	0.50	50	14	0.3	91	2

Silicon PIN Photodiodes - Standard N-Type – 400 nm to 1100 nm

The C308XX series devices are high-quality N-type Si PIN photodiodes in hermetically sealed TO packages designed for the 400 nm to 1100 nm wavelength region.

Si PINs – Standard N-Type

Typical Characteristics @ T = 22º C

Part #	Standard Package	Photo Sens. Diam. (mm)	Resp. @ 900 nm (A/W)	Dark Current Id (nA)	Spect. Noise Curr. Dens. (fA/√Hz)	Cap. @ 100 kHz Cd (pF)	Response Time tr (ns)	NEP @ 900 nm (fW/√Hz)	Bias Volt (V)
C30807E	A	1	0.6	1	18	2.5	3	30	45
C30808E	B	2.5	0.6	3	31	6	5	52	45
C30822E	C	5	0.6	5	40	17	7	67	45
C30809E	C3	8	0.6	7	47	35	10	79	45
C30810E	D	11.4	0.6	30	98	70	12	163	45

Typical Applications

Laser detection systems, photometry, data transmission, instrumentation, and high-speed switching.

Silicon PIN Photodiodes - Large Area, Fast Response Time – 400 nm to 1100 nm

The FFD series devices are high-quality, large-area, high-speed, N-type Si PIN photodiodes in hermetically sealed TO packages designed for the 400 nm to 1100 nm wavelength range. The FND-100Q has a quartz window to enhance UV responsivity.

Preamplifiers

Preamplifier modules incorporating these photodiodes are available on a custom basis.

Si PINs – Large Area, Fast Response

Typical Characteristics @ T = 22º C

Part #	Standard Package	Photo Sens. Diam. (mm)	Resp. @ 900 nm (A/W)	Dark Current Id (nA)	Spect. Noise Curr. Dens. In (fW/√Hz)	Cap. @ 100 kHz Cd (pF)	Response Time tr (ns)	NEP @ 900 nm (fW/√Hz)	Bias Volt (V)
FFD-040B	Y	1	0.58	1	18	1.8	2	31	15
FFD-100	B	2.5	0.58	2	25	8.5	3.5	44	15
FFD-200	C3	5.1	0.58	4	36	30	5	62	15
FND-100Q	B	2.5	0.58	10	60	8.5	2	100	90

Typical Applications

Laser detection systems, fast pulse detection, instrumentation, and high-speed switching.

6

Figure 7.22: Data sheet for the photo diode from Perkin Elmers C30822E.

19-0350; Rev 0; 12/94

MAXIM

Precision, Dual-Supply, SPST Analog Switches

General Description

The MAX320/MAX321/MAX322 are precision, dual, SPST analog switches designed to operate from ±3V to ±8V dual supplies. The MAX320 has two normally open (NO) switches and the MAX321 has two normally closed (NC) switches. The MAX322 has one NO and one NC switch. Low power consumption (1.25mW) makes these parts ideal for battery-powered equipment. They offer low leakage currents (100pA max) and fast switching speeds (t_{ON} = 150ns max, t_{OFF} = 100ns max).

The MAX320 series, powered from ±5V supplies, offers 35Ω max on-resistance (R_{ON}), 2Ω max matching between channels, and 4Ω max R_{ON} flatness.

These switches also offer 5pC max charge injection and a minimum of 2000V ESD protection per Method 3015.7.

For equivalent devices specified for single-supply operation, see the MAX323/MAX324/MAX325 data sheet. For quad versions of these switches, see the MAX391/MAX392/MAX393 data sheet.

Applications

Battery-Operated Systems	Sample-and-Hold Circuits
Heads-Up Displays	Guidance and Control Systems
Audio and Video Switching	Military Radios
Test Equipment	Communications Systems
±5V DACs and ADCs	PBX, PABX

Features

- **Low On-Resistance, 35Ω max (16Ω typical)**
- **R_{ON} Matching Between Channels <2Ω**
- **R_{ON} Flatness <4Ω**
- **Guaranteed Charge Injection <5pC**
- **Bipolar Supply Operation (±3V to ±8V)**
- **Low Power Consumption, <1.25mW**
- **Low Leakage Current Over Temperature, <2.5nA at +85°C**
- **Fast Switching, t_{ON} <150ns, t_{OFF} <100ns**
- **Guaranteed Break-Before-Make (MAX322 only)**

Ordering Information

PART	TEMP. RANGE	PIN-PACKAGE
MAX320CPA	0°C to +70°C	8 Plastic DIP
MAX320CSA	0°C to +70°C	8 SO
MAX320CUA	0°C to +70°C	8 µMAX
MAX320C/D	0°C to +70°C	Dice*
MAX320EPA	-40°C to +85°C	8 Plastic DIP
MAX320ESA	-40°C to +85°C	8 SO
MAX320EJA	-40°C to +85°C	8 CERDIP**
MAX320MJA	-55°C to +125°C	8 CERDIP**

Ordering Information continued at end of data sheet.

** Contact factory for dice specifications.*
*** Contact factory for availability.*

Pin Configurations/Functional Diagrams/Truth Tables

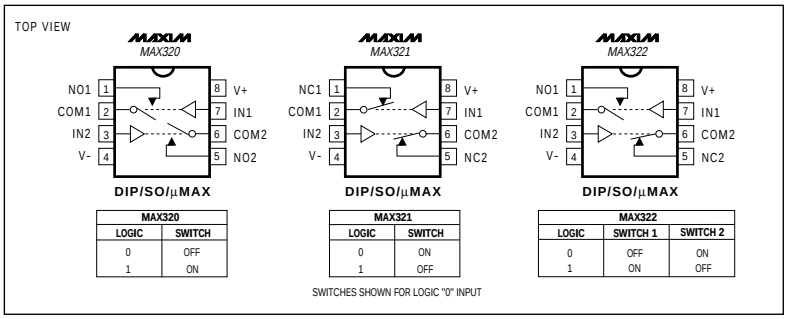

MAX320	
LOGIC	SWITCH
0	OFF
1	ON

MAX321	
LOGIC	SWITCH
0	ON
1	OFF

MAX322		
LOGIC	SWITCH 1	SWITCH 2
0	OFF	ON
1	ON	OFF

SWITCHES SHOWN FOR LOGIC "0" INPUT

Figure 7.23: Data sheet for the digital switch MAX322 from Maxim.

National Semiconductor

August 2000

LM741
Operational Amplifier

General Description

The LM741 series are general purpose operational amplifiers which feature improved performance over industry standards like the LM709. They are direct, plug-in replacements for the 709C, LM201, MC1439 and 748 in most applications.

The amplifiers offer many features which make their application nearly foolproof: overload protection on the input and output, no latch-up when the common mode range is exceeded, as well as freedom from oscillations.

The LM741C is identical to the LM741/LM741A except that the LM741C has their performance guaranteed over a 0˚C to +70˚C temperature range, instead of −55˚C to +125˚C.

Features

Connection Diagrams

Metal Can Package

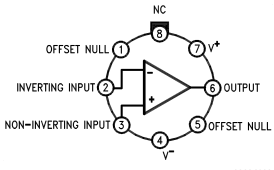

Note 1: LM741H is available per JM38510/10101

Order Number LM741H, LM741H/883 (Note 1), **LM741AH/883 or LM741CH**
See NS Package Number H08C

Dual-In-Line or S.O. Package

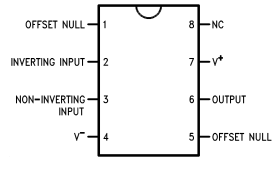

Order Number LM741J, LM741J/883, LM741CN
See NS Package Number J08A, M08A or N08E

Ceramic Flatpak

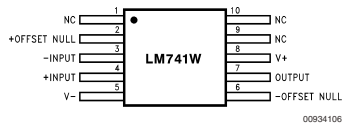

Order Number LM741W/883
See NS Package Number W10A

Typical Application

Offset Nulling Circuit

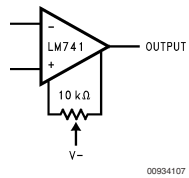

 DS009341

Figure 7.24: Data sheet for the operational amplifier LM741 from National Semiconductor.

ANALOG DEVICES

Low-Noise, Precision Operational Amplifier

OP27

FEATURES

Low Noise: 80 nV p-p (0.1 Hz to 10 Hz), 3 nV/$\sqrt{\text{Hz}}$
Low Drift: 0.2 μV/°C
High Speed: 2.8 V/μs Slew Rate, 8 MHz Gain Bandwidth
Low V_{OS}: 10 μV
Excellent CMRR: 126 dB at V_{CM} of ±11 V
High Open-Loop Gain: 1.8 Million
Fits 725, OP07, 5534A Sockets
Available in Die Form

GENERAL DESCRIPTION

The OP27 precision operational amplifier combines the low offset and drift of the OP07 with both high speed and low noise. Offsets down to 25 μV and drift of 0.6 μV/°C maximum make the OP27 ideal for precision instrumentation applications. Exceptionally low noise, e_n = 3.5 nV/$\sqrt{\text{Hz}}$, at 10 Hz, a low 1/f noise corner frequency of 2.7 Hz, and high gain (1.8 million), allow accurate high-gain amplification of low-level signals. A gain-bandwidth product of 8 MHz and a 2.8 V/μsec slew rate provides excellent dynamic accuracy in high-speed, data-acquisition systems.

A low input bias current of ±10 nA is achieved by use of a bias-current-cancellation circuit. Over the military temperature range, this circuit typically holds I_B and I_{OS} to ±20 nA and 15 nA, respectively.

The output stage has good load driving capability. A guaranteed swing of ±10 V into 600 Ω and low output distortion make the OP27 an excellent choice for professional audio applications.

(Continued on page 7)

PIN CONNECTIONS

TO-99
(J-Suffix)

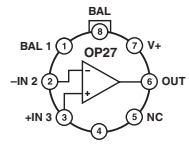

8-Pin Hermetic DIP
(Z-Suffix)
Epoxy Mini-DIP
(P-Suffix)
8-Pin SO
(S-Suffix)

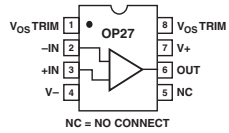

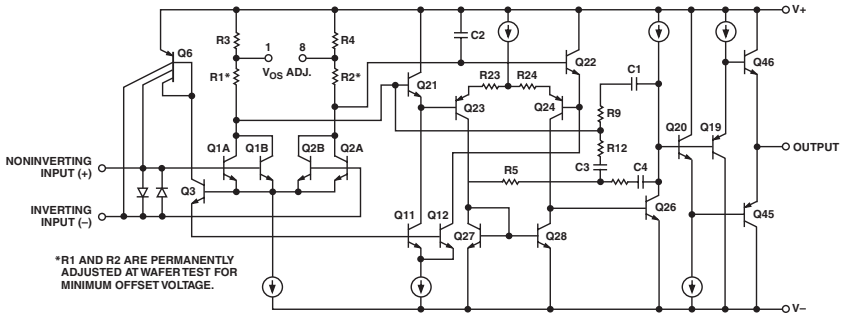

Figure 1. Simplified Schematic

Figure 7.25: Data sheet for the operational amplifier OP27 from Analog Devices.

Bibliography

[1] B. Agate, B. Stormont, A. J. Kemp, C. T. A. Brown, U. Keller, and W. Sibbett, *Simplified cavity designs for efficient and compact femtosecond cr:lisaf lasers*, Opt. Comm. **205** (2002), 207.

[2] D. W. Allan, *Statistics of atomic frequency standards*, Proc. of the IEEE **54** (1966), 221.

[3] D. W. Allan, J. H. Shoaf, and D. Halford, *Statistics of time and frequency data analysis*, NBS Monographs **140** (1974), 151.

[4] L. Allen, M. W. Beijersbergen, R. J. C. Spreeuw, and J. P. Woerdman, *Orbital angular momentum of light and the transformation of laguerre-gaussian laser modes*, Phys. Rev. A **45** (1992), 8185, .

[5] E. Arimondo, M. Inguscio, and P. Violino, *Experimental determination of the hyperfine structure in the alkali atoms*, Rev. Mod. Phys. **49** (1977), 31.

[6] C. Audoin, *Frequency metrology*, Rendiconti della Scuola Intern. di Fisica ?Enrico Fermi? **LIVIII or LXVIII** (1980), 169.

[7] X. Baillard, A. Gauguet, S. Bize, P. Lemonde, Ph. Laurent, A. Clairon, and P. Rosenbusch, *Interference-filter-stabilized external-cavity diode lasers*, Opt. Commun. **266** (2006), 609, .

[8] J. A. Barnes, L. S. Cutler, and et al., *Characterization of frequency stability*, IEEE Trans. Instr. Meas. **20** (1971), 105.

[9] D. R. Bates and A. Daamgard, *The calculation of the absolute strenghts of spectral lines*, Phil. Tr. R. Soc. A **242** (1949), 101.

[10] Sh. Bennetts, G. D. McDonald, K. S. Hardman, J. E. Debs, C. C. N. Kuhn, J. D. Close, and N. P. Robins, *External cavity diode lasers with 5khz and 200nm tuning range at 1.55 um and for linewidth measurement*, Opt. Exp. **22** (2014), 10642.

[11] J. Bergquist, R. G. Hulet, W. M. Itano, and D. J. Wineland, *Observation of quantum jumps in a single atom*, Phys. Rev. Lett. **57** (1986), 1699.

[12] Hans A. Bethe and Edwin E. Salpether, *Quantum mechanics of one- and two-electron atoms*, Springer-Verlag, 1 ed., Berlin, 1957, ISBN.

[13] G. C. Bjorklund, *Frequency-modulation spectroscopy: A new method for measuring weak absorptions and dispersions*, Opt. Lett. **5** (1980), 15.

[14] M. Born, 1980, ISBN.

[15] B. H. Bransden and C. J. Joachain, *Physics of atoms and molecules*, 1983, ISBN.

[16] C. J. Buczek, R. J. Freiberg, and M. L. Skolnic, *Laser injection locking*, Proc. IEEE **61** (1973), 1411.

[17] S. Bux, G. Krenz, S. Slama, C. Zimmermann, and Ph.W. Courteille, *Ultra-cold atoms in an optical cavity: Two-mode laser locking avoiding radiation pressure*, Appl. Phys. B **89** (2007), 181.

[18] G. Camy, Ch. J. Bordé, and M. Ducloy, *Heterodyne saturation spectroscopy through frequency modulation the saturating beam*, Opt. Comm. **41** (1982), 325, .

[19] J. S. Choi and J. C. Howell, *Paraxial ray optics cloaking*, Opt. Exp. **22** (2014), 29465, DOI.

[20] E. R. Cohen, *Uncertainty and error in physical measurements*, Rendiconti della Scuola Intern. di Fisica 'Enrico Fermi' **CX** (1992), 11.

[21] C. Cohen-Tannoudji, B. Diu, and F. Lao, *Quantum mechanics*, 1, vol. 1 & 2, 1977, ISBN.

[22] Ph. W. Courteille, D. J. Han, R. H. Wynar, and D. J. Heinzen, *New observation of Bose-Einstein condensation of ^{87}rb atoms in a magnetic top trap*, Proc. of SPIE **3270** (1998), 116.

[23] L. S. Cutler and C.L. Searle, *Some aspects of the theory and measurement of frequency fluctuations in frequency standards*, Proc. of the IEEE **54** (1966), 136.

[24] W. B. Davenport and W. L. Root, *An introduction to the theory of random signals and noise*, 1958, ISBN.

[25] W. Demtröder, *Laser spectroscopy*, 1988, ISBN.

[26] ———, *Atoms, molecules and photons: An introduction to atomic- molecular- and quantum physics*, Springer, 2006.

[27] G. Di Domenico, St. Schilt, and P. Thomann, *Simple approach to the relation between laser frequency noise and laser line shape*, Appl. Opt. **49** (2010), 4801, DOI.

[28] R. W. P. Drever, J. L. Hall, F. V. Kowalski, J. Hough, G. M. Ford, A. J. Munley, and H. W. Ward, *Laser phase and frequency stabilization using an optical resonator*, Appl. Phys. B **31** (1983), 97, .

[29] M. Ducloy and D. Bloch, *Theory of degenerate four-wave mixing in resonant doppler-broadened media II*, J. Physique **43** (1982), 57.

[30] A. R. Edmonds, *Angular momentum in quantum mechanics*, 1957.

[31] A. Einstein, *On the quantum theory of radiation*, Zeitschrift für Physik **18** (1917), 121.

[32] D. S. Elliott, Rajarshi Roy, and S. J. Smith, *Extracavity laser bandshape and bandwidth modification*, Phys. Rev. A **26** (1982), 12, .

[33] O. Föllinger, *Regelungstechnik*, 1985.

[34] ———, *Regelungstechnik: Einführung in die methoden und ihre anwendung*, Hütig, 2008.

[35] J. D. Gaskill, *Linear systems, fourier transforms and optics*, John Wiley & sons, 1978, ISBN.

[36] M. Gilowski, Ch. Schubert, M. Zaiser, W. Herr, T. Wuebena, T. Wendrich, T. Mueller, E. M. Rasel, and W. Ertmer, *Narrow bandwidth interference filter-stabilized diode laser systems for the manipulation of neutral atoms*, Opt. Commun. **280** (2007), 443.

[37] D. J. Griffiths, *Introduction to quantum mechanics*, Pearson Prentice Hall, New Jersey, 2005, ISBN.

[38] J. L. Hall, L. Hollberg, T. Baer, and H. G. Robinson, *Optical heterodyne saturation spectroscopy*, Appl. Phys. Lett. **39** (1981), 680.

[39] D. I. Herman, C. Weerasekara, L. C. Hutcherson, F. R. Giorgetta, and K. C. Coss, *Precise multispecies agricultural gas flux determined using broadband open-path dual-comb spectroscopy*, Science Advances **7** (2021), eabe9765.

[40] L. Hollberg, L. S. Ma, M. Hohenstatt, and J. L. Hall, *Precision measurement by optical heterodyne techniques*, Proc. SPIE **426** (1983), 91.

[41] R. Holzwarth, Th. Udem, T. W. Hänsch, J. C. Knight, W. J. Wadsworth, and P. St. J. Russell, *Optical frequency synthesizer for precision spectroscopy*, Phys. Rev. Lett. **85** (2000), 2264.

[42] R. Holzwarth, M. Zimmermann, Th. Udem, T. W. Hänsch, P. Russbüldt, K. Gäbel, R. Poprawe, J. C. Knight, W. J. Wadsworth, and P. St. J. Russell, *White-light frequency comb generation with a diode-pumped cr:lisaf laser*, Opt. Lett. **26** (2000), 1376.

[43] P. Horowitz and W. Hill, *The art of electronics*, Cambridge Universty Press, 2001, ISBN.

[44] S. Inouye, M. R. Andrews, J. Stenger, H.-J. Miesner, D. M. Stamper-Kurn, and W. Ketterle, *Observation of Feshbach resonances in a Bose-Einstein condensate*, Nature **392** (1998), 151, DOI.

[45] D. J. Jones, S. A. Diddams, J. K. Ranka, A. Stentz, R. S. Windeler, J. L. Hall, and S. T. Cundiff, *Carrier-envelope phase control of femtosecond mode-locked lasers and direct optical frequency synthesis*, Science **288** (2000), 635.

[46] R. K. Kaj, D. Bloch, J. J. Snyder, G. Camy, and M. Ducloy, *High-frequency optically heterodyned saturation spectroscopy via resonant degenerate four-wave mixing*, Phys. Rev. Lett. **44** (1982), 1251.

[47] H. Kogelnik and X. Y. Li, *Laser beams and resonators*, Appl. Opt. **5** (1966), 1550, DOI.

[48] P. Lesage and C. Au doin, *Characterization and measurement of time and frequency stability*, Radio Science (1979).

[49] M. D. Levenson and G. L. Eesley, *Polarization selective optical heterodyne detection for dramatically improved sensitivity in laser spectroscopy*, Appl. Phys. **19** (1979), 1.

[50] W. Lichten, *Precise wavelength measurements and optical phase shifts: I. general theory*, J. Opt. Soc. Am. A **2** (1985), 1869, .

[51] Zhixin Liu and R. Slávik, *Optical injection locking: From principle to applications*, J. Lightwave Techn. **38** (2020), 43.

[52] Zhixin Liu and Radan Slavík, *Optical injection locking: From principle to applications*, J. Lightwave Tech. **38** (2020), 43.

[53] R. Loudon, *The quantum theory of light*, Clarendon Press Oxford, 1982, ISBN.

[54] L. S. Ma, Ph. W. Courteille, G. Ritter, W. Neuhauser, and R. Blatt, *Spectroscopy of te_2 with modulation transfer: Reference lines for precision spectroscopy in yb*, Appl. Phys. B **57** (1993), 159.

[55] L. S. Ma and J. L. Hall, *Optical heterodyne spectroscopy enhanced by an external optical cavity: Toward improved working standards*, IEEE J. Quant. Electr. **26** (1990), 2006.

[56] H. Mann, H. Schiffelgen, and R. Froriep, *Einführung in die regelungstechnik*, Hanser-Verlag München, 2009, ISBN.

[57] T. Mayer-Kuckuk, *Atomphysik*, Teubner Studienbücher, 1985, ISBN.

[58] H. J. Metcalf and P. Van der Straten, *Laser cooling and trapping*, Springer, 1999.

[59] G. Milburn, *Intrinsic decoherence in quantum mechanics*, Phys. Rev. A **44** (1991), 5401, .

[60] P. W. Milonni and R. W. Boyd, *Momentum of light in a dielectric medium*, Adv. Opt. Phot. **2** (2010), 519, .

[61] K. Mølmer, Y. Castin, and J. Dalibard, *Monte-carlo wave-function method in quantum optics*, J. Opt. Soc. Am. B **10** (1993), 524, DOI.

[62] O. D. Mücke, R. Ell, A. Winter, Jung-Won Kim, J. R. Birge, L. Matos, and F. X. Kärtner, *Self-referenced 200 mhz octave-spanning ti:sapphire laser with 50 attosecond carrier-envelope phase jitter*, Opt. Exp. **13** (2005), 5163, .

[63] W. Nagourney, J. Sandberg, and H. G. Dehmelt, *Shelved optical electron amplifier: Observation of quantum jumps*, Phys. Rev. Lett. **56** (1986), 2797.

[64] A. Pikovsky, M. Rosenblum, and J. Kurths, *Synchronization: A universal concept in nonlinear sciences*, Cambridge, University press (2001).

[65] I. I. Rabi, *Space quantization in a gyrating magnetic field.*, Phys. Rep. **51** (1937), 652.

[66] N. F. Ramsey, *Molecular beams*, Clarendon Press, Oxford, 1985, ISBN.

[67] M. Rotenberg, N. Metropolis, R. Birins, and J. Wooten Jr., *The 3j and 6j symbols*, 1959, ISBN.

[68] Th. Sauter, R. Blatt, W. Neuhauser, and P.E. Toschek, *Observation of quantum jumps*, Phys. Rev. Lett. **57** (1986), 1696, .

[69] _____, *Quantum jumps observed in the fluorescence of a single ion*, Opt. Comm. **60** (1986), 287, .

[70] A. Schenzle, R. G. Devoe, and R. G. Brewer, *Phase modulation laser spectroscopy*, Phys. Rev. A **25** (1982), 2606, .

[71] E. Schrödinger, Brit. Journ. f. the Philos. of Science III (1952).

[72] J. H. Shirley, *Modulation transfer processes in optical heterodyne saturation spectroscopy*, Opt. Lett. **7** (1982), 537.

[73] J. J. Snyder, R. K. Kaj, D. Bloch, and M. Ducloy, *High-sensitivity nonlinear spectrocopy using a frequency-offset pump*, Opt. Lett. **5** (1980), 163.

[74] J. J. Di Steffano, A. R. Stubberud, and I. J. Williams, *Feedback and control systems*, Schaums outline series, McGraw-Hill, 1967.

[75] J. L. Stewart, *The power spectrum of a carrier frequency modulated by gaussian noise*, Proc. of the IRE **42** (1954), 1539.

[76] H. R. Telle, B. Lipphardt, and J. Stenger, *Kerr-lens, mode-locked lasers as transfer oscillators for optical frequency measurements*, Appl. Phys. B **74** (2002), 1.

[77] U. Tietze and Ch. Schenk, *Halbleiterschaltungstechnik*, ISBN.

[78] F. S. Vieira, F. C. Cruz, D. F. Plusquellic, and S. A. Diddams, *Tunable resolution terahertz dual frequency comb spectrometer*, Opt. Exp. **24** (2016), 30100, DOI.

[79] J. Weiner, V. S. Bagnato, S. Zilio, and P. S. Julienne, *Experiments and theory in cold and ultracold collisions*, Rev. Mod. Phys. **71** (1999), 1.

[80] J. Weiner and P.-T. Ho, *Light-matter interaction, fundamentals and applications*, John Wiley & Sons, Hokoken, New Jersey, 2003, ISBN.

[81] Amnon Yariv, *Quantum electronics*, 1967, ISBN.

[82] Amnon Yariv and P. Yeh, *Optical waves in crystals*, 2002, ISBN.

[83] Jun Ye, H. Schnatz, and L. W. Hollberg, *Optical frequency combs: From frequency metrology to optical phase control*, IEEE J. Sel. Top. QE **9** (2003), 1041.

Index